SPECTRAL SIGNATURES OF EXCITON-POLARONS IN TWO-DIMENSIONAL HYBRID LEAD-HALIDE PEROVSKITES

A Dissertation
Presented to
The Academic Faculty

By

Félix Thouin

In Partial Fulfillment
of the Requirements for the Degree
Doctor of Philosophy in the
School of Physics

Georgia Institute of Technology

August 2019

SPECTRAL SIGNATURES OF EXCITON-POLARONS IN TWO-DIMENSIONAL HYBRID LEAD-HALIDE PEROVSKITES

Approved by:

Dr. Carlos Silva, Advisor
School of Physics
Georgia Institute of Technology

Dr. Phillip N. First
School of Physics
Georgia Institute of Technology

Dr. Rick Trebino
School of Physics
Georgia Institute of Technology

Dr. Martin Mourigal
School of Physics
Georgia Institute of Technology

Dr. Jean-Luc Brédas
School of Chemistry and Biochemistry
Georgia Institute of Technology

Date Approved: July 15, 2019

One shouldn't work on semiconductors, that is a filthy mess; who knows whether any semiconductors exist.

Wolfgang Pauli in a letter to Peierls – 1931

À tout ceux et celles qui me portent sur leurs épaules.

ACKNOWLEDGEMENTS

Even though only my name is written on the front page of this document, I did not walk this tortuous path alone. The support and help of many was required for all of this to come to fruition and I would like to acknowledge here their contributions, direct or indirect, to the thesis you are holding in your hands. I would first like to thank all members of my thesis committee for accepting the laborious task of dissecting my work to verify that it upholds the high standards of the Georgia Institute of Technology. I am honored to have such a distinguished and prestigious committee evaluate what is so far the greatest achievement of my life.

At the heart of every experiment in condensed matter physics, there is at least one sample. Usually, there are dozens. The process of sample design for an experiment is an arduous one and I have been fortuitous enough to collaborate with talented and patient chemists, engineers and physicist to supply my experiments with the best samples in the world. I would like to sincerely thank Dr. Daniele Cortecchia and Pr. Petrozza for the constant stream of excellent, robustly characterized samples. Despite having an ocean between our laboratories, this collaboration was always easy and extremely fruitful. Every time I heard Ajay begin a sentence with ”Guess what Daniele just synthesized...”, I knew my jaw was about to drop. From what I have heard in the past months, I know his name will appear on many more amazing publications in the future. I would also like to highlight my esteemed colleague Marie-Hélène Tremblay's vivid intelligence and dedication to our collaboration. Not only does she seems to understand everything about materials and conjure any of them, she is not afraid to venture boldly into whatever field is necessary to push this understanding to new limits. If it were not for time constraints, our collaboration would have certainly shook the field of 2D-HOIPs down to its foundations. Sorry, Marie, I really wanted to graduate. I would also like to thank the members of the Stingelin group for the professionalism and expertise they brought with them in every collaboration. Even

though no publications came out of our collaborations, I learned (and drank) a lot.

Sometimes, extra theoretical muscles can push a publication much farther than any supplementary measurements could. When the time was right, I could always count on the input of brilliant theoreticians to do just that either through calculations or one of those illuminating discussions. I must give due credit to Pr. Bittner and his group for their numerous inputs in my academic career. To my continued amazement, they have always been able to quickly provide us with illuminating calculations and advice on measurements they had not heard about before lunch. I particularly want to acknowledge Dr. Xunmo Yang and Pr. Bittner for the rapid calculations they provided for the work presented in chapter 7. Without their input, this work would have been far less impactful than it is now. I would also like to thank Dr. Claudio Quarti and Pr. Beljonne for the calculations involved in the work of chapter 6. Without their contribution, the DFT calculations essential to reach such profound conclusions would have been missing, to the great detriment of all of this thesis work.

The quality of the multidimensional spectroscopy data ultimately reached at the end of my doctorate could have never been if it were not for the advice of the best ultrafast spectroscopists and engineers in the world. Pr. Giulio Cerullo and Dr. Cristian Manzoni dedicated on many occasions several hours to help me improve our home built NOPAs so that they could be reliably used to power highly-sensitive two-dimensional spectroscopy experiments. The hours they spent sharing with me their unpublished expertise and knowledge undoubtedly saved me many months or even years trying to improve it myself. I am extremely grateful for this and wish I could pay back the favor. The Nelson group, who originally designed COLBERT, has also been extremely generous of their time and knowledge with me. Before I even started ordering the parts to build COLBERT, they allowed me to spend a week in their laboratories, take pictures and ask questions relentlessly to the poor graduate student who had the bad luck of being assigned to this task. For this, I deeply indebted to Dr. Colby P. Steiner for sharing in a dedicated and pedagogical way

all he knew about the system. Furthermore, he also provided crucial guidance as I was building COLBERT. He was the one who pointed out that my pulse sequence was being sent backwards to the sample. I might have never realized had he not mentioned it.

Completing to fruition a PhD is easily the hardest thing I have done in my life. Even though it was an extremely positive experience, crushing setbacks and immense disappointments are part of the deal. All the successes in the world would have never allowed me to manage these alone. For this, I am forever indebted to my friends and family. Through their love, support, patience, and the occasional ”get back to reality” slap in the face, they shed light into dark moments and made successes even brighter. Even though most of them understand little about exciton-polarons, ultrafast optics or spectroscopy, they were just as important as all the other names mentioned so far in putting together this thesis work. I love you all.

I have also had the honor of being surrounded during these six years by wonderful colleagues. Even though some of them made the A-428 office a disaster in terms of productivity, they also made it the most lively office I have ever worked in. The vast collection of empty gin and vermouth bottles I left there can attest of the fun we had ”doing science” together. Of these, I must particularly salute Pascal’s contribution to my doctorate. Through his intellectual rigor and his dedication to his work, he has had a lasting influence on me which I carried on in my own work. Thanks to him and all of the others members of our group, my time in the Silva group was the most intellectually stimulating of them all. Thanks to your passion for science, I have shared with you memorable group meetings and corridor discussions about all sorts of topics which nourished my own reflections. Dr. Colin Nadeau-Brosseau has also been tremendously generous of his expertise in lasers, optics, spectroscopy, programming and all things manual that are part of the experimentalist’s life. To this end I am also grateful for the dedication and professionalism of Robert and Jean-Sébastien from the technical staff at UdeM. No request I ever came up with were too strange, complex or unimportant for them not to devote their entire talent to.

I am also grateful for the generosity of faculty members and students from other condensed matter groups at the Université de Montréal. The time was always right to ask Pr. Michel Côté about electronic structure calculations and exchange, Pr. Andrea Bianchi about superconductors, magnets and cryogenics or Pr. Richard Leonelli about spectroscopy, quantum optics and semiconductors. The quality of my work directly reflects the quality of the teaching I received from them and many others at UdeM both as an undergraduate and graduate student. I am also grateful for the financial support provided by the Fonds de recherche du Québec– Nature et technologies, the Natural Sciences and Engineering Research Council of Canada, the Faculté des arts et des sciences of the Université de Montréal, Georgia Tech's School of Chemistry, and Georgia Tech's School of Physics through the Amelio Award for Excellence in Research.

The contents of this thesis would have not been half as interesting as they are if it were not for the guidance and input of Dr. Ajay Ram Srimath Kandada. Not only is he able to turn the most obfuscated dataset into publishable gold, he has an outstanding scientific instinct and a boundless creativity. Indeed, early on in our investigation, he came up with the exciton-polaron hypothesis and the distinct couplings to the lattice. Although I met this idea with a lot of healthy scepticism, our experiments would prove him right time and time again. His creativity is only matched by his profound understanding of physics, which he carries with him in every discussion he is part of. I deeply enjoyed all of our scientific conversations for they were some of the most productive and intellectually stimulating ones I have had in my life. Indeed, my interactions with him completely changed the way I now see science for which I am extremely grateful. He showed me that science is a lot less about what we know than what we don't know. Science is about charging into these mysteries head-on. He embodies the qualities and traits every physicist should aspire to: boldness, rigor and curiosity. Now that he is starting his own research group, I am excited to see what wonderful discoveries his group and him will make in the future. I will miss our collaboration.

I kept the best for last. If I were to correctly praise Carlos for his role as my advisor during this thesis work, this section would be as lengthy as the rest of this thesis. Consider what follows a crude approximation of my gratitude. From the first day I set foot in Carlos' group, Carlos trusted me as if I were his research assistant. In conferences, he introduced me like he would introduce his longtime colleagues. When I came up with my own research ideas, he would encourage me to pursue them, and, putting his research funds where his mouth was, finance them with often little return on investment. This climate of trust and support was exactly what I needed to reach my full potential. The progress I made as a scientist is directly attributable to it and for that I am extremely grateful. Moreover, whenever I would need something, Carlos would provide. World-renowned expertise was accessible with a few emails or phone calls, brand-new equipment worth a small house would appear in our lab within a record time as well as the best samples and calculations in the world. Carlos's resourcefulness is mighty and he would split seas in half to provide his lab with the best conditions money could buy. I could have not hoped for a more well equipped laboratory then the one I played with during these past 6 years. Carlos's scientific impact on me is hard to overstate. He showed me that science is at its core about community, that it is through teamwork and cooperation, not competition, that humanity's understanding of the universe grows. It is by sharing and exchanging viewpoints, rather than confronting them, that a solid scientific theory emerges from the chaos of the scientific literature. For all of these reasons and the great time I had working with you during these past 6 years, I am deeply thankful. Above all, Carlos valued the success of his students and I felt it at every step of my doctorate. I could not have hoped for a better advisor.

TABLE OF CONTENTS

LIST OF TABLES

LIST OF FIGURES

SUMMARY

This thesis investigates the optical properties of two-dimensional hybrid organic inorganic perovskites (2D-HOIPs). These materials, consisting of stacked layers of metal-halide octahedras separated by long organic cations, feature a previously unexplained excitonic fine-structure in their low-temperature absorption and emission spectra. This thesis work shows that features within this fine-structure correspond to exciton-polarons of distinct polaronic nature. The first evidence to support this interpretation was provided by successfully reproducing the low-temperature absorption spectrum using a modified Wannier formalism supposing distinct excitonic states with contrasting couplings to the lattice. This hypothesis is then unambiguously confirmed by high-resolution resonant impulsive coherent stimulated Raman spectroscopy which revealed in detail the exact polaronic nature of each excitons within this fine structure. Having shown their distinct polaronic nature, we then show that it drives the relaxation dynamics of photoexcited species down this excitonic manifold. This highlights the importance of the proper consideration of these polaronic effects when optimizing these materials for optoelectronics. We also show, using two-dimensional coherent spectroscopy, that these effects protect the excitons from many-body interactions with other quasiparticles hinting at the importance of polaronic effects in polaritonic microcavities based on these materials. Finally, we also observe stable biexcitons in these materials up to room temperature using high-power two-dimensional coherent spectroscopy showing the importance of many-body interactions in these materials. Our conclusions are of broad fundamental importance to this class of materials for they suggests an avenue to unify the physics governing spectrally broad and narrow emitting 2D-HOIPs. Moreover, due to the high degree of tunability of their crystalline structure, 2D-HOIPs offer an ideal system on which to test models that account for both strong electron-hole and strong electron-phonon interactions. This is of fundamental importance to all two-dimensional polar semiconductors.

CHAPTER 1
INTRODUCTION

In 1926, Schrödinger proposed an equation that formalized de Broglie's view that all elementary particles, not just the photon, could have a wave-particle duality [1]. This equation, now called the Schrödinger equation, was a landmark in the development of quantum mechanics and provided an accurate formalism with which to predict the dynamics of non-relativistic particles. In principle, except for the fission of radioactive isotopes and spontaneous emission, this equation can fully describe with great accuracy all the properties of earth-occurring and man made materials known so far. In reality, this is only the case for one family of systems, the simplest materials of them all, hydrogen-like atoms. Any system more complex than these cannot be solved exactly and the solution of the associated Schrödinger equation becomes exponentially more demanding on computational resources with the number of degrees of freedom.

This opacity inherent to the Schrödinger equation is the driving force behind the field of condensed matter physics. Its goal is to discover conceptually and mathematically simpler models to accurately describe systems with a large number of degrees of freedom as well as tackle the emerging properties arising from this complexity. From these, new emergent physics can be discovered such as the BCS theory of superconductivity, topological insulators, quantum fluids and many more. Sometimes, these new emerging models paint a physical picture that is mathematically similar to other fundamental physical models such as those of Majorana fermions or massless Dirac particles in graphene. Given that these are manifested in man-made or naturally occurring materials, probing these phenomena is much easier that their high-energy physics counterparts. Emerging solid state physics model can even inspire high-energy physics, as was the case with the recent discovery of the Higgs boson whose theoretical formulation was inspired by the BCS theory of super-

conductivity [2]. Not only does progress in condensed matter physics affect the advancement of other disciplines, it also provides the scientific foundations of today's technological progress. Building a hierarchy of models to describe the properties of a family of materials with the desired amount of accuracy gives device engineers the required theoretical and conceptual tools to design the next generation of technological wonders. Therefore, materials which have great potential for both fundamental discoveries and technological applications are the most appealing systems to investigate.

Two-dimensional hybrid organic-inorganic perovskites (2D HOIPs) are a prime example of such a system. Not only do they strongly manifest nearly every phenomena discovered in direct bandgap semiconductors during the past century, they are also poised to be used in many novel technological applications. This family of solution-processable direct bandgap semiconductors consist of thin metal-halide inorganic layers separated by much longer organic cations. The inorganic layers where the carriers are confined can be reliably made a few atoms thin thus effectively confining carriers to a two-dimensional geometry. For this reason, they share many characteristics with the recently discovered monolayers of transition metal dichalchogenides (ML-TMDCs) such as very strong Coulomb correlation between carriers. This in turn yields high exciton and biexciton binding energies making them ideal for polaritonics even at room temperature. Contrarily to ML-TMDCs, these materials can be made as thick as required without affecting their electronic properties so that they can be used in powerful light emitting diodes or as a laser gain medium. Moreover, due to the presence of heavy metal atoms such as lead, strong spin-orbit effects are manifested in their electronic structure. Some reports even claim the presence of strong spin polarisation of the conduction bands due to a giant two-dimensional Rashba effect. Although this claim is debatable, this is a highly sought property for spintronics applications. Last but not least, the atomic bonds within the inorganic layers are of considerable ionic character, making electron-phonon effects potentially important. This aspect was given little attention in the literature despite strong evidences of large polaron formation in their bulk

counterparts as well as strong electron-phonon interaction. Faced with all these potentially large effects, building a hierarchy of models to describe these systems with various degrees of accuracy is challenging and has eluded the community for more than 20 years.

For instance, the nature of the first electronic excited states is unknown. While at first sight the Wannier exciton model seems to adequately reproduce the high temperature optical response, this breaks down at low temperature where the reduced thermal line broadening reveals a complex excitonic fine structure. All but one of the above phenomena have been claimed to account for this fine structure, echoing a similar debate in 3D HOIPs, but none have provided conclusive evidence of their claims. In this thesis, we provide on multiple spectroscopical fronts strong evidence for another interpretation of this excitonic fine structure: that each line represents a distinct exciton-polaron, quasiparticles composed of a Coulomb bound electron-hole pair entangled with lattice phonons.

This hypothesis will be expanded on in the rest of the thesis. The latter will be broken down as follows. In chapter 2, we introduce our hypothesis by first reviewing some concepts of condensed matter physics required to understand and interpret the prior work done on these systems. We will devote a large part of this chapter on the concepts of exciton, polaron and finally of exciton-polaron. These concepts will find their meaning when we review prior investigation on this family of materials at the end of the chapter. This thesis relies on the heavy use of advanced optical probes to reach its conclusions. Therefore, we devote chapters 3 and 4 to the theoretical and experimental aspects of these respectively. In chapter 5, we present our first publication on the matter where we explore the system's linear and non-linear optical response using a modified Wannier formalism to account for the fine structure and rationalize its complex lineshape. Doing so required the introduction of distinct coupling to low-frequency vibrational modes and prompted us to propose, without proof, the exciton-polaron hypothesis. In chapter 6, we provide unambiguous proof of the distinct electronic nature of each excitonic lines by measuring each feature's resonant Raman spectrum in the time domain showing that the excitonic fine structure cannot

arise from vibronic replicas. Furthermore, we also show that each excitonic line as well as the carrier continuum are coupled to different lattice vibration, thus proving that they each harbor a distinct polaronic character. In chapter 7, we propose that the peculiar excited state relaxation dynamics is a consequence of the distinct polaronic nature of each excitons and support this interpretation with a theoretical model. In chapter 8, we provide another unambiguous evidence of the distinct electronic character of each features. Their intrinsic homogeneous linewidths as well as their exciton-exciton and exciton-phonon scattering parameters were measured to be vastly different. The interaction parameters were also found to be two orders of magnitude lower than those found in ML-TMDCS. We attribute this to a polaronic protection effect, a screening of excitons by the polaronic cloud that surround them. In chapter 9, we investigate bound biexcitonic states in 2D-HOIPs and find them to be strongly bound, even at room temperature. The data shown in this publication also hints at a complex biexcitonic spectrum, a possible consequence of polaronic effects. This thesis is concluded by our conclusions on our own investigations in light of the state of the field and an outlook for the work we feel should be undertaken to further test this hypothesis. We nonetheless feel that the current work stands strongly as it is and urge others in the field to seriously consider the proposed hypothesis.

CHAPTER 2
NECESSARY ELEMENTS OF SOLID-STATE PHYSICS AND PRIOR INVESTIGATIONS

To properly understand our own investigatios of two-dimensional hybrid organic-inorganic perovskites, it is crucial to first understand a few elements of advanced solid-state physics. This chapter serves this purpose by providing an introduction to these concepts for someone with a graduate-level understanding of solid-state physics. To justify our choice of theoretical elements relevant to this thesis work, we first examine the measured crystal structure of these compounds as well as ab-initio electronic structure calculations. Then, we expand on these concepts in the following sections highlighting their most crucial aspects in the context of our investigation. Finally, we close this chapter by surveying the previous investigations that directly set the context of this thesis's work.

2.1 Atomic structure

Despite their names, two-dimensional or layered perovskites are not strictly speaking of the perovskite crystalline group for they do not share the cubic unit cell of the latter. They are nonetheless very similar as they both comprise of octahedral units encompassed in a cubic structure that are arranged to form a series of layered planes. The arrangement of these units within the planes, as well as the relative position of these planes within the unit cell, determines to which phase such a crystal belongs. In the context of hybrid organic-inorganic metal-halide two-dimensional perovskites (2D HOIPs), the Ruddlesden-Popper (RP) phase is by far the most common [3, 4] with over 200 compounds catalogued in the Cambridge Structural Database [5]. Luckily, it is also the simplest with a general formula given by $C_{n+1}M_nX_{3n+1}$ where M denotes a metallic atom, X a halogen atom, and C denotes a long molecular cation terminated by a positively charged ammonium group. This

mixed organic-inorganic nature is where these compounds get their names from. The crystal structure of a prototypical 2D HOIP, $(PEA)_2PbI_4$, (PEA=phenylethylammonium [6]) is shown to scale in Figure 2.1. In the RP phase, metal-halide octahedras within a layer are arranged in a square lattice with varying degrees of bond distortion depending on the choice of the organic cation. The interaction of the latter with its environment distorts the inorganic lattice and octahedras, sometimes quite considerably. This distortion is probably relevent to the optical properties of 2D HOIPs as it was empirically found that highly distorted inorganic lattices generally resulted in broad Stokes-shifted photoluminescence [7, 8].

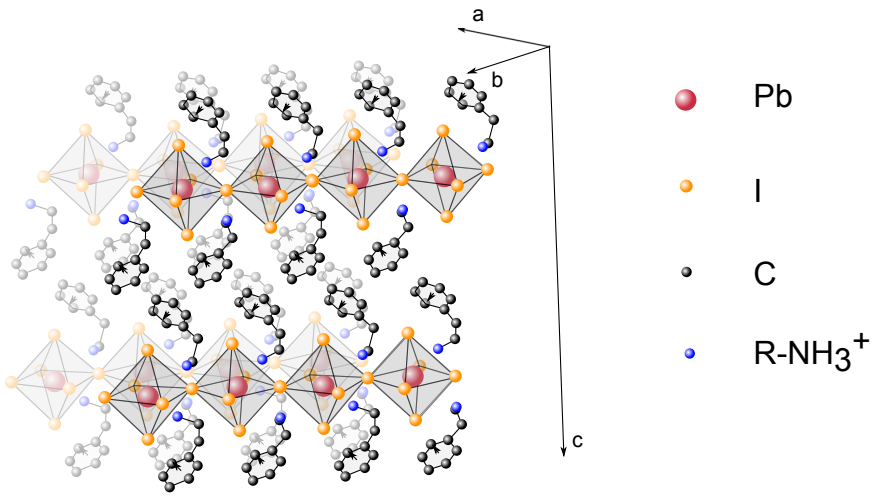

Figure 2.1: **Atomic structure of $(PEA)_2PbI_4$.** The structure shown was extracted from the compound's crystallographic data at room temperature from reference [9] and is to scale. The lattice vectors are also shown to scale with $|a|$=$|b|$=8.7 Å and $|c|$=33 Å. The arrows in the phenyl ring of the cations indicate the orientation of their visible face. The shaded structure corresponds to the normal one, albeit spatially shifted by $\mathbf{a}$.

Even when restricted to lead-halide HOIPs, the RP phase can be obtained for a wide variety of atomic compositions. Tin and lead can have been used as the metallic atom, chlorine, bromine and iodine as the halogen as well as a plethora of different organic molecules as a templating cation [4]. Exploring such a wide parameter space within the span of a typical doctorate would require inhuman efforts from one individual. For this reason, we

focused our efforts on a few simple compounds exhibiting no structural phase transition from cryogenic to room temperatures, narrow emission lines from which high-quality and stable samples can be synthesized and optical resonances comfortably within the visible spectrum. For these reasons, we decided to primarily investigate $(PEA)_2PbI_4$ as well as $(NBT)_2PbI_4$ (NBT=n-butylammonium) to support the extent of our conclusions to other materials as well. It is our hope that by studying simpler materials in greater details, deeper insights can be gained into their physics and applied to more complex materials later.

In the RP phase, each layers are intercalated with one another, separated by the long organic molecules. Ab-initio calculations based on density-functional theory (DFT) for a lead-iodine compound predict this material to be a semiconductor with a direct bandgap in the visible [10]. Moreover, these calculations predict that no electronic dispersion should occur along the axis perpendicular to the inorganic planes. This is a key signature of quantum confinement of carriers in the inorganic planes from which one can expect the presence of strong excitonic effects. How excitons arise from Coulomb correlations between carriers as well as their effect of optical properties is discussed in section 2.2. Due to the sizes and relatively large contrast in electronegativity of its constituent atoms, the bonds making up the inorganic layers are soft and of considerable ionic character. Therefore, electrons are expected be strongly responsive to displacement of atoms and vice-versa, a phenomenon know as electron-lattice or electron-phonon interactions. When these interactions become strong enough, carriers become quantum mechanically unseparable from the atomic displacements that follow them and are called polarons or exciton-polarons when these carriers are also strongly bound by the Coulomb force. The topics of electron-lattice interactions, polarons and exciton-polarons are central to this thesis work and are treated accordingly in section 2.3. Last but not least, the presence of heavy atoms in the inorganic layer is also expected to yield strong relativistic corrections to the electronic wavefunctions through an effect known as spin-orbit coupling. These effects can significantly alter

a material's electronic structure by lifting spin degeneracies, mixing the wavefunction of non-degenerate orbitals and changing the oscillator strength of many transitions. These effects take a different flavor when occurring in low-dimensional systems as it might be the case in 2D HOIPs. We briefly cover spin-orbit related effects and its approximations in system of reduced dimensionality in section 2.4. Finally, the diverse manifestations of these phenomena in 2D HOIPs investigated so far will be presented in section 2.4.

2.2 Excitons

Bloch's theorem states that the eigenstates of a particle in a spatially periodic potential are given by Bloch waves [11]. These periodic functions are each labelled by a wavevector, a direct consequence of the periodicity of the lattice, and a band index in the commonly used reduced-zone scheme. The energy of each of these states can be represented in a band diagram and fully characterizes the system's energetics. Crystalline solids are abundant physical systems where electrons are subject to a periodic potential due to the regular spatial arrangement of the crystal's atoms. However, due to the presence of other electrons, the single-particle picture breaks down and electronic degrees of freedom are no longer described by a single Bloch wave. In the non-interacting limit, also called a Fermi gas, the presence of other electrons is accounted for by using a properly anti-symmetrized many-body wavefunction built from many Bloch waves such as a Slater determinant or second quantization. In reality, electrons are charged particles and interact with each other through the Coulomb force. This dive into many-body physics drastically complexifies the task of accurately describing the behavior of realistic materials. For this reason, a plethora of models have been developed to easily account for many-body interactions such as Fermi liquid theory [12], Tomonaga-Luttinger liquid theory [13, 14] and BCS theory of superconductivity [15, 16] to name a few. In particular, the theory of excitons has been extremely successful at describing the optoelectronical properties of direct bandgap semiconductors.

The concept of excitons is almost as old as Bloch waves themselves, conceptualized shortly after by Frenkel [17] and then Wannier [18]. Both models attempt to solve the quantum dynamics of an electron-hole pair in a semiconductor subject to Coulomb forces between them. The quasiparticle that diagonalizes this many-body Hamiltonian is known as an exciton and is in this sense extremely similar to a Cooper pair in BCS theory. However, both exciton models use a vastly different approach to this end. The Frenkel exciton model poses the Hamiltonian from an atomic orbital basis between which excitations can hop, useful should electrons and holes be very tightly bound, while the Wannier exciton model starts from the perspective of interacting Bloch waves. In this section, we rigorously derive from a fundamental many-body Hamiltonian the hydrogen-like nature of Wannier excitons for both three and two-dimensional systems. We then discuss the consequences of this model, more specifically regarding its optical absorption spectrum, and discuss extensions to it to account for the presence of more than one electron-hole pair.

2.2.1 The Wannier-Mott model

Following the classic derivation of Hanamura and Haug [19], we start with the Hamiltonian for a two-band system in second quantization which reads as

$$\begin{aligned} H = \sum_{\mathbf{k},j} E_j^0(k) a^\dagger_{\mathbf{k}\,j} a_{\mathbf{k}\,j} + \frac{1}{2} \sum_{\mathbf{k}_1,\mathbf{k}_2,\mathbf{k}_3,\mathbf{k}_4} V^{c\,c\,c\,c}_{\mathbf{k}_1\,\mathbf{k}_2\,\mathbf{k}_3\,\mathbf{k}_4} a^\dagger_{\mathbf{k}_1\,c} a^\dagger_{\mathbf{k}_2\,c} a_{\mathbf{k}_3\,c} a_{\mathbf{k}_4\,c} \\ + \frac{1}{2} \sum_{\mathbf{k}_1,\mathbf{k}_2,\mathbf{k}_3,\mathbf{k}_4} V^{v\,v\,v\,v}_{\mathbf{k}_1\,\mathbf{k}_2\,\mathbf{k}_3\,\mathbf{k}_4} a^\dagger_{\mathbf{k}_1\,v} a^\dagger_{\mathbf{k}_2\,v} a_{\mathbf{k}_3\,v} a_{\mathbf{k}_4\,v} + \frac{1}{2} \sum_{\mathbf{k}_1,\mathbf{k}_2,\mathbf{k}_3,\mathbf{k}_4} V^{c\,v\,v\,c}_{\mathbf{k}_1\,\mathbf{k}_2\,\mathbf{k}_3\,\mathbf{k}_4} a^\dagger_{\mathbf{k}_1\,c} a^\dagger_{\mathbf{k}_2\,v} a_{\mathbf{k}_3\,v} a_{\mathbf{k}_4\,c} \\ + \frac{1}{2} \sum_{\mathbf{k}_1,\mathbf{k}_2,\mathbf{k}_3,\mathbf{k}_4} V^{c\,v\,c\,v}_{\mathbf{k}_1\,\mathbf{k}_2\,\mathbf{k}_3\,\mathbf{k}_4} a^\dagger_{\mathbf{k}_1\,c} a^\dagger_{\mathbf{k}_2\,v} a_{\mathbf{k}_3\,c} a_{\mathbf{k}_4\,v}, \end{aligned} \tag{2.1}$$

where $a^\dagger_{\mathbf{k}\,j}$ and $a_{\mathbf{k}\,j}$ are the fermionic creation and annihilation operators of an electron with wavevector $\mathbf{k}$ in the valence ($j = v$) or conduction ($j = c$) bands. The first term accounts for the electron's energy in the absence of other electrons and is dictated by the material's band structure. The two next terms arise due to intraband Coulomb scattering

while the last two terms arise from interband Coulomb scattering. It is the latter which will be responsible for excitonic effects. In particular, the last term is called the exchange scattering term, so-called since it vanishes when the particles are far apart, as we will show later. The Coulomb scattering coefficients are defined in terms of the Coulomb potential V as

$$V^{i\ j\ l\ m}_{\mathbf{k}_1\ \mathbf{k}_2\ \mathbf{k}_3\ \mathbf{k}_4} = \langle \mathbf{k}_1\ i, \mathbf{k}_2\ j | V | \mathbf{k}_3\ l, \mathbf{k}_4\ m \rangle, \tag{2.2}$$

where the bras and kets represent a two-body wavefunction composed of the direct product of two Bloch waves. In the derivation of 2.1, terms that do not conserve the number of pair excitations, such as $a^\dagger_{\mathbf{k}_1\ v} a^\dagger_{\mathbf{k}_2\ v} a_{\mathbf{k}_3\ v} a_{\mathbf{k}_4\ c}$, were discarded. While this is not an exact treatment of the full many-body Hamiltonian, the effects arising from these terms can be well approximated by replacing the vacuum permittivity in the Coulomb potential by the material's permittivity [20]. We can convince ourselves of this by noticing that the terms so neglected contribute to the polarization of the orbitals making up the valence and conduction bands and thus lead to screening of the electric field by these dipoles. To simplify this Hamiltonian, we now introduce the concept of a hole. In the situations we are interested in, the valence bands will be almost filled with electrons while the conduction band will be scarcely populated. Therefore, it is easier to talk about electron population in the conduction band and electron depopulation in the valence band. The absence of an electron is precisely what a hole is and can be rigorously defined by the hole or time-reversal transformation

$$K a_{\mathbf{k},v} K^\dagger = b_{\mathbf{k}}, \tag{2.3}$$

where K defines a unitary transformation and $b_{\mathbf{k}}$ is the hole annihilation operator. It is directly related to the valence electron annihilation operator by

$$a_{\mathbf{k},v} = b^\dagger_{-\mathbf{k}}. \tag{2.4}$$

A hole is therefore rigorously defined as the conduction band electron's anti-particle. Injecting this definition into equation 2.1 and rearranging the terms in normal order using the fermionic anti-commuting relations for creation and annihilation operators yields

$$H = E_0 + \sum_{\mathbf{k}} E_e(k) a^\dagger_{\mathbf{k}} a_{\mathbf{k}} + \sum_{\mathbf{k}} E_h(k) b^\dagger_{\mathbf{k}} b_{\mathbf{k}} + \frac{1}{2} \sum_{\mathbf{k}_1,\mathbf{k}_2,\mathbf{k}_3,\mathbf{k}_4} V^{c\,c\,c\,c}_{\mathbf{k}_1\,\mathbf{k}_2\,\mathbf{k}_3\,\mathbf{k}_4} a^\dagger_{\mathbf{k}_1} a^\dagger_{\mathbf{k}_2} a_{\mathbf{k}_3} a_{\mathbf{k}_4}$$
$$+ \frac{1}{2} \sum_{\mathbf{k}_1,\mathbf{k}_2,\mathbf{k}_3,\mathbf{k}_4} V^{v\,v\,v\,v}_{-\mathbf{k}_1\,-\mathbf{k}_2\,-\mathbf{k}_3\,-\mathbf{k}_4} b^\dagger_{\mathbf{k}_1} b^\dagger_{\mathbf{k}_2} b_{\mathbf{k}_3} b_{\mathbf{k}_4}$$
$$+ \frac{1}{2} \sum_{\mathbf{k}_1,\mathbf{k}_2,\mathbf{k}_3,\mathbf{k}_4} \left(V^{c\,v\,v\,c}_{\mathbf{k}_1\,\mathbf{k}_3\,\mathbf{k}_2\,\mathbf{k}_4} - V^{c\,v\,c\,v}_{\mathbf{k}_1\,\mathbf{k}_3\,\mathbf{k}_4\,\mathbf{k}_2} \right) a^\dagger_{\mathbf{k}_1} b^\dagger_{\mathbf{k}_2} b_{\mathbf{k}_3} a_{\mathbf{k}_4}, \quad (2.5)$$

where the energies and electron-hole interactions have been renormalized by exchange interactions through the hole transformation. We disregard shifts in the former and introduce the effective mass or parabolic bands approximation. We set the energy zero to be the top of the valence band and define the electron and hole energies as

$$E_e(k) = E_g + \frac{\hbar^2 k^2}{2m_e}, \quad (2.6)$$

$$E_h(k) = \frac{\hbar^2 k^2}{2m_h}, \quad (2.7)$$

where E_g is the electronic bandgap and $m_e > 0$ and $m_h < 0$ are the electron and hole effective masses respectively. While we suppose an isotropic band structure for simplicity's sake, this approach is still valid for anisotropic bands as shown by Dresselhaus in reference [21]. We can now solve the Hamiltonian in the basis of the most general single electron-hole pair state which reads

$$|X\rangle = \sum_{\mathbf{k},\mathbf{k}'} C_{\mathbf{k}\,\mathbf{k}'} a^\dagger_{\mathbf{k}} b^\dagger_{\mathbf{k}'} |0\rangle, \quad (2.8)$$

where $|0\rangle$ is the pair-wise vacuum state in which the conduction band is empty and the valence band filled with electrons. This form of the excitonic wave function is strikingly

similar to that of a Cooper pair states in BCS theory [16, 20]. Both are quasi-bosonic states [19] composed of pair-wise fermionic excitations of the vacuum ground state and diagonalize a many-body Hamiltonian. In the case of BCS theory, the interaction potential is mediated by phonons while photons are responsible for excitonic binding. We look for the coefficients $C_{\mathbf{k}\,\mathbf{k}'}$ such that $|X\rangle$ is an eigenstate which satisfies the eigenvalue equation $H|X\rangle = E_X|X\rangle$. This yields the following series of coupled linear equations

$$\left[E_e(k) + E_h(k') - E\right] C_{\mathbf{k}\,\mathbf{k}'} - \sum_{\mathbf{l},\mathbf{l}'} \left(V^{c\,v\,v\,c}_{\mathbf{k}\,-\mathbf{l}'\,-\mathbf{k}'\,\mathbf{l}} - V^{c\,v\,c\,v}_{\mathbf{k}\,-\mathbf{l}'\,\mathbf{l}\,-\mathbf{k}'}\right) C_{\mathbf{l}\mathbf{l}'} = 0. \tag{2.9}$$

We now introduce Wannier's approximation [18], valid when the paired electrons and holes are separated by many times the lattice constant or equivalently that they have a small crystalline momentum or wavevector. In this limit, the electron and hole Bloch waves become unmodulated Bloch states and thus define an orthonormal basis. This reduces the Coulomb interaction terms defined in equation 2.2 to

$$V^{c\,v\,v\,c}_{\mathbf{k}\,-\mathbf{l}'\,-\mathbf{k}'\,\mathbf{l}} \approx \frac{1}{V^2} \int \mathrm{d}^3\mathbf{x}\mathrm{d}^3\mathbf{y} \exp\left[i(\mathbf{l}-\mathbf{k})\cdot\mathbf{x} + i(\mathbf{l}'-\mathbf{k}')\cdot\mathbf{y}\right] \frac{e^2}{4\pi\epsilon|\mathbf{x}-\mathbf{y}|}, \tag{2.10}$$

$$V^{c\,v\,c\,v}_{\mathbf{k}\,-\mathbf{l}'\,\mathbf{l}\,-\mathbf{k}'} \approx 0, \tag{2.11}$$

where ϵ is the crystal's electric permittivity in MKS units. The direct term simply becomes a regular Coulomb interaction and the exchange term vanishes. Injecting this result into equation 2.9 and taking its Fourier transform, we get the famed Wannier equation

$$H_{\mathrm{ex}}\phi(\mathbf{x}_e, \mathbf{x}_h) = E_{\mathrm{ex}}\phi(\mathbf{x}_e, \mathbf{x}_h), \tag{2.12}$$

where

$$H_{\mathrm{ex}} = -\frac{\hbar^2}{2m_e}\nabla_e^2 - \frac{\hbar^2}{2m_h}\nabla_h^2 + E_g - \frac{e^2}{4\pi\epsilon|\mathbf{x}_e - \mathbf{x}_h|} \tag{2.13}$$

and

$$\phi(\mathbf{x}_e, \mathbf{x}_h) = \sum_{\mathbf{k},\mathbf{k}'} C_{\mathbf{k},\mathbf{k}'} \exp\left[i\mathbf{k}\cdot\mathbf{x}_e + i\mathbf{k}'\cdot\mathbf{x}_h\right], \tag{2.14}$$

which relates the exciton wave function to the coefficients $C_{\mathbf{k},\mathbf{k}'}$. Equation 2.13 should be familiar to anyone with a formal education in physics for it is of the same form as that of the hydrogen atom's Hamiltonian. The bound and unbound solutions to this equation are obtained through the familiar technique of variable separation and transition to the center-of-mass and relative coordinate systems [22, 23]. This brings about a new interpretation of the absorption spectrum of direct bandgap semiconductors. Unbound solutions to equation 2.12 are analogous to the hydrogen atom's ionization continuum. In the context of semiconductors, these states make up the so-called free-carrier continuum corresponding to optical transitions from the valence to the conduction band in the single particle picture. The bound state solutions of equation 2.12 are commonly known as Wannier excitons and their spectrum has the same functional form as that of the hydrogen atom albeit contracted due to the increased electric permittivity. Their energies from the ionization continuum, or binding energy, depends on the dimensionality of the system. In the three-dimensional case, we get

$$E_n = -E_0 \frac{1}{n^2} \quad \text{with } n = 1, 2, 3, ... \tag{2.15}$$

and in the two-dimensional case

$$E_n = -E_0 \frac{1}{(n+1/2)^2} \quad \text{with } n = 0, 1, 2, ... \tag{2.16}$$

where

$$E_0 = \frac{e^2}{8\pi\epsilon a_0} \tag{2.17}$$

is the excitonic Rydberg energy,

$$a_0 = \frac{4\pi\hbar^2\epsilon}{e^2 m_r} \tag{2.18}$$

is the exciton's Bohr radius and

$$m_r = \frac{m_e m_h}{m_e + m_h} \tag{2.19}$$

is the exciton's reduced mass. Using these equations, one can use the measured excitonic binding energy to extract the excitonic Bohr radius. This quantity is extremely useful to estimate the carrier densities at which an exciton gas becomes degenerate [24, 25], enters the electron-hole plasma regime [26, 27], or when many-body effects become important. It is also useful to assess the validity of the Wannier approximation, that of small relative momentum and therefore large inter-species separation with respect to the lattice constant. As we have shown right before equation 2.10, the Wannier approximation fails when an excitonic orbital is smaller than the lattice constant. A treatment based on atomic orbitals rather than plane waves, such as that of Frenkel excitons [17], is then more adequate. However, one should not immediately discard the validity of the Wannier approximation when faced with high excitonic binding energies. The system's dimensionality plays an important role there too. The consequences of quantum confinement, the reduction of the system's dimensionality, are manifest in the exciton's binding energy. All things being equal (same carrier effective masses and electric permittivity), equations 2.15 and 2.16 tell us that an exciton in a two-dimensional system will have its binding energy increased fourfold in comparison to a three-dimensional system. Therefore, when carriers are strongly confined along two-dimensions, excitons can be strongly bound while still harboring orbits spanning many unit cells and are thus adequately described by the Wannier model. The excitonic binding energy is often wrongly used as a criteria to distinguish between Wannier excitons and other models of excitonic correlations such as Frenkel excitons. As we have shown in details, Wannier excitons stem from correlations between electron and hole Bloch waves induced by the Coulomb force. Frenkel excitons, however, stem from spatial correlations between occupied and unoccupied neighbouring atomic orbitals through the possibility of energy transfer or hoping in the lattice. It is important to recognize that the physical picture of these two models are different and approximate the many-body interacting system in en-

tirely different ways.

It is important to mention a few potential pitfalls of the above treatment. First, when comparing the two- and three-dimensional cases, the effective masses of the carriers were taken to be the same. This implies that the band structure in the unconfined dimensions remained the same even down to atomic thicknesses. This assumption is found to fail spectacularly in some systems like transition metal dichalcogenides and graphene where the electronic structure changes abruptly when they are stripped down from few to a single atomic layer [28]. One must then be very cautious when using bulk values to predict the excitonic properties in systems where carriers are confined to a single atomic layer. Secondly, in physical realizations of quantum confinement, the confining structure is often embedded in a host of different composition such as AlGaAs for GaAs quantum wells. The assumption of isotropic electric permittivity therefore fails, but can be accounted for by using a modified coulomb potential in Wannier's equation such as those arising from the image charge method. These effects, also called dielectric confinement effects, can be important when the host material has a significantly lower electric permittivity than that of the thin active layer. Lastly, there are some situations in which carriers are not strictly confined to a two-dimensional plane but rather trapped inside a narrow well. The addition of a supplementary confinement potential to Wannier's equation can also account for these spatial confinement effects that do not modify the electronic band structure.

The Wannier model has been found to accurately predict the optical properties of most inorganic direct bandgap semiconductors such as Cu_2O [29, 30], bulk GaAs [31] and quantum wells [32], ZnO [33], PbI_2 [34] and many more as well as indirect bandgap semiconductors like silicon and germanium [35]. Due to the omnipresence of excitonic energy levels in direct bandgap inorganic semiconductors, some have wrongly [36] schematized the energy diagram of Coulomb correlated systems by adding sub-bandgap levels in the free-carrier picture. In the free-carrier picture, shown in Figure 2.2a, electronic eigenstates

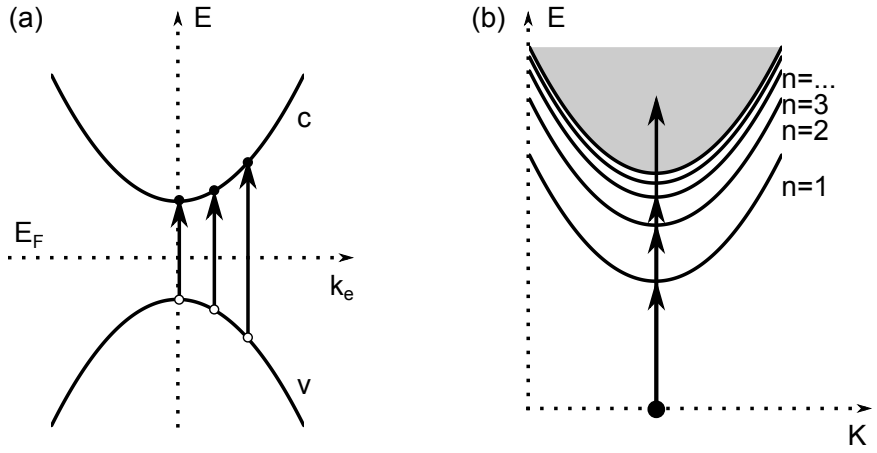

Figure 2.2: **Comparison of the free-carrier and exciton pictures for a direct bandgap semiconductor.** The free-carrier picture (a) is in comparison with the excitonic picture (b). Arrows represent examples of dipole allowed optical transitions. In the free-carrier picture. The states involved in an optical transition, the wavevector labelling the states and the curvature of the bands are of entirely different nature in these two picture and are therefore incompatible.

are labelled by their band index and their wavevector. The latter is possible solely because of the Hamiltonian's spatial periodicity. The addition of a Coulomb potential to the Hamiltonian breaks this periodicity and the electron or hole wavevector is no longer an adequate quantum number with which to label the Hamiltonian's eigenstates. The free-carrier picture is invalidated by the Coulomb interaction. Even if it did remain valid, the exciton wavevector corresponds to the electron-hole pair's center of mass motion and is incompatible with the single particle wavevector. It is therefore impossible to represent excitonic energy levels in the free-carrier picture. To do so, one would rather have to speak of distributions in the free-carrier picture which would be cumbersome and would say little about energetics but would be closer to ARPES measurements on excitonic systems [37]. The proper representation for energy eigenstates is that of the excitonic picture, shown in Figure 2.2b. Both pictures share the same ground state: an empty conduction band and a valence band filled with electrons. The ground state in the excitonic picture is a single point at a total momentum of $K = 0$ and corresponds to the trivial solution to Wannier's equation. Due to light's vanishingly small momentum, only vertical transitions to the various excitonic orbitals are

allowed. The Hamiltonian's translational symmetry with respect to the electron-hole pair's center of mass has excitons behave as free particles with an effective mass that is the sum of that of its constituents. This leads to a parabolic dispersion with increasing K. As the orbitals get closer and closer in energy with increasing n, a quasi-continuum forms E_0 above the lowest excitonic orbital. An exciton's binding energy is therefore a measure of the stability of excitons to ionization at a given temperature. If the excitonic binding energy is much larger than the thermal energy, excitons are said to be stable quasiparticles. This excitonic picture makes hot carrier relaxation, exciton formation and ionization processes conceptually much simpler by explicitly presenting in the same picture an exciton's energy and momentum. For instance, the connection between two excitonic energy level through a phonon of given wavevector and energy is easily identified. Moreover, in this picture hot carrier relaxation is not conceptually distinct from relaxation between atomic orbital and thus can be modelled using similar theoretical tools.

2.2.2 The absorption spectrum of excitonic systems

Now that the system of interacting electrons and holes has been diagonalized and that its eigenstates are known, we can calculate its optical properties using our favorite method, be it perturbation theory [38] or a treatment based on optical Bloch equations [23]. Doing so, one can compute the absorption spectrum $\alpha(\omega)$ of an excitonic system and obtain for the two-dimensional case that

$$\alpha(\omega) \propto \frac{\hbar\omega}{E_0}\left[\sum_{n=0}^{\infty}\frac{4}{(n+1/2)^3}\delta\left(\Delta+\frac{1}{(n+1/2)^2}\right)+\Theta(\Delta)\frac{e^{\frac{\pi}{\sqrt{\Delta}}}}{\cosh(\frac{\pi}{\sqrt{\Delta}})}\right]\otimes f(\omega), \quad (2.20)$$

where $\Delta = (\hbar\omega - E_g)/E_0$, $\Theta(\Delta)$ is the Heaviside step function, $\delta()$ is Dirac's delta function, $\otimes$ denotes a convolution, and $f(\omega)$ is the lineshape function for optical transitions. The latter is much more complex to calculate than the previous treatment and depends

on the excitons' interactions with its surrounding environment, be it thermal fluctuations, many-body interactions or the quantum electrodynamic vacuum [39]. Equation 2.20 is known as Eliott's formula [38] and can be derived for systems of any dimensionality. For a lorentzian lineshape with a full width at half maximum (FWHM) of 3 meV, the absorption spectrum of a semiconductor with a bandgap of 2 eV and an excitonic Rydberg energy of 50 meV is plotted in Figure 2.3.

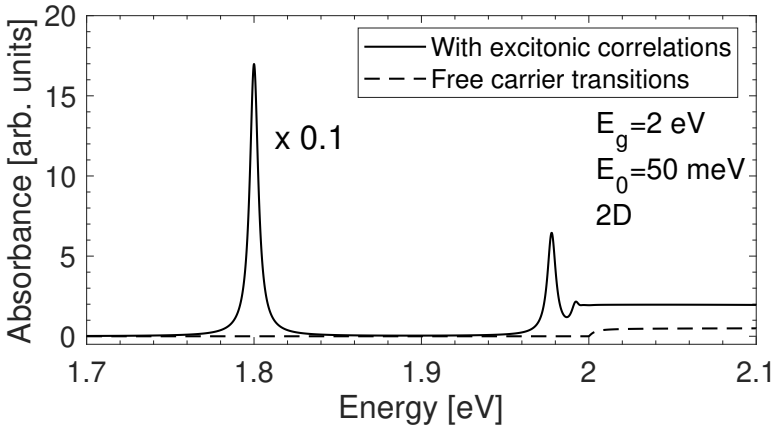

Figure 2.3: **Absorption spectrum of a direct bandgap 2D semiconductor with and without excitonic correlations.** The full and dashed lines respectively represent the absorption spectrum with and without excitonic correlations. A 3 meV wide (FWHM) Lorentzian profile was used as the lineshape function and an excitonic Rydberg energy of 50 meV as well as a bandgap of 2 eV were used. The lowest excitonic line was scaled down by a factor of 10 to better show the contribution from other excitonic energy levels and the ionization continuum.

For comparison, the absorption spectrum predicted for free-carrier transitions in the absence of Coulomb correlations is also plotted for the same material parameters. The most striking feature of the absorption spectrum of excitonic system is the appearance of a sharp and strong resonance below the absorption continuum. This strong feature arises due to a transition from the ground state to the 1s excitonic orbital and its shift from the continuum edge is a direct measure of the excitonic binding energy. Other lines below the continuum are also observed and correspond to transitions to higher lying excitonic states. Their intensities decrease with n^{-3} and quickly vanish into the contnuum. However, using ultra-high

resolution absorption spectroscopy, the presence of up to 25 of these hydrogenic lines before the ionization continuum has been observed in a naturally occurring Cu_20 crystal [40]. The broadening of the lineshape profile may, however, obscure the observation of these other states. At higher energies, the sharp excitonic lines merge into a broad absorption continuum. In the single particle picture, this feature corresponds to transition from the valence band to the unoccupied conduction band states. In the excitonic picture, it corresponds rather to transitions into an ionization quasi-continuuum. Excitonic effects also impact this feature by first drastically increasing the absorption coefficient in this spectral region compared to the free-carrier case, the so-called Coulomb enhancement [23]. Moreover, through the presence of broadened excitonic lines, it also obscures the edge of this carrier continuum, potentially making the measurement of the bandgap energy challenging. Being the lowest lying excited states, they also dominate carrier relaxation dynamics either through their luminescence or non-radiative electron-hole recombination. Therefore, the optical response of direct bandgap semiconductors with strong Coulombic interactions is dominated by the contribution from excitonic effects. Optical probes are therefore ideal to study these systems and the presence of excitonic effects in a given material is easily deduced from them.

2.2.3 Trions, biexcitons and other many-body interactions

When using equation 2.8 to define the basis in which to express the Hamiltonian of equation 2.5, we made a crude approximation. Indeed, by choosing this basis we restricted our treatment to that of a single electron-hole pair. This approach is usually valid in a low electron-hole pair density regime such as those typical of sunlight exposure but fails to describe regimes of higher densities crucial to laser or LED operation. In this case, the possibility of a higher number of electron and holes must be considered. One could go about in a similar way as that described in the previous sections and would end up with an infinite hierarchy of equations of motion for each order in electron-hole correlations [41].

This hierarchy then needs to be truncated to the desired level of approximation. However, these effects can be understood by extending the analogy of a Wannier exciton as an hydrogen atom to a greater number of carriers. In this case, quasiparticles arising from three carriers are called charged excitons or trions and are akin to H_2^+ or H_2^- depending on their overall charge. These complexes have been reported in many semiconductors with strong Coulomb interactions such as monolayer transition metal dichalcogenides [42]. Biexcitons occur when two electrons and two holes form a bound state, a molecule akin to H_2 and have also been observed in many semiconducting systems such as GaAs quantum wells [43] and monolayer TMDCs [44]. Neutral bound state of many more excitons such as triexcitons and quadriexcitons have also been observed in GaAs quantum wells [45] all the way to electron-hole droplets [46] or liquid [47]. At much higher densities, a small fraction of ionized excitons will release free-carriers which can screen the Coulomb interaction holding excitons together. This will ionize more and more excitons until they are not stable anymore due to the large screening from free-carriers. This is known as the ionization catastrophe [48] and occurs when the dilute insulating exciton gas becomes a conducting electron-hole plasma. This transition is also called the excitonic Mott transition [26] and the incorporation of this phenomenon in the Wannier model yields the Wannier-Mott model.

Many-body interactions can also have more subtle effects on excitons. One of these is exciton-exciton elastic scattering which conserves energy and momentum but reduces the coherence time of excitonic wavefunction without changing their lifetimes. This is the case since, as far as a single exciton is concerned, the other excitons act like a thermal bath and thus affect it in a similar way leading to the decoherence of its wavefunction. This effect is manifested in the homogeneous linewidth of optical transitions involving excitons and is strongly density dependent [49]. It is a very sensitive probe of the strength of Coulomb interaction of excitons and can be used to validate models regarding their scattering with other quasiparticles. It is also a phenomenon crucial to the physics of polaritons and their

condensation into a quantum fluid [50].

2.3 Interaction of electrons with the atomic lattice

Fundamentally, solids are held together because of the attraction between an atom's nucleus and the surrounding electrons and quantum mechanical exchange effect. Simply put, when atoms are closely packed together, electrons feel the atomic attraction of neighbouring atomic nuclei and form bonds between atoms. The exact nature of these bonds depend on the atoms and the number of electrons that accompany them. Conversely, atoms feel the electronic distribution surrounding them and adjust to it so as to minimize their potential energy. Electrons then adjust to this new atomic distribution and vice-versa until the electron-atom system has reached an equilibrium. For crystals, this new atomic arrangement is what gives rise to the periodic potential of which Bloch waves stem from. Therefore, when an electron is promoted from the valence band to the conduction band, the electronic density is changed slightly. The atomic positions then adjust to this change and thus modify the potential felt by electrons after the excitation, a phenomenon completely ignored in our previous treatment of interacting electrons in solids. Furthermore, given the ionic character of 2D HOIP lattices, these effects are expected to be strong. In this section, we discuss the various consequences of electron-lattice interactions starting from the simple Franck-Condon model to more involved polaronic and exciton-polaronic models. Their effects on the electronic structure as well as optical properties will be highlighted to guide us through the conclusions of reports prior to this thesis' work as well as those contained herein.

2.3.1 The Franck-Condon model

This picture of electronic transitions followed by atomic relaxation is taken quite literally in the case of the Franck-Condon model [51, 52]. It supposes a system whose electronic spectrum is composed of two discrete states $|g\rangle$ and $|e\rangle$ to which correspond different op-

timal lattice configurations. These configurations are represented by vectors $\mathbf{q}^{(g)}$ and $\mathbf{q}^{(e)}$ in the space of the system's normal coordinates of atomic motion. These vectors are DN dimensional where N is the number of atoms present in the system and D its dimensionality. Due to the atoms' much greater inertia, the absorption of a photon instantaneously promotes the system from the ground state $|g\rangle$ to the excited state $|e\rangle$. The atomic positions then relax from $\mathbf{q}^{(g)}$ to $\mathbf{q}^{(e)}$ before the system can relax to the electronic ground state. The absorption and emission spectra predicted by this model can be easily calculated making it a powerful and accurate tool to interpret molecular spectroscopy. The separation in time scales between electronic and atomic relaxation can be accounted for by separating the system's wavefunction $|\Psi\rangle$ into its atomic $|\psi_a\rangle$ and electronic parts $|\psi_e\rangle$, the so-called the Born-Oppenheimer approximation [53], so that

$$|\Psi\rangle = |\psi_e\rangle \otimes |\psi_a\rangle, \tag{2.21}$$

where $\otimes$ is the tensor product between these states in different vector spaces. We suppose that during absorption and emission, only small atomic displacements will occur. This allows us to approximate the atomic potentials in the ground and excited electronic states by harmonic oscillators of angular frequency ω_0 and force constant k displaced from each other by ΔQ in normal-coordinates space. The atomic spectrum is therefore discrete and given by a ladder of states each separated by $\hbar\omega_0$ in energy. These states $|n, \nu\rangle$ are represented by the electronic state index $n \in \{g, e\}$ as well as a vibrational index $\nu \in \{0, 1, 2, 3, ...\}$. Before the absorption of light, the system is in the ground electronic and atomic state. By Fermi's golden rule, the optical transition probability from this state to all of the excited states $P^{\text{abs}}_{0\mapsto\nu}$ is given by

$$\begin{aligned} P^{\text{abs}}_{0\mapsto\nu} &\propto |\langle g| \otimes \langle g, 0|\hat{d}|e, \nu\rangle \otimes |e\rangle|^2 \\ &\propto |d_{ge}|^2 |\langle g, 0|e, \nu\rangle|^2, \end{aligned} \tag{2.22}$$

where the dipolar moment operator $\hat{d}$ only affects the electronic degrees of freedom. The transition probability is given by the product of the electronic transition's dipolar moment $|d_{ge}|^2$ with the overlap between the atomic wavefunctions also known as the Franck-Condon factor. Using the definition of the harmonic oscillator eigenstates through Hermite polynomials and a table of Gaussian-like integrals, the Franck-Condon factor is found to yield

$$|\langle g,0|e,\nu\rangle|^2 = \frac{Z^\nu}{\nu!}e^{-Z}, \tag{2.23}$$

where

$$Z = \frac{1}{2}\frac{k(\Delta Q)^2}{\hbar\omega_0} \tag{2.24}$$

is called the Huang-Rhys factor. The absorption spectrum of this molecular system is therefore

$$\alpha(\omega) = \sum_{\nu=0}^{\infty}\delta(\hbar\omega - E_0 - \nu\hbar\omega)\frac{Z^\nu}{\nu!}e^{-Z} \otimes f(\omega), \tag{2.25}$$

where $\otimes$ denotes a convolution, $f(\omega)$ the lineshape function and E_0 the energy between the ground and excited electronic states. As shown by the orange curves of Figure 2.4, the absorption spectrum is therefore composed of a series of equally spaced lines distributed according to a Poisson distribution. The presence of a vibrational degree of freedom does not increase the overall oscillator strength of the ground to excited state transition, but merely redistributes it along these supplementary lines called vibronic replicas. The emission spectrum can be calculated in a similar fashion. This time, we suppose that the vibrational relaxation time is very short compared to the electronic relaxation time. This approximation, called Kasha's rule [54], implies that at temperatures lower than $\hbar\omega_0$ all emission processes will begin with the lowest vibrational state of the excited electronic state. Since the Huang-Rhys factor is even with respect to the potential displacement, the

emission probability $P^{\mathrm{em}}_{0\mapsto\nu}$ is also given by

$$\begin{aligned} P^{\mathrm{em}}_{0\mapsto\nu} &\propto |d_{ge}|^2 |\langle e,0|g,\nu\rangle|^2 \\ &\propto P^{\mathrm{abs}}_{0\mapsto\nu} \end{aligned} \tag{2.26}$$

from which we can directly infer the emission spectrum $I(\omega)$ to be

$$I(\omega) = \sum_{\nu=0}^{\infty} \delta(\hbar\omega - E_0 + \nu\hbar\omega) \frac{Z^\nu}{\nu!} e^{-Z} \otimes f(\omega) \tag{2.27}$$

and is therefore a mirror image of the absorption spectrum, as shown by the blue curve of Figure 2.4. This model has been extremely successful at describing the optical properties of molecules in the gas phase [53] and similar lineshapes are also observed in more complex aggregated systems [55]. Due to the discrete nature of its eigenstates, the absorption and emission spectra of Wannier excitons coupled to the lattice's motion can also be described using the Franck-Condon model provided they sufficiently displace the lattice upon their creation. Therefore, absorption or emission spectroscopies can be used to infer the magnitude and direction of the atomic potential energy surface (PES) displacement.

However, in some situations, these techniques may be inadequate for this purpose such as when the line broadening from the electronic part of the wavefunction is too large, when the electronic states are coupled to low frequency vibrations or when the displacement is too small. In these cases, such as the one plotted in dash dotted line in Figure 2.4, resonance Raman spectroscopy may be the only tool left to reliably measure this displacement [56]. Just like non-resonant Raman spectroscopy, resonance Raman spectroscopy is an inelastic light-scattering technique that probes the vibrational modes in a solid or molecule. From the energy shift and polarization of the scattered light with respect to the incident beam, one can infer the energy and symmetry of the system's vibrational modes. By tuning the incident beam's energy in resonance with a transition between two electronic states, the modes displaced by this electronic transition will see their signature in the resonant Ra-

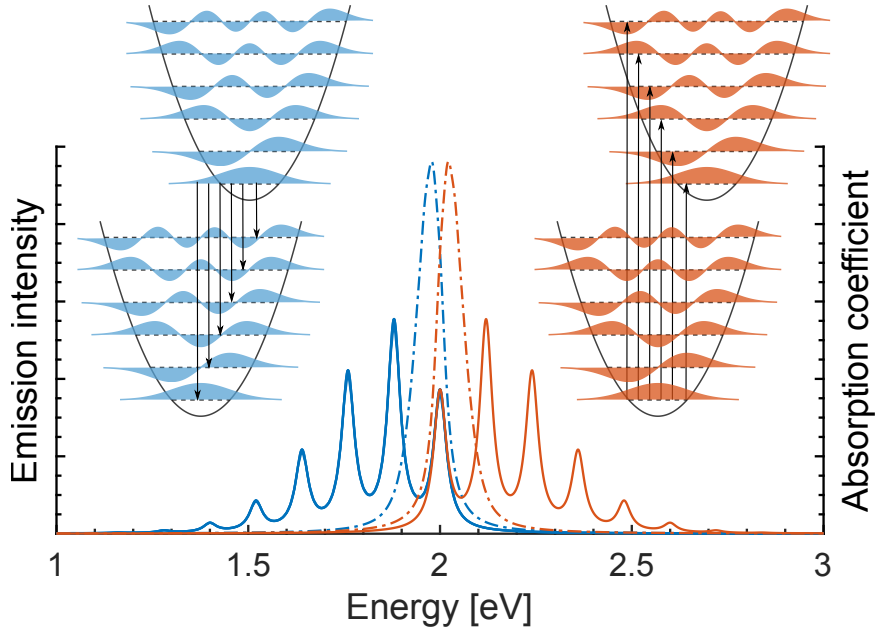

Figure 2.4: **Absorption and emission spectra predicted by the Franck-Condon model.** The blue and orange curves correspond to the absorption and emission spectra respectively. The spectra were plotted for an E_0 of 2 eV, a Huang-Rhys factor Z of 1.5, a vibrational energy of $\hbar\omega_0$=120 meV (solid lines) and 20 meV (dash dotted lines) and a lorenztian line-shape of 20 meV FWHM. The transitions between states responsible for these spectra are drawn in insets with matching colors.

man spectrum be amplified by orders of magnitude when compared to the non-resonant case [57]. This amplification is very large and the resulting signal is directly proportional to the displacement's magnitude. The spectral shifts from the incident beam's energy line remain very small. Therefore, as one can see from the optical spectra, such a measurement remains very challenging. The relatively weak resonant Raman signal might be drowned in the strong photoluminescence produced by the excitation laser. This case is typical of most HOIPs and require more advanced spectroscopic techniques to extract the coupling between excited electronic states and the lattice such as time-domain techniques, the subject of section 3.3.

Upon inspection of the absorption and emission spectra we just calculated, one could be tempted to naively assign each peak to a transition between distinct electronic states and the ground state. A correct understanding of the Franck-Condon model and the nature of

such spectral features reveals this assignment to be entirely wrong. All of these transitions involve a single electronic excited state coupled to a single atomic vibration. It is for this exact reason that the additional lines shifted from E_0 by multiples of the vibrational energy are called vibronic *replicas*. Therefore, apart from changes in its overall amplitude, the same resonant Raman spectrum will be obtained when pumping either replicas. This can be used to the spectroscopist's advantage when the replicas are clearly resolved by pumping a replica far from the strong photoluminescence signal. In this case, the signal is strong, free of background from photoluminescence and can be used along the absorption and emission spectra to accurately estimate the excited state potential energy surface displacements.

2.3.2 Interaction between electrons and a deformable continuum

The Franck-Condon model accounts for the interaction of molecular orbitals with molecular vibrations. What about the interaction of a continuum of electronic states (electrons) with a continuum of vibrational states (phonons)? Such a treatment gives rise to polarons: quasiparticles of both electronic and deformational nature analogous to bowling balls on a mattress. Polarons, and more specifically exciton-polarons, are at the core of the work of this thesis and the following intends to highlight that the existence of such quasiparticles in a stronlgy polar semiconductor is far from controversial. In the following, we will first discuss polarons using Emin's scaling formalism in the adiabatic limit [58]. This formalism is mathematically much simpler than more rigorous approaches (such as the Fröhlich Hamiltonian [59]) and still gives powerful insights into the physics of polarons. Suppose a single carrier of mass m and charge e interacting with a deformable continuum. The deformation of this continuum at a position $\mathbf{u}$ is denoted by $\Delta(\mathbf{u})$ and effectively shifts the energy of an electron at $\mathbf{r}$ by

$$V(\mathbf{r}) = \int \mathrm{d}\mathbf{u} Z(\mathbf{r}-\mathbf{u})\Delta(\mathbf{u}) \tag{2.28}$$

where $Z(\mathbf{r})$ is the electron-phonon interaction potential. There are many mechanisms

by which electrons can interact with phonons but can be broadly assigned to two categories: short and long-range interactions. Long-range interactions, also called Fröhlich coupling, are caused by Coulomb interactions between electrons and the dipoles induced by atomic displacement from their equilibrium such as those arising from the activation of optical phonons. For long range interactions, the change in a carrier's energy at $\mathbf{r}$ in the presence of a dipole at $\mathbf{u}$ it created by displacing the atomic lattice is

$$Z_{\mathrm{SR}}(\mathbf{r}-\mathbf{u}) = \sqrt{\frac{e^2}{4\pi}\left(\frac{1}{\epsilon_\infty}-\frac{1}{\epsilon_{\mathrm{dc}}}\right)\frac{k}{V_c}} \times \frac{\cos\theta}{|\mathbf{r}-\mathbf{u}|^2}, \tag{2.29}$$

where k is the force constant between the dipole's charges, V_c is the unit cell's volume, e the carrier's charge and θ the angle between the dipole's orientation and the vector $\mathbf{r}-\mathbf{u}$. In a microscopic treatment of the electron-phonon coupling, the strength of the electron-phonon coupling is often expressed in terms of the dimensionless Fröhlich coupling constant [60] α which reads

$$\alpha = \frac{e^2}{\hbar}\left(\frac{1}{\epsilon_\infty}-\frac{1}{\epsilon_{\mathrm{dc}}}\right)\sqrt{\frac{m}{2\hbar\omega}}, \tag{2.30}$$

where ϵ_∞ and ϵ_{dc} are the material's electric permittivity at very high and very low frequencies, ω is the frequency of the optical phonon involved and m is the carrier's mass. The peculiar nature of the coefficient in between large parenthesis can be accounted for by explicitly considering the effect of phonon modes on the material's electric susceptibility in the context of phonon-polaritons (see section 7.4.1 of reference [61]). A more intuitive interpretation is to consider that the polarisation caused by a high-frequency field on a dielectric material is mainly caused by electrons since only they can follow the electric field's rapid oscillations. Conversely, at low frequencies, both the atoms and the electrons can adapt to the electric field and thus both contribute to the low-frequency polarisation. Therefore, by taking the difference between the high-frequency and low-frequency polarisations, one obtains the contribution to the material's polarisation from phonons only which is precisely the aforementioned coefficient's form and aim.

When $\alpha < 1$, the electron-phonon interaction is weak and its effect on the electronic part of the system can be treated perturbatively. Such a procedure yields a small correction to an electron's energy linear in α so that

$$\Delta E = -\alpha\hbar\omega, \tag{2.31}$$

where ΔE is called the weak-polaronic binding energy. The electron-phonon interaction not only shifts the electronic bands but changes their curvature through the polaronic mass enhancement [61]. The latter effectively increases the electron's mass m by a factor of

$$\frac{m^*}{m} = 1 + \frac{\alpha}{6}, \tag{2.32}$$

where m^* is the electron's effective mass due to polaronic effects. Local distortions of the lattice at equilibrium also affect the electronic degrees of freedom through strain and shear or the piezoelectric effect. In these cases, the interaction potential is given by

$$Z_{\mathrm{SR}}(\mathbf{r} - \mathbf{u}) = -F\delta(\mathbf{r} - \mathbf{u}) \tag{2.33}$$

where F is some force constant. This interaction is called the short-range interaction and also reduces the energy of bands in the weak-coupling limit, albeit with a distinct dependence on the system's parameters. In both cases, the perturbative approach is valid only if the electron-phonon coupling is weak. For instance, for long range interactions, this happens when $\alpha > 1$ and the perturbative treatment no longer converges. In the case of 2D HOIPs, under reasonable assumptions [62], the coupling constant can be estimated to be between 1.67 and 2.2. This calls for another approach which does not suppose electron-phonon interactions to be weak.

2.3.3 Polarons

Following Emin [63], we start with a simple Hamiltonian H for an electron in a deformable continuum of the form

$$H = H_e + H_I + H_a, \tag{2.34}$$

where

$$H_e = -\frac{\hbar^2}{2m}\nabla^2_{\mathbf{r}} \tag{2.35}$$

is the electron's kinetic energy,

$$H_I = \int \mathrm{d}\mathbf{u} Z(\mathbf{r}-\mathbf{u})\Delta(\mathbf{u}) \tag{2.36}$$

arises from the interaction of electrons with the deformable medium and

$$H_a = \frac{S}{2}\int \mathrm{d}\mathbf{u}\Delta^2(\mathbf{u}) \tag{2.37}$$

is the contribution of strain to the system's dynamics with S the continuum's stiffness by unit volume. The total energy E is obtained by taking the above Hamiltonian's average value yielding

$$E = \langle\phi(\mathbf{r},\Delta)|H|\phi(\mathbf{r},\Delta)\rangle, \tag{2.38}$$

where $\phi(\mathbf{r},\Delta)$ is the electronic wavefunction which depends on the medium's deformation. We seek to remove the Hamiltonian's dependency on the latter to obtain a purely electronic Hamiltonian from which we can extract the system's electronic structure. We can do so by minimizing the system's energy with respect to $\Delta(\mathbf{u})$. This is done by taking the energy's functional derivative with respect to the medium's deformation and setting it to zero. Doing so, one obtains

$$\Delta_{eq}(\mathbf{u}) = -\frac{1}{S}\int \mathrm{d}\mathbf{r}|\phi(\mathbf{r},\Delta_{eq})|^2 Z(\mathbf{r}-\mathbf{u}), \tag{2.39}$$

where $\Delta_{eq}(\mathbf{u})$ is the continuum's deformation in equilibrium with the electronic wavefunction $\phi(\mathbf{r}, \Delta_{eq})$. We can therefore inject the result of equation 2.39 into the components of equation 2.34 and transform the system's Hamiltonian into a purely electronic one. By stripping the Hamiltonian of its atomic degrees of freedom in this way, we implicitely treat the electronic system adiabatically, that is, we suppose the electrons react to atomic displacements much faster than vice-versa. One can check that the injection of equation 2.39 into the Hamiltonian has the effect that $H_I = -1/2H_a$ and yields for the system's total energy

$$E_{ad}^{min} = \frac{\hbar^2}{2m} \int \mathrm{d}\mathbf{r} |\nabla_{\mathbf{r}}^2 \phi(\mathbf{r}, \Delta_{eq})|^2 - \int \mathrm{d}\mathbf{r} |\phi(\mathbf{r}, \Delta_{eq})|^2 \int \mathrm{d}\mathbf{r}^{'} |\phi(\mathbf{r}^{'}, \Delta_{eq})|^2 I(\mathbf{r}, \mathbf{r}^{'}), \quad (2.40)$$

where

$$I(\mathbf{r}, \mathbf{r}^{'}) = \frac{1}{2S} \int \mathrm{d}\mathbf{u} Z(\mathbf{r} - \mathbf{u}) Z(\mathbf{r}^{'} - \mathbf{u}) \quad (2.41)$$

is the interaction function. The interaction function for both short and long range interactions can be calculated and injected into equation 2.40 to yield

$$\begin{aligned} E_{ad}^{min} =& \frac{\hbar^2}{2m} \int \mathrm{d}\mathbf{r} |\nabla_{\mathbf{r}}^2 \phi(\mathbf{r}, \Delta_{eq})|^2 \\ & - \frac{e^2}{2} \left(\frac{1}{\epsilon_\infty} - \frac{1}{\epsilon_{\mathrm{dc}}} \right) \int \mathrm{d}\mathbf{r} \int \mathrm{d}\mathbf{r}^{'} \frac{|\phi(\mathbf{r}, \Delta_{eq})|^2 |\phi(\mathbf{r}^{'}, \Delta_{eq})|^2}{|\mathbf{r} - \mathbf{r}^{'}|} \\ & - \left(\frac{F^2}{2k} \right) V_c \int \mathrm{d}\mathbf{r} |\phi(\mathbf{r}, \Delta_{eq})|^4. \end{aligned} \quad (2.42)$$

Solving this non-linear equation can prove extremely challenging. However, using a scaling approach much can be said about bound states in this system without having to explicitly solve it. By scaling down the magnitude of all positions by a factor of L (e.g. as $\mathbf{r} \to \mathbf{r}/L$) and keeping the wavefunction normalized by multiplying it with $L^{-D/2}$ where D is the system's dimensionality, the above functional reduces to

$$E_{ad}^{min} = \frac{T_e}{L^2} - \frac{V_L}{L} - \frac{V_S}{L^D} \quad (2.43)$$

with each coefficient arising from contributions from the electron's kinetic energy

$$T_e = \frac{\hbar^2}{2m} \int \mathrm{d}\mathbf{r} |\nabla^2_{\mathbf{r}} \phi(\mathbf{r}, \Delta_{eq})|^2, \tag{2.44}$$

the long-range Fröhlich interaction

$$V_L = \frac{e^2}{2} \left(\frac{1}{\epsilon_\infty} - \frac{1}{\epsilon_{\mathrm{dc}}} \right) \int \mathrm{d}\mathbf{r} \int \mathrm{d}\mathbf{r}' \frac{|\phi(\mathbf{r}, \Delta_{eq})|^2 |\phi(\mathbf{r}', \Delta_{eq})|^2}{|\mathbf{r} - \mathbf{r}'|}, \tag{2.45}$$

and short-range interactions

$$V_S = \left(\frac{F^2}{2k} \right) V_c \int \mathrm{d}\mathbf{r} |\phi(\mathbf{r}, \Delta_{eq})|^4. \tag{2.46}$$

We therefore see that depending on the relative strengths of short and long range interactions, minima in the energy functional will be obtained for some values of L. This indicates that there is a particular scale for $\phi(\mathbf{r}, \Delta_{eq})$ which minimizes the total system's energy and thus corresponds to the polaron's size. If no electron-phonon interactions are present ($V_S = V_L = 0$), the energy is minimized for $L \to \infty$ and the electronic wavefunction is completely delocalized, as predicted by Bloch's theorem. When only long range interactions are present, the energy is minimized for $L = 2T_e/V_L$ and the system harbors a large polaron. When only short range interactions are present, its effect depend on the dimensionality of the system and the relative magnitude of T_e and V_S. For three dimensional systems, two minima occur at either $L \to 0$ where the energy diverges to ∞ or $L \to \infty$ where the energy approaches zero. The former divergence occurs because of the continuum description of the deformable system. In reality, one should impose a short range cutoff due to both the actually discrete nature of the deformable medium as well as exchange interaction in realistic many-body fermionic systems. In the three-dimensional case with only short-range interactions, the wavefunction is either that of a free-carrier ($L \to \infty$) or a so-called small polaron ($L \to 0$). An energetic barrier at $L = 3V_S/2T_e$ separates these

two solutions and have the effect of slowing down small polaron formation [64]. Once over this energetic barrier, carriers considerably shrink under their own effect on the atomic displacements and form small polarons through a process known as self-localisation. When both long-range and short range interactions are present in a three-dimensional system, the relative weight between these interaction's coefficients determine the size and nature of the resulting polaron as shown in Figure 2.5a. In two dimensional systems, the short-range interaction and electron kinetic energy have a functionally similar contribution to the energy functional. Therefore, the sign of $T_e - V_S$ will determine whether the bound states are large or small polarons. As shown in Figure 2.5b, increasing the short-range interaction's strength gradually contracts the polaron until it collapses into a small polarons when $T_e < V_S$. Therefore, in two-dimensions, short-range interactions help the formation of large polarons by reducing the kinetic energy's contribution to delocalisation. Moreover, it is not surprising that bound states between electrons and the lattice's deformation should always occur in the adiabatic limit for systems with reduced dimensionality. Quantum mechanical bound states are always found in such system regardless of the depth of the attractive potential [22]. Whether or not the polaronic treatment is useful then depends on the stability of polarons with respect to the system's temperature or, equivalently, on the depth of the energy functional's curve with L. Lastly, in the unidimensional case, given the similar functional contribution of the short- or long-range interactions, a small polaron never forms as shown in Figure 2.5c.

2.3.4 Exciton-polarons

Given our previous treatment of polarons and polaronic effects, one could argue that the mere notion of exciton-polarons is absurd on the following grounds: the electric neutrality of excitons, the ground-state approach we just employed, and that the term is superfluous. Before discussing the concept of exciton-polarons, I will expose these objections and then refute them. First, it is often held that excitons are neutral quasiparticles and therefore

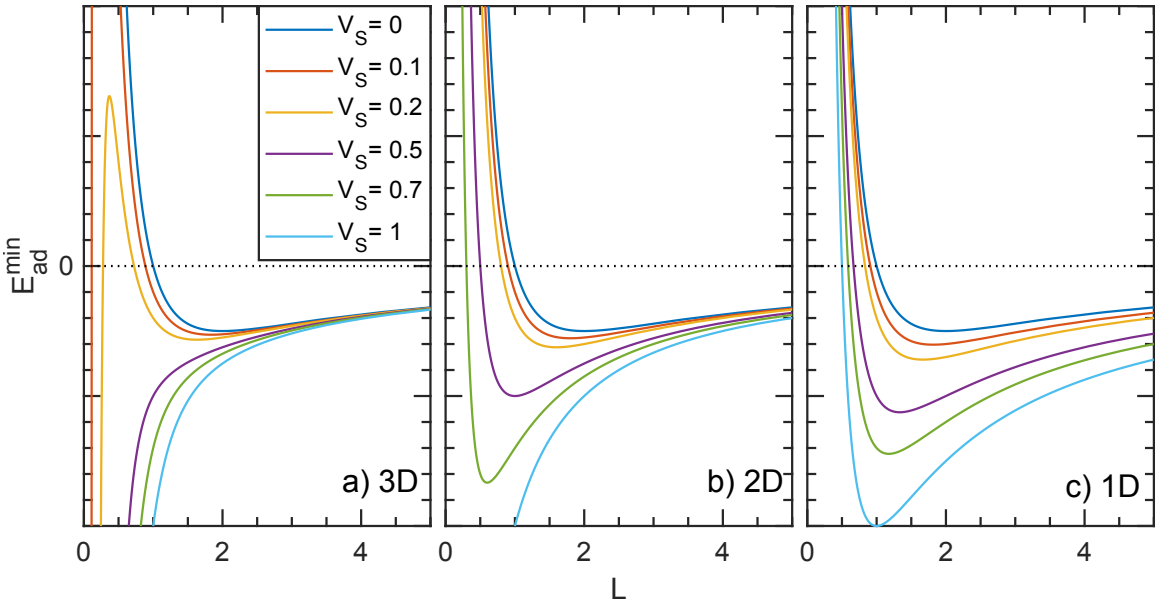

Figure 2.5: **Polaron energy functional for different system dimensionalities.** Equation 2.43 is plotted for the 3D (a), 2D (b) and 1D (c) cases with $T_e = V_L = 1$ while varying V_S from 0 to 1. In 3D, small and large polaron formation depend on the relative strength of each terms. In some cases, both small and large polarons are stable at finite temperatures. In the two-dimensional case, carriers form either large or small polarons and cannot coexist while in the unidimensional case, small polaron formation is impossible.

should couple too weakly to the lattice for polaronic effects to be of any importance. Although it is true that over long distances excitons behave as small dipoles with negligible total charge, they are still composed of two distinct charged particles: an electron and a hole. Therefore, if the radius of a polaronic distortion is smaller than the excitonic Bohr radius, strong polaronic effects could still be present. Even in the most strongly bound excitons in 2D HOIPs, the excitonic Bohr radius spans a few unit cells [4]. Secondly, it is also true that the above treatment is valid for a system's ground state only and therefore cannot be used to determine an excited state's polaronic character, like that of an exciton. Indeed, the previous treatment addresses polaronic effects on a system's ground state. It shows that the fact that solids hold together is the consequence of the polaronic effect. However, the treatment can be generalized to other excited states of the system, albeit perhaps not with the same simplicity. In the case of exciton-polarons, this ground state procedure could be directly used in the Wannier equation (see equation 2.13) to determine

the polaronic character of the excitonic ground state [65]. Finally, some might claim that the term exciton-polaron is superfluous since excitons in polaronic system are merely composed of two polarons of opposite charge orbiting each other. The resulting quasi-particle is therefore no different than a normal exciton and should be named as such. Again, this scenario is plausible but discards a host of rich physics which could arise from the presence of carrier correlations through both the intercarrier Coulomb interaction *and* and electron-phonon interactions. Indeed, polaronic effects screen electric fields, which in turn affects the Coulomb interaction which changes the electronic charge density. In response to this, the lattice rearranges and this cycle carries on. Thus, the inclusion of polaronic effects in a Coulomb correlated system could potentially affect the electronic structure of a material beyond the added individual contribution of both effects.

Therefore, exciton-polarons are the quasiparticles which diagonalize a system's Hamiltonian in which both strong electron-phonon and electron-hole pairwise interactions are present. It is not a new concept, used in the past to discuss polaronic effects on Wannier excitons [65], the properties of strongly confined excitons in quantum dots of polar semiconductor [66, 67, 68], quantum wells [69] and bulk systems [70]. These show that since the exciton and phonon wavefunctions are entangled by these polaronic effects, the exciton-phonon system must be considered as one for systems where both Coulombic and polaronic correlations are strong. In particular, a simultaneous theoretical treatment of both correlations for electrons in a quantum well surrounded by a medium with a distinct electronic structure and electric permittivity is done in reference [71]. The authors consider the contribution of both interfacial and bulk phonons to the Hamiltonian as well as dielectric confinement effects. Given the close analogy between 2D HOIPs and the system considered in these calculations, we will devote a few lines to some of their results. First, the calculations validates our intuition that polaronic effects reduce the excitonic binding energy. When the polaronic radius $R_p = (\hbar/2m_e\omega_0)$, a characteristic length scale of the

polaron problem, is comparable to the exciton's Bohr radius, polaronic effects are reduced and the exciton's binding energy increases. Surprisingly, for atom-thin wells, the ratio of the bare exciton's Rydberg energy to that of the phonon it is coupled to has a strong effect on the resulting binding energy. Therefore, if excitons are strongly coupled to distinct lattice modes, their energies will be altered as well. This ascertainment is central to the conclusions put forward in this thesis.

2.4 Spin-orbit effects

When an electron moves in a magnetic field $\mathbf{B}$, it experiences a correction to its energy by $\mu_B \sigma \cdot \mathbf{B}$ through the Zeeman effect where μ_B is Bohr's magneton and σ the vector of Pauli matrices. However, a Zeeman effect in the absence of a magnetic field is possible. Due to special relativity, an electron moving in an electric field $\mathbf{E}$ feels a magnetic field $\mathbf{B}_{\text{eff}} = -\mathbf{E} \times \mathbf{p}/mc^2$. The electric field felt by electrons in a solid is that of the atomic potential V such that $\mathbf{E} = -\nabla V$ which yields the spin-orbit part of the Hamiltonian

$$H_{SO} = \frac{\mu_B}{mc^2}(\nabla V \times \mathbf{p}) \cdot \sigma. \tag{2.47}$$

For this reason, the spin-orbit coupling is often said to arise from relativistic corrections and its effect on electronic band structure is the lifting of degeneracies related to the spin degree of freedom. In solid-state systems, this atomic spin-orbit coupling can be approximated by simpler expressions when the symmetry of the crystalline structure is known. For instance, in the case of bulk zinc-blende crystals, the spin-orbit coupling takes the form [72]

$$H_{DSO} \propto ((p_y^2 - p_z^2)p_x\sigma_x + \text{a.c.p.}), \tag{2.48}$$

where a.c.p stands for all circular permutation of indices. This spin-orbit Hamiltonian is known as the Dresselhaus spin-orbit coupling and can be further simplified when consider-

ing a strained zinc-blende structure along the (001) direction and reads

$$H_{DSO1} \propto p_z^2(p_x\sigma_x - p_y\sigma_y) \tag{2.49}$$

and is called the linear Dresselhaus spin-orbit coupling. More importantly in the context of 2D HOIPs is the following phenomenological spin-orbit coupling [73, 74]

$$H_{RSO} = \frac{\alpha_R}{\hbar}(\mathbf{z} \times \mathbf{p}) \cdot \sigma \tag{2.50}$$

and is called the Rashba spin-orbit coupling where α_R is the Rashba parameter. It is intended to describe spin-orbit coupling arising from interfacial electric fields in 2D degenerate electron gases. It is important to remark that due to its linear nature in momentum, this particular form of the spin-orbit coupling vanishes for systems with an inversion center. It can therefore be of considerable importance at surfaces or interfaces. All of the above yield energetic corrections to electronic bands depending on their spin degree of freedom. In the linear approximation, this yields a shift of the bands in momentum space, effectively lifting spin-related degeneracies. Such shifts in the electronic bands due to the Rashba effect have been observed on the surface of BiAg (111) alloy using ARPES [75] or in Shubnikov-de Haas oscillations in InAlAs/InGaAs heterostructures [76]. The Rashba parameter of the latter was found to be 0.67×10^{-11} eV m while the former was found to be 3.7×10^{-10} eV m almost two orders of magnitude larger. While the Rashba spin-orbit coupling seems like a fair approximation for some systems, it only partially reproduces the real effects of spin-orbit coupling on electronic bands and should be used carefully [77].

2.5 Previous investigations of the optical properties of two-dimensional perovskites

Having laid out the necessary theoretical elements, the experimental manifestations of these various solid-state phenomena in 2D HOIPs can now be discussed. We begin with excitonic effects, for they are the main focus of the work of this thesis. As we will show, the origin of

excitonic fine structure in these materials remains elusive. This mystery is the driving force behind much of the work presented in later chapters. We then turn our attention to reports related to signatures of electron-phonon interactions in these systems. These were known to be important in 3D HOIPs but, comparatively to their expected importance, few works have considered these effects in 2D HOIPs. Our attempts to verify a hypothesis pointing to a Franck-Condon interpretation of the excitonic fine-structure put forward in one of these reports turned out to invalidate it and launched the whole polaron hypothesis defended in this thesis. Finally, given that spin-orbit effects are usually manifested through degeneracy lifting of angular and spin degrees of freedom, we present some reports of these effects in 2D HOIPs. There is still much ongoing debate about the validity of these findings but some interesting reported coincidences make these effects potential candidates to explain the excitonic fine-structure splitting.

2.5.1 Excitonic effects

Due to their dominating contribution to the optical properties of two-dimensional lead-halide perovskites [78, 79], it was observed in the earliest works that excitonic effects are very strong in these materials. Exhibiting binding energies of hundreds of meV, on par with those of other strongly excitonic two-dimensional materials such as monolayers of transition metal dichalcogenides (TMDCs) [44, 80], excitons are tightly bound and therefore stable even at room temperature. This came as no surprise to the authors of these early reports given PbI_2's large binding energy [34] (about 30 meV) and the recent work on quantum wells of direct bandgap semiconductors such as GaAs. Moreover, signatures of bound biexcitons in the low temperature photoluminescence spectrum of 2D HOIPs were also reported early on [81]. A biexcitonic binding energy of the order of 50 meV was reported, the highest of any material known so far and again comparable to that of monolayers of TMDCs [82, 44]. Biexciton lasing was even claimed to occur in these same systems [83] although no sharp threshold in emission was observed in the reported data. The estima-

tion of biexciton binding energy through the non-linear growth with excitation power of a reshifted photoluminescence feature is a common practice but can also arise from defect emission. To unambiguously measure this binding energy, one must turn to multidimensional spectroscopy. A recent report [84] performed multidimensional spectroscopy on 2D HOIPs and obtained a binding energy of 40 meV at room temperature. There, they interpreted a featured shifted from another along the two-diagonal of a two-quantum spectrum to arise from a biexcitonic correlation. This is an incorrect interpretation of their own data as we will show in section 3.5 and we consider their estimate of the biexciton binding energy to be invalid.

Even though the optical signatures of excitons in these materials seem at first sight to match the predictions of the Wannier model, two major discrepancies were observed between the measured and predicted excitonic signatures. The first one involves the unusually high excitonic binding energies observed in lead-halide 2D perovskites. Although a fourfold increase in excitonic binding energy is expected due to the quantum confinement of the carriers in the lead-halide plane, this enhancement is insufficient to explain the binding energy's increase by about an order of magnitude in most lead-halide 2D perovskites [79, 85]. The solution to this puzzle lies not in the composition of the inorganic well, but what lies around it. If electrons are confined to a near two-dimensional geometry, the electric field is not. This flaw in our previous derivation of the Wannier model where we supposed an isotropic dielectric constant was highlighted near the end of section 2.2.1. In 2D HOIPs, the electric permittivity of the organic layer is about 10 times smaller than that of the inorganic layer [86] thus drastically lowering the effective electric permittivity relevant for the interaction between two charges in the inorganic layer. This effect, sometimes called dielectric confinement or image charge effect, is not unique to 2D HOIPs and is in fact observed in all atomically thin excitonic semiconductors of reduced dimensionality [80, 87]. In this situation, the proper Coulomb potential to be considered in equation 2.13 is the one that

arises from this heterogeneous dielectric environment. An analytical form for this potential can be obtained using the image charge method [88, 79] and accounts correctly for this increase in binding energy. However, the authors of reference [79] did not use the known effective masses of carriers in a bulk analogue to the inorganic single-layers. They rather adjusted the exciton's reduced mass to maximize the agreement between the predicted and measured binding energies of similar compounds. The agreement so reached is excellent, but this method casts doubt on the validity of the envelope function approximation for these materials. As previously argued from an experimental [89] and theoretical [90] standpoint, the quantum well model fails when each plane of 2D HOIPs are composed of a single layer. Not only is it impossible to use the same effective masses to predict excitonic properties from the single-layer to the bulk (unsurprising given they are different materials), this formalism predicts the formation of minibands due to superlattice effects. These are not observed in DFT calculations nor experimentally. In fact, single-layered 2D HOIPs behave more like isolated sheets of two-dimensional semiconductors like monolayers of transition metal dichalcogenides. This limitation of the Wannier model was mentioned in passing near the end of section 2.2.1 and does not imply that the Wannier formalism is invalid for these materials. It rather suggests that the correct material parameters can differ from those of analogous multilayered or bulk systems. In this sense, monolayered 2D HOIPs should be considered as different yet similar to these analogous systems.

The other discrepancy between the predictions of the Wannier model and the measured optical spectra is at the origin of this thesis's work and undoubtedly many more in the future: that of an excitonic fine structure in the low temperature absorption and photoluminescence spectra. This fine structure is consistently present across many 2D HOIPs with distinct organic cations [78, 79, 91, 8] and halogen atoms [92, 93]. It also persists up to room temperature as shwon by the properties of polaritonic emission when these materials are imbedded inside an optical microcavity [94]. Early work on these materials hypothe-

sized this fine structure to arise from the lifting of a degeneracy by spin-orbit coupling or crystalline fields [78]. The original and subsequent arguments were based on the electronic structure of PbI_2 and supposed them to be Frenkel excitons whose wave functions were solely composed of the s and p orbitals of Pb^{2+}, thus completely neglecting contributions from the iodine atoms and organic cations around it or any other structural details for that matter. Unsurprisingly, this assumption was found to be erroneous by recent DFT calculations including spin-orbit coupling for similar compounds [10]. These calculations show that the valence band maximum (VBM) and conduction band minimum (CBM) are confined to the inorganic plane and both occur at the Γ point. The VBM is composed of the hybridization between lead's 6s and iodine's 5p orbitals while the conduction band minimum is composed of iodine p orbitals. However, these bands could just as well be split by symmetry breaking effects such as exchange interaction, crystalline fields or spin-orbit effects and cause the observed excitonic fine structure. As a matter of fact, a fine structure was also observed in orthorombic nanocrystals of bulk hybrid organic-inorganic perovskites albeit with much smaller energy splittings [95] and were assigned by some to a degeneracy lifting by exchange interactions [96] and by others to spin-orbit effects [97]. Experimental results proved the former right [96] and showed that the result of these broken symmetries is an optically dark ground state and a bright non-degenerate triplet. Nevertheless, the close proximity between 2D HOIPs and their bulk counterpart suggest similar effects could be at play in the former.

2.5.2 Electron-phonon coupling and polaronic effects

As stated in section 2.1, from the atomic structure alone, one can deduce that the coupling between atoms and the lattice will be important. It is therefore tempting to interpret the excitonic fine structure as a vibronic replica like those predicted by the Franck-Condon model. This assignment is all the more sound when the fine structure consists of evenly spaced features of decreasing oscillator strength, as is the case in $(PEA)_2PbI_4$. In light of

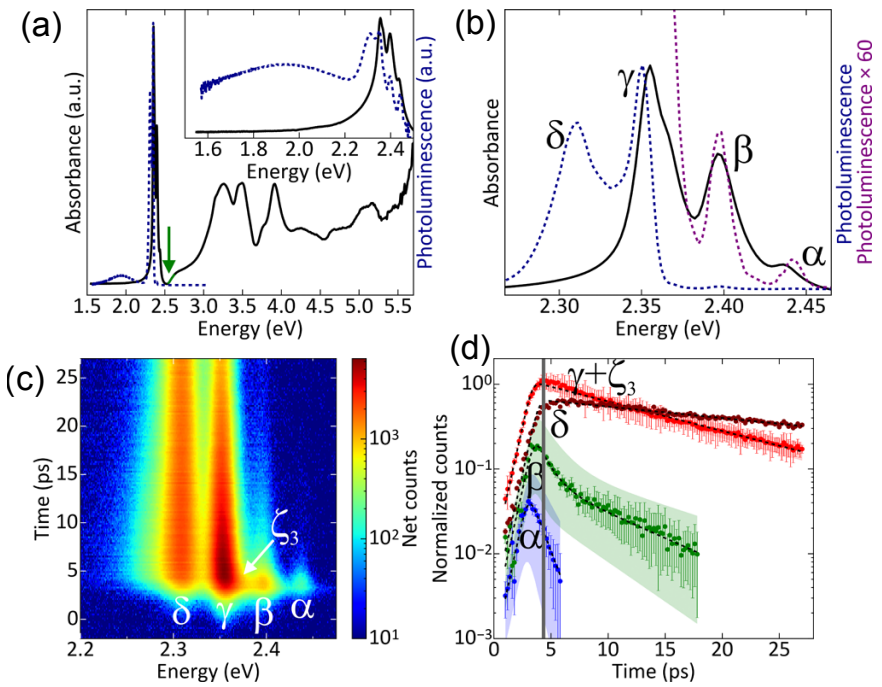

Figure 2.6: **Absorption and emission spectra used to justify the excitonic fine structure as a vibronic progression.** The absorption and photoluminescence of $(PEA)_2PbI_4$ at a temperature of 15 K on a regular (a) and expanded (b) scale. Features in the emission spectrum are labelled α, β, γ and δ with decreasing energy. The purple curve corresponds to the emission spectrum amplified by a factor of 60 to show low intensity features. The emission is time-resolved in panels (c) and (d) with the same feature labelling as in panel (b). Taken from reference [98].

photoluminescence and absorption spectroscopies shown in Figure 2.6 some have proposed this interpretation [98]. In the low-temperature absorption spectrum, the fine structure of $(PEA)_2PbI_4$ is clearly resolved and four distinct peaks are observed (Figure 2.6a). Four peaks are also observed in the photoluminescence spectrum but their intensities and energies do not mirror those of the absorption spectrum (Figure 2.6b), an indication that the basic Franck-Condon principle does not apply here. The authors explain this discrepancy by pointing out that when the emission is time-resolved (Figure 2.6c and d), each feature rises in a step-like fashion one after the other. They attribute this temporal emission profile to a slow relaxation down the excited state vibrational manifold, thus breaking Kasha's rule. If it were the case, the emission spectra at late times would then be Kasha-like emission, that is, once the population has relaxed to the lowest vibrational state. In this case,

the emission spectra would then be a mirror image of the absorption spectrum, which is not observed in their data. Therefore, unless the shape of the excited state potential energy surface changes during the relaxation, the time-resolved photoluminescence cannot be explained by slow vibrational relaxation. For this reason, we doubted the assignment of the excitonic fine structure to a vibronic progression is valid. Nonetheless, this work was central in launching our own investigation in the matter. Indeed, to experimentally verify the claim made by the authors, one would need to perform resonance Raman scattering on all features of the fine structure. If the spectrum does not change with pumping energy, all transitions share the same electronic character and are therefore vibrational replica of a single electronic state. This is exactly what we performed in section 6.

In three-dimensional HOIPs, another manifestation of electron-phonon coupling beyond a displaced excited state was observed, that of large polarons. In an attempt to explain the high carrier diffusion lengths, low recombination rates, strange temperature dependent transport properties and low scattering rates, it was proposed that carriers in these materials could in reality be large polarons [99]. Indications of polaron formation were later provided using transient optical Kerr effect and DFT based calculation [100] and used to rationalize the slow hot carrier cooling curves observed in these materials [101, 102]. This assignment was subsequently confirmed by impulsive coherent stimulated resonance Raman spectroscopy [103]. Surrounded by a large cloud of lattice distortion, electric fields outside the large polaron's radius would be screened thus shielding carriers from interactions with other quasiparticles and defects. Therefore, many-body interactions affecting polarons should be considerably reduced. Due to the similarity between 2D HOIPs and their bulk counterparts, carrier in the former might also share this polaronic character. Due to the polaronic effect's dependence on dimensionality, this effect might be enhanced as well. Indeed, in light of very broad and strongly Stokes-shifted photoemission in some 2D HOIPs with high octahedral distortions, self-localisation of excitons or small polaron formation

is believed to play an important role in these materials [8, 7]. As stated in section 2.3.3 for the two-dimensional case, according to equation 2.43 with $D = 2$, the delocalization from the carrier's kinetic energy term can be compensated by short-range electron-phonon interactions to yield a large polaron or amplified to yield a small polaron. 2D HOIPs could be at the threshold between these two regimes and exhibit both characters depending on the conformation imposed by the organic cations on the inorganic planes. This hypothesis has also been proposed by others in light for the increased thermal broadening of emissive lines in 2D HOIPs [104].

2.5.3 Spin-orbit effects

As mentioned in passing in section 2.5.1, spin-orbit coupling has a strong influence on the electronic structure of 2D HOIPs [10]. These effects effectively split two quasi degenerate conduction bands by about an electron volt. The spin-orbit coupling also mixes the character of these conduction bands. Both of these effects are much softer on the valence bands and does not significantly alter their nature. Small displacements of the lead atom inside its octahedral cage could lead to spatial inversion symmetry breaking and therefore give rise to a Rashba effect in 2D HOIPs [105]. In bulk HOIPs, the presence of a large Rashba effect was confirmed by ARPES measurements [106] and yielded a Rashba parameter of 11×10^{-10} eV m, an immense value when compared to those obtained for traditionnal semiconductors. Due to the surface nature of ARPES measurements, however, this value might be much larger than the correct one in the bulk. One may nonetheless expect these effects to be important in 2D HOIPs as well given their interfacial nature. Recently, ultrafast transient absorption spectroscopy measurements have observed an excited state absorption feature at a probe energy of 350 meV which they attribute to a transition from the exciton ground state to a shifted Rashba band [107]. Using the bandgap energy extracted from electroabsorption measurements and the photoinduced absorption feature's energy, they extract a Rashba energy of (38$\pm$3) meV and a Rashba parameter of (1.6$\pm$0.1)$\times10^{-10}$ eV m. While

a surprising result which could arise from Rashba effects, this feature could also be interpreted as photoionization of bound exciton species. Nonetheless, the similarity between the measured Rashba energy and the excitonic fine structure splitting is striking and hint that Rashba effects could be behind the observed excitonic fine structure in 2D HOIPs.

2.6 Conclusion

In this chapter, we have presented all the theoretical elements required to understand the current state of the field and interpret the literature it had generated so far. The portrait so painted is blurry: many different phenomena such as excitonic correlations, electron-phonon coupling as well as spin-orbit and exchange effects should be strongly manifested in 2D HOIPs. However, no conclusive evidence points to one of these as being at the origin of the observed excitonic fine structure splitting. Worse even, potential hypotheses involving all but one of these phenomena have been proposed to account for this fine structure some using debatable or downright wrong arguments. The phenomena cast aside, that of electron-phonon coupling, is expected to be strong but few in the field were aware of the experimental and theoretical literature concerning two-dimensional polarons and exciton-polarons. If electron-phonon coupling is sufficiently strong, that the excitonic fine structure arises of electronically distinct states and there is a spectral dependence on electron-phonon coupling within this fine structure, exciton-polaron effects could well be responsible for the observed fine structure. In the remainder of this thesis, we will gradually give credibility to this hypothesis using advanced optical probes. Before diving into the various experimental results we have gathered to this end, we will spend the next chapter laying out the necessary theoretical framework in which to interpret them. This shall not be in vain for it will give you a good sense of the elegance and rigor with which matter can be probed using coherent non-linear spectroscopy.

CHAPTER 3

SPECTROSCOPIC TOOLS: PROBING MATTER WITH LIGHT

It is by no coincidence that light is one of the most widespread tools used in the study of matter. Light interacts with many degrees of freedom for a vast ensemble of physical systems. It can be made to interact almost imperceptibly with a system, keeping the experiment in the perturbative regime, or with such strength that light and matter become indistinguishable. Moreover, the physical properties of light are numerous, readily measured and easily tuned making it a versatile tool too. Its scalar properties span multiple orders of magnitude in time (from the attosecond to the continuous), energy (from gamma rays to radio frequencies), lengths (down to the diffraction limit) and intensity (from the single photon to powers capable of ripping apart an hydrogen atom). Its numerous vectorial properties such as direction of propagation, polarisation, and degree of helicity are also extremely useful in isolating particular phenomena. Light's versatility and ease of use is such that it was instrumental to the development of nearly all fields of modern physics. This trend is not about to end given the astounding research efforts directed into pushing further this attribute, yielding new and promising ways to explore matter with light.

However, spectroscopy laboratories around the world aren't equipped to span all of light's parameter space and restrict themselves to a sub-region suited to the phenomena they wish to study. In the context of this thesis, we wish to study exciton dynamics in direct band-gap hybrid semiconductors. This requires the generation of short tunable pulses in the visible, so as to achieve the required temporal resolution and resonant excitation. In addition to excited state population dynamics, we wish to study the temporal evolution of a photocarrier's wavefunction, its coherent dynamics, as well. Since it can be detected through the optical dephasing of the corresponding optical transitions, we need our exper-

iments to be phase-resolved and non-linear. The former arises because of the coherent nature of optical dephasing processes while the latter is necessary to resolve sub-picosecond oscillations using stroboscopic measurements. Such experiments falls under the umbrella of time-resolved coherent non-linear spectroscopies such as transient absorption and multidimensional coherent spectroscopy (MDCS) [108].

In this chapter, I first expose the foundations on which the interpretation of coherent non-linear spectroscopy experiments rests. I will focus on the theoretical elements used in the interpretation and analysis of the measurements presented in later chapters. Along the way, the connection between these measurements and the system under study will be made explicit. Moreover, the formalism of double-sided Feynman diagrams will be presented and used to interpret typical multidimensional spectra. Finally, more intricate models will be used to show that non-linear coherent lineshapes are rich with information about some of the most elusive effects in semiconductor physics namely disorder and many-body interactions.

3.1 Fundamentals of non-linear coherent spectroscopy

The interpretation of almost every spectroscopic measurement stems from a perturbative treatment of a system's response to an applied electromagnetic field using time-dependent perturbation theory. Such an endeavor yields the time-dependent polarization induced in the material by the electric field. From it, one then obtains the frequency-domain response of the system under study. The derivation of the system's temporal response can be found in reference [109] and yields

$$P^{(n)}(\mathbf{r},t) = \int_0^\infty dt_n \int_0^\infty dt_{n-1} \cdots \int_0^\infty dt_1 S^{(n)}(t_n, t_{n-1}, ..., t_1) \times E(\mathbf{r}, t-t_n)E(\mathbf{r}, t-t_n-t_{n-1}) \cdots E(\mathbf{r}, t-t_n \cdots - t_1) \quad (3.1)$$

where $P^{(n)}(\mathbf{r},t)$ is the non-linear polarization induced in the system to the n-th order in the applied electric field $E(\mathbf{r},t)$, $\mathbf{r}$ and t are spatiotemporal coordinates and $S^{(n)}$ is the non-linear response function given by

$$S^{(n)}(t_n,t_{n-1},...,t_1) = \left(\frac{i}{\hbar}\right)^n \Theta(t_1)\Theta(t_2)\cdots\Theta(t_n) \\ \times \langle\hat{\mu}(t_n+\cdots+t_1)[\hat{\mu}(t_{n-1}+\cdots+t_1),[\cdots[\hat{\mu}(t_1),[\hat{\mu}(0),\rho(-\infty)]]\cdots]]\rangle \quad (3.2)$$

where $\Theta(t)$ is the Heavyside function, $\hat{\mu}$ the dipolar moment operator, $\langle\ \rangle$ denotes a quantum mechanical average, $\rho(-\infty)$ the system's density matrix before the experiment and $[\hat{A},\hat{B}]$ the commutator between two operators $\hat{A}$ and $\hat{B}$. All operators are expressed in the interaction picture. These equations are the foundation on which lay the interpretation of all coherent non-linear spectroscopy measurements. They state that the non-linear polarization is related to the applied electric field via their multitemporal convolution with the response function. The microscopic description of the system (and thus, its dynamics) enters these equations through the system's dipolar moment operator and the density matrix at equilibrium in the response function. Even in this general form, these equations are easily related to the experiment being performed. Indeed, it is easy to design a non-linear coherent spectroscopy experiment so that only the effects of the n-th order polarization are detected. Therefore, in most cases, it is not necessary to consider these equations to more than a single order. In this thesis, only experiments involving the first and third order polarisations were performed. To the first order, equations 3.1 and 3.2 take the form of

$$P^{(1)}(\mathbf{r},t) = \int_0^\infty dt' S^{(1)}(t')E(\mathbf{r},t-t') \quad (3.3)$$

and

$$S^{(1)}(t) = \left(\frac{i}{\hbar}\right)\Theta(t)\langle\hat{\mu}(t)[\hat{\mu}(0),\rho(-\infty)]\rangle \quad (3.4)$$

where it is now clear that $S^{(1)}(t)$ is simply the linear electric susceptibility $\chi^{(1)}(t)$ multiplied by the electric permittivity of free space ϵ_0. A linear coherent spectroscopy measurement is therefore equivalent to measuring the refractive index and attenuation coefficient of a material. Equation 3.4 shows that the first light matter interaction launches coherent oscillations between resonnant excited states which independently radiate a signal during time t. This radiation then interferes with the electric field used to generate this polarization yielding the transmitted and reflected beams measured in reflectance and transmittance experiments. These independent oscillations are the reason behind a linear measurement's fundamental ambiguity: it is impossible to tell apart a three level system from two uncoupled two-level systems. Linear techniques, such as absorption spectroscopy, are nonetheless extremely useful techniques notably to provide the energies of various excited states present in a material.

To alleviate this ambiguity, we must use techniques of higher order in light-matter interactions. Both transient absorption and all MDCS experiments presented in this thesis are third-order non-linear coherent spectroscopy experiments. Equations 3.1 and 3.2 then become

$$P^{(3)}(\mathbf{r},t) = \int_0^\infty dt_3 \int_0^\infty dt_2 \int_0^\infty dt_1 S^{(3)}(t_3,t_2,t_1) \times E(\mathbf{r},t-t_3)E(\mathbf{r},t-t_3-t_2)E(\mathbf{r},t-t_3-t_2-t_1) \quad (3.5)$$

and

$$S^{(3)}(t_3,t_2,t_1) = \left(\frac{i}{\hbar}\right)^3 \Theta(t_1)\Theta(t_2)\Theta(t_3) \times \langle \hat{\mu}(t_3+t_2+t_1)[\hat{\mu}(t_2+t_1),[\hat{\mu}(t_1),[\hat{\mu}(0),\rho(-\infty)]]]\rangle \quad (3.6)$$

The aforementioned ambiguity is thus alleviated. The second light-matter interaction maps

the independently oscillating coherences launched by the first one onto a population transient or another coherences which are then taken back onto oscillating coherences by the third interaction. These last coherences then radiate the signal detected in an experiment.

3.2 Time-ordering and the semi-impulsive limit

The conditions in which these experiments are performed allow a few further simplifications. First, the electric field applied on the sample is provided by a sequence of two (for transient absorption) or three (for MDCS) temporally well separated short pulses. For generality, we will present here the case relevant to MDCS. This allows us to split the general expression for the electric field present in equation 3.5

$$E(\mathbf{r},t) = E_a(\mathbf{r},t) + E_b(\mathbf{r},t) + E_c(\mathbf{r},t) \tag{3.7}$$

into three distinct electric fields

$$E_a(\mathbf{r},t) = E_a\delta(t)e^{i(\pm\omega t \mp \mathbf{k}_a\cdot\mathbf{r})} \tag{3.8}$$

$$E_b(\mathbf{r},t) = E_b\delta(t+\tau)e^{i(\pm\omega t \mp \mathbf{k}_b\cdot\mathbf{r})} \tag{3.9}$$

$$E_c(\mathbf{r},t) = E_c\delta(t+\tau+\tau')e^{i(\pm\omega t \mp \mathbf{k}_c\cdot\mathbf{r})} \tag{3.10}$$

where the subscripts a, b and c denote the electric field of the first, second and last beams to interact with the sample. The case for transient absorption is easily obtained by taking beam a and b to be identical and simultaneous. This approximation, known as the semi-impulsive limit, is valid when the pulses are short compared to the system's dynamics but long compared to the electric field's oscillation. This is why the pulses are represented using Dirac's delta functions but still carry a wavevector and a carrier frequency. We replace the first, second and last electric fields in equation 3.5 with E_a, E_b and E_c respectively to

obtain the non-linear polarisation under this approximation. It reads

$$P^{(3)}(\mathbf{r},t) = S^{(3)}(t,\tau,\tau')\exp\left[i\left(\omega t + \sum_{i\in\{a,b,c\}}(-1)^{S_i}\mathbf{k}_i\cdot\mathbf{r}\right)\right] \tag{3.11}$$

where S_i is positive for two indices and negative for the other. The time-ordered semi-impulsive limit greatly simplifies the interpretation of experimental data. For one, the measured signal is directly proportional to the response function. Moreover, by removing the ambiguity over the temporal ordering order in which each beam interacts with the sample, the number of terms contained in the response function that need to be considered is also drastically reduced. Similarly to the case of the general electric field, the general dipolar moment operator

$$\hat{\mu}(t) = \hat{\mu}_a(t) + \hat{\mu}_b(t) + \hat{\mu}_c(t) \tag{3.12}$$

as it appears in equation 3.6 is now replaced by the appropriate beam specific dipolar moment operator $\hat{\mu}_i(t)$ with $i \in \{a,b,c\}$. This reduces the number of terms to be considered in the response function by a factor of 27. The time ordered semi-impulsive limit is generally a good approximation. Full calculations involving a complete description of the electric field reveal the pulses' shape to merely act as a filter in the frequency domain and does not significantly alter the lineshapes [110, 111]. We have also imposed a condition on the phase of the polarisation in equation 3.11 by requiring that the polarisation oscillates at a frequency near that of the probed optical transitions. This requirement, called phase-matching, is the mathematical equivalent of experimentally detecting only light close to resonance with the system under study and not at two or three times its energy.

The description of the response function must also be subtly modified to be in agreement with the semi-impulsive limit. In reality, the response function as shown in equation 3.11 stems from the true response function integrated by a convolution with the electric fields. Therefore, some terms in this integral will oscillate at the difference between the op-

tical and material oscillation frequency while others will oscillate at their sum. The former will dominate the optical response under resonant pumping since the latter will cancel out in the integral, destructively interfering. Neglecting these terms from the response function in equation 3.11 is called the rotating wave approximation. It also drastically reduces the number of terms required to build the response function, making computations easier. Together, the time-ordered semi-impulsive limit and the rotating wave approximation yield one last simplification. Equation 3.11 shows that the many directions in which the signal $\mathbf{k}_s$ is radiated is given by

$$\mathbf{k}_s = \sum_{i \in \{a,b,c\}} (-1)^{S_i} \mathbf{k}_i. \tag{3.13}$$

We can thus further reduce the number of terms to be considered in the response function by spatially filtering the signal, isolating a particular $\{S_i\} \mid i \in \{a, b, c\}$ where S_i is positive for two indices and negative for the other. These then fix the form of each interaction's dipolar moment operator entering the computation of the response function so that the rotating wave approximation is satisfied. An interaction whose S_i is negative is called a conjugate interaction since the conjugate of the associated electric field contributes to the detected signal. Other interactions are called non-conjugates.

3.3 Resonant impulsive coherent stimulated Raman scattering

We are now ready to model our first non-linear coherent measurement, that of resonant impulsive coherent stimulated Raman scattering (RICSRS). This experiment consists in impulsively exciting an electronic transition using a simultaneous conjugate and non-conjugate interaction provided by a strong pump pulse and observing the temporal modulations in the dielectric permittivity using the transmission of a probe pulse. To model this experiment, we suppose as we did in section 2.3.1 that of displaced harmonic oscillators coupled to an electronic degree of freedom. Knowing the eigenstates of the system, we could di-

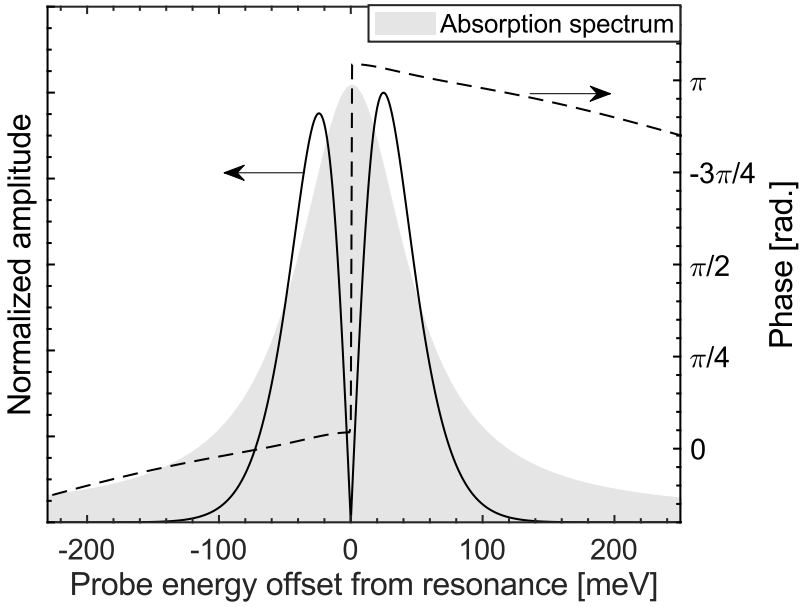

Figure 3.1: **Probe energy dependence of RICSRS signal for a single homogeneously broadened transition.** The spectral amplitude (line) and phase (dashes) are computed for an electronic linewidth of 50 meV coupled, a vibrational mode energy of 1 meV and a Huanhg-Rhys factor of 0.5 at a temperature of 50 K. The absorption lineshape used in the simulation is plotted as a shaded gray area.

rectly compute the system's response function to obtain the time-dependent polarisation. However, it is much wiser to separate the density matrix into its electronic and vibrational degrees of freedom and then compute an effective change in the equilibrium first-order permittivity induced by the pump pulse's excitation [112]. This useful trick allows us to easily distinguish between pump and probe interactions while drastically reducing the required computational resources when compared to a full $\chi^{(3)}$ calculation. The electronic density matrix is taken to be diagonal, neglecting effects from electronic coherences. This approximation is valid in the case of pump-probe measurements on two-level systems, but breaks down when more coupled electronic levels are taken in consideration. The problem is then reduced to the computation of the vibrational degrees of freedom's effects on the dielectric permittivity. To model these, the pump-induced modulation of the vibrational density matrices are computed for the ground and excited electronic states. The vibrational Hamiltonian is the same in both cases, except for a displacement Δ along the nuclear coordinate

associated to the vibrational mode. When the pump field interacts with the vibrational part of the system, it imparts a displacement in real and momentum space modeled using a moment generating function. All pump interactions are contained within this initial kick, after which the vibrational degree of freedom evolve freely according to their respective Hamiltonian before interacting with the probe pulse. The only free parameters of this model are the displacement of the vibrational Hamiltonian Δ upon excitation and the complex lineshape of the system under study. The latter supposes a single homogeneously broadened electronic state and its accompanying vibrational replicas. With these considerations and supposing undamped wavepacket motion, analytical expressions for the amplitude of the pump-probe modulation can be derived, and further reduce the required computation time. The result of such calculations are plotted in Figure 3.1. This yields the characteristic dual-peaked lineshape surrounding the transition coupled to the vibrational mode as well as the π phase shift upon crossing the central frequency. Not shown in the response so plotted is the signal's dependence on the pump pulse length. Indeed, the RICSRS signal is greater when the pump pulse duration matches the period of the displaced mode. Therefore, if the pulse is too short or too long, some modes could be unobservable using this technique despite being strongly coupled to electronic degrees of freedom. Moreover, the magnitude of the response depends on that of the displacement. It is therefore analogous to resonance Raman spectroscopy [113, 114] and can be used as a substitute to this technique when advantageous. This lineshape will become important for the results presented in chapter 6.

3.4 Double sided Feynman diagrams

Without specifying the system under consideration, it is hard to say much more about interpreting non-linear coherent spectroscopy techniques. However, certain aspects of the system under consideration are often well approximated by a single-particle occupying molecular-like discrete orbitals. In this case, the system's density matrix can be easily written down and each terms arising from the nested commutators of equation 3.6 can be

represented in a diagrammatic and useful way. Each diagrammatic elements are called double sided Feynman diagrams. These are constructed by observing the following rules:

1. Time flows from the bottom to the top of each diagram.

2. Each line represents the density matrix's state after a light-matter interaction.

3. Arrows represent light-matter interactions. Arrows pointing towards the right or the left represent a non-conjugate or conjugate interaction respectively. The last interaction arises from the quantum mechanical average to obtain $P^{(n)}$ and is different in nature from the other interactions. It is not associated to an applied electric field but rather spontaneous emission and so is represented by a different arrow.

4. Each Feynman diagram carries a sign of $(-1)^n$ where n is the number of light-matter interaction acting on the right. This property stems from the commutator's definition that is $[\hat{A}, \hat{B}] = \hat{A}\hat{B} - \hat{B}\hat{A}$. The final emission interaction is not counted in this rule.

5. An arrow pointing towards the system represent an excitation of the system and vice-versa for an arrow pointing outwards. This is a consequence of the rotating wave approximation and forbids the appearance of terms corresponding to emission from the ground-state.

6. After the final emission interaction, the system must be in a population state.

For example, the Feynman diagrams involved in the response function of a simple two level system (or V model) following a conjugate and two non-conjugate interactions are presented in Figure 3.2. By inspecting a Feynman diagram and supposing the density matrix dynamics obey the optical Bloch equations, one can easily deduce the temporal evolution of the associated term, its amplitude as well as its sign. For example, the term A associated to the diagram in the upper left corner of Figure 3.2b is positive and oscillates as

$$A(\tau, \tau', t) = e^{-i(\omega_X - i\gamma_X)\tau} e^{i(\omega_X + i\gamma_X)t} e^{-\Gamma_X \tau'} \tag{3.14}$$

where $\gamma_X = \gamma'_X + \Gamma/2$ is the dephasing rate, γ'_X the bath induced dephasing and Γ the radiative decay rate. During time τ and t, this term oscillates at ω_X the frequency difference between the states involved in the first and last coherence respectively. These coherences decay at a rate γ_X due to dephasing dynamics induced by radiative decay to the ground state and interactions with an incoherent thermal bath. During time τ', the density matrix is in a population state and the signal does not oscillate but rather decays at a rate Γ due to radiative decay. This basic model is useful to superficially interpret the results of coherent non-linear spectroscopy experiments, but fails to reproduce many behaviors observed in real experiments. First, it does not predict population relaxation within the excited state ladders. This can however be accounted for by introducing these dynamics in the optical Bloch equations. Secondly, it does not consider the effects of inhomogeneous broadening on the system's optical response, a broadening mechanism ubiquitous in even the purest of samples. To do so, one must turn to a much more involved formalism, that of the Brownian oscillator model [109] to predict their signature. Lastly, due to our choice of a single particle basis to represent the system's density matrix, this approach is ill-suited to discuss many-body effects on the non-linear optical response. To properly account for these, the double-sided Feynamn diagrammatic approach must be abandoned and the full many-body calculation must be performed using equations 3.11 and 3.6.

3.5 Interpreting a multidimensional spectrum

The goal of MDCS is to obtain information about the system under study through the full temporal dependence of its non-linear coherent response function. A MDCS measurement is performed by scanning a delay during which a coherence oscillates and recording the radiated signal's spectral amplitude and phase. The radiated signal arises from the sum of all the pathways taken by the density matrix following a defined sequence of light-matter interaction. The signals arising from different interactions sequences yield different information about the probed system. For instance, consider the case shown in Figure 3.2 of the third

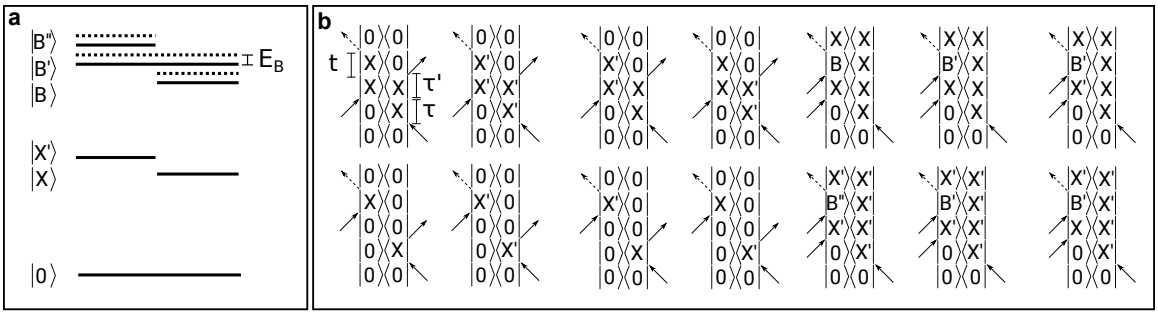

Figure 3.2: **Double-sided Feynman diagrams for a two level system with two ladders of excited states.** (a) Energy levels of the model system. It is composed of a ground state $|0\rangle$, two excitonic levels $|X\rangle$ and $|X'\rangle$, and three biexcitonic levels $|B\rangle$ (two bound X excitons), $|B'\rangle$ (two bound X and X' excitons) and $|B''\rangle$ (two bound X' excitons). These levels are redshifted from the sum of the energy of their constituents by a common binding energy E_B.(b) Double-sided Feynman diagrams responsible for the non-linear polarisation in the case of a conjugate interaction followed by two non-conjugate interactions.

order response resulting from a conjugated interaction followed by two non-conjugated interactions. In this case, all pathways feature coherent oscillations of opposite frequencies during the first and last interpulse delays. The resulting response is called rephasing since the coherent oscillations occurring during the first interpulse delay are rephased by the coherent oscillations occurring during the last interpulse delay. For this reason, the dephasing of the first coherent oscillations due to inhomogeneous broadening is cancelled after some time during the last coherent oscillation. However, dephasing occurring due to homogeneous broadening is not rephased, allowing us to segregate both of these contributions to line broadening using a rephasing measurement. If the population dynamics occurring during the second delay are not allowed to occur (by setting this delay to zero), this measurement is called a photon-echo and is used to extract the intrinsic homogeneous linewidth of an optical transition [115] as well as probe dephasing arising from many-body effects. A similar analysis can be performed for all of the three distinct interaction sequences allowed by a third-order non-linear measurement. These can be classified into three categories: one-quantum (1Q), two-quantum (2Q) and zero-quantum measurements (0Q). This nomenclature is based on the difference in number of quanta involved in the coherence oscillating during the scanned delays. Thus, n-quantum measurements probe

the coherences between states separated by n light-matter interactions. For this reason, 1Q measurements are the most common as they directly probe the optical transitions observable in photoluminescence and absorption spectroscopy. 2Q measurements are extremely useful to explore biexcitonic correlations and inelastic exciton scattering while 0Q measurements are great to probe vibronic coherences within an excitonic manifold.

A 2D spectrum is the result of a multidimensional Fourier transform of the measured signal's temporal dependencies along the time axes during which coherences oscillate. Generally, the Fourier transform along the emission time axis is experimentally performed by a coherent spectrometer so that only the first temporal axis needs to be transformed. The magnitude or real part of the 2D spectrum are then presented as 2D plots with two energetic axes corresponding to the frequency domain of the scanned delays. By convention, for 1Q measurements, the first scanned delay is called the absorption time t_{abs} and yields the absorption energy once transformed. For 2Q measurements, the corresponding axis is called the two-quantum energy axis and corresponds to the second interpulse delay during which coherences oscillate at twice the optical frequency. Finally, the time after the last light-matter interaction during which the signal is emitted is called the emission time. Once transformed, it yields the emission energy axis. For rephasing measurement, the initial coherence oscillates at a frequency with a sign opposite to the last coherence's oscillation frequency. For this reason, features appear in the negative part of the axis corresponding to the former delay. Since there are three light matter-interactions and an emission involved in generating a third-order non-linear signal, there remains another interpulse delay not presented in a 2D spectrum. This delay is often the one separating the second and third interactions in a 1Q measurement and yields important information about population induced dynamics. It is often specified in a 2D spectrum along with the type of measurement it represents.

We can now interpret experimental two-dimensional (2D) spectra using the formalism presented in section 3.1. To interpret a 2D spectrum, one could build a model for the system, use it to predict the system's temporal evolution and use equations 3.11 and 3.6 to compute the temporal dependencies of the non-linear polarisation. A two-dimensional spectrum is then obtained by taking the two-dimensional Fourier transform of the response function along the same time axes as those scanned in the experiment. By comparing a few calculations with the experimentally measured spectrum, one could hope to draw conclusions about the system from the experiment. This approach is sometimes used to interpret subtle effects in 2D spectra of well understood systems [116] but proves challenging without a minimal model. Another approach involves the use of double-sided Feynman diagrams to predict the spectral position of features as well as their overall relative sign. However, as previously mentioned, this formalism does not account for some many-body effects, disorder and fluctuations. It is nonetheless a useful paradigm in which to analyze experimental data and is used frequently within this thesis.

In this picture, a feature in a 2D spectrum arises due to the contribution of all terms that oscillate at the same frequencies during the scanned delays. Each term represents one of the many possible pathways for the system following a sequence of light-matter interactions and can be represented as double-sided Feynman diagrams. A diagram oscillating at a frequency ω during the first scanned delay and at a frequency ω' during the second will appear as a feature at an energy $\hbar\omega$ on the first energy axis and at an energy $\hbar\omega'$ on the second one. Each diagram's oscillation frequency can be determined using the same procedure that lead to equation 3.14. The number of light-matter interaction on the right side of the diagram determines the resulting feature's overall sign. By writing down all possible diagrams for a given interaction sequence, one can predict the energy, amplitude and sign of features in a 2D spectrum. For example, the 1Q rephasing spectrum and the 2Q non-rephasing spectrum of a simple two excitons and biexcitons model are shown in

Figure 3.3. The position and sign of the features in the rephasing spectrum are determined using the diagrams of Figure 3.2b and a similar procedure was used to construct the 2Q spectrum. While this is very useful to quickly predict a 2D spectrum, it still requires a basic model. However, a model such as the one presented in Figures 3.2 and 3.3 can be used to phenomenologically interpret many measurements.

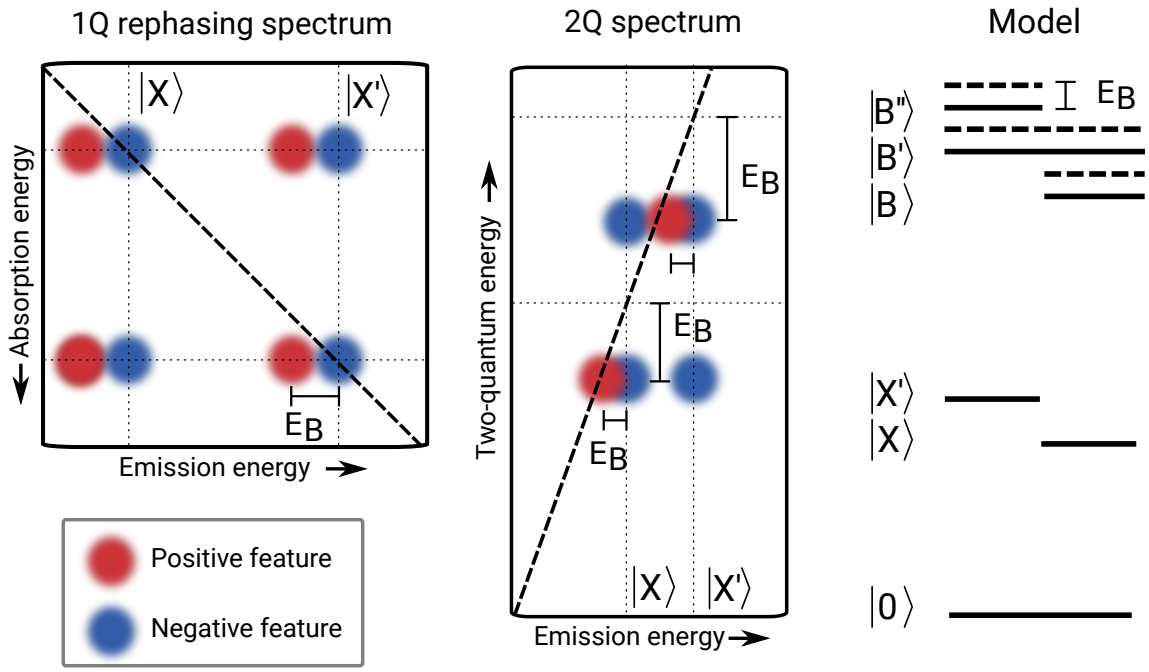

Figure 3.3: **One quantum rephasing spectrum and 2Q non-rephasing spectrum for a simple two excitons model with biexcitonic correlations.** Blue and red circles represent features of opposite sign. The dashed line represents the diagonal and two-diagonal of the 1Q and 2Q spectra respectively. The dotted lines represent the energy of the excitons while E_B indicates the biexcitonic binding energy.

To show how this can be done, I will demonstrate in the following how to reconstruct the model presented in Figure 3.3 from its 1Q rephasing spectrum and its 2Q spectrum. We first turn our attention to the 1Q rephasing spectrum. Two features are observed along the diagonal. These features are trivial and indicate that these optical transitions are correlated with themselves. Their emission and absorption energies correspond to their energy above the ground state. We thus know that there are two excitonic transitions at these energies,

something we could have deduced from a linear absorption spectrum alone. For both of them, features of opposite sign redshifted along the emission energy axis are observed. These features typically arise from diagrams involving transitions from the first excitonic manifold to the next and are called excited state absorption (ESA) features. These indicate that there is an excited state manifold whose energy is redshifted by E_B from twice the first manifold's energy. Features are also observed far off the diagonal and arise due to a common ground state between the excitonic features. These features, called cross-peaks, would not be observed if the system were to be composed of two independent transitions such as two distinct chromophores. This means that these features are intrinsic to the material and do not arise from inhomogeneities. Redshifted along the emission axis from these cross-peaks lie more ESA features indicating the presence of composite states in the higher-lying manifold, that is states which can be populated by an optical transition from both $|X\rangle$ and $|X'\rangle$. When the second excited state manifold is not shifted from twice the first manifold's energy, these ESA features cancel out the crosspeaks. While the 1Q measurement indicates the existence of a second manifold of excited states, it tells us nothing about its structure. To do so, we turn to the 2Q spectrum. It harbors negative features redshifted along the two-quantum energy from the two-diagonal indicating an ESA from the first to the second excited state manifold. This vertical shift indicates the amount of energy by which the state in the second manifold is redshifted from twice the emission energy. This information was already obtained through the 1Q rephasing spectrum, but it is now clear that each exciton can be excited into two distinct biexcitons. Moreover, each positive feature is accompanied by a negative feature redshifted by the same energy along the emission energy. This yields another method of estimating, for instance, a biexciton's binding energy.

This type of analysis is useful to guide the interpretation of 2D spectra without relying on a full model. From the energy and sign of features in a 2D spectrum alone, one can even deduce many of the profound aspects a minimal model would need to be faithful to

the system under study. In real systems, many more effects can be observed that were not included in our simple model such as repulsive exciton-exciton interactions in the 2Q spectrum [117] and population transfer channels through a cross-peak's time dependence and asymmetry between cross-peaks [118]. Vibrational coherences can also manifest themselves in beatings along the population time [119, 120] and yield similar information to that which is contained in a resonant Raman spectrum.

3.6 Lineshapes in two-dimensional spectra

So far, we have yet to discuss the lineshape of features observed in a 2D spectrum. These contain a wealth of information about many-body interactions as well as homogeneous and inhomogeneous broadening mechanisms. They arise from two distinct phenomena. The former is due to energetic fluctuations on an ultrafast timescale such as elastic collisions with other particles and defects, environmental fluctuations, radiative decay as well as other population dynamics and relates to a state's lifetime. The latter arises from fluctuations slower than the state's lifetime such as Doppler broadening or sample inhomogeneities [109]. Therefore, probing these effects would reveal a wealth of information about a system's dynamics and the mechanisms that drive them. In the limit of pure homogeneous dephasing, the 2D lineshapes are well described by the optical Bloch equations. Then, one simply needs to extract each term's multitemporal dependence as shown in equation 3.14 and Fourier transform it along all oscillating temporal axes. The oscillating terms merely shift the feature in the 2D spectrum as mentioned in the previous section. The exponentially decaying terms, however, yield a complex-valued 2D lineshape in the (ω_{abs}, ω_{em}) plane. For a 1Q rephasing term, it reads

$$S_R(\omega_{abs}, \omega_{em}) \propto \left[\frac{\gamma_2 + i(\omega_{em} - \omega_2)}{(\Delta\omega_{em} - \omega_2)^2 + \gamma_2^2} \times \frac{\gamma_1 + i(\omega_{abs} - \omega_1)}{(\Delta\omega_{abs} - \omega_1)^2 + \gamma_1^2} \right] \tag{3.15}$$

where ω_i and γ_i are the frequencies and decay rates of the i-th coherences while for a 1Q non-rephasing term, we get

$$S_{NR}(\omega_{abs}, \omega_{em}) \propto \left[\frac{\gamma_2 + i(\omega_{em} - \omega_2)}{(\Delta\omega_{em} - \omega_2)^2 + \gamma_2^2} \times \frac{\gamma_1 - i(\omega_{abs} - \omega_1)}{(\Delta\omega_{abs} - \omega_1)^2 + \gamma_1^2} \right]. \tag{3.16}$$

When inhomogeneous broadening is no longer negligible, the above expressions must be modified to account for this additional dephasing mechanism. We shall focus on the rephasing 2D lineshape in this limit, since through it we can separate the homogeneous and inhomogeneous contributions to the optical linewidth. Using results from Kubo's stochastic lineshape theory in the slow modulation limit [121] and the projection-slice theorem [122], one obtains an analytical expression for the rephasing lineshape. For a diagonal peak, the anti-diagonal lineshape is [123]

$$S_{AD}(\omega_{ad}) = \frac{\exp\left(\frac{(\gamma - i\omega_{ad})^2}{2\delta\omega^2}\right) \text{erfc}\left(\frac{(\gamma - i\omega_{ad})}{\sqrt{2}\delta\omega}\right)}{\delta\omega(\gamma - i\omega_{ad})}, \tag{3.17}$$

while the diagonal one reads as

$$\begin{aligned} S_D(\omega_d) = & \frac{\exp\left(\frac{(\gamma - i\omega_d)^2}{2\delta\omega^2}\right)}{\gamma\delta\omega} \\ & \times \left[\text{erfc}\left(\frac{(\gamma - i\omega_d)}{\sqrt{2}\delta\omega}\right) + \exp\left(\frac{2\gamma i\omega_d}{\delta\omega^2}\right) \text{erfc}\left(\frac{(\gamma + i\omega_d)}{\sqrt{2}\delta\omega}\right) \right]. \end{aligned} \tag{3.18}$$

Here erfc corresponds to the complementary error function, ω_{ad} and ω_d are the anti-diagonal and diagonal angular frequencies, respectively and $\delta\omega$ characterizes the inhomogeneous distribution. The real, imaginary and absolute lineshapes for various degrees of inhomogeneity are shown in Figure 3.4. Homogeneous broadening alone produces a symmetric lineshape across the anti-diagonal. The real and imaginary parts respectively feature distinct absorptive and dispersive anti-diagonal lineshapes so-called due to their close resemblance to the imaginary and real parts of the linear response function's spectrum. Upon

increasing the width of the inhomogeneous distribution of states, the feature is elongated principally along the diagonal but also slightly across it. To account for the latter, it is therefore necessary to use the full lineshape to accurately extract the homogeneous and inhomogeneous linewidths from a rephasing measurement.

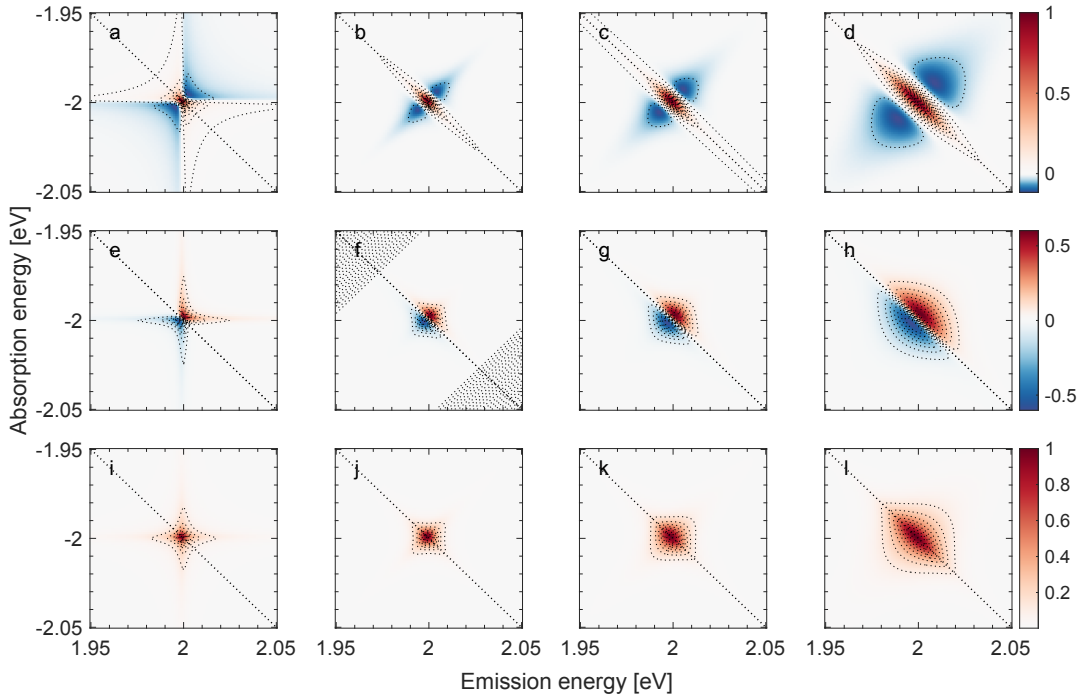

Figure 3.4: **Effect of inhomogeneous broadening on a feature's lineshape in a rephasing 2D spectrum.** The real (a, b, c and d) and imaginary parts (e, f, g and h) as well as the modulus (i, j, k and l) of a feature are shown for various degrees of inhomogeneous broadening. Features arising from pure homogeneous dephasing are shown in a,e and i for $\gamma = 6$ meV. The effects of an addiditonal inhomogeneous broadening are also shown for a $\delta\omega$ of 1 meV (b, f and j), 4 meV (c, g and k) as well as 10 meV (d, h and l).

The effects of many-body interactions on the 2D lineshape are much more challenging to account for and often require the use of an elaborate and realistic model for the system's temporal evolution between pulses [116]. When treating these effects, it is often necessary to truncate an infinite ladder of higher orders of many-body correlations [23]. The effects of the truncated contributions can be approximated by a population dependent

temporal modulation of an optical transition's frequency [124]. This effect manifests itself as both a population-dependent shift of the transition frequency called excitation-induced shift (EIS) as well as a population-dependent dephasing of the optical coherences called excitation-induced dephasing (EID) [125]. The latter manifests itself as an increased homogeneous linewidth due to inelastic scattering with other excitations. Counterintuitively, this term does not vanish at low fluences since it then contributes linearly to homogeneous broadening [49, 126]. Broadening due to scattering with other particles (such as phonons) yields a similar linear effect at low particle densities. Therefore, to accurately extract the single-particle homogeneous linewidth, one must extrapolate to zero density all many-body effects by measuring the homogeneous linewidth at many densities [123]. Lastly, both EIS and EID change the appearance of the real and imaginary parts of the lineshape. By using modified optical Bloch equations accounting for these effects, one can show that the real part of the rephasing spectrum changes from an absorptive to a dispersive character [124]. Therefore, both the linewidth and lineshape of features in a 2D spectrum can inform us on scattering processes and many-body interactions.

3.7 Conclusion

In this chapter, the theoretical foundations behind the interpretation of non-linear coherent spectroscopy experiments was exposed. In particular, the formalism was adapted to interpret linear measurements such as absorption spectroscopy as well as third-order measurements like transient absorption and MDCS. It showed that the result of these experiments are closely linked to a quantum mechanical system's coherent dynamics through the non-linear response function. The diagrammatic expansion of the latter proved very useful to predict the signal's dependence on the experimental conditions, to quickly build a 2D spectrum from simple models and to interpret experimental data. The results of more involved theoretical predictions were also presented to highlight the information contained in a feature's lineshape. These showed how the inhomogeneous and homogeneous contributions to

line broadening could be separated and how manifestations of many-body interactions arise in the coherent lineshape. There is therefore much to gain from the implementation of such powerful optical probes. However, given the stringent requirements of high relative phase stability, short pulse width and resonant excitation, this is no easy task. These experiments are as challenging to perform as they are powerful, but using an ingenious and rigorous experimental implementation, they can be routinely employed even by the uninitiated. In the following chapter, I will expose how we surmounted these technical challenges to perform state-of-the-art non-linear coherent spectroscopy.

CHAPTER 4

EXPERIMENTAL IMPLEMENTATIONS OF SPECTROSCOPIC PROBES

Some believe physics to be at its core an experimental endeavor, an empirical pursuit [127]. To understand nature, one must first observe it and build physical models upon these observations. The whole purpose of physics' experimental branches are to improve the scope of what is observable through better experimental techniques. These developments allow for new observations, which can be used to conceive better physical models and hypotheses. In practice, this means that no measurement is ideal and therefore that understanding the limitations of an experimental probe is required to correctly interpret its measurements. The first limitation encountered in the laboratory is that of insufficient experimental power such as insufficient resolution, scope or accuracy. This leads to a phenomenon being partially observed and could bring about its erroneous understanding. Another limitation arises from the opposite extreme, an insufficiently specific measurement. In this case, the experiment reports simultaneously the effects of too many different phenomena making the interpretation of the acquired data potentially challenging. Manifestations of this limitation are called experimental artifacts when the contribution from polluting phenomena is systematic and tractable or noise when it is pseudorandom.

In this regard, coherent non-linear spectroscopy is no different from any other experimental method. It too is prone to artefacts, noise and experimental limitations, perhaps even more so given the complexity of some of these techniques. The purpose of this chapter is to present the experimental implementations of these techniques highlighting the design choices made to achieve the desired performances and each setup's limitations. I begin by describing the various devices required to optically power our experimental apparatuses and then move on to the experiments themselves. A large part of this section is devoted

to our multidimensional spectrometer given its unusual nature. We conclude this chapter with methods used to compress and characterize the pulses used in our MDCS experiments.

4.1 Sources of light

Coherent non-linear spectroscopic apparatuses rely on appropriate sources of light to operate. The measurement at hand dictates the desired characteristics of the light source. In linear absorption spectroscopy, a spectrally broad source of light is all that is needed, whereas transient absorption spectroscopy and MDCS, due to the required temporal resolution and resonant excitation, demand short and spectrally tunable pulses of light. Thanks to half a century of development in the field of lasers and photonics, it has never been easier to manipulate light than it is today. In this section, I highlight how we generate light to suit our many experimental needs.

4.1.1 Femtosecond laser system

Most ultrafast measurement systems described in this section are powered by the output of a PHAROS commercial ultrafast laser system from Light Conversion. It is composed of a low-power and high-repetition rate femtosecond oscillator whose output is chopped down to 100 kHz using a pulse-picker and fed into a chirped pulse amplifier [128]. Both the oscillator and the amplifier use ytterbium doped potassium gadolinium tungstate (Yb^{3+}:$KGd(WO_4)_2$ or Yb:KGW) as a gain medium. This yields 200 μJ of energy per pulse (20W at 100 kHz) at a central wavelength of 1029 nm with a pulse duration of about 200 fs. While the laser does provide a stable train of short femtosecond pulses, the operation wavelength cannot be tuned to match the resonances in the materials we wish to study. Moreover, even if its emission wavelength could be tuned as such, the pulses are too long compared to electronic dephasing times making them useless for MDCS. We can however use its high-peak powers to generate pulses suitable for our needs using non-linear optical

devices.

4.1.2 OPA: Optical Parametric Amplifiers

Optical parametric amplifiers are light amplifiers [129, 130, 131]. The light to be amplified (the seed) interacts in an optically non-linear medium with an intense beam of higher energy (the pump). Through this non-linear interaction, the seed beam is coherently amplified generating the signal and the pump's excess energy is dumped into a third beam called the idler. The seed is usually provided using white light continuum (WLC) generation [132, 133] by focusing a small fraction of the laser's beam into a transparent material like sapphire. When done correctly, this generates a stable spectrally broad pulse of light with a high quality beam profile ideal for subsequent amplification. During the amplification, energy must be conserved so that

$$\omega_p = \omega_s + \omega_i \tag{4.1}$$

where ω_p, ω_s and ω_i are the frequencies of the pump, signal and idler respectively. These devices use difference frequency generation [134] to provide the required non-linear interaction. Since the gain depends on the relative phase between all beams, sizeable gain will only occur if the latter is constant throughout the interaction volume [135]. This requires that the beam's relative phases do not change when propagating through the non-linear medium so that

$$\Delta\vec{k} = \vec{k}_p - \vec{k}_s - \vec{k}_i = 0 \tag{4.2}$$

where $\Delta\vec{k}$ is the wavevector mismatch and $\vec{k}_p$, $\vec{k}_s$ and $\vec{k}_i$ are the wavevectors of the pump, signal and idler respectively. This condition is known as phase-matching, not to be confused with the phase-matching of section 3.2 whose physical origin is distinct. When the pump and signal beams propagate in the same direction, equation 4.2 becomes a single

scalar equation which can be reduced to

$$n_p\omega_p - n_s\omega_s - n_i\omega_i = 0 \tag{4.3}$$

where n_p, n_s and n_i are the refractive indices of the non-linear material at the frequency of the pump, signal and idler respectively. Due to the dispersive character of transparent mediums, it is impossible to satisfy both equations 4.2 and 4.3 simultaneously in isotropic medium [136]. For this reason, transparent uniaxial birefringent crystals with high $\chi^{(2)}$ values such as β-barium borate (BBO) are used to achieve phase-matching. The beams are polarized appropriately and, using the crystal's orientation or temperature [135], the effective indices of refraction for each beam are tuned to obtain phase-matching, and thus large gain, at the desired wavelength. The frequency tolerance of this process is usually small so that even though the seed is spectrally very broad (hundreds of nanometers) the resulting signal and idler beams are no broader than a few nanometers. This limits the temporal resolution of non-linear experiments to a few hundreds of femtoseconds. However, generally by tuning the non-linear crystal's orientation, the output of the amplifier is highly tunable. This tunability can be further enhanced by using an harmonic generator placed after the OPA to reach any wavelengths between 250 nm to 2500 nm. OPAs are very useful in high-resolution transient absorption experiments or ICSRS where moderate temporal resolution are required.

4.1.3 NOPA: Non-colinear Optical Parametric Amplifiers

When a greater temporal resolution is required, the amplifier's bandwidth must be drastically increased. This can be done by using a non-colinear geometry for the pump, signal and idler beams and requires considering the full vectorial version of equation 4.2. The non-colinear geometry amounts to matching the projection along the pump's wavevector of the signal and idler's group velocity, thus increasing the gain bandwidth [137] to tens

or hundreds of nanometers in the visible. By carefully matching the angle between the pump and seed beams, a NOPA's output is sufficiently broad to simultaneously cover many excitonic features and even sometimes the carrier continuum making these devices ideal light sources for MDCS experiments. However, given the large gain bandwidths, it is much harder to tune the output of these devices than it is for an OPA. The output spectrum being largely determined by the pump's wavelength, laboratories are typically equipped with a few NOPAs powered by different harmonics of the ultrafast laser's output such that the visible, near infrared and sometimes infrared regions are covered.

The spectral region of interest in the context of this thesis' work is located in the visible. Therefore, a home-made single pass NOPA pumped by the third harmonic of the femtosecond laser system was built to cover this spectral region with pulses of about 60 nm of bandwidth. A schematic of our implementation is presented in Figure 4.1. A beamsampler sends a tenth of the laser's output ($\sim$10 μJ/pulse) to the seed generation stage while the rest ($\sim$90 μJ/pulse) is used for the generation of the UV pump beam. To generate the seed, the former is focused by a lens into a 4 mm thick sapphire plate while its power and the location of its focal point inside the sapphire is trimmed to yield a single filament of WLC. The resulting beam is filtered by a dielectric short-pass filter with its cutoff at a wavelength of 750 nm to remove the light used to generate the WLC. The seed is then focused near the amplification crystal by a 2" metallic mirror on a translation stage to trim the size of the seed spot on this crystal. The use of a mirror instead of a lens minimizes the chirp added to the seed pulse thus improving the amplification bandwidth. To generate the pump beam, most of the laser's output enters a delay line to trim the temporal overlap between the seed and pump pulses before being entering the third harmonic generator. This device consists of a long non-magnifying Keplerian telescope with two BBO crystals close to the telescope's focal point to increase the device's power efficiency. The first crystal generates the second harmonic of the laser's fundamental while the second one sums the resulting

second harmonic with the remaining unconverted fundamental beam to generate the third-harmonic pump. By using a succession of type I and type II sum-frequency processes, the temporal overlap of all beams involved in the third-harmonic generation is kept optimal thus forfeiting the need for an additional delay line in the frequency converter [138]. The pump beam is then focused towards the amplification crystal so that its focal point lies right before it. This causes the pump beam to be slightly divergent in the crystal thus minimizing the detrimental effects of non-linear Kerr self-focusing during the amplification. This increases the maximal usable pump power before optical damage and amplified beam profile distortion are observed and therefore also increases the efficiency of the amplifier. When optimally aligned, the UV pumped NOPA can generate an output of around 200 nJ/pulse of broadband light with a good spatial profile to be used in MDCS experiments.

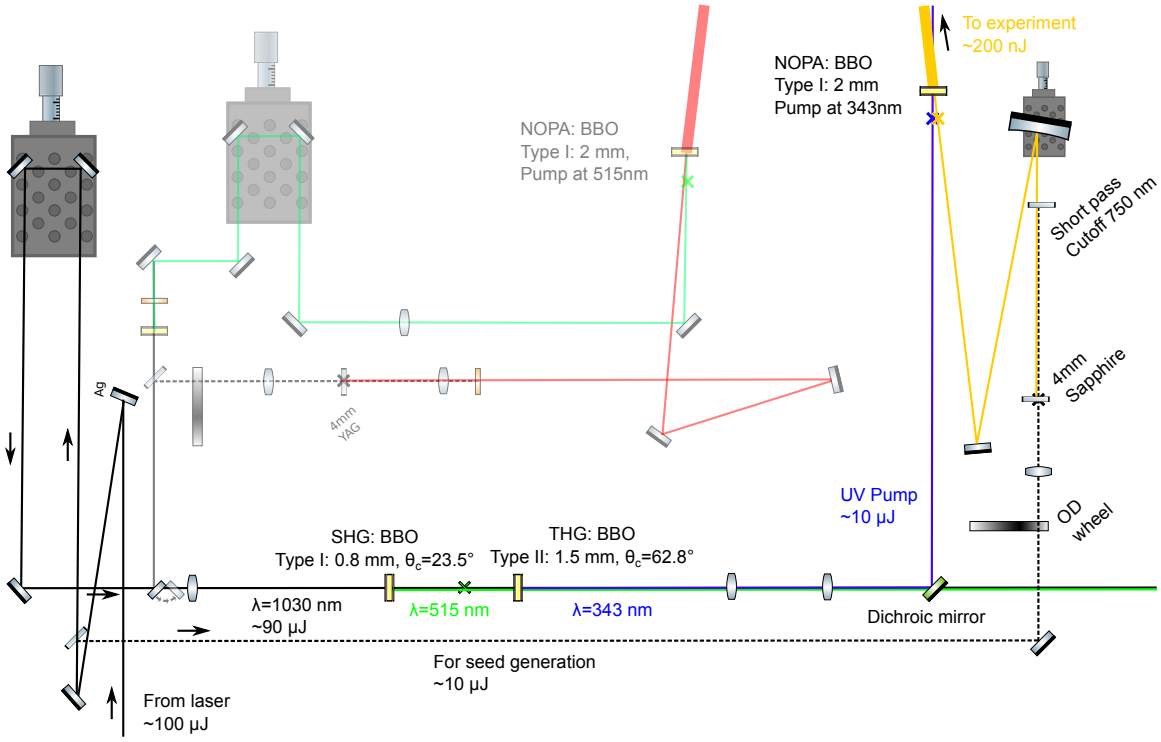

Figure 4.1: **Schematic of our non-colinear optical parametric amplifier.** The IR, green and UV beams are represented by black, green and blue lines respectively. The shadded portion of this drawing represents our implementation of the second harmonic pumped NOPA, not used in this thesis.

4.2 Absorption and transient absorption spectroscopy

Absorption spectroscopy is a linear measurement governed by the linear optical response of the system as stated in equations 3.3 and 3.4. To perform this measurement, a spectrally broad beam (for instance, as generated by a stabilized tungsten lamp) is sent to the sample and the transmitted beam's spectrum is recorded by a spectrometer. The beam interacts once with the sample and sends the density matrix into a coherence for every optical transition resonant with the incoming beam. This oscillating coherence in turns radiates light in the direction of the transmitted beam. This signal interferes with the original beam yielding the measured transmitted spectrum. As such it is a self-heterodyned measurement. The same also applies with reflectance spectroscopy, but the latter stems from the conjugate of the optical response. To extract the absorption spectrum or absorbance $A(\omega)$ from the transmitted spectrum $I_T(\omega)$ and the incident spectrum $I_I(\omega)$, one assumes Beer-Lambert's law and that most of the incident light has been absorbed yielding

$$A(\omega) = -\log_{10}\left(\frac{I_T(\omega)}{I_I(\omega)}\right). \tag{4.4}$$

Transient absorption spectroscopy is similar to absorption spectroscopy but is time-resolved and stems from a third-order polarization given by equation 3.11. As shown in Figure 4.2, a strong pulsed beam first interacts twice simultaneously through both its conjugated and non-conjugated part with the sample creating an excited state population or a coherence between two close-lying excited states. Some time later, called the pump-probe delay, a spectrally broad probe pulse interacts with the sample, mapping it back into an oscillating coherence. Just like with linear absorption spectroscopy, this coherence then radiates a signal that interferes with the transmitted probe beam. In practice, transient absorption measurement are often reported in terms of the transient differential transmission $\Delta T/T$. It consists in the difference between the transmitted spectrum when the pump is on and when the pump is off then normalized by the latter. The differential transmission

spectrum is then recorded for various pump-probe delays and yields a transient absorption spectrum. To carry on transient absorption experiment, we used the output of an optical parametric amplifier (OPA) to provide the pump pulse. The probe beam is generated using 2 W of power from the PHAROS focused into a 3 mm thick plate of sapphire to produce a stable white light pulse. The transient absorption spectrometer is a commercial setup (Hera) developed by Light Conversion and features an Andor Kymera i193 monochromator equipped with a full-frame transfer CCD to speed-up the acquisition time.

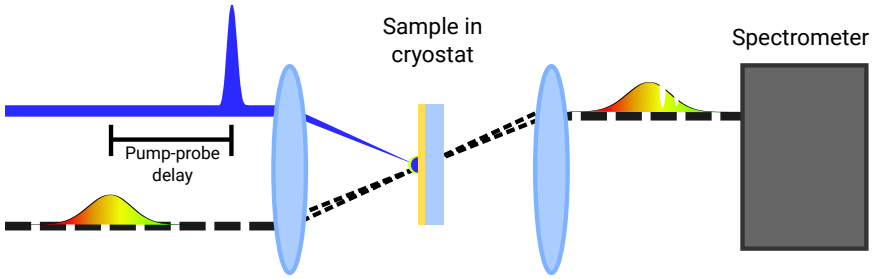

Figure 4.2: **Schematic of a transient absorption experiment.** A short pump pulse is sent onto the sample followed by the probe pulse after some delay. The transmitted spectrum is recorded for each time step by a fast spectrometer.

4.3 Four wave mixing-based multidimensional coherent spectroscopy using COLBERT

Multidimensional coherent spectroscopy (MDCS) refers to any measurement which fully characterises the n-th order non-linear response of equation 3.2. There are almost as many ways to perform this task as there are multidimensional spectroscopy groups. Some measure the non-linear response function through a final population state [139] instead of a non-linear polarisation. This method is extremely versatile, allowing one to detect the non-linear response through any population-related physical observable such as photoluminescence, photocurrent, photo-induced absorption or magnetization to name a few. This allows the investigation of coherent processes resulting in species which recombine non-radiatively, a feat unique to these methods. These, however, remain uncommon. Most

methods involve the detection of the light radiated by a non-linear polarisation in a phase-matched direction to measure the non-linear response function. To achieve this, many experimental implementations are used. Some use birefringent wedges inserted in a traditional pump-probe beam line to split the pump pulse into two pulses and therefore resolve coherent oscillations between the two first light matter interactions previously hidden in transient absorption [140]. Recently, the use of frequency-combs to acquire multidimensional spectra is being explored due to its increased resolution and acquisition speed [141]. Nonetheless, the most commonly employed MDCS method is that of a four-wave mixing (FWM) experiment, as shown in Figure 4.3a. Using FWM-based techniques, $n+1$ pulses are required to fully measure the n-th order response function: n are used to generate the n-th order non-linear polarisation and another one, the local oscillator (LO), is used to extract the signal's spectral amplitude and phase using a coherent detection technique called heterodyne detection. Experimental precautions are used to avoid any interaction between the local oscillator and the sample either by strongly attenuating it or by having it avoid the sample altogether. The n beams interact with the sample and generate the signal in the phase matched directions as given by equation 3.13. This direction is made to coincide with that of the local oscillator so that both interfere in the spectrometer allowing heterodyne detection of the FWM signal. The delays between the pulses are scanned and the signal's complex-valued spectrum is acquired for each step thus fully characterizing $S^{(n)}$.

In most implementations, four beams copropagating along the corners of a square (the so-called BOXCARS geometry, see upper left corner of Figure 4.3a) are used to measure $S^{(3)}$. Using a spatial mask, only the LO and any light copropagating with it is detected fixing the contribution of the other beams to the detected FWM signal. Due to phase-matching, the signal results from a conjugate interaction with the beam in the opposite corner to the local oscillator (beam A*) and non-conjugated interactions from the other beams (beams B and C). The time-ordering of these pulses determines which type of mea-

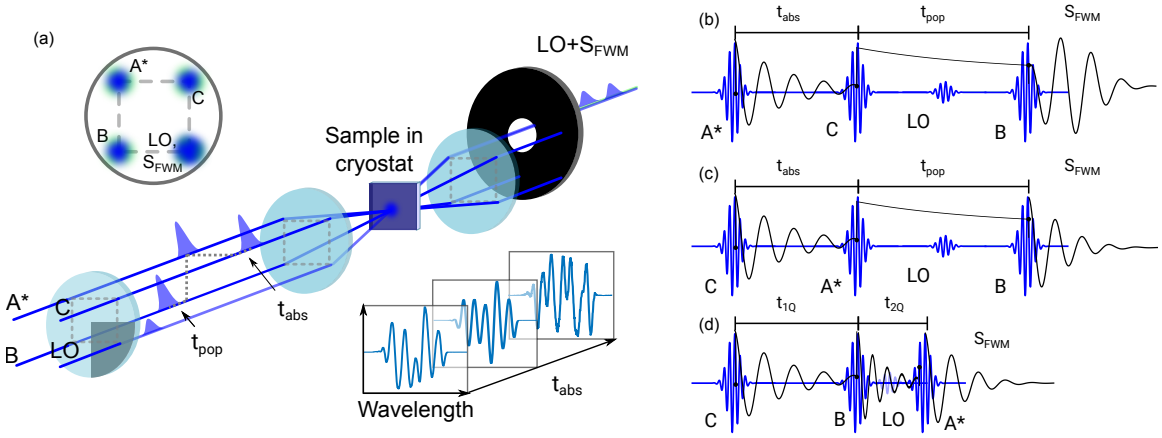

Figure 4.3: **Schematic of a FWM based MDCS experiment and of the various measurements it can perform.** (a) Schematic of a MDCS experiment in the BOXCARS geometry. The signal is generated in the same direction as the local oscillator for subsequent heterodyne detection. Before being sent to the sample, all beams go through a partially etched OD filter that attenuates only the local oscillator. The three types of measurements that can be performed by COLBERT: 1Q rephasing (b), 1Q Non-rephasing (c) and 2Q non-rephasing (d). The blue lines represent the indicent electric field and the black lines track the evolution of the relevent terms in the system's density matrix.

surement is being performed. When the conjugate beam or a non-conjugate beam interacts first, 1Q rephasing or non-rephasing measurements are respectively performed (Figure 4.3b and c) and the first interpulse delay t_{abs} is scanned. When the conjugate beam interacts last, a 2Q non-rephasing measurement is performed (Figure 4.3d) and the second interpulse delay t_{2Q} is scanned. After a scan, one has an energy (the spectrally resolved FWM signal) and time (the scanned delay) two-dimensional map. Fourier-transforming this along the scanned delay axis yields an energy-energy spectrum, otherwise known as a multidimensional spectrum. This last step is only possible because of the coherence along both the energy axis (trivial, a pulse is by definition self-coherent) and the delay axis. It is from this last requirement that stems the phase stability condition, that is, the beams' relative phases must be constant throughout the experiment.

4.3.1 Overview

The goal of a multidimensional spectrometer is therefore to generate a sequence of phase-locked pulses resonant with the optical transitions in the sample, delay them with respect to each other and record the signal at each step. Starting from a single pulsed laser source, this can be done using traditional beamsplitters and delay lines [142]. However, the requirement of phase stability make such an implementation complex since the beams' phases must be actively stabilized using a reference beam co-propagating through the setup and a servo loop. To circumvent this requirement, I implemented COLBERT (Coherent Optical Light BEam Recombination Technique), a phase-shaper based multidimensional spectrometer designed by the Nelson group [143]. It uses no moving parts and all beams travel through the same set of optical elements. Doing so forfeits the need for active interpulse phase stabilisation. This passive phase stabilisation scheme drastically simplifies its design. A schematic of our implementation of COLBERT is presented in Figure 4.4. COLBERT first splits the incoming beam into four using a diffractive beam shaper. As discussed in section 4.3.2, splitting the beam this way has the benefit of high interbeam phase stability but requires a careful alignment to avoid spatiotemporal beam distortions at the sample. These four trains of pulses are then temporally shaped by a diffractive pulse shaper to generate the required pulse sequence for each measurements. The workings of this device are described in section 4.3.3 along with the intrinsic limitations of pixelated pulse shaping. I also significantly improved the original COLBERT design by implementing a rigorous pulse compression scheme whose functioning principles are presented in section 4.4. Three beams and the local oscillator attenuated by a neutral density filter are then sent to the sample held in a cryostat to generate the FWM signal to be coherently detected using a spectrometer. The principles behind the coherent detection scheme used in COLBERT, that of heterodyne detection, are presented in section 4.3.4. To achieve high sensitivity and near background free measurements, COLBERT uses a phase-cycling scheme presented in section 4.3.5 which removes any signal that does not arise from a phase-matched interaction in the sample.

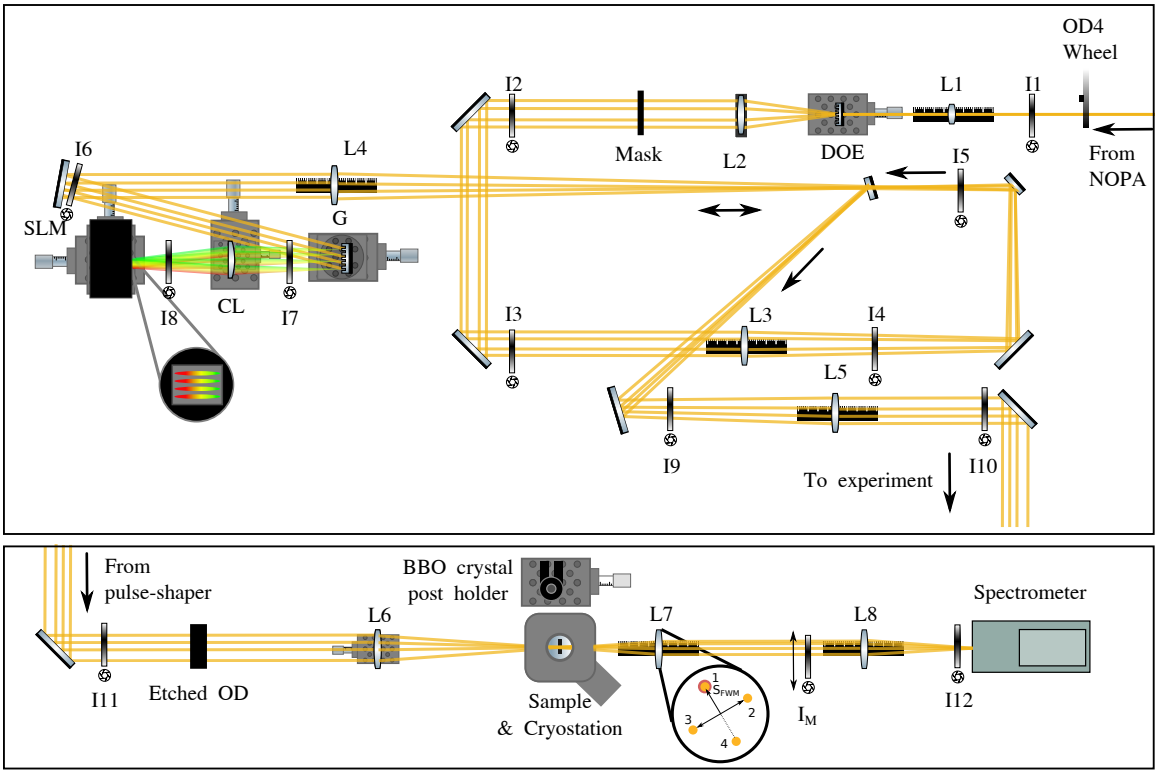

Figure 4.4: **Schematic of our implementation of COLBERT.** Irises (Ix), lenses (Lx) are numbered according to their placement in the beam line. Other labelled elements are the diffractive optical element (DOE), cylindrical lens (CL), grating (G) and spatial light modulation (SLM)

4.3.2 Beam shaping using a DOE and relay imaging

To generate four beams from a single one, COLBERT uses a diffractive optical element (DOE). It consists of a two-dimensional phase mask which diffracts the input beam into four beams. As illustrated in Fig. 4.5, this diffraction imparts a tilt of front on the outgoing pulses [144, 145]. Since tilt of front is mathematically equivalent to spatial chirp, the beams are slightly dispersed after the DOE. This is useful though: should the beams then travel through proper imaging, the pulses will recombine perfectly on the sample [146]. When improperly imaged, the pulses recombine at the sample with an angle between their pulse front, resulting in a small interaction volume, phase related artefacts in the signal and

reduced temporal resolution despite a perfect compression.

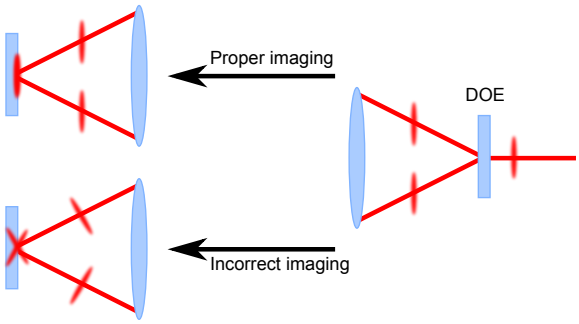

Figure 4.5: A schematic of the effect of the DOE on the generated beams' pulse fronts. The DOE imparts tilt of front on the generated beams. Through proper imaging, a total overlap of the beams can be obtained at the sample. Improper imaging induces partial beam overlap and spatial chirp at the sample, yielding artefacts in the signal as well as reduced temporal resolution.

How does one properly image the pulses? The secret lies in relay imaging. When using beams of light with no tilt of front, it is sufficient to ensure that the distance between two lenses in a telescope is the sum of their focal lengths. Relay imaging also requires the distance between two lenses to be the sum of their focal length even when the beams are collimated. In other words, the purpose of relay imaging is to image the DOE's phase mask on the sample. The better the imaging, the better will be the experiment's signal to noise ratio and temporal resolution.

4.3.3 Diffraction-based pulse shaping

Pulse shaping is a field as old as femtosecond lasers themselves [147]. It can be done using acousto-optic modulator (AOMs), deformable mirrors, MEMs-based micro mirror arrays or liquid crystals on silicon (LCOS) placed inside a 4f spectral filter geometry [148]. The purpose of these devices is to modify the phase of light incident on them. Most modern phase shapers are pixelated in one dimension so that they can spatially modify the phase of an incident beam and are thus called spatial light modulators (SLM). In principle, SLM-based pulse shaping is simple: the first grating separates the spectral components of the input beam so that they are imaged at the focal plane of the following cylindrical lens as

shown in Fig. 4.6. The SLM is placed at this focal plane and modulates the spatial phase of the beam spread on its active area. Because of the aforementioned grating and lens, a position on the SLM corresponds to a particular wavelength of the diffracted beam. Thus, by modifying the beam's spatial phase at the center of the 4f shaper, the SLM modifies the spectral phase of the incoming beam and performs pulse-shaping. If the SLM is transmissive, the dispersed beam is modulated by going through the SLM and is then imaged by another lens and grating arranged symmetrically to the first pair. If the SLM is reflective, the beam is modulated and reflected back into the lens and grating it came from. In both cases, even if no phase modulation is applied by the SLM, a slight deviation from the optimal 4f geometry will add a temporal chirp to the beam [147]. It is thus crucial that this distance be accurately set so that the added chirp does not exceed the limitations of the pulse shaper.

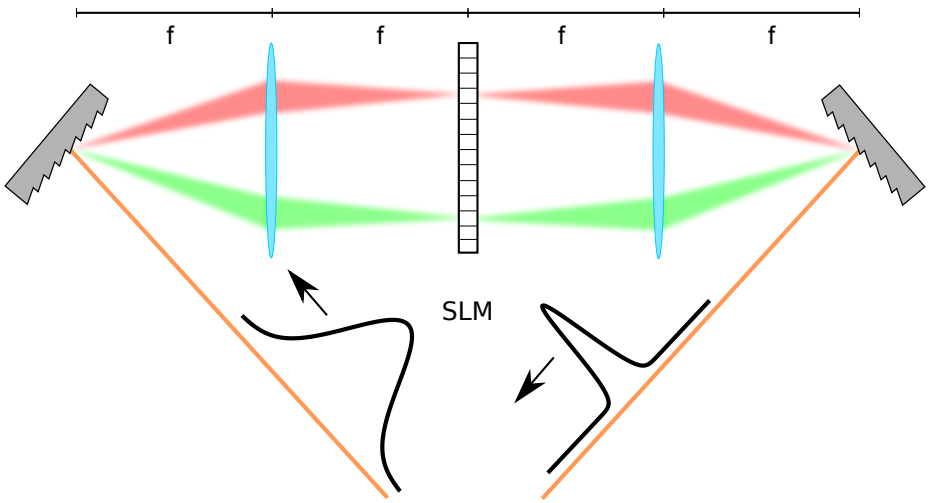

Figure 4.6: **Schematic of 4f spectral filter geometry with a transmissive SLM at its center.** The spectrum of the input beam is dispersed on the SLM so that it may modify its spectral phase and perform pulse-shaping. The spectral components are then recombined yielding the outgoing beam.

To simultaneously shape all the beams as required by MDCS, COLBERT uses a 2D-LCOS SLM, a reflective SLM with its pixels arranged in a two-dimensional array. In early designs of COLBERT, a beamsplitter was used to extract the reflected shaped pulses [43].

However, a small fraction of each pulses was reflected unmodulated from the surface of the SLM yielding artefacts in the output pulse train. Moreover, the spectral range of the pulse shaper was limited by that which over which the SLM can provide a full 2π phase shift. As we will show in the following, we can overcome these limitations using diffraction-based pulse shaping. Following the derivation of Vaughan et al. [149], consider the Fraunhofer diffraction pattern caused by a vertical phase pattern $\Phi(\nu, y)$ at a horizontal position where the dispersed beam's frequency is ν such that

$$\Phi(\nu, y) = \alpha_\nu \left[\frac{1}{2} + A(\nu) S_{d,\phi(\nu)}(y) \right] \tag{4.5}$$

where α_ν is the maximal phase shift the SLM can achieve at this frequency, $A(\nu)$ is a number between 0 and 1 and $S_{d,\phi(\nu)}(y)$ is a sawtooth function of period d and phase $\phi(\nu)$ going from -1/2 to 1/2 along the vertical direction y of the SLM. The electric field at the

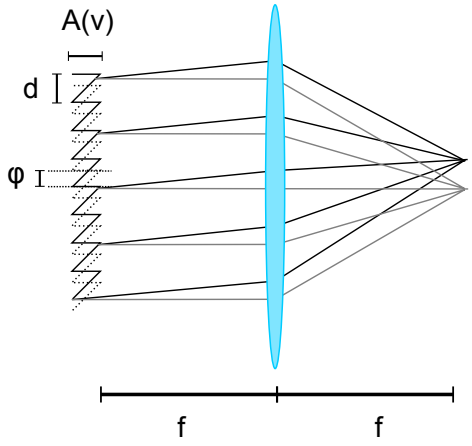

Figure 4.7: **Schematic of the effect of a vertical sawtooth phase function on an incoming beam.**The gray and black lines represent the trajectories of the incoming and outgoing beams respectively. d, ϕ and $A(\nu)$ are as defined in the text and f represents the lens' focal length.

position of the first-order of diffraction $E(\nu)$ thus created at the Fourier plane of an imaging lens is given by

$$E(\nu) = \exp[-i\phi(\nu)] \operatorname{sinc} \left[\pi - \frac{\alpha_\nu}{2} A(\nu) \right]. \tag{4.6}$$

This result is of the utmost importance. It first shows that it is possible to directly modify the spectral phase of the diffracted component by changing the phase of the sawtooth pattern. Moreover, it shows that even if the SLM cannot supply a full phase shift at a given wavelength ($\alpha_\nu < 2\pi$), it is still possible to fully shift the spectral phase of the beam at the cost of a reduced diffraction amplitude. The SLM used in our implementation of COLBERT can induce a full phase rotation up to 700 nm but using diffraction based pulse shaping, this range extends as far as there is sufficient power in the input beam to compensate the decreased diffraction efficiency. Lastly, the position of the first order of diffraction depends on the sawtooth's period. Therefore, a pickup mirror can be placed right below the incident beam to extract a shaped beam free of polluting replicas (see Figure 4.7). However, for pulses with large bandwidths, this will induce a noticeable vertical spatial chirp. It is possible to compensate this effect by adjusting the grating's period with respect to the wavelength of the light incident on a column of pixels.

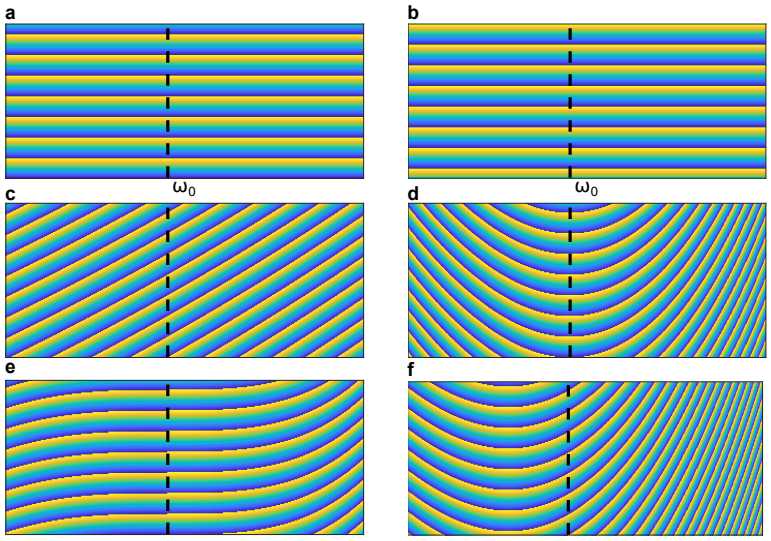

Figure 4.8: **Examples of phase gratings used in diffraction based pulse shaping for various spectral phases.** The dashed black line represents the column at the carrier frequency ω_0. (a) A flat phase profile (b) A flat phase profile shifted by π. (c) A delay of 100 fs with respect to the carrier frequency (d) A GDD of 1000 fs^2 around the carrier frequency (e) A third-order chirp of 2000 fs^3 (f) A GDD of 1000 fs^2 and a delay of 100 fs.

Pulse shaping is a method by which a pulse's temporal profile is shaped as desired through the modification of its spectral amplitude and phase. This allows us to control a pulse's phase, delay and compress it as well as generating perfect temporal replicas [150]. The former is achieved by applying a flat phase pattern across all frequencies (see Figure 4.8a and b). To delay a pulse, we apply a linear phase profile with respect to frequency (Figure 4.8c). We can see this effectively delays the pulse by the Fourier Shifting theorem,

$$\mathscr{F}^{-1}[e^{-i(\omega-\omega_c)\tau}\mathscr{F}[f(t)]] = f(t+\tau), \tag{4.7}$$

where $\mathscr{F}$ and $\mathscr{F}^{-1}$ denotes the Fourier transform and its inverse, ω the angular frequency, ω_c the carrier frequency, τ a temporal delay, t a time variable and $f(t)$ some function of time. This is how COLBERT can delay pulses without any moving parts. Moreover, it is possible to select a frequency for which the phase will remain constant when delaying the pulses, the carrier frequency. This is an extremely appealing feature of pulse-shaping for MDCS since it allows for the rotating frame detection of the coherent signals. Instead of oscillating at their natural frequencies, the coherences oscillate at the difference between their natural frequencies and the carrier frequency. This allows us to sample the coherent decay using much larger time steps and hereby reduces the time required to acquire a MDCS spectrum. Using traditional delay lines, the probed coherences would oscillate at optical frequencies. One would need to acquire a spectrum every half optical period, a factor of ten more points than those typically required when using rotating frame detection.

Using diffraction-based pulse shaping allows us to shape the spectral phase and amplitude of a pulse. This is particularly powerful and allows us to create complex pulses with relative ease. A useful implementation of this dual-shaping is the generation of a pulse pair from a single one [150]. To do so, we need to convolute in the time domain our pulse's

electric field with the appropriate temporal response such as

$$E_{\text{after}}(t) = E_{\text{before}}(t) * M(t) \tag{4.8}$$

where $*$ denotes a convolution, $E_{\text{after}}(t)$ and $E_{\text{before}}(t)$ are the electric fields after and before the pulse shaper and $M(t)$ is the filter applied by the pulse shaper in the time domain. For two pulses to be generated from one, $M(t)$ must be composed of two Dirac's delta functions temporally separated by τ such as

$$M(t) = \frac{1}{2}\left[\delta(t - \tau/2) + \delta(t + \tau/2)\right]. \tag{4.9}$$

Since a convolution in the time domain is equal to a product in the frequency domain, the required spectral filter $M(\omega)$ is given by the Fourier transform of $M(t)$ and yields

$$M(\omega) = \left|\cos\left(\omega\frac{\tau}{2}\right)\right| \exp\left\{i \arg\left[\cos\left(\omega\frac{\tau}{2}\right)\right]\right\} \tag{4.10}$$

where $\arg()$ denotes the argument of its input. Applying such a spectral phase and amplitude pattern on the SLM will perfectly split a pulse into two pulses separated by τ. This can be very useful to perform temporal autocorrelation measurements such as colinear frequency resolved optical gating (CFROG) [151].

Diffraction based pulse shaping as described above only holds when applying a continuous spectral phase profile. The pixelated nature of real SLMs imposes limits on the performance of this method. The main limitation in the context of MDCS is the amplitude modulation of the diffracted beam with applied delay given by

$$E_{\text{diff.}}(\tau) = \exp(-\sigma\tau^2)\,\text{sinc}(\epsilon\tau) \tag{4.11}$$

where $E_{\text{diff.}}(\tau)$ is the amplitude of the diffracted beam when delayed by τ and σ and ϵ are constants that depend on the resolution of the pulse shaper [152]. Using an imaging lens with a focal length of 15 cm and a bandwidth of 80 nm over a 800 pixel wide SLM, delays up to 1 ps are comfortably achieved before substantial amplitude decay is observed. For greater delays, the diffracted pulse's amplitude decays which broadens features observed in two-dimensional spectra. In theory, it is possible to compensate this effect by deconvoluting the two-dimensional spectrum or by reducing the phase grating's amplitude at earlier delays so that the diffracted pulse power is constant throughout the scan.

Due to the linear nature of pulse shaping, it is also possible to apply any linear combination of phase profiles. Fig. 4.8 d to f show examples of quadratic, third-order and delayed quadratic spectral phases. We can thus compensate chirp to any order and theoretically always compress our pulses to their transform limits. Which spectral phase should we then apply to obtain transform limited pulses? We can only know by measuring the spectral phase of our pulses, the topic of section 4.4.

4.3.4 Heterodyne detection

For the Fourier transform of the time-energy correlation map along the time axis to be fruitful, the FWM signal must be fully characterized. This means both the spectral amplitude and phase of the signal must be measured. Measuring the spectral amplitude is easy, one only needs a spectrometer, but the spectral phase, however, proves to be a little more challenging. Luckily, since we have properly compressed all of our pulses to the transform limit (flat spectral phase), we can use heterodyne detection to simultaneously measure the spectral amplitude and phase of the FWM signal.

Heterodyne detection is a coherent detection technique that allows the full characterization of a time-varying signal by measuring its spectral interference with another signal

of known spectral amplitude and phase called a local oscillator (LO). In our case, the LO is the attenuated fourth beam which copropagates with the FWM signal after it has been generated. Both pulses copropagate into the spectrometer, which is a spectral intensity detector yielding the following detected spectrum $I(\omega)$

$$I(\omega) = |E_s(\omega) + E_{\mathrm{LO}}(\omega)|^2 \tag{4.12}$$

where $E_s(\omega)$ and $E_{\mathrm{LO}}(\omega)$ are the complex electric field of the signal and the LO in the spectral domain. Expanding the norm gives us

$$I(\omega) = I_s(\omega) + I_{\mathrm{LO}}(\omega) + I_{\mathrm{X}}(\omega) \tag{4.13}$$

The two first terms are simply the spectrum of the signal and the LO respectively while the last term is the heterodyne term defined as $I_{\mathrm{X}}(\omega) = 2|E_s(\omega)|E_{\mathrm{LO}}(\omega)| \cos[\phi_s(\omega) - \phi_{\mathrm{LO}}(\omega)]$. It contains information about both the spectral amplitude and phase of the signal. Since it is a real number, we can turn it into a complex number by filtering out the negative axis of its inverse Fourier transform such that

$$A_s(\omega)A_{\mathrm{LO}}(\omega)e^{i[\phi_s(\omega)-\phi_{\mathrm{LO}}(\omega)]} = \mathscr{F}[\Theta(\omega)\mathscr{F}^{-1}[I_{\mathrm{X}}(\omega)]] \tag{4.14}$$

where $\Theta(\omega)$ is the Heavyside step function and $A_s(\omega)$ and A_{LO} are the spectral amplitudes of the signal and LO electric fields. To cleanly separate the negative and positive frequencies of the signal in the temporal domain, we slightly delay the LO from the signal's emission by τ_{LO} by applying on the LO a linearly increasing phase profile of the form

$$\phi_{\mathrm{LO}}(\omega) = (\omega - \omega_c)\tau_{\mathrm{LO}} \tag{4.15}$$

where ω_c is the delay carrier frequency. This delay will cause the appearance of spectral interference fringes in the measured spectra. This delay cannot be too large, for it will

otherwise yield strong artefacts in the extracted signal phase [153] when interpolating from wavelengths to frequency. An accurate sampling can however circumvent this problem. We can then extract the signal's full electric field from the heterodyne term by removing the LO's contribution to its amplitude and phase such that

$$E_s(\omega) = \frac{A_s(\omega)A_{\mathrm{LO}}(\omega)e^{i[\phi_s(\omega)-\phi_{\mathrm{LO}}(\omega)]}e^{i\phi_{\mathrm{LO}}(\omega)}}{A_{\mathrm{LO}}} \tag{4.16}$$

$$= A_s(\omega)e^{i[\phi_s(\omega)+\Delta\phi]} \tag{4.17}$$

where $\Delta\phi$ is called the global phase offset. It arises due to the ambiguity of equation 4.15 up to a phase constant. To obtain the signal's true spectral phase profile, one must phase the signal. This amount to the proper identification of in-phase and out of phase components of the signal, or the determination of its real and imaginary parts. Due to pulse shaping, this part is exceptionally easy in COLBERT since we can directly change each beam's phase and thus extract this global phase offset. The heterodyne signal we detect is of the form:

$$I_X \propto \cos\left[\phi_s(\omega) - \phi_{\mathrm{LO}}(\omega)\right] = \cos\left[\Delta\phi\right] \tag{4.18}$$

with $\Delta\phi = \phi_b + \phi_c - \phi_a + \phi_{\mathrm{LO}}$. Thus, by scanning the phase of one of the beams, measuring the heterodyne signal at each step and fitting it to a phase-shifted cosine, we can extract $\Delta\phi$ and remove it from our measurements when analyzing our data.

4.3.5 Phase cycling

In an ideal context, only the LO and the FWM signal are detected by the spectrometer, all the other beams and sources of light pollution being appropriately blocked. However, no experiment is performed in such conditions and despite great efforts to isolate the desired signal, the latter will be only a small fraction of the detected light. The main source of signal pollution is that of scattering of the other beams on the sample or on the surface of the SLM. For most fluences used in MDCS, the FWM signal is 4 to 6 orders of magnitude

weaker than the beams used to generate it. Thus, even the slightest amount of scattering will compose a large fraction of the light to be detected by the spectrometer. Therefore, extracting the heterodyne signal will be challenging. Luckily, MDCS is a coherent measurement which means the detected signal's phase has a clear dependency on those of the beams that generated it. We can therefore design a measurement scheme in which the undesired signals destructively interfere while the heterodyne signal is amplified. Such a measurement scheme is called phase-cycling and is responsible for COLBERT's high sensitivity.

The procedure involves cycling the phase of each beams and recording the resulting spectrum at each cycling step. The spectra are then linearly combined together so that only the heterodyne term remains. Based on Turner's work [143] for a fifth-order, two-beam measurement, the procedure for a BOXCARS geometry in which beam a is the conjugate beam is outlined here. In this case, the signal's phase is given by

$$\phi_s = \phi_b + \phi_c - \phi_a \tag{4.19}$$

where $\{\phi_i\}$ with $i \in \{a, b, c\}$ are the phases of beams a,b or c. The intensity I detected by the spectrometer arises from contributions from the signal, the LO and scattering from all beams such that

$$I(\phi_a, \phi_b, \phi_c, \phi_{\text{LO}}) = |E_{\text{LO}}e^{i\phi_{\text{LO}}} + E_a e^{i\phi_a} + E_b e^{i\phi_b} + E_c e^{i\phi_c} + E_s e^{i\phi_s}|^2 \tag{4.20}$$

where the spectral dependence of the detected amplitudes E_i and phases ϕ_i were omitted. By expanding this expression and writing ϕ_s explicitly in terms of the phases of the beams,

we get

$$\begin{aligned} I(\phi_a, \phi_b, \phi_c, \phi_{\text{LO}}) =& I_s + I_a + I_b + I_c + I_{\text{LO}} \\ &+2E_{\text{LO}}E_a \cos(\phi_{\text{LO}} - \phi_a) \\ &+2E_{\text{LO}}E_b \cos(\phi_{\text{LO}} - \phi_b) \\ &+2E_{\text{LO}}E_c \cos(\phi_{\text{LO}} - \phi_c) \\ &+2E_a E_b \cos(\phi_a - \phi_b) \\ &+2E_{\text{LO}}E_s \cos(\phi_{\text{LO}} - \phi_b - \phi_c + \phi_a) \\ &+2E_a E_c \cos(\phi_a - \phi_c) \\ &+2E_a E_s \cos(\phi_a - \phi_b - \phi_c + \phi_a) \\ &+2E_b E_c \cos(\phi_b - \phi_c) \\ &+2E_b E_s \cos(\phi_b - \phi_b - \phi_c + \phi_a) \\ &+2E_c E_s \cos(\phi_c - \phi_b - \phi_c + \phi_a) \end{aligned} \tag{4.21}$$

Cycling the phase of the LO by π gets rid of terms that do not involve the LO's phase yielding

$$\begin{aligned} I_{II}(\phi_a, \phi_b, \phi_c, \phi_{\text{LO}}) =& I(\phi_a, \phi_b, \phi_c, \phi_{\text{LO}}) - I(\phi_a, \phi_b, \phi_c, \phi_{\text{LO}} + \pi) \\ =& 4E_{\text{LO}}[E_b \cos(\phi_{\text{LO}} - \phi_b) + E_c \cos(\phi_{\text{LO}} - \phi_c) \\ &+E_a \cos(\phi_{\text{LO}} - \phi_a) + E_s \cos(\phi_{\text{LO}} - \phi_b - \phi_c + \phi_a)]. \end{aligned} \tag{4.22}$$

We then cycle beam b's phase with two more steps to get

$$\begin{aligned} I_{IV}(\phi_a, \phi_b, \phi_c, \phi_{\text{LO}}) =& I_{II}(\phi_a, \phi_b, \phi_c, \phi_{\text{LO}}) - I_{II}(\phi_a, \phi_b + \pi, \phi_c, \phi_{\text{LO}}) \\ =& I(\phi_a, \phi_b, \phi_c, \phi_{\text{LO}}) - I(\phi_a, \phi_b, \phi_c, \phi_{\text{LO}} + \pi) \\ &-I(\phi_a, \phi_b + \pi, \phi_c, \phi_{\text{LO}}) + I(\phi_a, \phi_b + \pi, \phi_c, \phi_{\text{LO}} + \pi) \\ =& 8E_{\text{LO}}[E_b \cos(\phi_{\text{LO}} - \phi_b) + E_s \cos(\phi_{\text{LO}} - \phi_b - \phi_c + \phi_a)] \end{aligned} \tag{4.23}$$

Finally, a last cycling of beam c's phase isolates the heterodyne term and removes the

pollution for the scatter of other beams yielding

$$\begin{aligned} I_{VIII}(\phi_a,\phi_b,\phi_c,\phi_{\mathrm{LO}}) =& I_{IV}(\phi_a,\phi_b,\phi_c,\phi_{\mathrm{LO}}) - I_{IV}(\phi_a,\phi_b,\phi_c+\pi,\phi_{\mathrm{LO}}) \\ =& I(\phi_a,\phi_b,\phi_c,\phi_{\mathrm{LO}}) \\ & -I(\phi_a,\phi_b,\phi_c,\phi_{\mathrm{LO}}+\pi) \\ & -I(\phi_a,\phi_b+\pi,\phi_c,\phi_{\mathrm{LO}}) \\ & +I(\phi_a,\phi_b+\pi,\phi_c,\phi_{\mathrm{LO}}+\pi) \\ & -I(\phi_a,\phi_b,\phi_c+\pi,\phi_{\mathrm{LO}}) \\ & +I(\phi_a,\phi_b,\phi_c+\pi,\phi_{\mathrm{LO}}+\pi) \\ & +I(\phi_a,\phi_b+\pi,\phi_c+\pi,\phi_{\mathrm{LO}}) \\ & -I(\phi_a,\phi_b+\pi,\phi_c+\pi,\phi_{\mathrm{LO}}+\pi) \\ =& 16E_{\mathrm{LO}}E_s\cos(\phi_{\mathrm{LO}}-\phi_b-\phi_c+\phi_a) \end{aligned} \tag{4.24}$$

By going through these eight acquisition steps, not only is the measurement background free, the desired signal is also amplified. However, this procedure supposes that the signal and scattered light do not change in time. Therefore, in practice, some noise due to scattering will remain in the acquired signal even after the phase-cycling procedure due to small fluctuations in the NOPA's output power. For this reason, the temporal stability of the laser determines the noise floor of a COLBERT measurement, not the beams' power. To improve the robustness of this procedure to laser instabilities, it is possible to use a non-integer based cycling procedure which requires fewer steps and is therefore faster [154]. Nonetheless, this procedure as it is yields spectacular results and allows us to measure the non-linear polarisation induced in the sample with high sensitivity.

4.4 Pulse compression

To perform the experiment in the semi-impulsive limit, one needs resonnant pulses much shorter than the optical dephasing time of probed transitions. In COLBERT, pulses of about

60 nm in bandwidth travel through 10 m of air and 8 cm of glass before reaching the sample. This temporally stretches the pulses so that, without a proper pulse compression scheme, they are inadequate for MDCS and would yield practically uninterpretable two-dimensional spectra. In this section, the foundations behind the pulse compression and characterization schemes used before every COLBERT multidimensional measurement are presented. All pulse compression and characterization methods are based on second harmonic generation using an ultra-thin (10 μm) BBO crystal so that the spectral and angular tolerances allow the simultaneous compression of all beams over their whole spectrum. Moreover, to ensure the reliability of the procedures, both compression and characterization are done at the sample's exact location during the experiment.

4.4.1 Chirp-scan and MIIPS

The biggest improvement made by the Silva group on the original COLBERT design is the integration of a rigorous pulse compression scheme instead of COLBERT's original compression routine. Using it, one can routinely obtain sub-20 fs pulses close to the transform limit. There are many spectral phase measurement methods out there, but we opted for a method which could be performed at the exact same location as the sample's and required a minimal amount of added components, a combination of chirp-scan [155] and multiphoton intrapulse interference (MIIPS) [156]. Both techniques apply, using a pulse shaper, a known parametrized non-linear spectral phase (for instance, a quadratic chirp) and acquire the second harmonic (SH) spectrum of the beam. By repeating this measurement for different spectral phase parameters, it is possible to infer the spectral phase of the pulse under test. The principle behind this method can be understood by examining the process of second harmonic generation for a broadband pulse. For a complex broadband electric field $E(\omega)$ expressed in the spectral domain, the SH spectrum is given by

$$E(2\omega) \propto \int_{-\infty}^{\infty} \int_{-\infty}^{\infty} E(\sigma)E(\gamma)\delta(\sigma+\gamma-2\omega)d\sigma d\gamma \tag{4.25}$$

where $\delta(\sigma + \gamma - 2\omega)$ is Dirac's delta function and follows from conservation of energy during the second harmonic generation. Carrying on the integral over σ, we get rid of the delta-function and obtain

$$E(2\omega) \propto \int_{-\infty}^{\infty} E(2\omega - \gamma)E(\gamma)d\gamma. \tag{4.26}$$

Representing the electric field's complex spectrum in its polar form

$$E(\omega) = \tilde{E}(\omega)\exp(i\phi(\omega)) \tag{4.27}$$

where $\phi(\omega)$ is the spectral phase we would like to measure and $\tilde{E}(\omega)$ the spectral amplitude. Injecting this into equation 4.26, we get

$$E(2\omega) \propto \int_{-\infty}^{\infty} \tilde{E}(2\omega - \gamma)\tilde{E}(\gamma)e^{i(\phi(2\omega-\gamma)+\phi(\gamma))}d\gamma. \tag{4.28}$$

The SH intensity at 2ω will be maximal when $\phi(2\omega - \gamma) = -\phi(\gamma)$ so that the integrant in eq. 4.28 is always positive. Defining $\gamma = \omega - \Omega$, this condition becomes

$$\phi(\omega + \Omega) = -\phi(\omega - \Omega). \tag{4.29}$$

To fully appreciate the importance of this condition, let's expand the spectral phase in a Taylor's serie centered at Ω, the compression carrier frequency. We get

$$\phi(\omega - \Omega) = \phi_0 + \phi'(\omega - \Omega) + \frac{1}{2}\phi''(\omega - \Omega)^2 + \frac{1}{6}\phi'''(\omega - \Omega)^3 + ... \tag{4.30}$$

Using our pulse shaper, we can apply an arbitrary chirp Δ to our pulse. We can rewrite the spectral phase's Taylor expansion in term of the pulse's original chirp GDD and the added

chirp Δ as

$$\phi(\omega - \Omega) = \phi_0 + \phi'(\omega - \Omega) + \frac{1}{2}(\text{GDD} + \Delta)(\omega - \Omega)^2 + \frac{1}{6}\phi'''(\omega - \Omega)^3 + ... \quad (4.31)$$

We see that equation 4.29 will be satisfied only if the coefficients of even powers of Ω in equation 4.31 vanish. These can be obtained with a binomial expansion of equation 4.31 and yields

$$(\text{GDD} + \Delta_{opt.}(\omega)) + 2\sum_{n=3}^{\infty} \binom{n}{2} \frac{\phi^{(n)}}{n!}\omega^{n-2} = 0 \quad (4.32)$$

where $\Delta_{opt.}(\omega)$ is the added chirp that maximizes the SH signal at 2ω, $\phi^{(n)}$ the n-th derivative of $\phi(\omega)$ at $\omega = \Omega$ and $\binom{n}{k}$ the binomial coefficient defined as

$$\binom{n}{k} = \frac{n!}{k!(n-k)!}. \quad (4.33)$$

By inserting the binomial coefficient explicitly into equation 4.32, we get

$$(\text{GDD} + \Delta_{opt.}(\omega)) + \sum_{n=3}^{\infty} \frac{\phi^{(n)}}{(n-2)!}\omega^{n-2} = 0 \quad (4.34)$$

which we rewrite as

$$-\Delta_{opt.}(\omega) = \text{GDD} + \sum_{n=3}^{\infty} \frac{\phi^{(n)}}{(n-2)!}\omega^{n-2} \quad (4.35)$$

We now see how we can extract the spectral phase from measurements of the SH's spectrum for different added chirps. Since each powers of ω are linearly independent from each other, we can fit $\alpha_{opt.}(\omega)$ with a polynomial of sufficient order and extract the non-linear phase coefficients $\phi^{(n)}$ thus measuring the spectral phase to the desired order. This technique is known as chirp scan [155]. This derivation also explains why maximizing the SH signal using stochastic algorithms to extract the spectral phase [157] (trial and error or genetic algorithms) performs poorly. Looking at equation 4.31, we indeed see that individ-

ually tuning higher-orders of chirp also affects the optimal value for lower orders of chirp.

Another way to understand equation 4.35 is to state it in terms of an arbitrary non-linear parametrized phase function $f(\omega)$. In the case of chirp scan $f(\omega) = \Delta(\omega - \Omega)^2$. Equation 4.35 can then be rewritten as

$$f''(\omega) = -\phi''(\omega) = -\text{GDD} + \sum_{n=3}^{\infty} \frac{\phi^{(n)}}{(n-2)!}\omega^{n-2} \tag{4.36}$$

and we can now use any non-linear function of ω to extract the phase of our pulses. MIIPS uses a sinusoidal phase function defined as

$$f(\omega) = \alpha \cos(\gamma(\omega - \Omega) - \delta) \tag{4.37}$$

where δ is the scanned parameter and $\gamma/2\pi$ is the inverse of the pulse's transform limited duration. This parameter is scanned to extract $\delta_{opt.}(\omega)$, the parameters that maximize the SH signal at 2ω. Injecting MIIPS's definition of $f(\omega)$ into eq. 4.36 we get

$$f''_{opt.}(\omega) = \alpha\gamma^2 \cos(\gamma(\omega - \Omega) - \delta_{opt.}(\omega)) = \text{GDD} + \sum_{n=3}^{\infty} \frac{\phi^{(n)}}{(n-2)!}\omega^{n-2} \tag{4.38}$$

which can be also fitted to a polynomial to extract the pulse's spectral phase to the desired order. This technique yields greater phase accuracy than chirp scan for flat spectral phases at the cost of poor performance for severely chirped pulses. For this reason, we use this function only to trim a pulse's phase after it was compressed with chirp scan.

4.4.2 FROG: Frequency-Resolved Optical Gating

By far the most common technique to characterize ultrashort pulses is that of second-harmonic frequency-resolved optical gating [158] or SH-FROG. It consists in recording the spectrum of the second harmonic generated by the autocorrelation of a pulse in a non-

linear medium for various interpulse delays. The obtain FROG trace is then used to extract the pulse's spectral amplitude and phase using an iterative reconstruction algorithm [159]. However, the most common implementations of this technique use a thin beamsplitter and a delay line to generate the pulse's autocorrelation. To avoid the addition of more optical components to our experimental setup, we instead implemented versions of this technique compatible with our pulse-shaper based apparatus namely colinear SH-FROG and cross-correlation SH-FROG. The first technique uses the pulse shaper to split into two a single pulse and delay them. This is done by applying on top of the beam's optimal phase profile the filter of equation 4.10. Due to the colinear nature of the measurement, terms corresponding to the second harmonic of each pulse replica as well as the FROG term are measured simultaneously. The FROG term is extracted by applying a filter in the space conjugate to the inter-replica delay [151] from which the pulse's amplitude and phase can then be extracted using the aforementioned algorithm. This technique, however, does not easily detect the effects of tilt of front mentioned in section 4.3.2. To do so, we turn to cross-correlation FROG where the cross-correlation between two of the four beams used in COLBERT is instead measured. Not only does this also provide an estimate of a pulse's duration but also the amount of tilt of front by comparing it to the pulse durations obtained from CSH-FROG. In fact, this measurement is the one routinely used for each beam pairs to check if the compression and imaging were correctly performed prior to any COLBERT experiment [143].

4.5 Conclusion

As we have shown in this chapter, generating and managing short pulses of light is a challenging endeavor but thanks to nearly three decades of efforts by the ultrafast community, these can now be used in evermore complex experiments provided they are rigorously characterized beforehand. Tremendous progress on the implementation and interpretation of these experimental techniques have also allowed these experiments to be performed on

more and more delicate or complex samples. They are no longer secluded to the fringes of the spectroscopist's toolbox and can now be used a tool to study poorly understood materials beyond textbook systems. In the next chapters, I hope to convey through the example of our own investigations of 2D HOIPs this idea that non-linear coherent spectroscopy, particularly multidimensional spectroscopy, are much more than fancy experiments heavy on the taxpayer's wallet. They elegantly provide profound insights into the quantum mechanical behavior of a material which are impossible to obtain with traditional linear methods such as photoluminescence and absorption spectroscopies. This is manifest when comparing the intellectual acrobatics required to interpret the linear spectroscopy data of chapter 5 with the straightforward, rigorous and unambiguous conclusions of the following chapters.

CHAPTER 5
EXCITON-POLARON SPECTRAL STRUCTURES IN TWO-DIMENSIONAL HYBRID LEAD-HALIDE PEROVSKITES

Motivated by our disagreement regarding the interpretation of the linear spectroscopy performed in reference [98], we began our investigation of 2D HOIPs by exploring their linear absorption and emission spectra in order to propose an alternative view on the origin of the excitonic fine structure. Nonetheless, we agreed that strong electron-phonon correlations could be manifested in the optical response and sought to account for it as well in our investigation. The Bohr radius estimated from the measured exciton binding energy (about 200 meV) was sufficiently large to encourage us to use the Wannier formalism described in section 2.2.1. The 2D Bohr radius was initially wrongly estimated to be 12 nm due to a confusion in the units used in a cited reference and is actually closer to 2 nm. Nonetheless, to account for the observed fine structure, we modified the Wannier formalism by considering 4 excitonic states of distinct electronic nature separated by about 35 meV. These four states, being electronically distinct, could couple differently to low-energy lattice vibrations resulting in their distinct Franck-Condon like lineshapes. The energy of the relevent modes for that matter were extracted from non-resonant Raman measurements, presented in chapter 9, and were found to be comparable to the excitonic linewidths contrarily to the one previously proposed to account for the fine structure. This yields a slightly asymmetrical lineshape (see for example the dash-dotted lines of Figure 2.4) instead of a sharp vibronic progression (full lines of Figure 2.4). This modified formalism does not interpret the fine structure as a vibronic progression. Rather, it interprets the fine structure as arising from electronically distinct excitons and their lineshapes as the consequence of broadened low-energy vibronic replicas, a sharp contrast with the interpretation of reference [98]. To test this formalism, we fit it to the temperature dependent spectra of two distinct single layered

2D-HOIPs and found it to be able to reproduce their absorption spectra up to 100 K. This suggested, but did not prove, that our interpretation of the lineshape could be correct.This interpretation is further supported by the observation in MDCS of couplings in the fine structure through excited-state absorption features. The presence of such correlation also shows that these states are connected through common states including a common ground state. Whatever their nature it, this shows they are intrinsic to the material and do not arise from sample inhomogeneities.

It is also in this publication that we first hypothesize the fine structure to arise of polaronic effects. We first noticed that although the fine-structure splitting was similar to the suggested Rashba energy [107] in these material, the lack of apparent dependence on the inorganic layer thickness suggested this was not a dimensional effect but could be inherent to the lattice. This prompted us to put aside the hypothesis of Rashba effects as the origin of the fine structure. At the time, we were not aware of experimental reports of the excitonic fine structure in 3D perovskites [95, 96] and hypothesized they could also exhibit an excitonic fine structure. A back-of-the-envelope calculation showed that the weak-coupling polaron binding energy matched curiously well with the observed fine-structure splitting, and planted in our minds the idea that polaronic effects might be responsible for it. As the next chapters will show, this idea grew stronger with each new experimental result.

This work was published in Physical Review Materials in 2018 [62] and can be found on the arXiv under the same title. Dr. Neutzner (CNST@PoliMi, IIT) acquired the temperature dependent absorption spectra, designed the modified Wannier model and performed the fits on the absorption and photoluminescence spectra. Dr. Neutzner and I acquired the multidimensional and photoluminescence spectra and I performed the analysis of the former. Dr. Cortecchia (CNST@PoliMi, IIT) synthesized the high-quality samples used for this study. The work was advised and supervised by Pr. Petrozza (CNST@PoliMi, IIT), Pr. Silva (GaTech) and Dr. Srimath Kandada (CNST@PoliMi, IIT and GaTech). All authors contributed to the redaction of the manuscript and its intellectual development.

5.1 Abstract

Owing to both electronic and dielectric confinement effects, two-dimensional organic-inorganic hybrid perovskites sustain strongly bound excitons at room temperature. Here, we demonstrate that there are non-negligible contributions to the excitonic correlations that are specific to the lattice structure and its polar fluctuations, both of which are controlled via the chemical nature of the organic counter-cation. We present a phenomenological, yet quantitative framework to simulate excitonic absorption lineshapes in single-layer organic-inorganic hybrid perovskites, based on the two-dimensional Wannier formalism. We include four distinct excitonic states separated by 35 ± 5 meV, and additional vibronic progressions. Intriguingly, the associated Huang-Rhys factors and the relevant phonon energies show substantial variation with temperature and the nature of the organic cation. This points to the hybrid nature of the lineshape, with a form well described by a Wannier formalism, but with signatures of strong coupling to localized vibrations, and polaronic effects perceived through excitonic correlations. Our work highlights the complexity of excitonic properties in this class of nanostructured materials.

5.2 Introduction

Organic-inorganic hybrid perovskites (HOIPs) consist of metal-halide octahedral motifs that form multi-dimensional lattice planes structurally separated by coordinating organic counter cations [4]. While the frontier orbitals that give rise to the semiconductor electronic structure are contributed by the metal-halide network, the organic cation plays a key role in the structural configuration as well as the stability of the lattice [160]. When the organic moieties are long enough to isolate the lattice planes electronically, the latter form quantum-well-like structures with strong two-dimensional (2D) electronic confinement within the metal-halide layer [90].

A consequence of such confinement is the creation of strongly bound excitons, which

have been reported as early as 1989 by Ishihara et al. [78], with binding energies of 200–300 meV. In a general context, a variational approach of electron-hole correlations predicts that excitons in strongly confined quantum wells experience a four-fold enhancement in binding energy with respect to the bulk semiconductor [161], assuming a smooth dielectric environment around the well. This enhancement is generally observed in systems such as GaAs, which is characterized by an exciton binding energy of 4 meV in the bulk and 16 meV in quantum wells [162]. Intriguingly, there is more than a ten-fold increase in the binding energies going from 3D lead-halide perovskites (10–20 meV [163]) to their 2D counterparts [78]. Beyond quantum confinement, dielectric confinement arising from the intercalating organic layers increases the Coulomb correlations substantially, resulting in such a strong increase in the exciton binding energy [78, 90, 164, 165].

There is now an increasing consensus that the charge carriers in 3D lead halide perovskites behave as large polarons within an intermediate electron-phonon coupling regime [166]. In addition to this conventional behaviour of any polar lattice, local lattice disorder induced by the relative motion of the organic cation has been suggested to affect the excitation dynamics substantially [163, 166]. Within such a context, the contribution of the lattice dynamics to excitonic and other multi-body correlations in two dimensional perovskites is a very pertinent question. We have recently demonstrated that modulation of the lattice degrees of freedom with temperature in fact changes the exciton and biexciton binding energies [167], highlighting the importance of the crystal structure and its lattice dynamics on the multi-body physics.

Owing to the large binding energy, clear and distinct excitonic transitions are observed in the linear absorption spectrum. However, contrary to the characteristics of conventional 2D Wannier excitons, the spectra also exhibit a rich fine structure with the presence of multiple peaks distributed around the most intense one [98]. Previously, the presence of similar spectral structure also in the photoluminescence (PL) spectrum motivated the inclusion of vibronic progressions [168, 98], as widely used in the case of localized states in molec-

ular semiconductors. Here, we provide a more quantitative description of these spectral structures invoking various considerations of exciton-lattice coupling. First, we hypothesize the presence of distinct excitonic states, possibly generated via degeneracy lifting mechanisms driven by polaronic effects. This, however, does not discount the contribution of low-energy lattice vibrations to the optical absorption in the form of vibronic progressions. We analyze the vibrational and structural contributions to the excitonic correlations by systematically tuning the lattice parameters using temperature, the chemical nature of the organic cation, and the thickness of the quantum well. Based on these considerations, we phenomenologically introduce additional parameters in the established Elliott's formula for the absorption coefficient [38, 169] evaluated from a 2D Wannier equation, and we quantitatively reproduce the linear absorption spectra of prototypical 2D HOIPs.

5.3 Experimental methods

5.3.1 Sample preparation

For the preparation of $(PEA)_2PbI_4$ thin films (PEA = phenylethylammonium), the precursor solution (0.25 M) of $(PEA)_2PbI_4$ was prepared by mixing (PEA)I (Dyesol) with PbI_2 in 1:1 ratio in N,N-dimethylformamide(DMF). For example, 62.3 mg of (PEA)I and 57.6 mg of PbI_2 were dissolved in 500 μL of DMF (anhydrous, Sigma Aldrich). For the preparation of $(NBT)_2PbI_4$(NBT = n-butylammonium), 50.3 mg on NBT)I (Dyesol) and 57.6 mg of PbI_2 are dissolved in 500 μlLof DMF (0.25 M solution). For (EDBE)PbI_4 (EDBE = 2,2-(ethylenedioxy)bis(ethylammonium))), (EDBE)I was synthetized by dissolving 1 mL of (ethylenedioxy)bis(ethylamine) in 10 mL of ethanol and reacting the amine with 6 equivalents of hydroiodic acid (HI 57% water solution, Sigma Aldrich). The resulting precipitate was washed several times with ethanol/diethyl ether and dried under vacuum at 60^{o}C. The spin coating precursor solution was prepared by mixing 100 mg of (EDBE)I and 115.2 mg of PbI_2 in 500 μL of DMSO (0.5 M solution). All the perovskite thin films were prepared by spin coating the precursor solutions on glass substrates at 4000 rpm, 30 s, followed by

annealing at 100^{o}C for 30 min.

5.3.2 Absorption and photoluminescence measurements

Temperature-dependent absorption measurements were carried out using a commercial Perkin-Elmer UV/Vis spectrophotometer. The sample was kept in a continuous flow static-exchange gas cryostat (Oxford Instruments Optistat CF). Measurements were taken in steps during the heating up cycle, after going to liquid helium temperatures. Photoluminescence spectra were taken by shining 405nm light on the sample sitting inside a closed-cycle gas exchange cryostat. The incident power was measured using a calibrated photodiode and the photoluminescence collected by a set of lens and sent to a spectrometer.

5.3.3 Two-dimensional coherent excitation spectroscopy

The multidimensional spectrometer, developed by Turner and Nelson [143], has been described in detail elsewhere [167]. In this design, phase stability is passively achieved by delaying the pulses using phase-shaping, and by propagating the beams through a common set of optics. The spectrometer uses pulses generated by a home-built two-pass non-collinear optical parametric amplifier (NOPA) pumped by the output of a 1-kHz Ti:Sapphire regenerative amplifier system (Coherent Astrella). Before entering the spectrometer, the NOPA's output is spatially filtered using a pinhole to obtain a clean Gaussian profile. The pulse shaper is also used to compress the pulses near the transform limit using chirp scan [155] and multiphoton intrapulse interference phase scan (MIIPS) [170]. For the dataset presented here, this resulted in pulses centered at 520 nm of 21-fs temporal full-width at half-maximum (FWHM) as measured by second harmonic generation collinear frequency resolved optical gating (SHG-CFROG) [151] and cross-correlation between the beams.

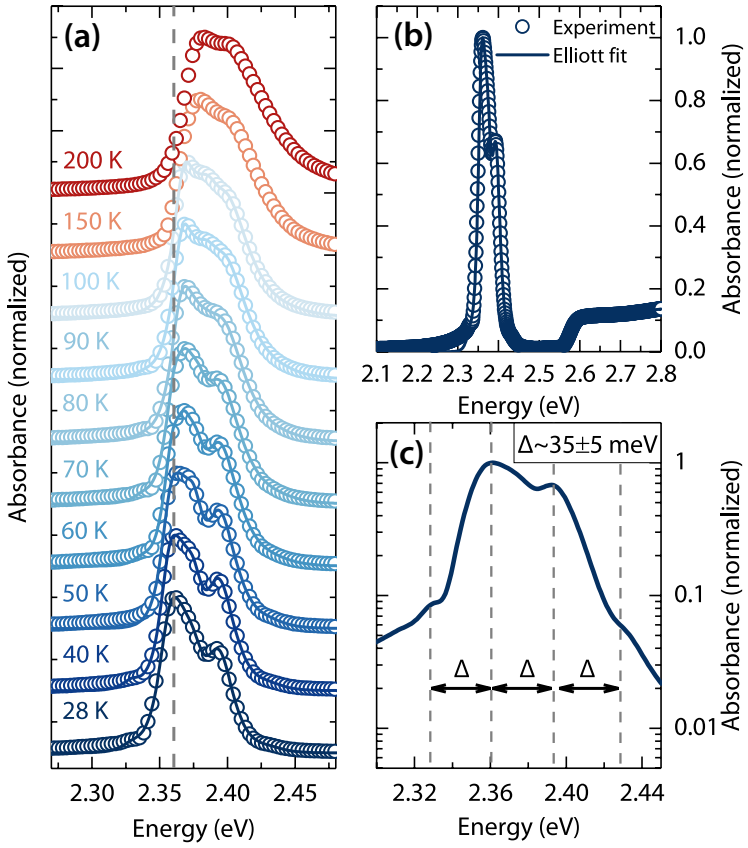

Figure 5.1: **Experimental absorption spectra of polycrystalline films of $(PEA)_2PbI_4$.** (a) Absorption spectra at different temperatures (plotted as symbols) and numerical fits done using Eqs. 5.1–5.4 (plotted as solid lines). (b) Experimental and fitted absorption spectrum at 28 K showing both exciton and continuum contributions. (c) Zoom of the exciton lineshape at 28 K(best fit shown in part (b)) plotted in logarithmic scale showing the presence of four distinct lines.

5.4 Results and analysis

5.4.1 Exciton absorption lineshape in $(PEA)_2PbI_4$

We first consider a model HOIP, $(PEA)_2PbI_4$ (PEA= phenylethylammonium), to establish a formalism for the absorption spectral lineshape before exploring other model systems incorporating alternative organic cations that induce different degrees of octahedral distorion and connectivity. The absorption spectra of a polycrystalline film of $(PEA)_2PbI_4$ taken at different temperatures are shown in Figure 5.1(a), focusing on the exciton resonance re-

gion. The spectrum at 28 K, shown in Figure 5.1(b) over a broader spectral range, reveals an excitonic peak at about 200 meV below the well-defined continuum edge, indicating a high exciton binding energy. In addition, the excitonic peak exhibits a rich fine structure. A closer inspection of this lineshape, as shown in Figure 5.1(c) by the fit to the exciton model described below, reveals four distinct peaks separated by 35 ± 5 meV. The most intense peak also exhibits an asymmetric lineshape with a shoulder at higher energies, suggesting the presence of further buried structure within the broad lineshape. Upon increasing the temperature, the most intense peak consistently red-shifts following the lattice expansion effects and the subsequent change in the band-gap, as we have shown previously [167]. In addition, there is a relative increase in the absorption cross section at higher energies and a reduction in the clarity in the spectral fine structure.

Given the strong carrier confinement within the lead-iodide layer [90, 171], the absorption spectrum can be quantitatively modeled assuming a two-dimensional Wannier-Mott exciton. Following Elliott [38, 169], the absorption coefficient reads as:

$$\begin{aligned}\alpha(\omega) &= \alpha_{exc} + \alpha_{cont} \\ &= \alpha_0 \Big[\sum_{n=1}^{\infty} \frac{4E_0}{\left(n-\frac{1}{2}\right)^3} \operatorname{sech}\left(\frac{\hbar\omega - E_g + \frac{E_0}{(n-1/2)^2}}{\Gamma_{ex}} \right) \\ &\quad + \int_{E_g}^{\infty} \operatorname{sech}\left(\frac{\hbar\omega-\varepsilon}{\Gamma_c}\right) \frac{2}{1+\exp\left(-2\pi\sqrt{\frac{E_0}{\hbar\omega-E_g}}\right)} \frac{1}{1-(8\alpha m^*/\hbar^4)(\varepsilon-E_g)} \,\mathrm{d}\varepsilon \Big].\end{aligned} \tag{5.1}$$

Here, E_g and m^* are the bandgap energy and exciton effective mass, $E_b = E_0/\left(n-\frac{1}{2}\right)^2$ is the exciton binding energy and $n = 1, 2\ldots$ is an integer. While the first term of Eq. 5.1 represents the discrete excitonic transitions below the band-edge, the integral in the second term accounts for the absorption into the free-carrier continuum. The spectral width is accounted for by hyperbolic secant functions [172], characterized by the broadening

parameters, Γ_c and Γ_{ex}, corresponding to the free-carrier and excitonic transitions, respectively.

Such a standard 2D exciton model, however, is not sufficient to reproduce the observed fine-structure. In order to numerically do so, we introduce two modifications to Eq. 5.1. We conjecture that the four observed transitions correspond to distinct excitonic states and accordingly we re-distribute the intensity of the primary excitonic transition from Eq. 5.1 among three additional transitions of similar analytical form, but with binding energies set at $E_b + \Delta$, $E_b + 2\Delta$ and $E_b - \Delta$, where E_b is the binding energy of the primary exciton binding energy and Δ is approximately 35 meV. The relative intensities (X_i) of each of the four transitions are set as fit parameters:

$$\alpha_{exc} = X_1\alpha_{exc}(E_b) + X_2\alpha_{exc}(E_b + \Delta) + X_3\alpha_{exc}(E_b + 2\Delta) + X_4\alpha_{exc}(E_b - \Delta). \quad (5.2)$$

Secondly, to account for the asymmetric lineshapes, and more importantly to reproduce their temperature dependence, we introduce the contribution of electron-phonon coupling via appropriate Frank-Condon progressions on top of the exciton lines [173]. Due to the presence of multiple lattice vibrational modes that can couple to the electronic transitions, we employ a generalized Frank-Condon formalism represented in Eqs. 5.3–5.4. We consider a redistribution of oscillator strength according to Eq. 5.3, where W_0 is the intensity of the primary excitonic line and f is the line-shape function, both derived from Eq. 5.1. $F_{0,n}$ is the overlap integral of the corresponding vibronic wave-functions given by Eq. 5.4, with S, the generalized Huang-Rhys factor, which takes the form of a Poisson distribution:

$$W(\omega) = W_0 \sum_n F_{0,n} f(\omega, n, \Gamma), \quad (5.3)$$

$$F_{0,n} = \frac{e^{-S} S^n}{n!}. \quad (5.4)$$

Shown as solid lines in Figure 5.1(a) are the numerical fits of absorption spectra with

T (K)	E_g (eV)	E_b (meV)	X_2/X_1	X_3/X_1	X_4/X_1	S_1	S_2	S_3	Γ_c (meV)	Γ_{ex} (meV)
28	2.576	197.95	0.86	0.055	0.055	2.15	—	0.44	10.4	7
40	2.5775	199.32	0.86	0.055	0.065	2.49	—	0.44	11.3	6.4
50	2.579	199.72	0.86	0.055	0.0	2.77	—	0.44	12.1	6.2
60	2.5803	199.7	1.2	0.05	0.05	2.75	1.13	0.44	14.1	5.6
70	2.5809	198.5	1.3	0.045	0.05	2.55	1.2	0.44	15.8	6
80	2.5814	196.25	1.59	0.04	0.03	1.2	1.2	0.44	18	6.8
90	2.5814	195.7	1.5	0.045	0.03	—	1.2	0.44	20	6.5
100	2.5814	195.37	1.42	0.045	0.01	—	1.2	0.44	22	6.4

Table 5.1: : **Parameters used to fit the temperature dependent linear absorption spectra of $(PEA)_2PbI_4$** shown in Figure 5.1, using Eqs. 5.1–5.4. The Huang-Rhys parameters S_i correspond to modes with energy 8 meV ($i = 1$), 9.8 meV ($i = 2$), and 17.4 meV ($i = 3$), extracted from the non-resonant Raman spectrum [167]

Eqs. 5.1,5.2, 5.3, 5.4 (see Appendix I for the combined expression), assuming a spacing between the excitonic states to be $\Delta = 35 \pm 5$ meV and considering three dominant phonon energies, $\hbar\omega_1 = 8$ meV, $\hbar\omega_2 = 9.8$ meV and $\hbar\omega_3 = 17.4$ meV, identified via non-resonant Raman measurements published elsewhere [167]. Although it appears that the multitude of variable fit parameters can compromise the robustness of the formalism, it must be noted that the well-defined spectral features impose strict tolerance limits over most of the fit parameters. For example, given the clear separation between the excitonic transition and continuum edge, the bandgap and binding energies can be directly *read-out* from the experimental data and are constrained during the fitting procedure. Similarly, well defined rising edges for the primary excitonic line and the continuum impart rigid conditions over the choice of broadening parameters. Finally, the normal-mode frequencies used in the vibronic progression are constrained to those extracted from Raman spectra [167]. Thus, the only effective free-fit parameters are the Huang-Rhys factors and the relative intensities of the four excitonic transitions (X_i/X_1). The complete set of parameters used to obtain the fits is listed in Table. 5.1.

Upon increasing temperature, we observe a monotonic blue-shift of the bandgap due to lattice expansion effects [174, 167]. The binding energy, on the other hand, remains

relatively unperturbed by the temperature change, except for a minor reduction at higher temperatures. Although one would expect a contribution to the electronic polarization, and thus to the exciton binding energy, from the polar lattice vibrations that are activated at higher temperatures [164], the small exciton radius (associated with the large binding energy) makes the excitonic characteristics immune to such fluctuations [167]. The relative intensities of the excitonic states also show a moderate variation with temperature. While the third and fourth transitions, which are at the highest and lowest energies relative to $E_g - E_b$, have low cross section with respect to X_1, the second transition (X_2 in Figure 5.1(c)) gains in its relative intensity at higher temperatures.

The other fit variables are the Huang-Rhys factors, S_i ($i = 1$ (8 meV), 2 (9.8 meV), 3 (17.4 meV)), listed in Table 5.1. For spectra below 60 K, only two modes at 8 and 17.4 meV contribute to the absorption. For a brief temperature range between 60 and 80 K, all the three modes are required to reproduce the experimental lineshape. Spectra at 90 and 100 K can be fitted by considering only two modes, but at 9.8 and 17.4 meV. At higher temperatures (150 and 200 K in Figure 5.1(a)), the spectrum develops a strong asymmetric shoulder extending towards the continuum. Such a lineshape, which probably stems from the creation of shallow defect states, cannot be accounted for by the considered theoretical framework. The variation of the Huang-Rhys factors and the associated modes may be related to the increased flexibility of the lattice at higher temperatures. However, due to the lack of in-depth comprehension of the nature of the vibrational modes, it is not possible, at the moment to provide a conclusive explanation of this trend.

To gain further insights into the origin of the 35-meV spaced transitions, we analyze the total-correlation two-dimensional coherence excitation spectrum, shown in Figure 5.2(a), taken at room temperature. The 2D spectrum is composed of negative diagonal features (labelled 1 and 2), which correspond to the uncorrelated excitations from the ground state to the excitonic states. The off-diagonal features are composed of contributions from inter-exciton correlations and transitions to higher lying biexcitonic states (labelled α, β, γ). We

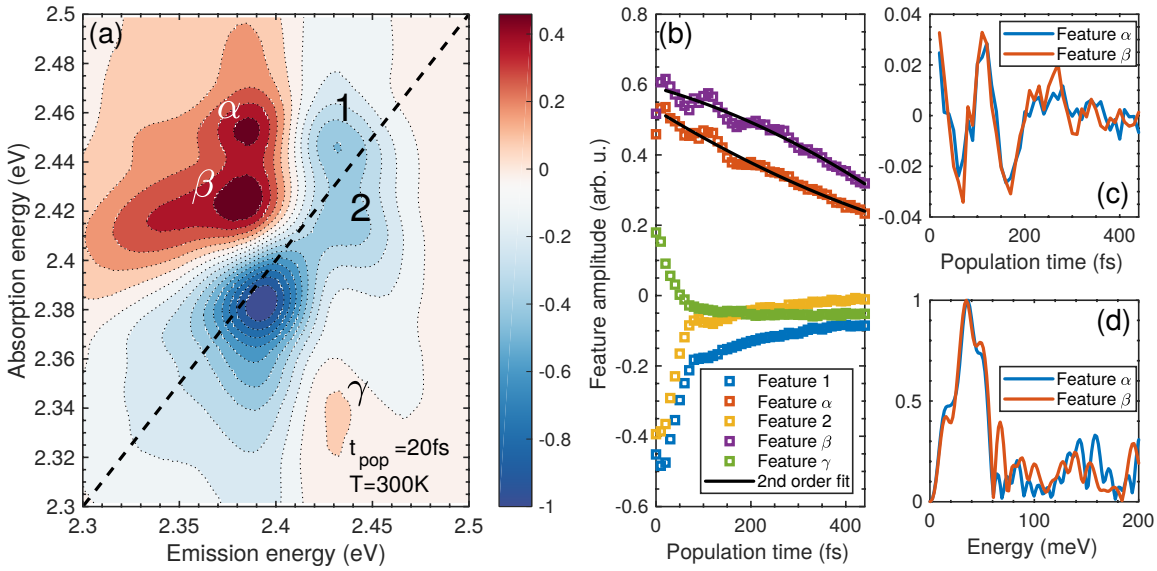

Figure 5.2: **Room temperature total correlation 2D coherent excitation spectrum and associated coherent dynamics.** (a) Total correlation 2D coherent excitation spectrum taken at room temperature for a population time delay of 20 fs. (b) Signal of various features labelled in (a) as a function of population time delay. The α and β features are fitted with a quadratic polynomial to isolate the oscillatory components. The residual of this fit is shown in (c) and the norm of its Fourier transform is shown in (d).

have discussed the assignment of each of these features in detail in ref. [167], but the important point to highlight here is that we have assigned α and β as excited-state absorption features to bound biexciton states. Here we wish to consider their evolution with population waiting time, which can be considered to be equivalent to a pump-probe delay. The most relevant observation here lies in the evolution of each of the identified features, shown in Figure 5.2(b). While features 1, 2 and γ monotonically decay, the excited-state absorption features α and β show a clear oscillatory behavior on top of the monotonic decay. To isolate these coherent oscillations and to remove the monotonically decaying component, we fit the evolution curves of features α and β phenomenologically with a second-order polynomial, which is not intended to reflect any physics but is merely intended to represent non-exponential decay. The purely oscillatory residual signal (see Figure 5.2(c)) is then Fourier transformed to obtain the spectra displayed in Figure 5.2(d). Both the spectra exhibit a couple of minor peaks at 15 ± 5 and 47 ± 5 meV, and one dominant peak at

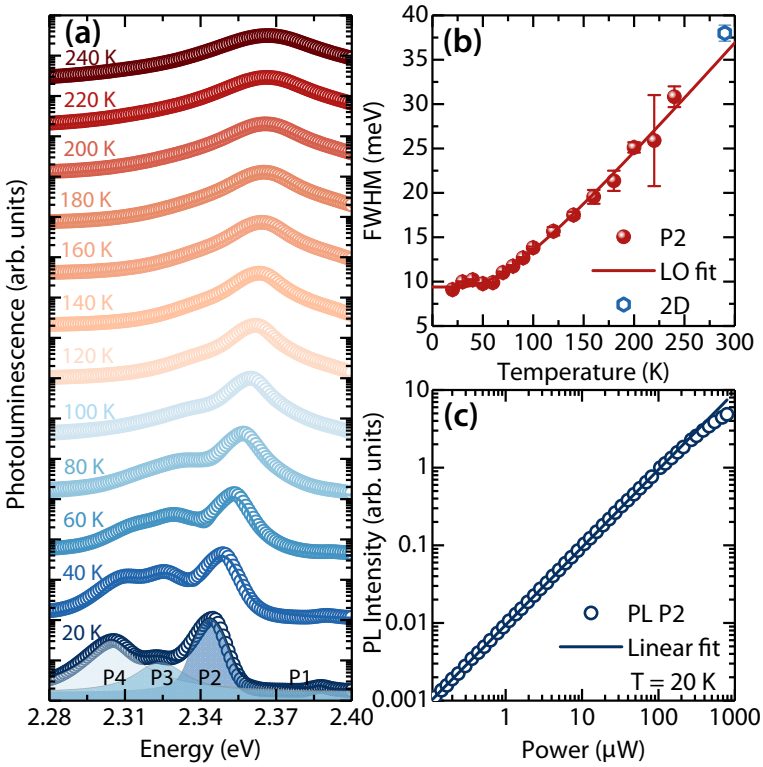

Figure 5.3: **Analysis of the PL spectra of polycrystalline films of $(PEA)_2PbI_4$.** (a) PL spectra of polycrystalline films of $(PEA)_2PbI_4$ taken at different temperatures. (b)Full width at half maximum of the most intense PL peak as a function of temperature. (c) Pump power dependence of the most intense PL peak at 20 K.

34 ± 5 meV, corresponding to the energy separation of the distinct excitonic states. During the population time, the system is in a coherent superposition of states in the same excitation manifold leading to oscillatory components along the population time delay. Importantly, this behavior is observed exclusively in features α and β, which have signatures of exciton-biexciton coherences (see Appendix and ref. [167]) but not in features 1 and 2, which are composed of population contributions. Thus, the observation of 35 meV energy mode not only confirms the presence of distinct exciton states even at room temperature, but also indicates the existence of coherent coupling between them when excited with an ultrashort laser pulse. Moreover, the presence of a 17-meV mode emphasizes significant electron-phonon coupling effects as evidenced by the absorption lineshape analysis.L.

Let us return to the absoprtion lineshape analysis, particularly to the apparent weak

temperature dependence of the exciton linewidth. While the primary excitonic linewidth fluctuates around 6.45 ± 0.53 meV (Table.5.1), the free-carrier linewidth exhibits a clear temperature dependence that can be effectively explained by a carrier-LO phonon scattering mechanism [175]. Note that the linewidth Γ_{exc} in Table.5.1 is that of the most intense transition, while all the other three transitions also exhibit similar trend with a maximum variance of 5 meV in their absolute value. Such a behavior, in spite of the Frank-Condon contributions to the absorption, suggests an anomalous nature of the exciton-phonon interactions. However, our absorption lineshape analysis is difficult at temperatures higher than the range shown in Figure 5.1(a) due to the loss of spectral structure. In order to explore further the temperature dependence of the exciton linewidth, we have carried out temperature-dependent PL measurements. Figure 5.3(a) shows the PL spectra at different temperatures. The PL spectrum displays structure that is consistent with that identified in the absorption spectrum, namely distinct spectral features separated by ~ 35 meV. Although the integrated PL intensity is linear over a broad laser intensity range (Figure 5.3(c)), careful spectral analysis is complicated by the underlying contribution of biexcitons, given their ever-present contribution due to their high binding energy [167]. Nevertheless, we can extract the full width at half maximum for the most intense peak as a function of temperature, shown in Figure 5.3(c). We observe a clear temperature dependence over a range spanning up to room temperature with the trend indicating scattering from LO phonons[176] within a Fröhlich formalism described by:

$$\Gamma(T) = \Gamma_0 + \gamma_{LO}\Big[\frac{1}{\exp(E_{LO}/k_BT) - 1}\Big]. \tag{5.5}$$

The fit obtained using Eq. 5.5 is shown in Figure 5.3(b), with the temperature independent linewidth $\Gamma_0 = 9.4$ meV, the LO phonon energy $E_{LO} = 17$ meV and the exciton-phonon coupling parameter $\gamma_{LO} = 25.6$ meV. Intriguingly, the extracted coupling parameter is much smaller than what has been reported for the three dimensional perovskites [175]. It

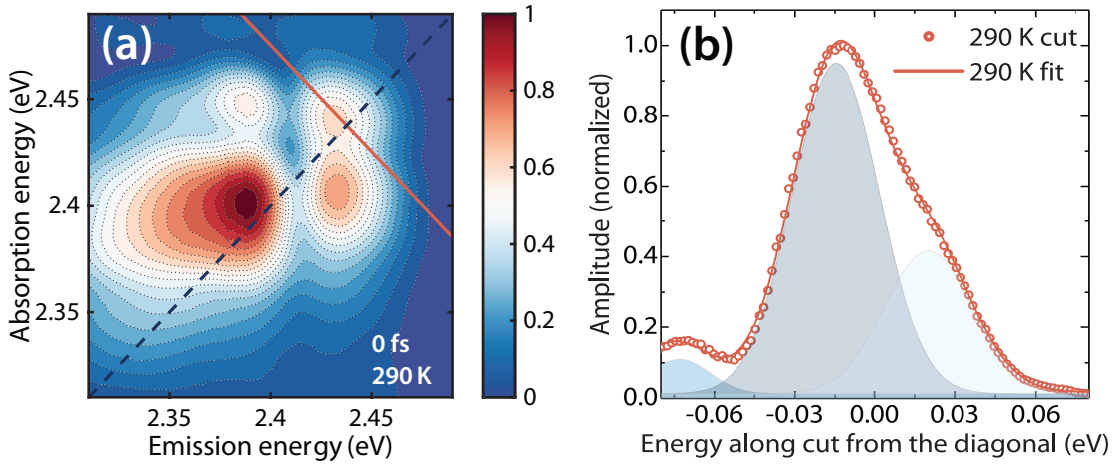

Figure 5.4: **Room temperature rephasing 2D spectrum of $(PEA)_2PbI_4$ and homogeneous linewidth extraction.** (a) Modulus of rephasing 2D spectrum of $(PEA)_2PbI_4$ taken at zero population time at room temperature. (b) Anti-diagonal cut taken along the red line shown in the 2D map plotted along with the fits from Voigt functions.

must be noted that the linewidths extracted from PL do not vary substantially below 100 K in agreement with the absorption analysis.

Let us consider the linewidths reported in Figure 5.3(c) for PL measurements and Table 5.1 for the absorption analysis, and consider to what extent they are due to inhomogenous broadening mechanisms. Within linear spectroscopies, contributions from non-negligible inhomogenous effects can hinder the direct measurement of the pure homogenous linewidths that carry signatures of electron-phonon scattering. Non-linear spectroscopies, such as the two-dimensional coherent spectroscopy described above, offer an effective way to distinguish the homogenous and inhomegneous contributions [177]. The most widely used implementation involves measurement of the amplitude and phase of the zero-time rephasing resonant four-wave mixing signal. The absolute value, zero-time rephasing spectra of $(PEA)_2PbI_4$ polycrystalline films taken at room temperature is shown in Figure 5.4(a) [1]. It is well understood that the inhomegenous contributions broaden the

[1]Note that the spectrum displayed in Figure 5.2(a) is the real part of the total correlation spectrum, that is the sum of rephasing and non-rephasing spectra, while that in Figure 5.4(a) is the absolute value of the rephasing spectrum only.

2D rephasing spectra along the diagonal while the homogenous rephasing effects are manifested along the anti-diagonal direction [115]. Figure 5.4(b) shows anti-diagonal cuts along the line shown in the 2D spectra in Figure 5.4(a) taken across a chosen peak on the diagonal with minimum overlap of off-diagonal features. The observed lineshape can be fitted using multiple Voigt functions (fits shown as solid lines in Figure 5.4(b)) yielding a linewidth $\Gamma \sim 38$ meV. This homogeneous linewidth is similar to the total linewidth measured by PL at room temperature, arguing that the observed exciton linewidths are dominated by homogeneous broadening effects. The corresponding dehasing times associated with the homogeneous linewidth at room temperature are $\tau = h/\Gamma \sim 110$ fs, indicating the dominant role of dynamic energetic disorder in this system [167], which establishes conditions in which homogeneous dephasing dominates total line broadening mechanisms. This is a significant fraction of the period of the mode associated with broadening of the PL spectrum, highlighting the dominant role of that mode in line-broadening processes and in the origin of dynamic disorder.

5.4.2 Dependence of exciton absorption lineshape on degree of octahedral distortion

Based on the empirical framework developed for $(PEA)_2PbI_4$, we now investigate other 2D-HOIP systems. We consider films intercalated with two different organic cations (NBT: n-butylammonium and EDBE: 2,2-(ethylenedioxy)bis(ethylammonium)) in addition to the previously considered PEA compound. The absorption spectra of $(NBT)_2PbI_4$ films taken at various temperatures are shown in Figure 5.5(a). Also shown in the same figure, as solid lines, are the fits obtained using Eqs. 5.1–5.4. Figure 5.5(b) shows the spectrum taken at 20 K which includes the continuum contribution along with the fit thus substantiating the generality of the developed framework. The inter-exciton spacing considered here is again 35 ± 5 meV, similar to the case of $(PEA)PbI_4$ films. The relative intensities of the excitonic transitions also follow a similar trend. In addition, the linewidths of the free-carrier states increases with temperature due to increased electron-phonon scattering while

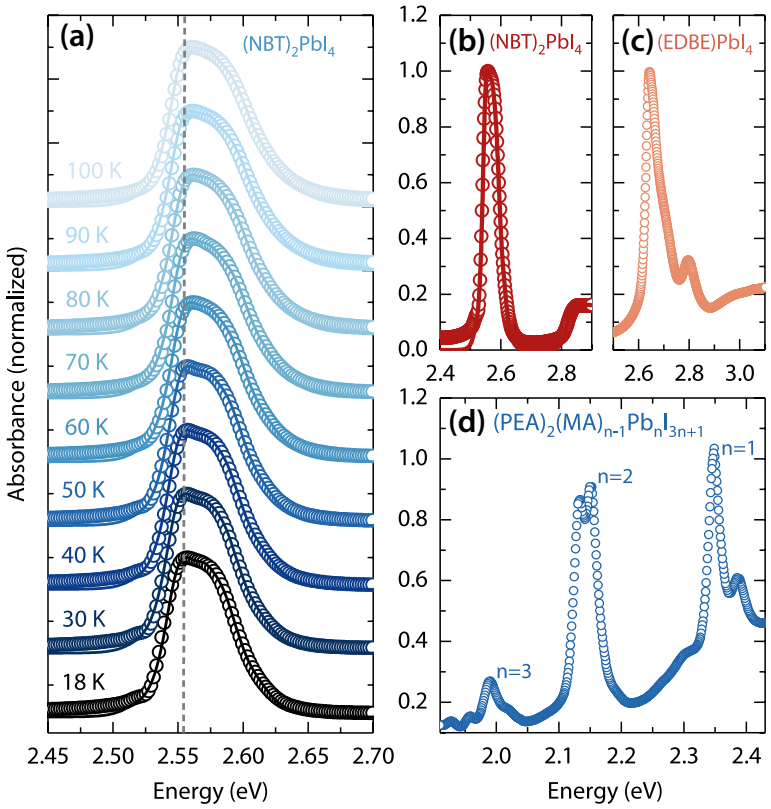

Figure 5.5: **Experimental absorption spectra of polycrystalline films of $(NBT)_2PbI_4$** taken at different temperatures (plotted as symbols) and numerical fits (plotted as solid lines), (b) Experimental absorption spectrum and numerical fit of $(NBT)_2PbI_4$ at 20 K showing both exciton and free carrier bands. (c) Experimental absorption spectrum of $(EDBE)_2PbI_4$ film taken at T = 20 K. While the excitonic line shows finestructure, no clear band-edge is visible. (d) Low temperature Absorption spectrum of polycrystalline film of $(PEA)_2(MA)_{n-1}Pb_nI_{3n+1}$.

the excitonic linewidth remains approximately constant (see Table. 5.2 for the complete list of fit parameters)

One of the pertinent differences with respect to the fits of $(PEA)_2PbI_4$ lie in the choice of the phonon modes used in the Franck-Condon analysis, which are set at 8.9 and 22 meV. The crystal structures of both the films are very similar with regards to the connectivity of the PbI_6 octahedra, since they are both (100)-oriented structures. However, the choice of the organic cation imposes different degrees of conformational constraint of the ammonium moieties and their interaction with the inorganic layer. This results in a variation in

T (K)	E_g (eV)	E_b (meV)	X_2/X_1	X_3/X_1	X_4/X_1	S_1	S_2	Γ_c (meV)	Γ_{ex} (meV)
20	2.818	253.4	0.89	0.004	0.19	1.4	0.7	12.5	9.5
30	2.819	253.37	0.97	0.027	0.215	1.4	0.7	13.2	9.6
40	2.82	253.35	0.99	0.025	0.22	1.4	0.7	13.8	9.6
50	2.821	253.65	1	0.025	0.22	1.4	0.7	14	9.5
60	2.823	253.53	1.02	0.025	0.22	1.4	0.7	14.8	9.7
70	2.824	253.35	1.05	0.025	0.23	1.4	0.7	15.6	9.8
80	2.824	253.28	1.13	0.01	0.23	1.4	0.7	16.4	9.7
90	2.824	253.53	1.2	0.01	0.24	1.4	0.69	17.2	9.7
100	2.824	253.65	1.25	0.01	0.24	1.4	0.69	17.6	9.7

Table 5.2: : **Parameters used to fit the temperature dependent linear absorption spectra of $(NBT)_2PbI_4$** shown in Figure 5.1, using Eqs. 5.1–5.4. The Huang-Rhys parameters S_i correspond to modes with energy 8.9 meV ($i = 1$) and 22 meV ($i = 2$).

the extent of geometrical distortion of the lead-halide octahedra [8]. In the present case, the $(NBT)_2PbI_4$ lattice exhibits greater octahedral distortion, and we hypothesize that this results in the increase in the energies of local lattice vibrations as can be seen in the change in the relevant vibrational frequencies. On the other hand, the re-organization energy of the excited state reduces as evidenced by the lower values for the Frank-Condon factors with respect to $(PEA)_2PbI_4$ (see Table 5.2).

The $(EDBE)PbI_4$ lattice exhibits even larger octahedral distortion in addition to being a rippled (110)-oriented zigzag structure [8]. As can be seen in the absorption spectrum shown in Figure 5.5(c), this not only modifies the phonon landscape, but also increases the inter-exciton spacing by a factor of 2. It can also be seen that there is no clear and distinct band-edge even at very low temperatures, suggesting a breakdown of the Wannier-like scenario. In fact, it is not possible to reproduce such a spectral structure in a robust way with the considered framework, pointing to a much higher degree of localization of both excitons and free-carriers induced by the large structural deformation. This also correlates with the observation of broadband photoluminescence reported earlier in these films, attributed to self-trapped excitons at defect centers [8]. In spite of such strong localization, the presence of the exciton fine structure, albeit with larger energy spacing, indicates the role of lattice

structure in their origin.

Similar spectral structure is also observed when the layer thickness is increased, as shown in Figure 5.5(d). Here, we investigate multi-layered films by introducing methylammonium ($CH_3NH_3^+$) cations to form $(PEA)_2(CH_3NH_3)_{n-1}Pb_nI_{3n+1}$ films, which contain n sheets of PbI_6 layers. Due to solution growth process, such a film comprises of polycrystalline grains with varying layer thickness [178]. Absorption stemming from polycrystalline domains with different layer thicknesses can be clearly distinguished in the absorption spectrum shown in Figure 5.5(d) due to the reducing bandgap with the increasing number of layers. In particular, we identify excitonic peaks associated with one to three-layer components and all of them show clear fine structure, albeit with variable relative intensities. While this observation re-iterates the importance of lattice structure, it also suggests that such a excitonic sub-structure may be intrinsic to the perovskite lattice and not just a consequence of confinement.

5.5 Discussion

We developed a quantitative framework to rationalize spectral lineshapes observed in the linear spectra in different 2D HOIPs. While the formalism reproduces the spectra of systems with no strong octahedral distortion, it is not sufficient for highly distorted lattices. More importantly, we have identified various manifestations of electron-phonon coupling in the optical spectra, the most obvious being the phonon replicas. Different lattice degrees of freedom associated to both crystal phonons and local vibrations contribute to these lineshapes with varying Huang-Rhys factors.

Phonon replicas are not uncommon in the optical spectra of semiconductors with non-negligible electron-phonon interactions [179]. Interestingly, most of the reported replicas in inorganic semiconductors have been observed exclusively in the PL spectra associated with bound excitons at defect centers and have been rationalized based on a phonon-assisted emission processes involving Fröhlich-like electron scattering with the polar lattice vibra-

tions [180, 181, 179, 182]. On the other hand, such signatures are clearly observed even in the absorption spectra of organic semiconductors [183], similar to the current scenario, and discussed as a consequence of the distinct lattice configuration of the excited electronic state. Some of us have recently demonstrated in the case of 3D perovskites that the excited photoexciation indeed perceives a distinct lattice configuration [184] much like the molecular systems involving Frenkel states. Our observation here of the phonon replicas with large Huang-Rhys factors, an order of magnitude larger than that of free excitons in polar semiconductors [179], also suggests a similar scenario even in the case of 2D perovskites. We consider that deeper and more quantitative understanding is required to expand on this concept.

While all the three dominant Raman modes appear to be contributing to the observed phonon replicas, only one of them contributes strongly to the line broadening, as evidenced by the weak temperature dependence of the exciton linewidth in the absorption spectrum in a low temperature range, as well as the clear temperature dependence of the PL spectral width, shown in Figure 5.3(b). This can be understood by considering the distinct mechanisms leading to broadening and the phonon replicas, although both of them involve exciton-phonon coupling. As proposed by Hochstrasser and Prasad [185] in the context of Frenkel excitons in molecular crystals or by Duke and Mahan [180] in the context of bound excitons associated to defect centers in inorganic lattices, the exciton-phonon coupling can be elaborated as:

$$H(\vec{r}) = H_{ex}(\vec{r}_0) + H_M(\vec{r}) + H_D(\vec{r}), \tag{5.6}$$

where H_D and H_M are the coordinate-dependent terms describing the exciton-phonon interactions in the vibrating lattice, and are composed of interaction energies that arise from the following distinct physical phenomena. H_M represents an exciton scattering with a phonon and is described by the excitation exchange interactions M_{nm} between two lattice sites m and n. Such a mechanism leads to the broadening of the excitonic transition in the optical spectra. On the other hand, H_D describes the energy required to displace the equi-

librium lattice configuration in order to accommodate the photoexcitation. In other words, it is the lattice recoil energy which generates lattice vibrations at the site of the photoexcitation. As pointed out earlier, such a reconfiguration of the lattice manifests as strong vibronic replicas in the optical spectra.

Such a Frenkel-like perspective, however, contradicts the considered Wannier formalism described in Eq. 5.1. Given that the estimated exciton Rydberg energy ($E_0 = E_b/4$) from the fits is around 50 meV implying a Bohr radius ($a_0 = e^2/(4\epsilon_r\epsilon_0 E_0)$) of approximately 12 nm (assuming $1/\epsilon_r = 1/\epsilon_\infty - 1/\epsilon_s$ and $\epsilon_\infty = 5$ and $\epsilon_s = 15$) [86], the exciton is far from the Frenkel limit when the exciton size is smaller than the lattice constant [53]. At the same time, such a treatment is necessary to account for the observed phonon replicas. This apparent inconsistency only highlights the limitation of both Wannier and Frenkel limits for these systesm and calls for the development for more comprehensive treatment, especially with regards to exciton-phonon coupling.

With this caveat in mind, for molecular systems, the inequality $H_D >> H_M$ holds true due to the substantial localization of the Frenkel excitons which deform the lattice locally. In inorganic systems, the other extreme limit of exciton-phonon interaction is observed, termed as the weak coupling limit by Davydov [183], where $H_D << H_M$ and the excitons are delocalized. Based on the analysis of the 2D perovskites presented here, we suggest that we are in the intermediate limit where both localized and delocalized effects manifest albeit in distinct physical observables. For example, the large Huang-Rhyss factors of the low energy phonon modes (at 8 meV for $(PEA)_2PbI_4$ films and 8.9 meV for $(NBT)_2PbI_4$ films) suggests their dominant role in the local lattice re-organization. At the same time, there is a well defined reciprocal lattice where the delocalized excitons scatter of a particular lattice phonon (17 meV [2] and 22 meV for $(PEA)_2PbI_4$ and $(NBT)_2PbI_4$ respectively). For a more rigorous discussion there is a need for a robust assignment of the resonance Raman

[2] We had previously assigned this mode to a local lattice vibration [167]. In the light of the discussion here, we now consider it to be a lattice phonon instead. Nevertheless the argument of dynamic disorder made in the previous work still holds.

modes to specific lattice symmetries, accompanied by *ab initio* calculations that can take into account all excitonic correlation effects and their coupling to lattice motion, as well as possible effects of spin-orbit coupling, both of which are out of the scope of this work.

Another important observation from this work is the presence of distinct transitions around the primary exciton line separated by around 35 ± 5 meV. As noted earlier, this separation energy does not correspond to any vibrational energy, at least to our knowledge, and thus cannot be considered as a simple vibronic progression. Rather, we consider them to be arising from excitons with renormalized binding energies. We discuss a few mechanisms that can lead to such a renormalization.

Polaronic effects have been considered extensively to explain the carrier transport and recombination dynamics in 3D perovskites. The polaron coupling coefficient α, a measure of electron-phonon coupling assuming a Fröhlich interaction, is given as [58]

$$\alpha = \frac{e^2}{\hbar} \frac{1}{4\pi\epsilon_0} \sqrt{\frac{m^*}{2\hbar\omega_{LO}}} \Big[\frac{1}{\epsilon_\infty} - \frac{1}{\epsilon_s} \Big]. \tag{5.7}$$

Considering a carrier effective mass $m^* = 0.2m_0$ [171] and the LO phonon energy to be 17.4 meV, following the linewidth analysis of $(PEA)_2PbI_4$ films, we obtain a coupling constant of $\alpha = 1.67$ assuming $\epsilon_s = 15$. Although there is no direct experimental measurement of the static dielectric permittivity, the maximum value is set by that of 3D perovskites ($\epsilon_s = 35$) [86], with which we obtain $\alpha = 2.2$. An estimate of the polaron binding energy (E_p) can be evaluated within a perturbative approach as [186]

$$E_p = -\hbar\omega_{LO} \left[\alpha + 0.0158\alpha^2 + 0.00081\alpha^3 \right]. \tag{5.8}$$

Using the calculated values of α in Eq. 5.8 gives a polaron energy $29.6 - 39$ meV (bound by the two values of static permittivity above), very close to the observed inter-exciton spacing Δ in Figure 5.1. Thus, one may hypothesize that the multiple transitions are a consequence of polaronic effects in these systems [187, 188], as also suggested by Gauthron et al [104].

The mechanism which stabilizes distinct transitions instead of a single renormalized exciton, on the other hand, may lie in the lattice symmetry arguments driven by phonons with the interaction energy given by the polaron energy (E_p). It is worth noting that the system here is not strictly 2D, unlike transition-metal dichalcogenides, with a non-trivial extension of the carrier wavefunctions in the z-direction, perpendicular to the lattice plane. Any phonon driven distortions of the octahedra may lift hidden orbital degeneracies giving rise to the multiple transitions [189]. More systematic investigation of this process requires rigorous group theoretical analysis of the lattice in conjunction with the vibrational degrees of freedom.

Alternatively, the degeneracy lifting can also be driven by the large spin-orbit coupling (SOC) due to the presence of lead, which can result in the Rashba-Dresselhaus effect [190] when coupled with the asymmetry intrinsic to the 2D HOIP lattice. Briefly, lack of symmetry creates a gradient in the crystal potential and thus a local electric field. An electron in the lattice will be accelerated to relativistic velocities by such a field, inducing a magnetic field in its frame of reference. Thus, even in the absence of external magnetic field, and merely by virtue of the the SOC field, spin degeneracies will be lifted, splitting the carrier bands. In the case of stable-exciton states such an effect can lead to the mixing of singlet and triplet states and the lifting of associated degeneracy, perceived via excitonic signatures in optical absorption. In fact, Zhai et al. report a Rashba splitting of 40 meV in $(PEA)_2PbI_4$ [107], consistent with the observed energy spacing. Such a mechanism, on the other hand, must be very sensitive to the thickness of the metal-halide layer, which determines the strength of the crystal potential. As we do not observe a substantial change in the inter-exciton spacing as can be seen in the absorption spectrum of a multi-layered 2D-HOIP film shown in Figure 5.5(d), we deem this to be an unlikely mechanism for the fine-structuring of the exciton. We do emphasize that this observation does not rule out a Rashba effect as reported by Zhai et al., it merely argues against it accounting for the exciton spectral structure reported here.

5.6 Conclusions and outlook

By means of temperature-dependent linear absorption measurements and modeling with a simple two-dimensional Wannier exciton formalism, supported by two-dimensional coherent excitation spectroscopy, we have identified excitation spectral lineshapes that are consistent with polaronic effects on the exciton. Spectral features are homogeneously broadened, which is indicative of the dominant role of dynamic disorder (see also ref. [167].) This is reflective of the highly polar nature of the lattice in this class of materials, as well as its hybrid organic-inorganic nature, in which delocalized phonons as well as more localized vibrations couple to the electronic degrees of freedom on the lead-halide single plane. Excitons in these complex quantum-well-like structures are well described by a Wannier model, appropriate for excitons in quantum-confined semiconductor materials, but also show signatures of strong lattice deformation effects induced by the photoexcitation itself, which are not generally manifested in common semiconductor nanostructures. We consider that understanding the intricate details of exciton-lattice coupling dynamics in 2D metal-halide perovskites will uncover a wealth of information on their electronic and optical properties.

5.7 Appendix I: Modified Elliott formula

The complete expression for the absorption obtained by combining Eqs.5.1,5.3 and 5.4 and used to obtain the fits presented in this work:

$$
\begin{aligned}
\alpha\left(\hbar\omega\right) &= \alpha_{exc} + \alpha_{cont} \\
&= \alpha_0 \Big[\sum_{n=1}^{\infty} \Big[\sum_{j=2}^{j=4} \frac{X_j \cdot E_j}{\left(n-\frac{1}{2}\right)^3} \operatorname{sech}\left(\frac{\hbar\omega - Eg + \frac{E_j}{\left(n-\frac{1}{2}\right)^2}}{\Gamma_{exc}} \right) + \\
&\quad + \sum_{m_i} \frac{X_1 \cdot E_0}{\left(n-\frac{1}{2}\right)^3} \operatorname{sech}\left(\frac{\hbar\omega - Eg + \frac{E_0}{\left(n-\frac{1}{2}\right)^2}}{\Gamma_{exc}} \right) \cdot \\
&\quad \cdot \delta\Big[\hbar\omega - \left(E_g - \frac{E_0}{\left(n-\frac{1}{2}\right)^2} \right) - \sum_i m_i \hbar\omega_i \Big] \cdot \prod_i \frac{e^{-S} S_i^{m_i}}{m_i!} \Big] \\
&\quad + \int_{E_g}^{\infty} \operatorname{sech}\left(\frac{\hbar\omega - \varepsilon}{\Gamma_c} \right) \frac{2}{1 + e^{-2\pi\sqrt{\frac{E_0}{\hbar\omega - E_g}}}} \frac{1}{\left[1 - \frac{\alpha 8 m_*}{\hbar^4}\left(\varepsilon - E_g\right)\right]} d\varepsilon \Big].
\end{aligned}
\tag{5.9}
$$

5.8 Appendix II: Origin of oscillatory dynamics in a 2D coherent excitation spectrum

Below, we elaborate the origin of the oscillations observed in figure 5.2 and most importantly, why they only appear in the excited state absorption features. Features α and β each stem from the contribution of two pathways: one going through a population of the higher energy excitons and one involving a coherence between states of the same excited state manifold (shown in Fig.5.6(d)). While the former does not oscillate with population time the non-rephasing part of the latter oscillates at the difference in energy between the states involved in the coherence. Diagonal terms, by definition, do not involve such coherences and therefore do not exhibit oscillations during the population time. Furthermore, off-diagonal features caused by pathways which do involve coherences during the population time could be cancelled by pathways involving and slightly repulsive unbound two-quantum states (Figure 5.6(b) and (c)). Lastly, excited-state absorption features shifted

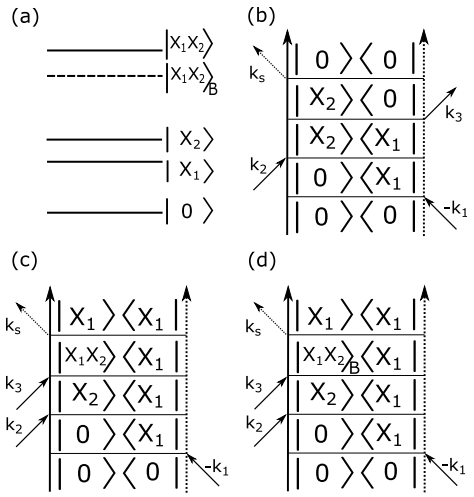

Figure 5.6: **Double-sided Feynman diagrams responsible for population time oscillations in a 2D spectrum's excited state feature.** (a) A representative scheme consisting of two excited states ($|X_1\rangle$ and $|X_2\rangle$) and a biexciton state ($|X_1X_2\rangle_B$) arising from their binding along with the unbound state $|X_1X_2\rangle$. (b),(c) and (d) Double-sided Feynman diagrams showing the excitation pathways which lead to the off-diagonal feature in a rephasing 2D spectrum.

from off-diagonal features (such as γ) do not involve oscillations since they too go through population of lower-energy excitons during the population time.

5.9 Acknowledgements

ARSK acknowledges funding from EU Horizon 2020 via Marie Sklodowska Curie Fellowship (Global) (Project No. 705874). SN and AP acknowledge funding from EU Horizon 2020 Research and Innovation Program under grant agreement no. 643238 (SYNCHRONICS). FT acknowledges a Doctoral Postgraduate Scholarship from the Natural Sciences and Engineering Research Council of Canada and Fond Québécois pour la Recherche: Nature et Technologies. CS acknowledges support from the School of Chemistry and Biochemistry and the College of Science of Georgia Institute of Technology.

SN collected and analyzed the temperature-dependent absorption and photoluminescence data supervised by ARSK and AP. FT and SN collected the 2D coherent rephasing spectra, directed by ARSK. DC synthesized the samples. CS and ARSK led the intellec-

tual development of the project. All authors contributed to the redaction of the manuscript. ARSK and CS are to be considered co-principal investigators of this project.

CHAPTER 6

PHONON COHERENCES REVEAL THE POLARONIC CHARACTER OF EXCITONS IN TWO-DIMENSIONAL LEAD-HALIDE PEROVSKITES

In the previous chapter, we hypothesized that the states involved in the excitonic fine structure were of different electronic character and that their lineshapes reflected different couplings to the lattice phonons. This hypothesis can be directly tested using resonance Raman spectroscopy in which spectral features arising from modes displaced by the resonant transition to the electronic excited state are enhanced by many orders of magnitude. As stated in section 2.3.1, pumping vibronic replicas will not change the resonance Raman spectrum and thus can be used to separate vibronic replicas from distinct electronic states. However, the energies of optical phonons in 2D-HOIPs are low and their photoluminescence strong, making such measurements in the frequency domain nearly impossible. To circumvent this, one can instead use resonant impulsive coherent stimulated Raman spectroscopy (RICSRS), the time-domain equivalent of resonance Raman spectroscopy. With this technique, the low energies of the lattice phonons are no longer an obstacle and allows one to use temporally longer and thus spectrally sharper pump pulses. This in turn, grants the desired spectral resolution to individually probe each resonances in the fine structure.

We carried on these experiments on two 2D-HOIPs and obtained distinct resonant Raman spectra when pumping different lines of the excitonic fine structure or the absorption continuum. This unambiguously proves that the fine structure does not arise from a vibronic replica since it arises from a manifold of electronically distinct states thus confirming the hypothesis put forward in the last chapter. Moreover, it also show that each of these states harbors a distinct polaronic character as evidenced by the great differences in their RICSRS spectra and its modulation with probe energy.

We also performed DFT calculations and surprisingly obtained an excellent agreement

with our experimental results This allowed us to dissect thoroughly the exciton-phonon coupling. Not only could we assign each observed mode to a specific correlated atomic motion in the inorganic layer, we were also able to propose which component of each excitons, the electron or the hole, are more responsible for these contrasting polaronic characters. These calculations, however, were not excited state calculations. Their conclusions can only be applied to the system's ground state and should thus be taken lightly.

It is hard to overstate the importance of the results presented in this chapter. Not only do they infirm an hypothesis about the nature of excitons in these systems widely held to be true by many researchers, but also expose a whole range of phenomena previously unknown to occur in these systems. At the very least, these effects should be an outcome predicted by future models describing 2D-HOIPs. We further believe these results to be the first direct evidence of the polaronic nature of excitons in 2D-HOIPs: each line of fine structure corresponds to a distinct exciton-polaron. These effects are central in understanding the properties of primary photoexcitations in these materials since, as we will show in the next chapters, they are strongly felt in many fundamental processes such as carrier relaxation and emission as well as excitonic many-body interactions and scattering.

This work was published in Nature Materials in 2019 [191] and can be found on the arXiv under the same title. Dr. Valverde-Chávez (GaTech) and I are to be considered first co-authors. Dr. Srimath Kandada (CNST@PoliMi, IIT and GaTech), Dr. Bargigia (GaTech), Dr. Valverde-Chávez and I acquired the transient absorption data. I analyzed the data. Dr. Cortecchia (CNST@PoliMi, IIT) synthesized the samples and Dr. Quarti (U. Mons) performed the DFT calculations. The work was advised and supervised by Pr. Petrozza (CNST@PoliMi, IIT), Pr. Silva (GaTech), Pr. Beljonne (U. Mons) and Dr. Srimath Kandada. All authors contributed to the redaction of the manuscript and its intellectual development.

6.1 Abstract

Hybrid organic-inorganic semiconductors feature complex lattice dynamics due to the ionic character of the crystal and the softness arising from non-covalent bonds between molecular moieties and the inorganic network. Here we establish that such dynamic structural complexity in a prototypical two-dimensional lead iodide perovskite gives rise to the coexistence of diverse excitonic resonances, each with a distinct degree of polaronic character. By means of high-resolution resonant impulsive stimulated Raman spectroscopy, we identify vibrational wavepacket dynamics that evolve along different configurational coordinates for distinct excitons and photocarriers. Employing density functional theory calculations, we assign the observed coherent vibrational modes to various low-frequency ($\lesssim 50\,\mathrm{cm}^{-1}$) optical phonons involving motion in the lead-iodide layers. We thus conclude that different excitons induce specific lattice reorganizations, which are signatures of polaronic binding. This insight on the energetic/configurational landscape involving globally neutral primary photoexcitations may be relevant to a broader class of emerging hybrid semiconductor materials.

6.2 Introduction

Hybrid organic-inorganic metal-halide perovskite quantum-well-like derivatives are of increasingly sharp focus due to the presence of strongly bound, stable excitons at room temperature [78, 90, 164, 4, 192, 62]. These excitons are viewed broadly as analogous to those in epitaxial semiconductor quantum wells, which generally feature much lower binding energies. Nevertheless, the distinct ionic character, and the 'softness' of the lattice resulting from organic counter-ion coordination, give rise to strong electron-phonon coupling and dynamic disorder effects, which influence the optical and electronic properties of this class of materials [165, 193, 100], and their consequences on excitonic structure are not thoroughly explored. There are therefore currently open questions on the peculiar nature

of excitons in these structurally complex materials, which are argued to be in an intermediate regime between extended Wannier excitons in quantum-confined semiconductors and localized excitons in molecular semiconductors [194]. We establish here that excitons in two-dimensional (2D) hybrid perovskites are dressed by the ionic lattice leading to the coexistence of multiple excitons with distinct lattice couplings. This has consequences in the formation of biexcitons [167], for example, which would have profound implications for the development of light-emitting devices [83, 195, 196, 197]. More generally, our conclusions will shape the detailed description of fundamental excitonic processes — energy transport, population dynamics, quantum dynamics (involving dynamics of many-body couplings and of dephasing dynamics, for example) in 2D hybrid perovskites. Beyond these materials, this knowledge represents an acute contribution to the comprehension of ionic semiconductors with elaborate hybrid lattices [67, 198].

Unlike excitons in (non-ionic) semiconductor quantum wells, for which their resonances are characterized by sharp, structureless spectral lineshapes, excitons in these materials display rich spectral structure that depends on the degree of lattice distortion imposed by the organic cationic ligands [199, 91, 200, 201, 92, 93, 202, 104, 98, 203, 62]. To account for this structure, we have invoked a general framework of a delocalized Wannier exciton with binding energy ~ 200 meV but with substantially large coupling to local lattice vibrations, modelled by four distinct, non-degenerate excitonic transitions, spectrally separated by multiples of 35 meV [62]. Previously, we hypothesized that polaronic effects play a role in such a rich excitonic spectral structure [62] ubiquitously observed in 2D perovskites. A direct optical probe of polaronic effects on the nature of excitons would be resonance-Raman spectroscopy [204]. However, the high photoluminescence background in these materials obscures the relatively weak Raman signal, making such a measurement a practically arduous task. Here, we find direct and unambiguous evidence for this hypothesis by implementing high-resolution resonant impulsive stimulated Raman spectroscopy (RISRS) [114, 113]. We establish polaronic effects on discrete non-degenerate excitonic

transitions, evident via distinct coupling to low-frequency phonons. We find that the coupling of carriers to lattice degrees of freedom is stronger than that for excitons in general, which we rationalize by the ionic nature of the crystal. Nevertheless, different excitons with common ground state and with specific polaronic character coexist in this class of materials.

6.3 Results

We focus on two prototypical single-layer perovskite systems, $(PEA)_2PbI_4$ (PEA = phenylethylammonium) and $(NBT)_2PbI_4$ (NBT = n-butylammonium), which have slightly different structural disortions imposed by the organic cation [8]. The exciton absorption spectrum of $(PEA)_2PbI_4$ measured at 5 K, is shown in Figure 6.1(a) and the representative crystal structure is depicted in Figure 6.1(b). The spectrum is characterized by a very well defined lineshape composed of two dominant transitions at 2.37 and 2.41 eV, labeled A and B, respectively in Figure 6.1(a), and two additional peaks with the same energy spacing above and below these two main peaks, with much lower oscillator strength [62]. We have carried out transient absorption measurements by pumping into the conduction band at 3.06 eV, shown in Figure 6.1(c). These excitation conditions generate an initial hot charge-carrier density. The spectra and dynamics follow the reported trends dominated by carrier thermalization[205, 206]. During the first picosecond, the differential transmission spectrum is composed of a strong negative feature across the A band and a positive feature at the B band. This lineshape is characteristic of a superposition of excitation-induced shift and broadening of the excitonic transition by many-body interactions along with the bleach of higher lying electronic states [169]. In a few picoseconds, the positive signal corresponding to the ground-state bleach gains in intensity, indicating carrier thermalization into the A exciton. The spectrum still contains the signatures of pump-induced spectral shifts induced by the substantial photocarrier population over picosecond time windows. The low-energy negative feature below 2.3 eV can be attributed to the excited-state absorption from the

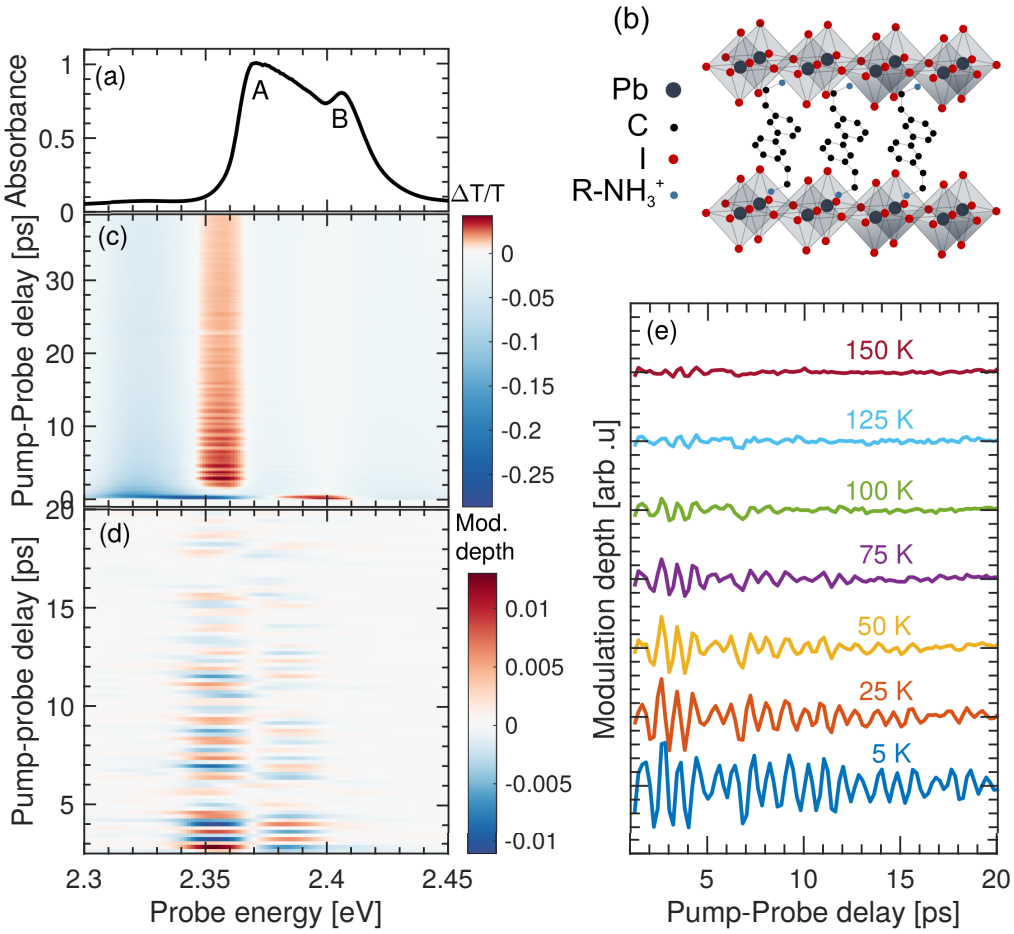

Figure 6.1: **Impulsive coherent vibrational dynamics of $(PEA)_2PbI_4$.** (a) Absorption spectrum measured at 5 K. (b) Schematic of the lattice structure of $(PEA)_2PbI_4$ (see Supporting Information section S1 for X-Ray diffraction data). (c) Time-resolved differential transmission spectrum measured at 5 K and with pump photon energy of 3.06 eV. (d) Oscillatory components of the time-resolved differential transmission spectrum, obtained by subtracting the population dynamics (empirically approximated as twelfth-order polynomials) from the transient spectrum in part (c). (e) Temperature-dependent cuts of the oscillatory response obtained by binning transient maps such as that displayed in part (d) around a probe energy of 2.35 eV.

exciton to mutli-particle states [167].

In addition to the population dynamics, we observe a periodic modulation of the differential transmission signal, particularly strong in the spectral region that corresponds to absorption of exciton A. The oscillatory components can be clearly seen after subtracting the population dynamics at all detection energies as shown in Figure 6.1(d). We identify these

as the signatures of coherent phonons generated via resonant impulsive stimulated Raman scattering (RISRS) induced by the ultrashort pump pulse [114]. When the duration of the pulse is much shorter than the period of Raman-active low-frequency vibrations, Raman interactions generate an impulsive force on the lattice driving its coherent motion [114]. This modulates the permittivity at the frequency of the lattice motion, which can be detected as the oscillatory component of the differential transmission signal.

As shown in Figure 6.1(e), at higher temperatures the coherent oscillations not only dephase faster due to phonon-phonon scattering [207], but they also exhibit reduced modulation depth. The latter can be attributed to the presence of strong dynamic disorder, especially above 100 K as we have demonstrated previously [167]. We only focus on the coherent phonon dynamics at 5 K in the rest of the manuscript because the conclusions that we draw by analyzing the vibrational coherences under resonant excitation at low temperature are relevant over the entire range up to room temperature, as we have established that the same excitonic spectral structure persists over this range [167, 62]. The full temperature-dependent dataset is presented in Figs. S2 and S3 of SI.

By Fourier-transforming the measured oscillatory response in Figure 6.1 along the pump-probe time axis, we obtain a RISRS spectrum. We identify six vibrational modes that we label M1–M6, with peak energies reported in Table 6.3. The peaks display well-defined Lorentzian lineshapes with full-width-at-half-maximum ≤ 0.33 meV, as shown by the fit in Figure 6.2(a).

To properly discern the nature of coupling and to assign the observed energies to specific lattice vibrations, we calculated the vibrational normal modes of $(PEA)_2PbI_4$ by using density functional theory (DFT) within the harmonic approximation. This (almost) parameter-free computational approach represents the current state-of-the art in the simulation of the vibrational spectroscopic response of solid-state materials including hybrid perovskites [208, 209, 210, 207]. The calculations do not yield negative vibrational frequencies at the Γ point, further indicating that the crystalline structure used to model PEA_2PbI_4

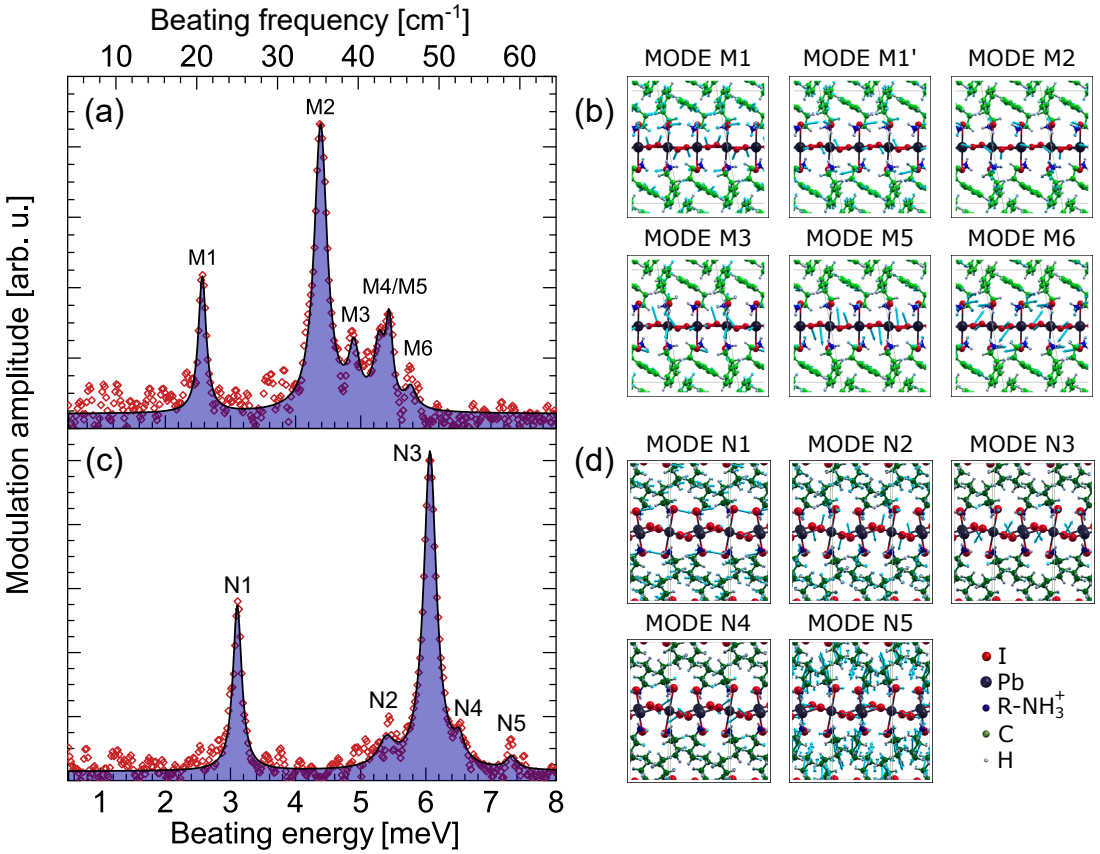

Figure 6.2: **Integrated resonant impulsive stimulated Raman spectrum of $(PEA)_2PbI_4$ and $(NBT)_2PbI_4$ at 5 K and associated phonon modes.** (a) and (c) Fourier-transform spectrum of the oscillatory components such as those displayed in Figure 6.1(d), and integrated over all the detection energies probed in Figure 6.1 for $(PEA)_2PbI_4$ and $(NBT)_2PbI_4$ respectively. The pump energy is tuned to 3.06 eV and 3.1 eV respectively. The continuous line with blue shade is a fit to a function composed of six and five Lorentzian components respectively. (b) and (d) Diagrammatic representations of the vibrational modes obtained via DFT calculations. The black spheres at the center of the octahedra represent the Pb ions, while the red spheres represent the iodine. The green structures represent the organic cations - PEA in (b) and NBT in (d). The cyan arrows represent the motion of the each of the ions within the lattice.

is a real minimum of the potential energy surface (the full list of computed vibrational frequencies is reported in Section S5 in SI).

The electron-phonon coupling is estimated by displacing the crystalline structure along the normal mode (Q_i) and evaluating the corresponding variation of the single-particle electronic band gap (E_g). For each normal mode Q_i in the energy region of interest, we find a linear relationship between the displacement and the band gap (i.e. linear electron-

Mode	Measurement [meV]	Calculation [meV]	λ [meV]	Mode Assignment
			$(PEA)_2PbI_4$	
M1	2.57 ± 0.01	3.18	0.609	Octahedral twist along a axis on the inorganic sheet
M1′	—	3.93	0.94	Octahedral twist along a axis on the inorganic sheet[1]
M2	4.38 ± 0.01	4.51	5.21	Octahedral twist and Pb-I-Pb bending
M3	4.89 ± 0.02	4.51	3.49	Pb Displacement and Pb-I-Pb bending
M4	5.22 ± 0.06	—	—	—[2]
M5	5.41 ± 0.02	5.34	4.54	Pb-I-Pb bending and Pb-I stretching
M6	5.75 ± 0.01	5.86	4.78	Scissoring of Pb-I-Pb angle
			$(NBT)_2PbI_4$	
N1	3.10 ± 0.01	2.93	0.76	Octahedral twist along a axis on the inorganic sheet
N2	5.42 ± 0.02	5.38	4.42	Octahedral twist along a axis on the inorganic sheet
N3	6.06 ± 0.01	5.97	16.29	Octahedral twist along axis orthogonal to the inorganic sheet
N4	6.52 ± 0.15	6.60	8.69	Scissoring of Pb-I-Pb angle
N5	7.31 ± 0.19	7.37	0.12	Scissoring of Pb-I-Pb angle

Table 6.1: **Assignment of the resonant impulsive stimulated Raman spectrum of $(PEA)_2PbI_4$ and $(NBT)_2PbI_4$.** Experimental vibrational energies from the spectrum in Figure 6.2, and normal-mode energies obtained from density functional theory calculations, along with the mode assignment.

phonon coupling regime) and calculate the relaxation energy λ_i as: [211, 212]

$$\lambda_i = \left(\frac{\partial E_g}{\partial Q_i}\right)^2 (4\alpha_i)^{-1}, \tag{6.1}$$

where α_i is the curvature of the ground state potential energy surface along the Q_i normal mode of vibration. Among all normal modes below 8 meV, our calculations identify a few with frequency similar to those showed in Figure 6.2(a) and associated with sizable relaxation energy (few meV), i.e. coupled to bandgap excitations. In Table 6.3, we compare the experimental vibrational frequencies with those obtained from DFT, together with the corresponding relaxation energies and a description of the characteristic atomic displacements.

The agreement between calculation and measurement is remarkable, especially considering the inherent difficulty in computing normal-mode vibrations at such low frequency, where anharmonic effects can play a significant role [213]. The lattice motion corresponding to each of these modes is pictographically represented in Figure 6.2(b), and is also available in animated files as Supplementary Information. We have further verified the present results against calculations including spin-orbit coupling and found close agreement with the results in Table 6.3 (see Table S2 in SI).

As previously demonstrated in other lead-halide hybrid materials, the identified modes in this energy range correspond to the motion of the lead-iodide network [214, 210, 215]. All the modes have contributions from rotation of the octahedra along the two pseudocubic axes lying within the inorganic sheet. With increasing energy, we also find additional contributions from the I-Pb-I bendings and I-Pb stretching or octahedral rotations orthogonal to the inorganic sheets (represented as the scissoring mode), indicative of the larger stiffness of these co-ordinates. The nature and energy of some of these modes are strikingly similar to those reported for three-dimensional perovskites based on experimental [214, 165, 215] as well as theoretical [210] investigations.

To further generalize the experimental findings and provide further validation for the theoretical methodology, we also investigated polycrystalline films of $(NBT)_2PbI_4$. Figure 6.2(c) shows the integrated RISRS spectrum when the sample is photo-excited at 3.06 eV. We observe five modes with full-widths-at-half-maximum ≤ 0.29 meV, distinct from the case of $(PEA)_2PbI_4$, but again in very close agreement with the DFT predictions, see Table 6.3. All the modes appear to be shifted to higher energies, possibly due to the stiffening of the lattice induced by the octahedral distortions ubiquitous in the low-temperature phase of $(NBT)_2PbI_4$ [8]. Similar to the case of $(PEA)_2PbI_4$ we can assign the observed modes to the octahedral twist along or perpendicular to the inorganic sheet as well as the scissoring of the Pb-I-Pb angle, see Figure 6.2(d) for diagrammatic representation of the vibrations. Additional data on this material is presented in Figs. S8 and S9 of SI.

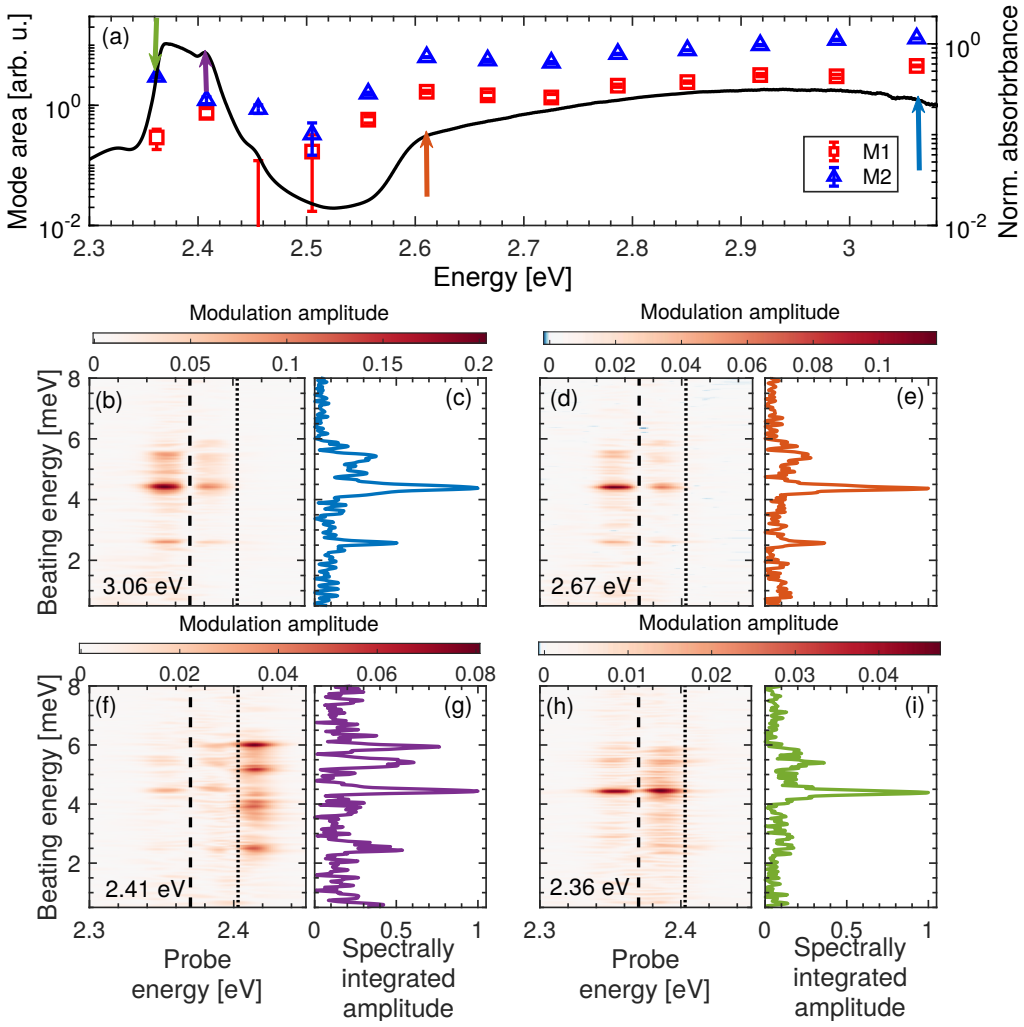

Figure 6.3: **Pump wavelength dependence of the resonant impulsive stimulated Raman spectra of $(PEA)_2PbI_4$ at 5 K.** (a) Excitation profiles of modes M1 and M2 as defined in Figure 6.2 (represented as symbols indicated in the inset), plotted with the linear absorption spectrum. Error bars represent statistical error arising from noise in the beating spectra. (b,d,f,h) Beating spectra as a function of detection (probe) energies. Probe-energy-integrated vibrational spectra are also shown in (c,e,g,i). The pump energies are (b/c) 3.06 eV, (d/e) 2.67 eV, (f/g) 2.41 eV and (h/i) 2.36 eV. The dashed and dotted lines over the beating maps indicate the peak energies of excitons A and B respectively, as defined in Figure 6.1(a).

We now return to the vibrational coherences observed in $(PEA)_2PbI_4$ to demonstrate contrasting coupling of the lattice to the two most intense excitonic transitions A and B, and also to photocarriers. Figure 6.3(a) shows the excitation profiles of modes M1 and M2 plotted along with the linear absorption spectrum. Due to the resonant excitation, the

RISRS driving the coherent lattice motion is enhanced for those ground-state vibrational coherences that are strongly coupled to the electronic transitions[114, 216]. This is clearly observed as a monotonic increase of the intensity of both the modes in the excitation spectra when the excitation energy is tuned to higher energies into the carrier continuum, at pump energies ≥ 2.56 eV. The photon-flux at each excitation energy is kept constant to directly correlate the mode intensity to the absorption cross-section. The full beating maps and integrated spectra corresponding to these excitation conditions are presented in Figs. S4 and S5 of SI.

In Figs. 6.3 (b,d,f,h), we show the two-dimensional beating maps, which represent the probe-energy-resolved Raman spectra, obtained by Fourier transforming the dynamics at all the detection energies for each of the excitation energies marked by shaded regions in Figure 6.3(a). We display two spectra resulting from pumping into the continuum at 3.06 and 2.67 eV (Figs. 6.3(b) and 6.3(d) respectively), one spectrum resulting from pumping exciton B (Figure 6.3(f)), and one exciting exciton A (Figure 6.3(h)). Figs. 6.3 (c,e,g,i) show the integrated spectra across all the detection energies. The raw pump-probe data and cuts corresponding to these pumping conditions are presented in Figs. S10 to S12 of SI.

In the cases of the free-carrier excitations, we observe identical vibrational coherences with the dominant signal at modes M1 and M2. While the resonant excitation of exciton A reveals predominant coupling to mode M2, excitation of exciton B displays strikingly different vibrational spectral structure. As evident in Figure 6.3(g), we observe more intense signals at mode M6 and M4 along with diminished intensity of mode M2. These observations suggest rather distinct lattice couplings exhibited by each of the exciton states. Another important observation from the beating maps is the non-uniformity of the amplitude across the detection energy axis for different excitation energies. For instance, the free-carrier excitation beating maps reveal dominant signal only at the detection energies around the exciton A absorption resonance. The amplitude spectrum has a characteristic dual-peaked lineshape with a dip at the peak energy of exciton A [217], indicated by

dashed lines in the beating maps. Importantly there is no notable signal at the energy of exciton B, which is indicated by dotted lines. The only exception to this is the case shown in Figure 6.3(f), where most of the signal is present around the energy of exciton B. This data corresponds to resonant excitation of exciton B, and establishes that the vibrational coherences associated with this transitions differ to those due to exciton A, as well as those generated by photocarriers. We employ this intriguing observation as the key evidence in this work to differentiate the polaronic character of each of the excitons and that of free-carrier excitations.

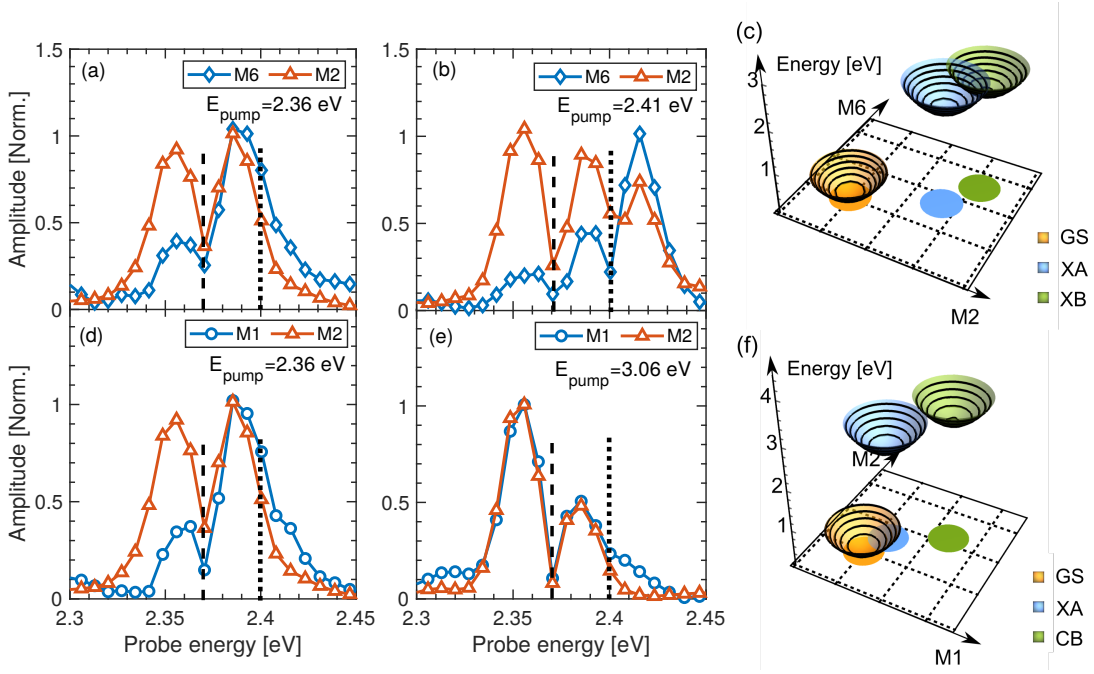

Figure 6.4: **Consequences of the wavepacket dynamics in $(PEA)_2PbI_4$ at 5 K.** Amplitude spectra of M2 and M6 modes when the pump energy is (a) resonant with exciton A at 2.36 eV and (b) with exciton B at 2.41 eV. (c) Configuration-space representation of the harmonic potentials of ground state (GS), exciton A and exciton B. Amplitude spectra of M1 and M2 modes when the pump energy is (d) resonant with exciton A at 2.36 eV and (e) with the carrier continuum at 2.41 eV. (f) Configuration space representation of the harmonic potentials of ground state (GS), exciton A (XA, displaced predominantly along M2 coordinates) and the free carriers (CB, with strong and approximately equal displacement along M1 and M2 coordinates).

We now discuss the nature of the observed lineshapes by comparing the amplitude spectra obtained by taking horizontal cuts of the probe-energy-resolved beating maps from

different cases in Figure 6.4. We first consider exciton A in Figure 6.4(a) and exciton B in Figure 6.4(b). Given that M2 and M6 are the dominant vibrational modes in these two cases, we plot the amplitude spectra taken at those energies. The lineshapes in Figure 6.4(a) are indicative of vibrational wavepacket dynamics often observed in molecular systems [216, 217], where the energy of exciton A is modulated by the motion of a vibrational wavepacket along the a real-space vibrational coordinate associated with the coherently excited phonon. The dual-peaked lineshape and the π phase shift at the peak energy (not shown here but displayed in section S4 of the Supplemental Information) is clearly indicative of such dynamics, where the detection energies around the exciton peak display the most prominent oscillations. The observed lineshape can be reproduced using a simple harmonic oscillator model involving two electronic states, which are defined by their respective potential energy surfaces (PES). The PES minimum of the excited state is displaced along one of the vibrational normal coordinates due to electron-phonon coupling. Impulsive optical excitation generates a vibrational wavepacket, which oscillates along the PESs. The effect of these vibrational degrees of freedom on the permittivity can be computed as described in ref. [112]. A detailed description of this model and the results of such simulations are given in the Supplemental Information (Section S3). The observed dynamics are a consequence of the displacement of the PES of the excited state perceived via spectator lattice modes and thus are indicative of polaronic effects [184, 103]. We can compare the relative displacement (Δ) of the PES in the excited state across each of the normal mode coordinates. The Raman cross section is proportional to $\Delta^2\omega^2$, with $\hbar\omega$ being the phonon energy, and thus the analysis of relative intensities of each of the modes at different pump energies provides a representation of the complex excited-state landscape in $(PEA)_2PbI_4$, as depicted schematically in Figure 6.4(c). By pumping exciton A, we can infer that its PES is displaced strongly along the normal coordinate defined by the phonon at M2, with a relatively more limited displacement along all the other co-ordinates, as represented by the *blue* PES shown in Figure 6.4(c). The absence of any modulation

at the energy of exciton B in this case suggests the relative immunity of exciton B to the wavepacket dynamics only along the co-ordinate defined by the normal mode M2. This is duly supported by the amplitude spectra shown in Figure 6.4(b), where the M6 mode also modulates the exciton B transition strongly. We may infer that the PES of exciton B is displaced along both M2 and M6 axes as represented by the *green* PES in Figure 6.4(c).

We highlight that the PES associated with exciton A is also displaced, albeit slightly, along the coordinate axis associated with M1, as evident from the amplitude spectra shown in Figure 6.4(d) and represented schematically in Figure 6.4(f). The PES of photocarriers (Figure 6.4(f)), on the other hand, shows much more significant displacement along both M1 as well as M2, which can also be observed in the relatively higher intensity for these modes when the pump is tuned to the carrier continuum (see Figure 6.3). This suggests that the photocarrier induces substantially larger lattice reorganization than the two excitons. This can be rationalized by considering the ionic nature of the perovskite lattice, which is subjected to stronger Coulomb potential in the presence of charged photoexcitations [58], in contrast to a globally neutral excitonic quasi-particle.

An important question is whether the modes reported in in Table 6.3 are primarily sourced by the lattice reorganization around the hole or the electron. According to Eq. 6.1, the relaxation energy is calculated from the change in the single-particle bandgap (E_g) when the atomic positions are displaced along the coordinates of the various normal modes Q_i. Using the same protocol, we can track the variations in the bandgap that are due to a shift in the valence or in the conduction band edge to assess hole and electron polaron relaxation energies, respectively. The obtained dimensionless electron-phonon couplings for holes and electrons in $(PEA)_2PbI_4$ and $(NBT)_2PbI_4$, listed on Table S1 in SI, clearly demonstrate that for $(PEA)_2PbI_4$, M1′, M2, M5 and M6, contribute to the formation of hole-polarons, while M1 and M3 contribute to the formation of electron-polarons. On the other hand, for $(NBT)_2PbI_4$, all vibrational modes are more strongly coupled to holes than electrons. The fact that changes in the electronic structure induced by reorganization of

the lattice are more pronounced for the valence band edge is not surprising. The valence band is indeed primarily composed by antibonding combination of 5p atomic orbitals from iodine and 6s orbitals from lead. Thus, any change in the relative distance and orientation of the lead and iodine ions, as induced by displacement along the inorganic lattice vibrational modes, is expected to significantly affect the wavefunction overlap and Pb-I hybridization, hence energy, of the valence band. By comparison, the conduction-band edge is instead mostly composed by 6p orbitals of lead. It does, therefore, not come as a surprise that mode M3 in $(PEA)_2PbI_4$ couples more strongly to the conduction band, as this mode is associated with the displacement of Pb ions within the PbI_6 octahedron, and that a change along this coordinate should strongly affect the atomic overlap among the 6p orbitals of lead.

6.4 Conclusion

Our analysis highlights the complex landscape encountered by a charge carriers before they relax to the excitonic states, scanning across different lattice configurations. We have already demonstrated that the exciton-phonon coupling can be tuned by the nature of the organic cation and the thickness of the quantum-well [62, 218]. In the context of growing number of custom-designed organic molecules that are being developed to template the 2D hybrid perovskite for optoelectronics, our observation garners fundamental importance to establish the optimum relaxation pathway following charge-carrier injection. We consider that the type of quantitative development of the relevant PESs is a challenging but fundamentally important task for large-scale molecular dynamics simulations that capture accurately the nonadiabatic quantum dynamics implied by this work [219, 103].

Lastly, we have unambiguously demonstrated the presence of multiple distinct excitonic transitions separated by 35 meV [62]. Our observation of vastly different spectral structures in the resonant vibrational excitation spectra effectively rules out their previous assignments to vibronic progressions [98]. It also establishes substantial and importantly

distinct polaronic character of each of the excitons. We consider that this observation strongly suggests the role of polaronic binding as at least part of the origin of the spectral fine structure, which we have considered in ref. [62]. This was initially motivated by a simple estimate of the polaron binding energy that was consistent with the energy splitting of 35[107], exchange interactions [92, 202, 220], many-body correlations [167] and based on our current observation, non-negligible yet complex polaronic effects [71].

It has been suggested in the case of bulk lead-halide perovskites that polaronic effects shield the photo-generated carriers from lossy scattering pathways involving defects, LO phonons or Auger-like processes [221, 100]. We identified a diminished polaronic character of excitons that can potentially enhance the multi-particle scattering processes. Intriguingly, in our earlier work on the multi-dimensional spectroscopy of $(PEA)_2PbI_4$, we observed signatures of bound biexcitons with different binding energies for AA and BB, with additional evidence that A-excitons also experience repulsive interactions [167]. The consequences of the nature of excitonic structure on these many-body physics are clearly critical in the context of, for example, biexciton lasing [83, 197].

6.5 Acknowledgements

A.R.S.K. acknowledges funding from EU Horizon 2020 via a Marie Sklodowska Curie Fellowship (Global) (Project No. 705874). F.T. acknowledges support from a doctoral postgraduate scholarship from the Natural Sciences and Engineering Research Council of Canada and Fond Québécois pour la Recherche: Nature et Technologies. This work is partially supported by the National Science Foundation (Award 1838276). C.S. acknowledges support from the School of Chemistry and Biochemistry and the College of Science of Georgia Institute of Technology. The work at Mons was supported by the Interuniversity Attraction Pole program of the Belgian Federal Science Policy Office (PAI 6/27) and FNRS-F.R.S. Computational resources have been provided by the Consortium des Équipements de Calcul Intensif (CÉCI), funded by the Fonds de la Recherche Scien-

tifique de Belgique (F.R.S.-FNRS) under Grant No. 2.5020.11. D.B. is a FNRS Research Director.

6.6 Methods

6.6.1 Sample preparation

For the preparation of $(PEA)_2PbI_4$ thin films (PEA = phenylethylammonium), the precursor solution (0.25 M) of $(PEA)_2PbI_4$ was prepared by mixing (PEA)I (Dyesol) with PbI_2 in 1:1 ratio in N,N-dimethylformamide(DMF). For example, 62.3 mg of (PEA)I and 57.6 mg of PbI_2 were dissolved in 500 μL of DMF (anhydrous, Sigma Aldrich). The thin films were prepared by spin coating the precursor solutions on fused-silica substrates at 4000 rpm, 30 s, followed by annealing at 100^{o}C for 30 min. The extensive structural characterization of these films are reported in our earlier works [167, 62].

6.6.2 Ultrafast differential transmission measurements

Differential Transmission spectroscopy measurements were performed using an ultrafast laser system (Pharos Model PH1-20-0200-02-10, Light Conversion) emitting 1030-nm pulses at 100 KHz, with an output power of 20 W and pulse duration of ~ 220 fs. Experiments were carried out in an integrated transient absorption/time-resolved photoluminescence commercial setup (Light Conversion Hera). Pump wavelengths in the spectral range 360–2600 nm (see Fig. S13 of SI for typical pump excitation spectra) were generated by feeding 10 W from the laser output to a commercial optical parametric amplifier (Orpheus, Light Conversion, Lithuania), while 2 W are focused onto a sapphire crystal to obtain a single-filament white-light continuum covering the spectral range $\sim 490 - 1050$ nm for the probe beam. When higher energy probe light was required, a blue white-light continuum was similarly obtained by using the second harmonic of the laser output instead. The probe beam transmitted through the sample is detected by an imaging spectrograph (Shamrock 193i, Andor Technology Ltd., UK) in combination with a multichannel detector (256 pix-

els, 200–1100-nm wavelength sensitivity range). Energy densities used vary in the range 25–1100 nJ/cm^2, most of the measurements were carried out at 215 nJ/cm^2; with a typical spot diameter of 1.9 mm estimated at the 1/e^2 plane). Beating maps and integrated spectra corresponding to these fluences are presented in Figs. S6 and S7 of SI. All measurements were carried in a vibration-free closed-cycle cryostation (Montana Instruments). We disclose that we observed a slow degradation of the sample over long exposure to the laser light. Such a process, also widely reported for three-dimensional perovskites, appears to be reversible and can be slightly negated by photo-exposing the sample for an hour prior to the experiment. While the extent of degradation is not substantial enough to make the observed trends unreliable, the shape of the excitation spectrum should nevertheless be considered only as qualitative. Nevertheless, we consider that the comparison of excitation spectrum for different modes is rigorous.

6.6.3 Density functional theory calculations

The present calculations are based on the harmonic approximation, which solely relies on the availability of realistic crystallographic models that, in the present case, are provided by established X-ray diffraction measurements [222, 8, 167]. The crystalline model is relaxed using the van der Waals corrected DFT-D2 method. The Hessian matrix of the forces is then calculated on the fully relaxed structure and diagonalized to obtain the vibrational frequencies. The calculations have been performed by adopting periodic boundary conditions and localized atomic basis set as implemented in the CRYSTAL17 program [223]. The computational set-up consists of double split quality basis sets which include polarization, along with the PBE functional for the description of the exchange-correlation [224]. An automatic 4x4x1 sampling of the first Brillouin zone was selected [225], where the less dense sampling is related to the direction associated to the inorganic-sheet stacking, in the reciprocal lattice. The Grimme-D2 approach was included, to improve the description of the atomic forces between the organic cations. The SCF accuracy has been increased to

10^{10} Hartree, to obtain accurate interatomic forces. This computational set-up has been already tested for the parental $CH_3NH_3PbI_3$ perovskite in reference [207] and resulted in DFT vibrational spectra in excellent agreement with the experimental data available.

CHAPTER 7

POLARON-DRESSING PHONONS DRIVE EXCITON DYNAMICS IN TWO-DIMENSIONAL METAL-HALIDE PEROVSKITES

The previous chapter concluded beyond any reasonable doubt that the excitons responsible for the optical fine structure in 2D-HOIPs are electronically distinct and each bear a specific polaronic character. This is a crucial piece of information with which to build a model describing these materials, but what about its impact on phenomena directly relevant to optoelectronical devices? Should the engineer be concerned at all by this discovery? In this chapter, we provide our own answer to this question by studying the relaxation dynamics of photoexcited species using time-resolved photoluminescence as well as transient absorption. We show that the relaxation dynamics depend strongly on the polaronic character of the initially excited specie. Indeed, the relaxation is simultaneously electronic *and* vibrational due to the entanglement between these two degrees of freedom caused by polaronic effects. This is not to be confused with the slow vibrational relaxation proposed in reference [98]. There, the slow relaxation is said to occur within the ladder of a *single* displaced vibrational mode. Here, based on the results from the previous chapter, we rather show the slow relaxation to arise from the relaxation between *different* vibrational modes out of which Kasha emission is observed.

This investigation of the relaxation between distinct exciton-polaron states can also help elucidate a subtle ambiguity in our previous measurements with crucial consequences on excited state relaxation dynamics. Using RICSRS, all phonon modes displaced by light absorption are excited and subsequently detected. Some displacements are common to all excited states and do not contribute to the observed polaronic diversity while others do. The former, called spectator modes, have little impact on the relaxation dynamics since the lattice doesn't need to adjust along these normal coordinates to accommodate the

relaxation between excited states. The other modes, however, must adjust for the relaxation to occur and are thus called driving modes. Using a theoretical model developed by our colleagues and the measured relative displacement given by RICSRS, we identify which of these modes are spectator modes. We cannot directly infer from this analysis that the other modes are the dominant driving modes for we have at our disposition only the displacement for modes with an energy below about 8 meV. However, by fitting the observed temperature dependence of the relaxation rates to an Arrhenius law, we present evidence that these low energy non spectator modes could indeed dominate the interexcitonic relaxation process. Thus, these vibrational modes not only dress the excitons as exciton-polarons but are also important to the excited state relaxation. This shows that the matter of exciton-polaronic effects is much more than a question of mere semantics: they dominate the hot-carrier relaxation in 2D-HOIPs. Understanding these is therefore crucial to the design of devices based on these materials.

This work was submitted to Chemistry of Materials in 2019 and can be found on the arXiv under the same title. Dr. Srimath Kandada (CNST@PoliMi, IIT and GaTech) and I are to be considered co-first authors. Dr. Srimath Kandada, Dr. Bargigia (GaTech), Dr. Valverde-Chávez (GaTech) and I acquired the transient absorption (TA) data. Dr. Srimath Kandada also acquired the time-resolved photoluminescence (TRPL). I analyzed the TRPL and TA data. Dr. Cortecchia (CNST@PoliMi, IIT) synthesized the samples and Dr. Yang (Google) performed the mode-projection calculations. The work was advised and supervised by Pr. Petrozza (CNST@PoliMi, IIT), Pr. Silva (GaTech) and Pr. Bittner (U. Houston). All authors contributed to the redaction of the manuscript and its intellectual development.

7.1 Abstract

We report on the exciton formation and relaxation dynamics following photocarrier injection in a single-layer two-dimensional lead-iodide perovskite. We probe the time evolution

of four distinct exciton resonances by means of time-resolved photoluminescence and transient absorption spectroscopies, and find that at 5 K a subset of excitons form on a $\lesssim$ 1-ps timescale, and that these relax subsequently to lower-energy excitons on $\sim$ 5–10 ps with a marked temperature dependence over $<$ 100 K. We implement a mode projection analysis that determines the relative contribution of all observed phonons with frequency $\leq$50 cm^{-1} to inter-exciton nonadiabatic coupling, which in turn determines the rate of exciton relaxation. This analysis ranks the relative contribution of the phonons that participate in polaronic lattice distortions to the exciton inter-conversion dynamics and thus establishes their role in the nonadiabatic mixing of exciton states, and this in the exciton relaxation rate.

7.2 Introduction

Hybrid organic-inorganic metal-halide two-dimensional perovskites (2D-HOIPs) have attracted considerable interest over the past two decades due to their promising optoelectronic characteristics [226, 227] and due to their structural and dynamic complexity as strongly quantum-confined materials [228, 229]. These are direct-bandgap semiconductors that are composed of two-dimensional (2D) planes of ionic metal-halide lattice layer separated by long organic cations. Thus, carriers are confined to the few-atom-thick inorganic lattice planes. Due to strong quantum [192] and dielectric [79] confinement effects, tightly bound excitons and biexcitons [81, 167, 62, 90] are primary photoexcitations. The ionic character and the softness of the lattice both lead to strong electron-phonon interactions while the localized uncorrelated motion of the organic cations leads to strong dynamic disorder [167]. Unlike other 2D semiconductors such as III-V quantum wells and transition-metal dichalcogenide monolayers, very clear spectral structure is present in the exciton absorption in this class of materials, which reflects the presence of at least four distinct exciton resonances that are evenly separated in energy [91]. We have recently demonstrated through resonant impulsive stimulated Raman spectroscopy that these multiple excitons

and photo-carirers are dressed by lattice phonons via polaronic interactions [191]. We also observed that the lattice configurations of the excited states (free carriers and multiple excitons) are displaced along specific and distinct lattice coordinates, predominantly involving motion within the two-dimensional lead iodide layer. This suggests a complex scenario for carrier relaxation and exciton formation where excitation dynamics may be driven by specific lattice phonons that also participate in the lattice polaronic reconfiguration. Here, we address the role of the phonon modes that dress the exciton-polarons in the exciton relaxation dynamics and differentiate between active *driving* modes from passive *spectator* modes.

We employ temperature-dependent transient absorption and time-resolved photoluminescence spectroscopies on $(PEA)_2PbI_4$ (PEA = phenylethylammonium), a prototypical 2D-HOIP. We use a mode projection scheme [230, 231, 232, 233], in which experimentally measured phonon frequencies and Huang-Rhys parameters [191] are used to construct the smallest possible subspace of modes that optimizes the electron-phonon coupling that drives exciton dynamics. We find that a subset of three modes is sufficient to reproduce the experimentally measured electron-phonon coupling parameters, and we link these to the formation dynamics of the lowest-energy exciton on picosecond timescales. We, therefore, conclude that these specific modes drive the exciton formation dynamics, with the rest of the polaronic dressing modes playing a spectator role. With this analysis, we highlight the correlation between the phonon dynamics that define exciton polarons and photo-excitation relaxation dynamics following hot carrier injection, which is of fundamental importance in light-emitting diodes and related optoelectronic technologies.

7.3 Results and Analysis

7.3.1 Linear Spectroscopy

The absorption and time-integrated photoluminescence (PL) spectra of a polycrystalline film of single-layer $(PEA)_2PbI_4$ at a temperature of 5 K are presented in Figure 7.1. We

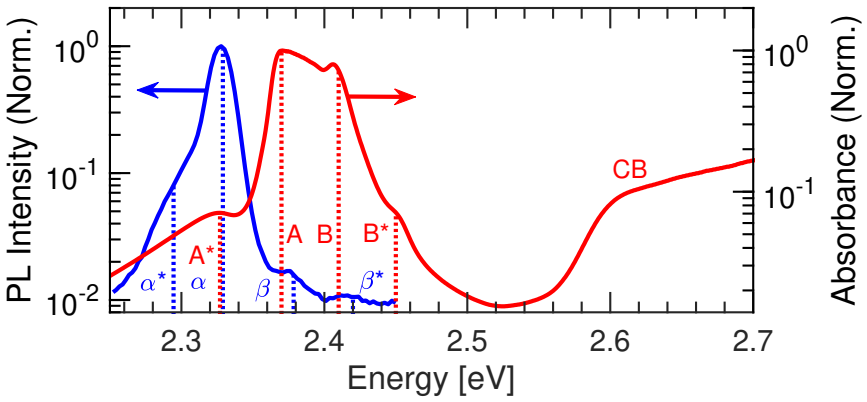

Figure 7.1: **Low temperature absorption and photoluminescence spectra of single-layer $(PEA)_2PbI_4$.** Normalized absorption (red) and time-integrated photoluminescence (PL) intensity (blue) of a polycrystalline film of single-layer $(PEA)_2PbI_4$ at a temperature of 5 K. Features in the PL spectrum are labelled by blue Greek characters while those in the absorption spectrum are labelled by red Latin characters. Their spectral positions are denoted by dotted lines of the appropriate color. We note that the PL spectrum is not corrected for the experimental spectral response.

have reported the complete structural and optical characterization of this material elsewhere [167, 62]. Four distinct transitions (labelled A*, A, B and B*) are observed in the absorption spectrum, with the most intense resonance (A) peaked at 2.36 eV, which is 253 meV below a sharp continuum band edge (labelled CB) [62]. Four features (labelled α*, α, β and β*) are also observed in the PL spectrum, and are red-shifted by approximately 35 meV from their associated peaks in the absorption spectrum. The relative intensity of these peaks differs from those observed in the absorption spectrum, indicating inter-species relaxation before the population of the final emissive states. To probe these exciton dynamics, we performed transient absorption (TA) and time-resolved photoluminescence (TRPL) spectroscopies.

7.3.2 Exciton formation and decay dynamics

We first focus on dynamics observed in TRPL at a temperature of 5 K upon injection of hot carriers by tuning the pump energy to 3.06 eV, displayed in Figure 7.2(a). The four transitions identified in the time-integrated PL spectrum are also observed, but with con-

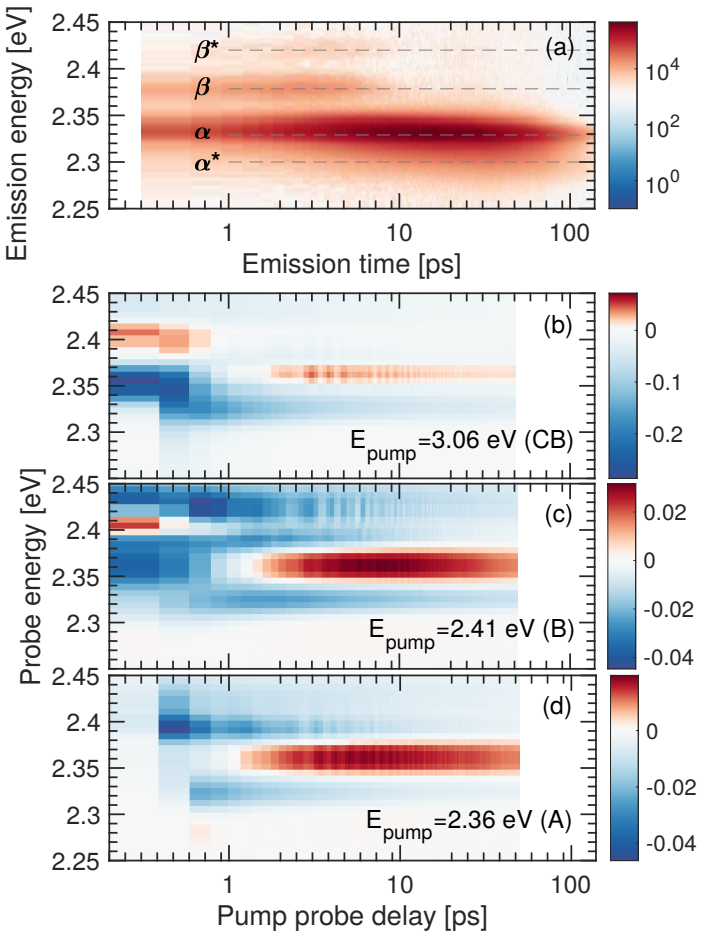

Figure 7.2: **Time-resolved photoluminescence and transient absorption spectroscopy of single-layer $(PEA)_2PbI_4$ at low temperature.** (a) Time-resolved photoluminescence intensity of the sample at 5 K under low excitation fluence. The features identified in Fig. 7.1 are indicated by dotted lines and labelled accordingly. Time-resolved differential transmission ($\Delta T/T$) spectra measured at 5 K at a constant pump photon flux of (4.32×10^{11} photons/cm^2) when pumping (a) hot carriers into the CB, (c) exciton B, or (d) exciton A.

trasting temporal evolution. Within the picosecond time resolution of our instrument, we observe prompt formation of features β and β*, and they decay on a longer picosecond timescale, concomitant with a rise of feature α, followed by feature α*. We note that this TRPL behavior is consistent with that reported previously [98].

We observe related dynamics in corresponding TA measurements upon pumping at 3.06 eV and probing the exciton bleach spectral region. The differential transmission ($\Delta T/T$) spectrum under these conditions is shown in Figure 7.2(b). In general, the transient bleach lineshape in HOIPs is dominated by carrier thermalization [234, 235], exciton-

screening mechanisms [236], and photoinduced changes of the permittivity function [237], so we refrain from mapping the bleach lineshape onto the linear spectrum. We note, however, that a positive feature with instrument-limited rise time at a probe photon energy of 2.45 eV decays on sub-picosecond timescales, concomitant with the evolution of an initially negative feature at a probe energy of 2.36 eV into a longer-lived positive component. We also highlight a negative differential transmission feature at a probe energy of 2.32 eV, which rises within hundreds of femtoseconds and monotonously decays over tens of picoseconds. We note the similarity in the timescale of the transient behavior of the feature at 2.36 eV in the TA spectrum with the rise time of the α peak in Fig 7.2(a). We also associate the decay of the 2.32-eV negative signal in Figure 7.2(b) with that of the β peak in Figure 7.2(a).

We examine further the TA spectral features by resonantly exciting the two main excitonic transitions, namely pumping exciton B or A. These TA spectra are presented in Figure 7.2(c) and (d), respectively. Upon pumping exciton B, we observe similar temporal evolution at 2.36 eV, namely an initially negative signal that evolves into a positive signal with a time constant of several picoseconds. On the other hand, when we pump exciton A resonantly, we only observe the corresponding rise of a positive signal at that probe energy. This supports the conjecture that the dynamics at this probe energy represent the B $\rightarrow$ A exciton conversion, and can be associated with the dynamics of the β peak in TRPL. We also note that the relaxation dynamics probing at 2.32 eV are weakly dependent on whether we excite into the conduction band or either exciton.

The picture that emerges from Figure 7.2 is that upon injection of hot photocarriers at a temperature of 5 K, these recombine to populate excitons B and B* within ~ 1 ps. These excitons feed excitons A and A* over several picoseconds, and the resulting population decays on tens of picoseconds. We next consider the decay dynamics of the transient feature at 2.32 eV given its omnipresence at all three pump energies. Given non-exponential decay behavior, we plot the inverse half-life as a function of pump energy. The decay-rate depen-

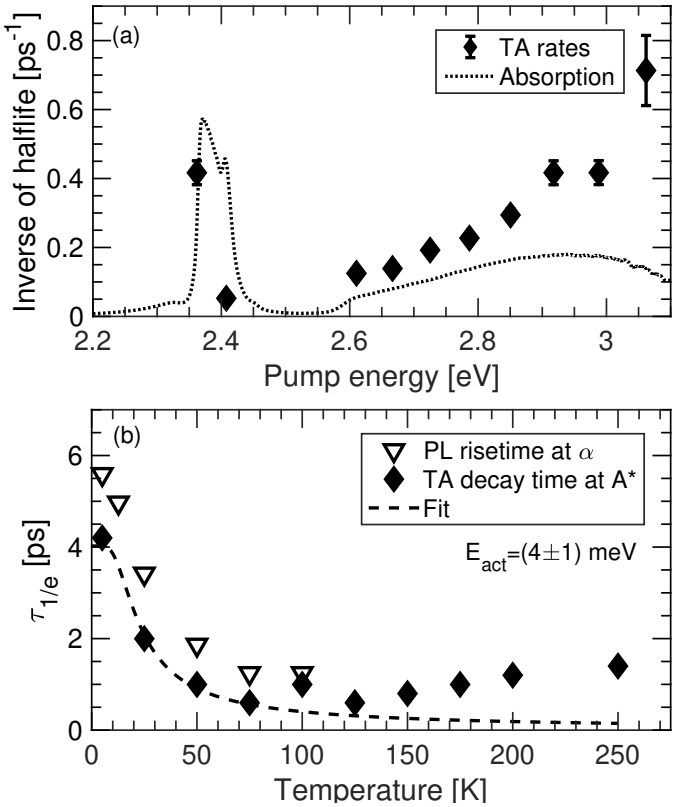

Figure 7.3: **Pump energy and temperature dependence of transient absorption and photoluminescence dynamics of single-layer $(PEA)_2PbI_4$.** (a) Inverted half-life of the 2.32-eV TA trace (filled diamonds) compared with the absorption spectrum (dotted line). The uncertainties represent the time resolution of our measurements (200 fs). (b) Dependence of the lifetime of the 2.32-eV TA feature on sample temperature at a pump energy of 3.06 eV. Plotted alongside is the rise time of the α TRPL feature when pumped at the same energy. The dotted line represent the best fit of the rate model described in the text.

dence on pump energy at 5 K is presented in Figure 7.3(a), along with the low-temperature absorption spectrum for comparison. The decay rates increase monotonously with increasing excess energy above the continuum band edge. This pump-energy dependence is consistent with carrier cooling dynamics driven by phonon scattering. We highlight that even at this low temperature, the relaxation time ranges from $\sim$ 1.5 ps at the highest probed energy to $\sim$ 20 ps near the bandedge. Such rapid relaxation dynamics are unsurprising in a semiconductor in which electron-phonon coupling is strong. Strikingly, when pumping resonantly exciton B, the decay rate is about an order of magnitude lower than that upon resonant pumping of exciton A. This marked pump excitation spectrum reveals that the

exciton decay rate depends strongly on the nature of the vertical excitation: pumping into the conduction band reflects a pump energy dependence that is consistent with hot carrier relaxation [238, 239], while excitons that are pumped resonantly display clear spectral structure on the decay rate. Given the resonant exciton-phonon coupling excitation spectrum reported in Ref. [191], this implies that excitons are locked depending on the polaronic nature of the vertical excitation.

The temperature dependence of the $1/e$ decay time of the same 2.32-eV TA feature upon 3.06-eV excitation is plotted in Figure 7.3(b). This decay lifetime exhibits a non-trivial behavior, first decreasing with increasing temperature before reaching a minimum around 100 K and then slowly rising again up to room temperature. In order to gain deeper insights into the dynamics at play following hot carrier photoexcitation, we also plot the temperature dependence of the rise time of feature α in TRPL in Figure 7.2(a), defined as the time taken for the signal to reach 90% of its maximum value from 10% of that value. This rise time qualitatively follows that of the 2.32-eV transient decay time over the probed temperature range. Under these excitation conditions, we thus assign the decay of this TA feature with the rate of B $\rightarrow$ A exciton interconversion. Supposing that this process is thermally activated, we fit the low temperature (< 150 K) decay time $\tau_{1/e}$ with an inverted Arrhenius equation which reads

$$\tau_{1/e} = \left[C \exp\left(-\frac{E_{\mathrm{act}}}{k_B T} \right) + \Gamma_0 \right]^{-1}, \tag{7.1}$$

where E_{act} is the activation energy of the interconversion process, C is a proportionality constant, T is the temperature, k_B is the Boltzmann constant and Γ_0 is the zero-temperature rate. From this, we extract an activation energy of 4 ± 1 meV, which is close to the energies of low-frequency phonons observed by vibrational coherences identified on top of the TA dynamics [191]. Those coherences involve phonons characterized by octahedral twist coupled to Pb—I—Pb bending motion, as well as Pb displacement coupled Pb—I—Pb

bending. This suggests that the lattice motion coupled distinctly to excitons A and B [191] are involved in driving the exciton interconversion dynamics.

In this section, we have exploited the apparent correlations between the rise time of feature α in TRPL with the decay time of feature near the A* absorption (2.32 eV) in TA to interpret the dependence dynamics of the A* exciton on pump energy. From the TRPL measurement presented in Figure 7.2(a), we deduced that excitons cascade from the conduction band into exciton B* and then trickle down the excitonic ladder until they reach exciton A*. Therefore, the rise time of feature α in TRPL corresponds to the time taken by B excitons to transfer to state A. Based on this and the matching dependencies of feature A* in TA and α in TRPL, we interpret the former as being related to transfer of excitons from state B to A. According to the pump energy dependence of the decay time of these features, we conjecture that the polaronic character of the excited transition dictates the transfer rate.

7.3.3 Mode projection analysis

We now examine more rigorously the mechanistic role that these lattice dynamics play in the conversion of exciton B $\rightarrow$ A. Our approach involves a simplified model that consists of a system with electronic states $|A\rangle$ and $|B\rangle$ coupled to a set $\mathbf{Q}$ of phonon modes $\mathbf{q}$ using as input experimental mode frequencies and Huang-Rhys factors reported in reference [191]. We represent the electron-phonon coupling by the compact notation

$$\mathbf{g}_i \cdot \mathbf{Q} = \sum_q \frac{g_{iq}}{2} \left(a_q^\dagger + a_q \right), \tag{7.2}$$

where $\mathbf{g}_i$ are the linear force vectors due to electrons acting on the lattice, g_{iq} are coupling constants, $a_q^\dagger$ and a_q are phonon creation and annihilation operators, respectively, and $[a_{q'}, a_q^\dagger] = \delta_{qq'}$. In general, these are referenced to a particular electronic energy minimum. For the case at hand, we use the electronic ground-state whereby the modes $\mathbf{q}$ are measured

and assigned by a ground-state density-functional-theory calculation and the couplings by the experimental relative Huang-Rhys factors λ_{iq} such that $g_{iq}^2 = (\hbar\omega_q)^2\lambda_{iq}$ [191]. The model Hamiltonian then reads

$$\begin{aligned} H &= \begin{bmatrix} \epsilon_A & V_{ab} \\ V_{ab}^* & \epsilon_B \end{bmatrix} + \begin{bmatrix} \mathbf{g}_A \cdot \mathbf{Q} & 0 \\ 0 & \mathbf{g}_B \cdot \mathbf{Q} \end{bmatrix} \\ &+ \sum_q \hbar\omega_{1q} \left(a_q^\dagger a_q + \frac{1}{2} \right), \end{aligned} \tag{7.3}$$

where $\epsilon_{A(B)}$ is the energy of exciton A (B) and V_{AB} is the phonon-mediated nonadiabatic coupling term for excitons A and B. The second term in Eq. 7.3 contains the electron-phonon couplings in Eq. 7.2, and the third term accounts for the vibrational energy and sums over all the relevant phonons $\mathbf{q}$. By diagonalizing this Hamiltonian, the role of V_{AB} is to mix the diagonal states A and B, which is a necessary ingredient in the radiationless transition B $\rightarrow$ A. Physically, the spectrum of phonon-driven fluctuations in V_{AB} gives rise to a so-called spectral density [240, 39]

$$S_{BA}(\omega) = \int_{-\infty}^{\infty} \mathrm{d}t\, e^{-i\omega t} C_{BA}(t), \tag{7.4}$$

where

$$C_{BA}(t) = \left\langle \sum_q \hat{V}_{ABq}(t) \hat{V}_{BAq}(0) \right\rangle \tag{7.5}$$

is the autocorrelation function of the polaron-transformed electron-phonon coupling operator in the Heisenberg representation, where $\langle \cdots \rangle$ denotes a thermal average. The function $C_{BA}(t)$ thus contains all the information on the nonadiabatic coupling of states A and B due to the ensemble of phonons $\mathbf{q}$. We will evaluate this function as a means to examine the role of polaronic-dressing phonons found in Ref. [191]. The explicit form for the kernel in Eq. 7.4 is quite lengthy and is given in Refs. [231] and [241].

At the adiabatic transition frequency $\tilde{\omega}_{BA}$, Eq. 7.5 produces the golden-rule B $\rightarrow$ A transition rate constant,

$$k_{BA} = \lim_{\tau \to \infty} 2\mathrm{Re} \int_0^\tau \mathrm{d}t \, C_{BA}(t) e^{-i\tilde{\omega}_{BA}t}. \tag{7.6}$$

However, given that the absolute value of the experimental Huang-Rhys factors is unknown, our analysis does not produce the diabatic coupling (or mixing angle) needed to directly compute this rate constant, so we will restrict our analysis to the evaluation of Eq. 7.5, which will permit quantitative examination of the role of specific phonons in the exciton dynamics reported above.

In general, the sum in Eq. 7.5 spans all phonon modes, $\mathbf{Q} = \{q_1, q_2, \cdots, q_N\}$. Insight can be gained by analyzing which of these give the most important contributions to the conversion of exciton B to A. For this, we use the "mode-projection" approach developed by Bittner *et al.*, which uses a Lanczos projection scheme to construct the smallest possible subspace which optimizes the electron-phonon coupling. The result is a list of modes $\mathbf{Q}_{\mathrm{opt}} = \{q_a, q_b, q_c, \cdots\}$ ranked according to their electronic coupling. We can then calculate the correlation function $C_{BA}(t)$ and spectral density $S_{BA}(\omega)$ with these new modes. Including all the modes gives the exact correlation function. However, we gain insight into the dynamics of the transition by comparing the convergence with respect to the number of modes included in the summation in Eq. 7.5. This analysis does not depend upon the diabatic coupling for Hamiltonians in which the off-diagonal term is independent of the phonon coordinates [230, 233, 231, 232], and therefore does not necessitate knowledge of the *absolute* Huang-Rhys parameters.

In Figure 7.4, we show the results of the projection analysis, showing the three dominant contributions to the electronic coupling modes (ECM) to Eq. 7.4, with ECM1 $>$ ECM2 $>$ ECM3. For consistency, we shall refer to the lattice motions according to our recent work in Ref. [191] with added subscripts to mode M1 to account for its fine structure. First, the

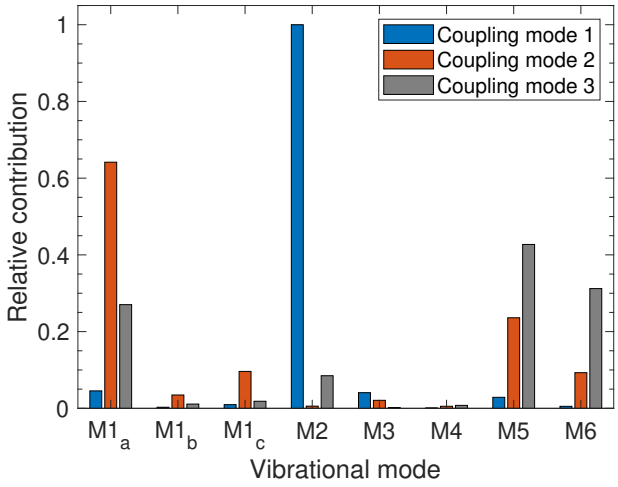

Figure 7.4: **Electronic coupling modes projected onto the vibrational mode basis ranked according to their contribution to the electronic coupling from exciton B to A.** The labeling scheme is chosen to be consistent with Ref. [191] with the addition of subscripts to mode M1 to account for its fine structure.

highest-ranked mode ECM1 is dominated by a phonon (M2) characterized by an octahedral twist and Pb–I–Pb bending. In Ref. [191], we identified this as a dominant mode driving phonon coherences resulting from resonant, impulsive excitation of exciton A. The second-ranked mode ECM2 is dominated by a combination of normal modes M1 (octahedral twist along one of the two pseudocubic axes of the inorganic sheet), M5 (Pb–I–Pb bending and P–I stretching), and M6 (scissoring of Pb–I–Pb angle), with a more modest contribution of M2. Finally, the third-rank mode ECM3 is dominated by normal modes M1, M5 and M6 similar to ECM2.

The correlation function (Eq. 7.5) obtained by including one, two, three or all of the dominant ECMs is presented in Figure 7.5. Over the first cycle, one mode (ECM1) is sufficient to reproduce the exact correlation function obtained by inclusion of all modes but quickly becomes insufficient at longer times. Inclusion of the three dominant ECMs does reproduce the exact function, and, therefore, the exact spectral density.

On the face of this analysis, it would seem that the exciton B $\rightarrow$ A dynamics are primarily driven by the M2 motion with other modes largely playing a spectator role by accom-

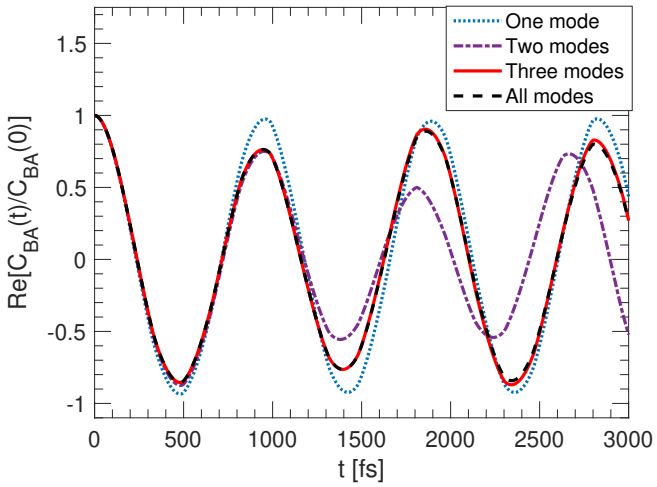

Figure 7.5: **Real part of the normalized correlation function between exciton B and A** when one, two, three or all electronic coupling modes are considered.

modating the associated energy change [230, 233, 231, 232]. Nevertheless, the inclusion of all phonons, but predominantly M1, and M5, and M6, is necessary to reproduce the exact spectral density. Polaronic dressing phonons for excitons A and B therefore play active roles to a varying degree in driving inter-conversion dynamics in a way that is ranked according to Figure 7.4.

7.4 Discussion

In the previous section, we have reported that upon hot photocarrier injection at 5 K, exciton B, as labelled in Figure 7.1, is populated on a sub-picosecond timescale, and that it feeds the population of exciton A within < 10 ps. We have furthermore addressed whether phonons identified via coherences resulting from impulsive stimulated Raman processes on top of the TA dynamics are spectator modes or whether they drive the observed exciton inter-conversion dynamics. We have concluded that the polaronic-dressing phonon modes drive exciton inter-conversion, with a dominant contribution of an in-plane phonon mode with frequency 35 cm^{-1}, involving combined octahedral twist and Pb—I—Pb bending [167]. This conclusion highlights the role of exciton-phonon coupling, which we have

previously ascribed to the polaronic nature of excitons in 2D-HOIPs [62], in their relaxation dynamics. Given that the thermal activation energy for the B $\rightarrow$ A inter-conversion matches the energies of the driving phonons, and that these phonons are known to dress excitons A and B distinctly [191], we put forth here that polaronic modes not only dominate the vibrational coupling between excitons, but are the ones driving the inter-exciton conversion process. We underline that without knowledge of the absolute Huang-Rhys factors for each modes, it is not possible to assess their absolute contribution to the B $\rightarrow$ A excitonic inter-conversion rate as required in Eq. 7.6. Nonetheless, using the mode projection analysis permits us to establish the active role of polaronic modes on exciton dynamics with confidence. This conclusion is supported by the observation that if such an interconversion process is driven by phonons, one expects the process to have a corresponding activation energy as we observe here.

Importantly, a previous report on TRPL measurements on 2D-HOIPs at low temperature revealed similar step-like temporal evolution as the one presented in Figure 7.2(a) [98]. In that work, the spectral fine structure was interpreted as a vibronic progression from a single excitonic state. This led the authors to interpret the short-time PL decay as the non-Kasha emission of population relaxing down a unique vibrational manifold associated with the exciton. That interpretation was able to rationalize the spectral ineshape and dynamics. While this is certainly plausible given the early-time lineshape, we might expect that the excitation spectrum would be described within a Franck-Condon progression incorporating relevant optically active modes [191], which should be manifested throughout the excitation profile. In Ref. [191], we show that over a frequency range $\leq 50\,\mathrm{cm}^{-1}$, excitons A and B show markedly different coupling to phonons, which would not be the case if they are vibronic replicas of a single exciton, where the displacement along each vibrational coordinate would be invariant. For the purposes of the analysis presented above, we therefore conclude that each spectral feature in Figure 7.1 is a distinct exciton as we proposed in Ref. [62] and concluded in Ref. [191]. This perspective is supported by the cumula-

tive observations that excitons A and B have distinct biexciton spectral structure [167]. Indeed, if distinct excitons are dressed differently by phonons, this difference should also be manifested in the resulting composite multi-particle binding energy, whereas a single exciton reflected in a vibronic progression should not display distinct binding energies by the phonon replicas.

We consider that polaronic effects determine in a more general way the exciton dynamics in 2D-HIOPs. In a separate work, we argued that polaronic effects also play an important role in modulating exciton many-body quantum dynamics [242], although for different reasons as those presented in this paper. Many-body quantum dynamics are mediated by the electron-hole Coulomb field produced between excitons, which is dynamically screened by polaronic coupling. We have proposed that this polaronic protection mechanism is responsible for the weakening of exciton-exciton elastic scattering processes by two-to-three orders of magnitude compared to other monolayer two-dimensional materials that are not strongly polaronic [242]. Our view from that separate work is that polaronic effects are instrumental to attenuate long-range Coulomb-mediated elastic scattering. In contrast, here we argue that the phonon modes that are active in the long-range polaronic screening of excitons, in fact, are also key in the nonadiabatic electronic dynamics of the system, driving transitions from one electronic state to another.

The conclusions reached in this paper concerning the mechanism behind the relaxation dynamics of photoexcitations are far-reaching for the design of high-efficiency lasers and light-emitting diodes using this class of materials. Knowledge of the relaxation and recombination mechanism of injected carriers to form the emissive state is of central fundamental importance, particularly concerning the role of lattice coupling in the nonadiabatic relaxation dynamics. This report provides strong evidence of the importance of polaronic effects in this broad class of materials. Not only do they lead to a distinct dressing of photocarriers by the lattice modes [191], modulate exciton [62] and biexciton [167] binding energies, and screen them from many-body interactions [242], but they also drive their relaxation

dynamics. Our view is that the consequences of polaronic effects on excitonic properties of 2D-HOIPs is clear, but we have limited understanding regarding the mechanism behind this distinct polaronic nature, and indeed, the extent to which polaronic effects fundamentally give rise to multiple excitons via diverse polaron-free-carrier correlation, or whether the multiple excitons merely reflect distinct polaronic character for other reasons. This chicken-and-egg question should be central to the fundamental spectroscopic and theoretical investigation of excitons in 2D-HOIPs.

7.5 Methods

7.5.1 Sample preparation

For the preparation of $(PEA)_2PbI_4$ thin films (PEA = phenylethylammonium), the precursor solution (0.25 M) of $(PEA)_2PbI_4$ was prepared by mixing (PEA)I (Dyesol) with PbI_2 in 1:1 ratio in N,N-dimethylformamide(DMF). For example, 62.3 mg of (PEA)I and 57.6 mg of PbI_2 were dissolved in 500 μL of DMF (anhydrous, Sigma Aldrich). The thin films were prepared by spin coating the precursor solutions on fused-silica substrates at 4000 rpm, 30 s, followed by annealing at 100°C for 30 min. The extensive structural characterization of these films are reported in our earlier works [167, 62].

7.5.2 Ultrafast differential transmission measurements

Differential Transmission spectroscopy measurements were performed using an ultrafast laser system (Pharos Model PH1-20-0200-02-10, Light Conversion) emitting 1030-nm pulses at 100 KHz, with an output power of 20 W and pulse duration of $\sim$ 220 fs. Experiments were carried out in an integrated transient absorption/time-resolved photoluminescence commercial setup (Light Conversion Hera). Pump wavelengths in the spectral range 360–2600 nm were generated by feeding 10 W from the laser output to a commercial optical parametric amplifier (Orpheus, Light Conversion, Lithuania), while 2 W are focused onto a sapphire crystal to obtain a single-filament white-light continuum covering the spec-

tral range $\sim 490 - 1050$ nm for the probe beam. The probe beam transmitted through the sample was detected by an imaging spectrograph (Shamrock 193i, Andor Technology Ltd., UK) in combination with a multichannel detector (256 pixels, 200–1100-nm wavelength sensitivity range). Energy densities used vary in the range 25–1100 nJ/cm^2, most of the measurements were carried out at 215 nJ/cm^2; with a typical spot diameter of 1.9 mm estimated at the $1/e^2$ plane). All measurements were carried in a vibration-free closed-cycle cryostation (Montana Instruments).

7.5.3 Time resolved Photoluminescence measurements

Time-resolved Photoluminescence spectroscopy was performed using tunable Ti:sapphire oscillator (Coherent Chameleon) operating at 800 nm, 80 MHz and an output pulsewidth of 150 fs. The pump pulses at 400 nm were generated by frequency doubling the fundamental output in a BBO crystal. The sample was kept in a continuous-flow static exchange gas cryostat (Oxford Instruments) to enable temperature-dependent experiments. The PL from the samples was collected and dispersed by a spectrometer (Princeton Instruments) and coupled into a Streak Camera (Hamamatsu). The maximum available time resolution is approximately 2–3 ps.

CHAPTER 8

ENHANCED SCREENING AND SPECTRAL DIVERSITY IN MANY-BODY ELASTIC SCATTERING OF EXCITONS IN TWO-DIMENSIONAL HYBRID METAL-HALIDE PEROVSKITES

From now onwards in this thesis, we tackle the question of many-body interactions in 2D-HOIPs beginning in this chapter with elastic scattering between exciton-polarons and other quasiparticles. The conceptual image of a large polaron is one of a charge carrier surrounded by a cloud of optical phonons. These waves of oscillating dipoles should therefore react to external fields as well, screening the charge carrier. This picture is that of the polaronic protection effect mentioned in section 2.5.2 and yields a reduction of the exciton-polaron's binding energy by screening the Coulomb field between an exciton's electron and hole [71]. Similarly, this effect should have a similar consequence on the Coulomb mediated scattering of exciton-polarons with other quasiparticles. Moreover, due to the distinct polaronic character of excitons in 2D HOIPs, it should affect each of those in a discernible way. As stated in section 2.2.3, elastic scattering leads to the decoherence of an exciton's wavefunction with time and increases its homogeneous linewidth. In this chapter, we measure this parameter as a function of exciton density and phonon population to investigate polaronic effects on elastic many-body interactions. This is done using power and temperature dependent two-dimensional spectroscopy with a rephasing pulse sequence.

The first conclusion emerging from these measurements should be no longer a surprise at this point. The intrinsic linewidths of each excitons are distinct, further confirming their distinct electronic character but are however comparable, each between 2 and 3 meV. Their exciton-exciton interaction parameters, however, differ by almost as much as a factor of two. Moreover, these interactions parameters are all about three orders of magnitude lower than that of excitons in monolayers of WSe_2, a 2D covalent excitonic semiconductor. Com-

pared to this semiconductor where the excitons are known to be non-polaronic, excitons in 2D HOIPs seem protected against many-body interactions. Moreover, the strength of this protection strongly differs from one exciton to the other. We attribute this observation to exciton-polaronic effects since we know each exciton bears a distinct polaronic character and that polaronic effects should lead to the screening of Coulomb fields outside the polaronic radius. The scattering off lattice phonons, however, seems to be on par with that in WSe_2 despite the ionic nature of the bonds in 2D-HOIPs. We hypothesize this to be a consequence of polaronic protection effects. The Coulomb field arising from optical phonons outside the polaronic radius could be screened by the polaronic cloud and therefore reduce their interaction with the excitons within it.

This publication is the last one of this thesis explicitly dedicated to the consequences of the polaronic nature of excitons on the photophysics of 2D-HOIPs. With the preceding three chapters, a solid case is made that excitons are more than electronically distinct excitons with contrasting lattice-coupling: they are exciton-polarons from their coupling with the lattice to their many-body interactions.

This work was submitted for publication in Physical Review: Research in 2019 and can be found in the arXiv under the same name. I performed the two-dimensional measurements and analyzed them and Dr. Cortecchia (CNST@PoliMi, IIT) synthesized the samples. The work was advised and supervised by Pr. Petrozza (CNST@PoliMi, IIT), Pr. Silva (GaTech) and Dr. Srimath Kandada (CNST@PoliMi, IIT and GaTech). All authors contributed to the redaction of the manuscript and its intellectual development.

8.1 Letter

In two-dimensional hybrid organic-inorganic metal-halide perovskites, the intrinsic optical lineshape reflects multiple excitons with distinct binding energies [104, 62], each dressed differently by the hybrid lattice [191]. Given this complexity, a fundamentally far-reaching issue is how Coulomb-mediated many-body interactions — elastic scattering

such as excitation-induced dephasing [126], inelastic exciton bimolecular scattering [243], and multi-exciton binding [45, 167] — depend upon the specific exciton-lattice coupling. We report the intrinsic and density-dependent exciton pure dephasing rates and their dependence on temperature by means of a coherent nonlinear spectroscopy. We find exceptionally strong screening effects on multi-exciton scattering relative to other two-dimensional single-atomic-layer semiconductors. Importantly, the exciton-density dependence of the dephasing rates is markedly different for distinct excitons. These findings establish the consequences of particular lattice dressing on exciton many-body quantum dynamics, which critically define fundamental optical properties that underpin photonics and quantum optoelectronics in relevant exciton density regimes.

Spectral transition linewidths provide pertinent insights into the system-bath interactions in materials because they depend on optical dephasing dynamics — the processes by which the coherence that the driving electromagnetic wave imparts on the optical response dissipates due to scattering processes with lattice phonons, other excitations, and defects. Dephasing rates thus are very sensitive probes of the consequences of lattice dressing effects on excitons. Nevertheless, these are challenging to extract directly from linear optical probes such as absorption or photoluminescence spectroscopy given that the experimental linewidths typically arise from two distinct but co-existing contributions: homogenous and inhomogenous broadening (see Figure 8.1a). While the former is due to dephasing and is governed by the intrinsic finite lifetime of excited states and by dynamic disorder, the latter is caused by a statistical distribution of the transition energy due to static disorder, defects or grain boundaries. The exciton homogeneous linewidth 2γ (full width at half maximum) is limited by the exciton lifetime (Γ^{-1}) and the dephasing rate mediated by exciton-exciton elastic scatterting (excitation-induced dephasing, $\gamma_{\mathrm{EID}}/\hbar$) and phonon scattering ($\gamma_{\mathrm{ph}}/\hbar$):

$$\gamma = \frac{\hbar\Gamma}{2} + \gamma_{\mathrm{EID}} + \gamma_{\mathrm{ph}}. \tag{8.1}$$

An accurate estimate of γ is thus crucial to quantify the magnitude of the inter-exciton and exciton-phonon scattering cross-sections, which, in turn, influence the radiative rates and transport characteristics. Exciton-density-dependent transient photobleach linewidth analysis has been applied to address time-dependent lineshapes in a 2D hybrid perovskite [244]. However, it is challenging to separate homogeneous dephasing effects from other $\vec{k}$-space-filling density effects by this means, and therefore to rigorously quantify γ. Here, we implement a nonlinear coherent spectroscopy to unambiguously extract the homogeneous dephasing rates of the various excitonic transitions in a polycrystalline thin film of single-layered $(PEA)_2PbI_4$ (PEA = phenylethylammonium). Figure 8.1b shows the linear absorption spectrum measured at 5 K. Four distinct excitons (labelled A, A′, B and B*) are observed about 200 meV below the continuum band edge (see Supporting Information Figure S1 for the temperature-dependent absorption spectra). We quantify γ as a function of exciton density and temperature and find that these different excitons display peculiar many-body phenomena.

Four-wave-mixing spectroscopies measure coherent emission due to a third-order polarization induced in matter by a sequence of phase-locked femtosecond pulses, and its dissipation reports directly on dephasing processes. In a two-dimensional coherent excitation geometry, one spectrally resolves this signal, and a 2D spectral correlation map of excitation/emission energies is constructed by time resolving the four-wave-mixing spectrum along a coherent excitation time variable and by Fourier transformation of the resulting coherence decay function. The absorption/emission diagonal axis thus contains the individual exciton resonances identified in the linear absorption spectrum, with any off-diagonal cross peaks displaying spectral correlations between them. With so-called rephasing phase matching, this 2D lineshape permits separation of the homogeneous and inhomogeneous contributions to the optical linewidth. Specifically, if the homogeneous and inhomogeneous linewidths are comparable, which is the case for $(PEA)_2PbI_4$ [167, 62], the anti-diagonal

lineshape is [122, 123]

$$S_{AD}(\omega_{ad}) = \left| \frac{\exp\left(\frac{(\gamma - i\omega_{ad})^2}{2\delta\omega^2}\right) \text{erfc}\left(\frac{(\gamma - i\omega_{ad})}{\sqrt{2}\delta\omega}\right)}{\delta\omega(\gamma - i\omega_{ad})} \right|, \tag{8.2}$$

while the diagonal one reads as

$$S_D(\omega_d) = \sum_j \alpha_j \left| \frac{\exp\left(\frac{(\gamma - i(\omega_d - \omega_j))^2}{2\delta\omega^2}\right)}{\gamma\delta\omega} \right.$$
$$\left. \times \left[\text{erfc}\left(\frac{(\gamma - i(\omega_d - \omega_j))}{\sqrt{2}\delta\omega}\right) + \exp\left(\frac{2\gamma i(\omega_d - \omega_j)}{\delta\omega^2}\right) \text{erfc}\left(\frac{(\gamma + i(\omega_d - \omega_j))}{\sqrt{2}\delta\omega}\right) \right] \right|. \tag{8.3}$$

Here erfc corresponds to the complementary error function, ω_{ad} and ω_d are the anti-diagonal and diagonal angular frequencies, respectively, and $\delta\omega$ characterizes the inhomogeneous distribution. The sum in equation 8.3 runs over the relative amplitudes α_j and the central diagonal energies ω_j of optical transitions of excitons A, A′, B and B*.

The laser spectrum used in this experiment, which covers all excitonic absorption features, is displayed in Figure 8.1b. The zero-population-time 2D map of the absolute value of the rephasing signal from $(PEA)_2PbI_4$ at 5 K and a fluence of 40 nJ/cm^2 (excitation density 8.8×10^{18} cm^{-3} or 3.5×10^{13} cm^{-2}) is shown in Figure 8.1c. A schematic of our pulse sequence for this experiment is displayed in Figure S2, Supplemental Information, and the corresponding real components for different fluences are shown in Figure S3, as are details on the excitation density calculation. Four features are observed elongated along the diagonal axis, corresponding to excitons A, A′, B and B*. Faint cross-peaks between all excitonic features are also observed, indicating that all the transitions share a common ground state. An intense cross peak at an emission energy of 2.305 eV is observed for exciton A despite the presence of a much weaker diagonal feature at lower energy than that dominant peak. Given the opposite phase of this feature (the real part of the spectra shown in

Supplemental Information Figure S3) when compared to the corresponding diagonal peak, we attribute it to an excited-state absorption from a singly bound A exciton to a bound AA biexciton [167].

The diagonal and anti-diagonal cuts at the energies of excitons A, A′ and B, along with the best fits to equations 8.3 and 8.2, are plotted in Figure 8.2a, b and c respectively. The only fit parameters are the amplitudes α_j, homogeneous dephasing width γ and inhomogeneous width $\delta\omega$ of each optical transition.

To assess the contribution of many-body interactions on the dephasing dynamics of the different excitons, we acquired 2D coherent excitation spectra for a wide range of excitation fluences and sample temperatures (see Figure S4 and S5 of Supplemental Information for the raw data used here). The monotonic rise of γ with the excitation fluence at 5 K is shown in Figure 8.3. Such a dependence on exciton density n is a consequence of broadening induced by exciton-exciton elastic scattering mediated by long-range Coulomb interactions:

$$\gamma_{\mathrm{EID}}(n) = \gamma_0 + \Delta \cdot n. \tag{8.4}$$

Here, γ_0 is the density-independent (intrinsic) dephasing rate and Δ is the exciton-exciton interaction parameter. Excitons in 2D metal-halide perovskites are confined to one of the inorganic quantum wells and are electronically isolated from the others due to the large inter-layer distance [191] ($\sim$ 8 Å) imposed between them by the long organic cations. However, the sample itself, 40-nm thick, is composed of tens of these quantum wells, leading to a highly anisotropic exciton-exciton interaction. To allow for some form of comparison with other 2D semiconductors and quasi-two-dimensional quantum wells of similar thicknesses, we report the exciton-exciton interaction parameter, Δ in units of energy per area. The associated fits and the fit parameters are displayed in Figure 8.3a, b and c. While γ_0 is approximately 2 meV with modest variation across the three probed excitonic transitions, Δ varies more substantially. It is 2.7×10^{-12} μeV cm^2 for exciton B,

Polarization	γ_A (meV)	$\gamma_{A'}$ (meV)	γ_B (meV)
Horizontal	2.37±0.07	3.89±0.06	2.89±0.07
Left circular	2.70±0.10	4.35±0.08	3.27±0.07
Right circular	2.60±0.10	4.69±0.09	3.40±0.07

Table 8.1: Extracted γ for excitons A, A′ and B, using linearly or circularly polarized pulses at an excitation fluence of 50 nJ/cm^2 and at 5 K.

increases to 4.3×10^{-12} μeV cm^2 for exciton A, and to 8.6×10^{-12} μeV cm^2 for exciton A′. It is not straight-forward to compare these values with those of other materials due to the ambiguities over the relevant values of the permittivity function and thus the Bohr radii. However, given the two-dimensional nature of the exciton and comparable exciton binding energies, monolayers of transition metal-dichalchogenides (TMDCs) provide a realistic benchmark. Intriguingly, previous 2D coherent excitation measurements on unencapsulated WSe_2 [126] and encapsulated $MoSe_2$ [245] revealed $\Delta = 2.7 \times 10^{-12}$ meV cm^2 and 4×10^{-13} meV cm^2, respectively, three and two orders of magnitude higher than the value obtained here for $(PEA)_2PbI_4$. This and the linearity of the dephasing rates over a wide range of excitation densities [49] highlights the substantial screening of the exciton-exciton interactions in these 2D perovskites. This is especially surprising given the high biexciton binding energy [167], another characteristic that $(PEA)_2PbI_4$ shares with TMDC monolayers [44, 246]. We will return to these differences in Δ below.

To further highlight differences in multi-exciton elastic scattering behavior, we explore the dependence of the laser polarization state on γ, reported in Table 8.1 at a fluence of 50 nJ/cm^2 and 5 K. For all excitons, γ is consistently smaller with linearly polarized excitation than with circularly polarized pulses. Moreover, except for exciton A′, it is independent on the helicity of the exciting pulses within our experimental uncertainty. When exciting the sample with linearly polarized pulses, excitons can scatter on both left and right circularly polarized excitons. However, they can only scatter with excitons of the same polarization when excited with circularly polarized pulses due to conservation of angular momentum [49]. Table 8.1 further points to differences in scattering behavior of

distinct excitons.

We now turn to the temperature dependence of γ to investigate exciton-phonon interactions. The measured γ for excitons A, A′ and B as a function of temperature are presented in Figure 8.3d, e and f, respectively. We fit this data with

$$\gamma_{\mathrm{ph}}(T) = \gamma_{T=0} + \alpha_{\mathrm{LO}} \left[\frac{1}{\exp(E_{\mathrm{LO}}/k_B T) - 1} \right], \tag{8.5}$$

which assumes that line broadening arises from scattering of excitons with a single thermally populated phonon mode of effective energy E_{LO} with an effective interaction parameter α_{LO}. The parameters representing the best fit for each exciton are shown in Figure 8.3d and f. This model approximates well the behavior of excitons A and B but fails to reproduce that of exciton A′, an indication of the presence of complex lattice interactions as elucidated in our recent works [167, 62, 191]. To compare the strength of the obtained interaction parameters with those of other semiconductors, we obtain the linear interaction parameter Δ_{ph} by taking the low-temperature limit of equation 8.5, yielding $\Delta_{\mathrm{ph}} = \alpha_{\mathrm{ph}} k_B / E_{\mathrm{LO}}$. This gives linear interaction parameters of 70 ± 20 and 130 ± 10 μeV/K for exciton A and B, respectively. These are almost an order of magnitude larger than those in two-dimensional quantum wells [247, 248] and curiously comparable to monolayers of (covalent) TMDCs [126] given the ionic character of the lattice and the resulting strong electron-phonon coupling.

Despite the strong polaronic dressing of the excitons with distinct yet multiple phonon modes [191], here we find that only one phonon effective energy dominates the scattering process via weak interactions. Exciton A, dressed primarily by the in-plane lattice modes [191], interacts with optical phonons at 6.5 meV, which correspond to lattice modes within the inorganic lead-halide network. Exciton B, which is predominantly dressed by out-of-plane lattice modes [191] (see also ref. [94]), interacts with higher-energy phonons at 21 meV, which we have identified to have large contributions from the motion of the

organic cation, particularly from the π–π motion of the phenyl groups [249]. This behavior only highlights the complex phonon coupling scenario which may be beyond a conventional Fröhlich formalism and calls for further experimental and theoretical investigations.

We consider that polaronic effects rationalize the two peculiar observations of this work in the context of many-body interactions in 2D perovskites — the remarkably low values of Δ, and non-trivial differences of this parameter and Δ_{ph} for diverse exciton resonances. Remarkably low inter-exciton scattering rates along with relatively weak exciton-phonon interactions may be attributed to a polaronic protection mechanism [99, 100], where Coulomb interactions that are at the heart of both of these scattering events are effectively screened by the dynamic lattice motion. Such a mechanism has been invoked in the case of bulk 3D perovskites to explain slow cooling of hot carriers [250] and long carrier lifetimes [251, 252], and analogous comparisons can be drawn in their 2D counterparts. Excitons reorganize the lattice along well-defined configurational coordinates [191], which dresses the exciton with a phonon-cloud. Although we currently do not have a reliable estimate of the spatial extent of this deformation, i.e., the polaron radius, based on the polaron coupling constants in lead-halide perovskites [100], we may hypothesize that the radius is much larger than the exciton radius. Such polaronic contributions effectively screen exciton-exciton interactions. At higher densities, we expect a high probability of multiple excitons within the polaron radius, in which case biexcitons may be populated given their high binding energy [167].

Lastly, we note that the zero-density (γ_0) and the zero-temperature ($\gamma_{T=0}$) dephasing widths for all the excitonic transitions are between 2–3 meV, which corresponds to a pure dephasing time $T_2^* = \hbar/\gamma_{0,T=0} \approx 500\,\mathrm{fs}$. Time-resolved photoluminescence measurements performed at 5 K have revealed a lower limit for the exciton lifetime to be around 100 ps [98], suggesting a radiative width $\gamma_{\mathrm{rad}} \sim 0.04\,\mathrm{meV}$, which is much lower than the measured lower-limit $\gamma_{0,T=0}$. This clearly demonstrates the presence of an additional dephasing mechanism in addition to inter-exciton and phonon scattering, possibly due to the

defective nature of the polycrystalline film, the presence of other degenerate dark states which excitons scatter in and out of, or via low-energy acoustic phonons unresolved in the current experiment. We note that similar subpicosecond dephasing times were measured at low temperature for photocarriers in $CH_3NH_3PbI_3$, which were noticed to be a factor of ~ 3 times longer than in bulk GaAs [253]. This was ascribed to weaker Coulomb interactions in that perovskite, limiting the role of excitation-induced dephasing effects compared to III-V semiconductors. In ref. [253], it was speculated that dynamic large polarons account for the relatively long photocarrier dephasing time. We point out that these relatively slow dephasing rates are still much too fast for quantum optoelectronics applications such as single-photon emitters [254], which require coherence times approaching the radiative lifetime.

In a general sense, multi-exciton interactions are determined by an interplay of Coulomb forces, and in ionic crystalline systems, the role of the lattice in mediating them is of fundamental importance. We have focused on the comparison of elastic scattering processes of spectrally distinct excitons within the excitation fine structure, manifested via the dephasing rate. In a previous publication, we have reported high biexciton binding energies in this material [167], and importantly, that biexcitons display distinct spectral structure. We highlight that in ref. [167], the biexciton binding energy of excitons A and B appears to be different, and exciton A displays clear evidence of repulsive interactions in the two-quantum, two-dimensional spectral correlation map. Such interactions might give rise to inelastic scattering of exciton A, perhaps related to Auger recombination [243]. These overlapping dynamics would be deterministic in biexciton lasers [197], for example, if these devices were to be rigorously implemented. The extent to which the spectral scattering rates depend on spectral structure might also determine the dynamics of exciton polaritons in semiconductor microcavities, in which quantum fluids are formed by polariton-polariton inelastic scattering [50]. It has been demonstrated that polariton-polariton interactions in 2D lead-halide perovskites are strong [255], such that the ~ 0.5-ps intrinsic dephasing

times reported here are long compared to Rabi oscillation periods given $\gtrsim 150$-meV Rabi splittings [256]. In the search for room-temperature polartion condensates, it is important to know how polaronic effects control exciton many-body dephasing dynamics, and how hybrid perovskites differ in this respect from other two-dimensional candidate semiconductor systems such as monolayer TMDCs [126, 245]. If polaronic effects mitigate excitation induced dephasing in 2D hybrid perovskites, then the quantum dynamics in a vast range of structurally diverse derivatives merit profound experimental and theoretical investigation.

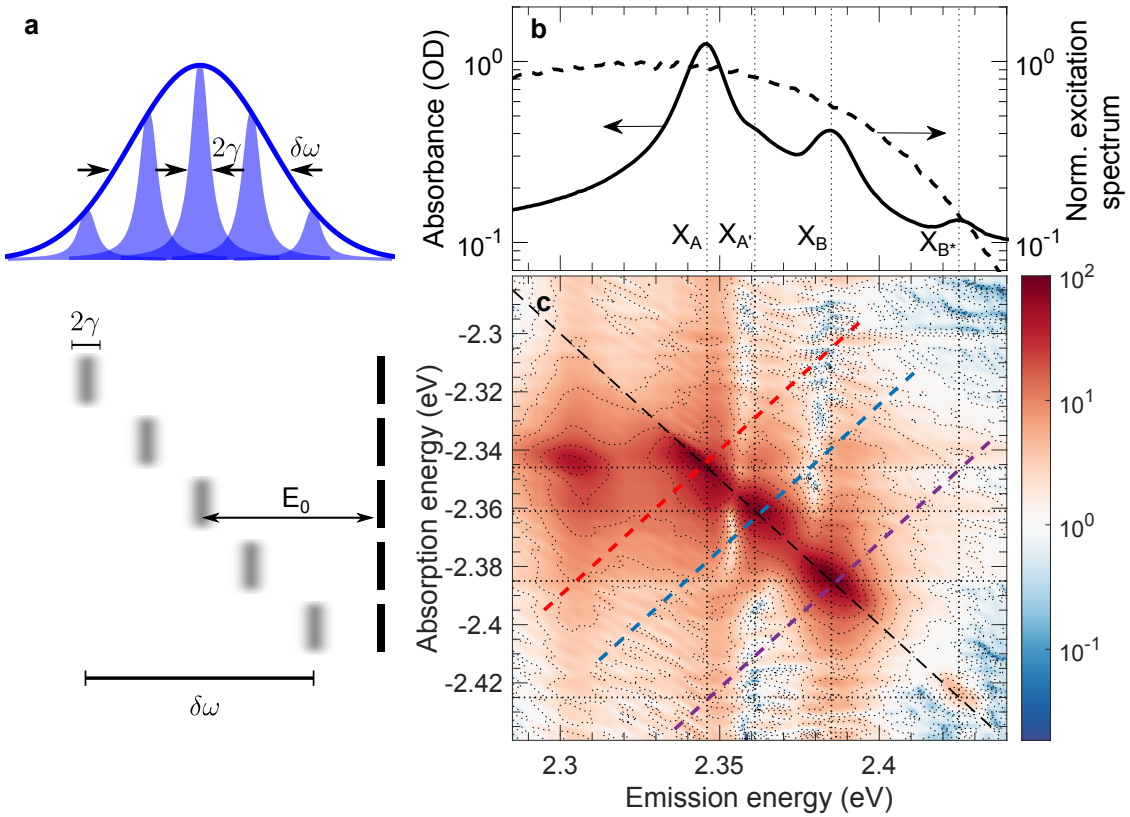

Figure 8.1: **Linear and two-dimensional coherent spectroscopy of $(PEA)_2PbI_4$ at 5 K.** (a) Illustration of the inhomogeneous and homogeneous nature of line broadening. The total linewidth (blue line) is composed of a distribution of homogeneously broadened lines (blue areas). This arises from the simultaneous existence of uncorrelated transitions from the ground state (black lines) to short-lived excited states (blurred lines). E_0 represents the central energy, $\delta\omega$ and 2γ the inhomogeneous and homogeneous linewidths respectively. (b) Absorption spectrum of $(PEA)_2PbI_4$ measured at 5 K (black line) and normalized spectrum of the pulses used in 2D coherent excitation spectroscopy measurements (dashed line). Both scales are logarithmic. Dotted lines indicate the energy of excitons A, A′, B, and B*, respectively, with increasing energy.(c) Absolute value of the 2D coherent rephasing spectrum of $(PEA)_2PbI_4$ measured at 5 K with a pulse fluence of 40 nJ/cm^2 and a pump-probe delay of 20 fs. The color scale is logarithmic. Dotted lines indicate the energies of the aforementioned features. The paths of the diagonal cut (black dashed line) and anti-diagonal cuts at the diagonal energy of excitons A, A′ and B (red, blue and purple dashed lines, respectively) are also shown.

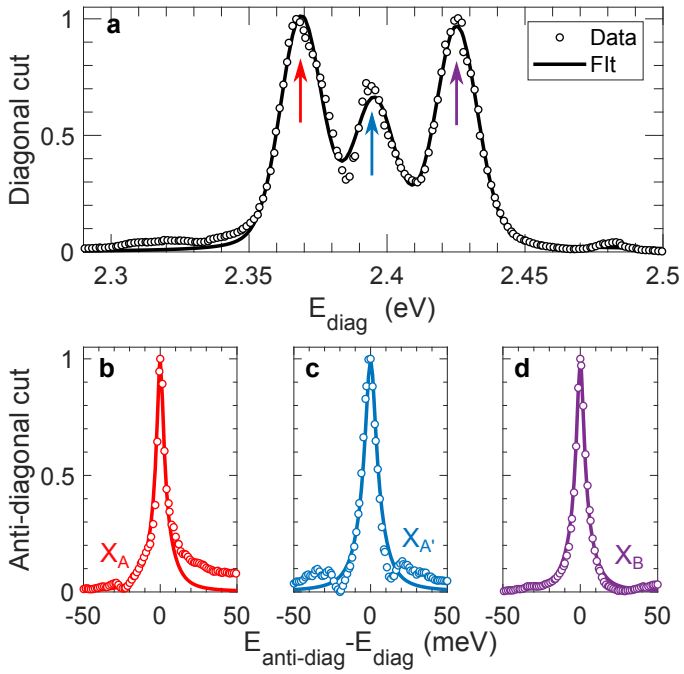

Figure 8.2: **Fitting diagonal and anti-diagonal spectral cuts to a lineshape model.** Normalized diagonal cut(a) and anti-diagonal cuts at diagonal energies of excitons A, A′ and B (b, c and d respectively) of the two-dimensional coherent excitation rephasing spectrum presented in Figure 8.1 c) (circles) and the result of the fitting procedure described in the main text (lines). Arrows in (a) mark the position along the diagonal where the antidiagonal cuts cross it. Due to the presence of low-amplitude cross peaks in the 2D spectrum, these also appear in the tails of the anti-diagonal cuts. To minimize their effect on the quality of the fits and to avoid overestimation of the linewidths, only points higher than 15% of an anti-diagonal cut maxima were included in the fit. The quality of the fits presented here are representative of all the presented dataset. To test the robustness of the fits and to estimate the uncertainties on the extracted linewidths, we repeated the fitting procedure numerous times while adding white noise (5% of the cut's maximum peak to peak) to the data.

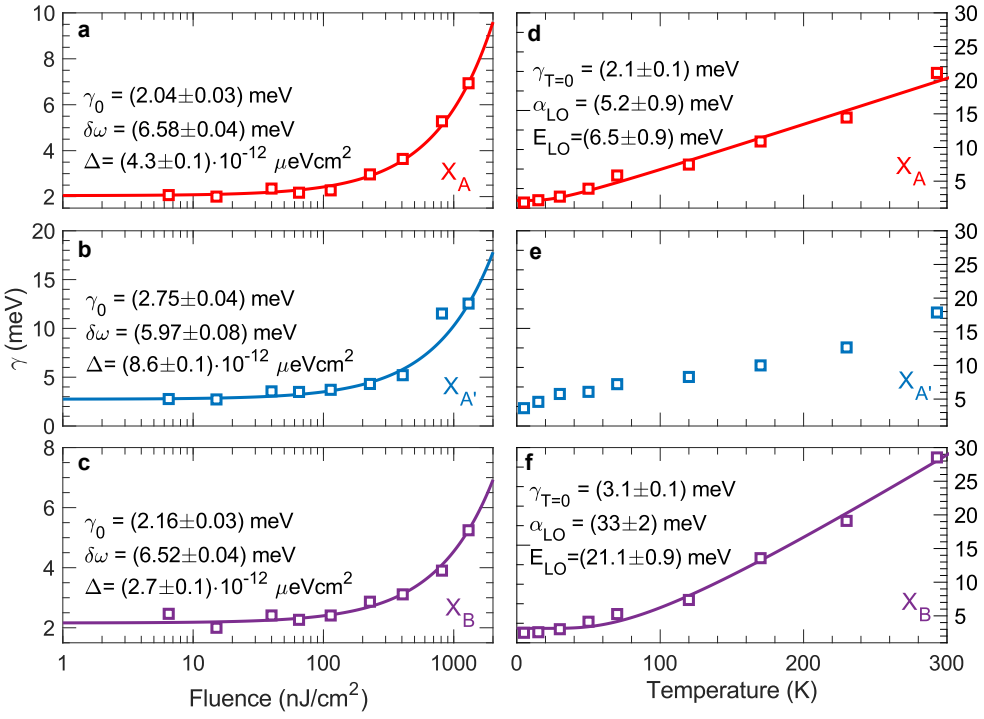

Figure 8.3: **Fluence and temperature dependence of the exciton dephasing rates.** Dephasing parameters γ of excitons A, A′ and B (a and d, b and e and c and f respectively) obtained from the simultaneous fitting of diagonal and anti-diagonal cuts, plotted as a function of excitation fluence (a, b and c) or temperature (d, e and f). Squares represent the experimental linewidths and lines are the best fit to the relevant model described in the main text. Error bars on the data are contained within the markers. For a, b and c, the sample's temperature is maintained at 5 K while the excitation fluence is kept at 50 nJ/cm^2 for measurements presented in panels d, e and f.

CHAPTER 9

STABLE BIEXCITONS IN TWO-DIMENSIONAL METAL-HALIDE PEROVSKITES WITH STRONG DYNAMIC LATTICE DISORDER

The previous study focused on elastic scattering, a regime of many-body interactions occurring at low excitonic densities. At higher densities such as those typical of high-power LED or laser operation, the probability of two excitons being in close proximity is higher and can lead to biexciton formation. Prior work had indirectly shown that biexcitons were strongly bound in these materials at low temperature. What about at room temperature? This question could be easily answered for most semiconductors by simply comparing the biexcitonic binding energy to the thermal energy. However, given the polaronic protection mechanisms highlighted in the previous chapter, the contributions of thermally activated phonons complexifies the case of 2D-HOIPs.

In this chapter, we directly address this question using high-power two-dimensional spectroscopy. We here show that indeed, biexcitons are stable up to room temperature and that their binding energy changes by a quarter of its low-temperature value due to thermal effects. We confirm that even at room temperature, biexcitons are primary photoexcitations such that, at sufficient densities, only 10% of biexcitons will dissociate into excitons. Presented somehow anachronistically, this work was published before we devised our exciton-polaron hypothesis and changes with temperature were interpreted as arising from dynamic disorder within the lattice. As we mentioned in the discussion of the temperature dependence of the ICSRS signal in figure 6.1(e), excitons and carriers in 2D HOIPs are subject to strong dynamic disorder. Dynamic disorder consist in rapid fluctuations of the energetic landscape due, in this case, to the uncorrelated motion of the organic cation. These fluctuations are distinct from those arising from phonons since they are spatially incoherent: each molecule oscillates independently. We also provide evidence for this behavior in this

chapter using non-resonant Raman spectroscopy where we observe strong mode softening and broadening with increasing temperature.

This work was published in Physical Review Materials in 2018 and can be found using reference [167] or on the arXiv under the same title. Dr. Neutzner (CNST@PoliMi, IIT) and I are to be considered co-first authors. Dr. Neutzner and I acquired the multidimensional spectra and performed its analysis. Dr. Neutzner also acquired the temperature dependent absorption spectra. Dr. Cortecchia (CNST@PoliMi, IIT) synthesized the high-quality samples used for this study and Mr. Dragomir carried on the temperature dependent non-resonant Raman experiments. Dr. Salim measured the temperature dependent X-ray scattering data. The work was advised and supervised by Pr. Petrozza (CNST@PoliMi, IIT), Pr. Silva (GaTech), Dr. Srimath Kandada (CNST@PoliMi, IIT and GaTech), Pr. Leonelli (U. Montréal) and Pr. Lam (Nanyang Tech. U.). All authors contributed to the redaction of the manuscript and its intellectual development.

9.1 Abstract

With strongly bound and stable excitons at room temperature, single-layer, two-dimensional organic-inorganic hybrid perovskites are viable semiconductors for light-emitting quantum optoelectronics applications. In such a technological context, it is imperative to comprehensively explore all the factors — chemical, electronic and structural — that govern strong multi-exciton correlations. Here, by means of two-dimensional coherent spectroscopy, we examine excitonic many-body effects in pure, single-layer $(PEA)_2PbI_4$ (PEA = phenylethylammonium). We determine the binding energy of biexcitons — correlated two-electron, two-hole quasiparticles — to be 44 ± 5 meV at room temperature. The extraordinarily high values are similar to those reported in other strongly excitonic two-dimensional materials such as transition-metal dichalchogenides. Importantly, we show that this binding energy increases by $\sim 25\%$ upon cooling to 5 K. Our work highlights the importance of multi-exciton correlations in this class of technologically promising, solution-processable

materials, in spite of the strong effects of lattice fluctuations and dynamic disorder.

9.2 Introduction

Excitonic interactions in two-dimensional (2D) semiconductors garner considerable attention, both due to their relevance in quantum optoelectronics and to the richness of their physics [257, 258]. Whilst their peculiar electronic characteristics have been observed in many single-layer, atomically thin systems, most recently in transition-metal dichalcogenides [259, 260, 261, 262], two-dimensional hybrid organic-inorganic perovskites (HOIP) offer a valuable alternative test system due to the ability to dramatically alter the structure of the inorganic sub-lattice via choice of the organic component [8]. Specifically, we consider HOIPs that consist of lead-iodide octahedra forming 2D lattice planes, separated by long organic cationic ligands (see inset of Figure 9.1), resulting in quantum-well-like structures with strong electronic confinement within the isolated octahedral layers [4]. HOIPs can be readily processed from solution and yet keep the strong excitonic character, even when embodied within polycrystalline films. In that regard, they not only offer an experimentally accessible material system to study 2D many-body exciton physics, but also make a compelling case for novel quantum optoelectronic technologies. In this manuscript, we quantify many-body electron-hole correlations, and we find that these are strong enough to make multi-excitons stable and relevant quasi-particles at ambient conditions, even in the presence of robust energetic disorder.

Though HOIPs fall in the family of excitonic 2D semiconductors, they exhibit many distinct photophysical characteristics, mainly due to their unique chemical and stuctural composition [263]. For example, dielectric confinement arising from the intercalating organic layers increases the Coulomb correlations substantially, resulting in a strong increase in the exciton binding energy [78, 90, 164, 165]. Moreover, the highly polar lattice, prone to different degrees of local fluctuations [214] highlights the importance of lattice motion and exciton-phonon interactions in establishing electronic correlations [264, 163, 265,

175]. Particularly, the HOIP lattice is susceptible to dynamic disorder induced by local lattice motion related to vibrations of the organic moiety [160]. This gives rise to a complex disordered energy landscape, governed by both static and dynamic disorder, that depends on the structure imposed by the organic templating ligand. This makes the electronic characteristics of the material sensitive to the organic-inorganic lattice interactions, which have been previously considered in 2D HOIPs [8, 168, 266, 267, 268]. However, fundamentally important questions remain concerning the role of the dynamic disorder on their ability to sustain strong excitonic multi-particle correlations as seen in other 2D materials. In particular, in this work we ask the following question: given the complex nature of dynamic disorder, are exciton-exciton correlations strong enough to give rise to stable biexcitons at room temperature? This is a fundamentally and broadly important question because biexcitons may play a key role in the photophysics relevant to lasing [269], for example.

The role of biexcitons, bound exciton pairs in two-dimensional HOIPs, has been discussed previously by others [81, 83, 270, 271, 84]. Employing the excitation power dependence of the photoluminescence (PL) spectrum, Ishihara et al. [81] estimated the biexciton binding energy, the difference between the energy of the bound exciton pair and the energy of two unbound excitons, to be around 50 meV at low temperature. In addition, Kondo et al. claimed biexciton lasing in a 2D HOIP [83], and subsequently, Kato et al. [270] measured mutiphoton absorption as well as photoluminescence in a related 2D perovskite, reporting a comparably large binding energy as suggested by Ishihara et al., which was consistent with later measurements on a doped bismuth-doped lead-halide perovskite [271]. More recently, Elkins et al. have shown, using two-quantum two-dimensional coherent spectroscopy, that excitons in multi-layered system undergo strong many-body interactions [84].

In this work, we address directly excitonic correlations in a prototypical single-layer 2D HOIP. We use temperature as an effective variable to tune the degree of dynamic disorder and to establish its role in the biexciton screening. Given the intrinsic complications in the PL lineshape analysis due to temperature dependent linewidth broadening

effects, in order to perform a reliable measurement of the biexciton binding energy, we choose to implement two-dimensional coherent excitation spectroscopy [44]. By studying a material system consisting of well-defined single-lattice layers that are well separated by templating organic cations, and exploiting the high spectral resolution and selectivity of 2D coherent spectroscopy, we unambiguously determine the biexciton binding energy of *single-lattice-layer* perovskite quantum-well semiconductors, which we find to be comparable to that measured [44] and calculated [246] in strongly excitonic 2D materials such as transition-metal dichalcogenides. We find that biexciton binding energies in these systems are strongly affected by dynamic disorder due to both optical phonons and local lattice vibrations induced by the organic spacer cations. Nonetheless, even in the presence of such strong disorder at room temperature, biexcitons are strikingly stable photoexcitations. This has profound implications for the understanding of electronic correlations in these class of materials, and provide a benchmark for the development of detailed theoretical treatment of their many-body physics.

9.3 Results

We consider polycrystalline films of $(PEA)_2PbI_4$ constituting of monolayers of lead iodide octahedra lattices separated by phenylethlyammonium (PEA) cations (see inset of Figure 9.1). The wide-angle X-ray scattering (WAXS) data, shown in Figs. S1–S3 in Supplemental Material, supports the monolayer architecture. Whilst all the optical characterization presented here has been done on polycrystalline films, the structural data have been extracted from powder X-ray diffraction patterns. Detailed analysis of the WAXS data from films and powdered samples, presented as Supplemental Material, establishes the equivalence of their structural characteristics.

The absorption spectra of the sample under investigation, taken at room temperature and at 30 K, are shown in Figure 9.1(a). Both spectra show a distinct excitonic transition shifted from the band edge by about 200 meV. At lower temperatures, the exciton peak

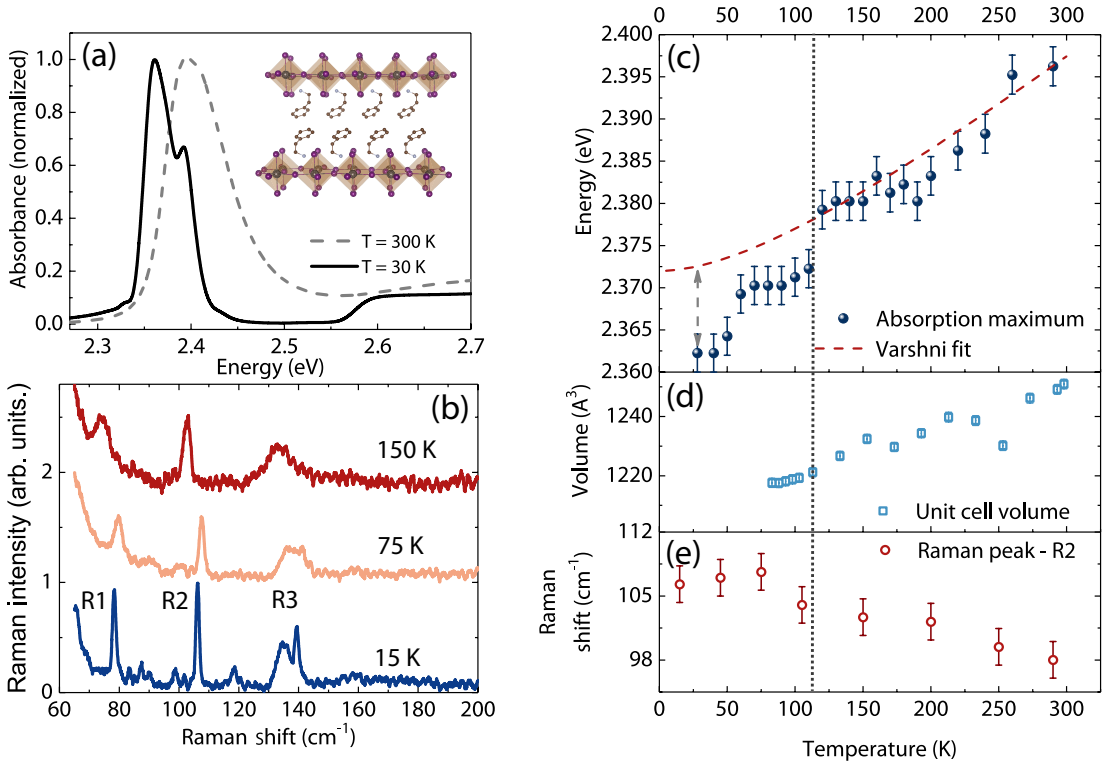

Figure 9.1: **The relationship between optical and structural properties of $(PEA)_2PbI_4$.** (a) Absorption spectra and structure (inset) of $(PEA)_2PbI_4$ monolayer 2D perovskite at low (30 K) and room temperature (300 K). (b) Non-resonant Raman spectra of the sample taken at three different temperatures. The main modes identified within this range are labelled as R1, R2, R3 (c) Position of the excitonic peak in the absorption spectrum, plotted as a function of the temperature. Also shown as a dotted line is a Varshini fit of the trend, assuming temperature independence of the exciton binding energy. (d) Unit cell volume estimated from the wide-angle X-ray scattering data shown at various temperatures. (e) Position of the peak R2 in the Raman spectrum plotted at different temperatures. The uncertainty bars represent instrument resolution.

develops a fine structure, identified initially by Gautron et al. [104], and discussed within the context of a polaron model. A few subsequent works have attempted to explain this phenomenon by invoking phonon vibronic replicas [98, 8], although the lack of clear vibrational modes at the frequencies that would be required to account for the spacing of the peaks in the exciton spectrum (~ 35 meV) makes these assignments inconclusive. We consider that this structured lineshape could arise from other electron-phonon coupling effects that renormalize the excitonic Rydberg energy, thereby producing distinct excitonic states separated by coupling energies. Such effects have been reported in cesium halides [189] and in other semiconductors such as GaAs, CuCl, and CdTe [188, 187]. Alternatively, the spectral structure could arise from Rashba effects. In fact, Zhai et al. report a Rashba splitting of 40[107], consistent with the energy spacing of the features that we observe in the linear absorption spectrum at low temperature. Irrespective of the physical origin of their structure, the spectra confirm the presence of four distinct excitonic transitions separated by about 35–40 meV. Although they become more evident at low temperature due to reduced thermal disorder, their presence even at room temperatures cannot be discounted, as will be demonstrated by our coherent nonlinear spectroscopy measurements discussed below.

A closer inspection of the temperature dependence of the exciton absorption spectrum reveals the relationship between crystal and electronic structures. Figure 9.1(c) shows the exciton peak absorption energy plotted as a function of temperature (for the complete spectra, refer to Figs. S4–S5 in Supplemental Material), and we observe a red shift with decreasing temperature. This trend is monotonic until about 120 K and can be explained via lattice contraction effects. The unit cell volume reduces upon lowering the temperature, as shown in Figure 9.1(d) (see Figure S3 and Figure S6 in Supplemental Material for more details), which subsequently reduces the bandgap (E_G). Assuming that the exciton binding energy (E_X) is temperature independent, the exciton peak energy, $E_0(T) = E_G(T) - E_X$, will follow a similar trend. This dependence can be fitted by an empirical Varshni law [174], given by $E_0(T) = E_0(0) + \alpha T^2/(T + \beta)$, shown as dashed line in Figure 9.1(c). The fit

parameters used here are, $E_0(0) = 2.372\,\text{eV}$, $\alpha = 1.1 \times 10^{-4}\,\text{eV K}^{-1}$ and $\beta = 151\,\text{K}$. Concomitantly, we also observe an increase in the energy of the vibrational modes, as seen in the temperature dependence of the Raman peak $R2$ in Figure 9.1(e), which corresponds to an optical longitudinal phonon [272]. The temperature dependence of the energies of the other Raman modes is shown in Figure S7 in Supplemental Material.

Below approximately 100–120 K, we observe a sharp deviation from the behavior described above. The exciton energy now shows abrupt shifts with decreasing temperature over relatively well defined temperatures. The structural parameters extracted from WAXS and Raman spectroscopy also show distinct trends. It must be emphasized that we did not observe a first order phase transition over the measured temperature range by means of WAXS measurements, with the lowest probed temperature of 83 K. This is also in agreement with earlier works on this material [273]. Instead, at this lower temperature range, the contraction of the unit cell with decreasing temperature appears to level off (Figure 9.1(d)), although we recognize that the experimentally available temperature range is limited. Below $\sim 100\,\text{K}$, we also note that the Raman linewidths (R1 and R2) are weakly temperature dependent down to 15 K. In conjunction, these observations suggest possible stiffening of the crystal lattice as the two inorganic layers come closer, largely due to the steric hindrance between the organic moieties.

While the Raman shift itself evolves into an anomalous range, where the energy reduces upon lowering the temperature, the most striking evolution at low temperature can be seen in the spectral lineshape, particularly that of the mode labelled $R3$ in Figure 9.1(b). We observe a well-defined peak within this vibrational band, which gains intensity at lower temperatures. Based on earlier work [274, 275], we assign this mode to the motion of the lead iodide octahedra induced by the relative motion of the the organic cation. Due to the localized nature of these vibrations and to the large dynamic disorder intrinsic to the perovskite lattice, the observed mode is usually broadened via inhomogeneous effects as can be seen in the 150-K spectrum (Figure 9.1(b)). We consider that a sub-ensemble

of oscillators perceive similar local environment below 100 K due to a disorder-order-like transition, as also suggested by the apparent lattice stiffening, leading to the narrowing of the energetic distribution perceived by $R3$. This establishes temperature as an effective means to vary the degree of dynamic disorder within the lattice and thus to investigate the role of the latter in the excitonic correlations. We note that temperature-dependent spectral narrowing of $R1$ and $R2$ modes is weak in this lower-temperature regime, further pointing to the likely lattice stiffening effects (see Figure S8 in Supplemental Material).

Such a change in the order parameter of the lattice indeed results in the re-normalization of the exciton binding energy by about 10 meV. Although this amounts to less than a 5% correction to the two-particle correlation energy, it nevertheless suggests a finite contribution of the lattice fluctuations to the electronic polarization. There is indeed an observable evolution in the spectral fine structure of the excitonic line in absorption below 100 K(shown in Figure S5 in Supplemental Material) due to non-trivial corrections in exciton-phonon coupling. However, the relatively small change in the binding energy indicates that intrinsic electron-hole interactions are not strongly perturbed by the slow lattice vibrations. This may not necessarily be the case for bound multi-excitons, which are expected to have binding energies that are a fraction of the single exciton binding energy as suggested by intensity-dependent photoluminescence measurements [81]. In order to explore this proposition, we require a measurement of the excitation lineshape that permits direct identification of multiquantum resonances, that is, spectral signatures of exciton-exciton correlations, beyond the linear absorption probe discussed thus far, and beyond steady-state photoluminescence, where the biexciton contribution needs to be extracted from within the inhomogeneously broadened exciton spectrum over the *entire* temperature range of interest. We achieve this by performing multi-dimensional coherent spectroscopy at room temperature and at 5 K, the two experimentally accessible extremes of the range in dynamic disorder of the lattice considered in Figure 9.1. The key conclusion that we will draw from this spectroscopy is that the excitonic spectral structure discerned from linear

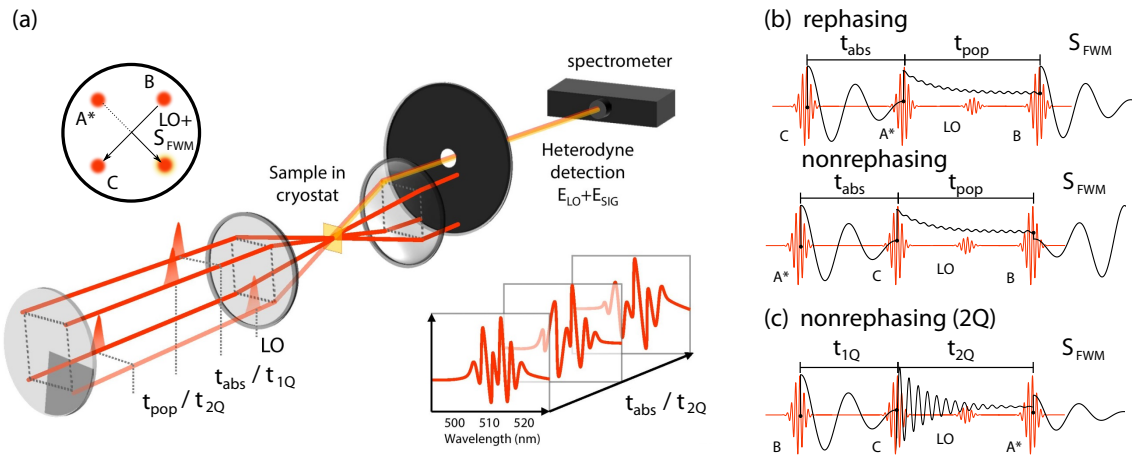

Figure 9.2: **Schematic representation of the two-dimensional coherent spectroscopy experiment implemented in this work.** The geometry of the excitation pulse-train beam pattern (red) and the resonant four-wave mixing signal (S_{FWM}, yellow-orange), detected by interference with a local oscillator (LO), is shown in (a). We use a so-called BOXCARS beam geometry, in which three pulse trains (A, B, C) propagating along the corners of a square are focused onto the sample with a common lens, defining incident wavevector $\vec{k}_{\mathrm{A}}$, $\vec{k}_{\mathrm{B}}$, and $\vec{k}_{\mathrm{C}}$. The LO beam, on the fourth apex of the incident beam geometry, co-propagates with S_{FWM} with wavevector imposed by the chosen phase matching conditions. The spectral interferogram of S_{FWM} and the LO beam is recorded at every time step. (b) By controlling the order of the pulse sequence with this beam geometry, we measure two distinct S_{FWM} responses: the *rephasing* signal with wavevector $\vec{k}_{\mathrm{B}} - \vec{k}_{\mathrm{A}} + \vec{k}_{\mathrm{C}}$ and *non-rephasing* signal with wavevector $\vec{k}_{\mathrm{A}} - \vec{k}_{\mathrm{B}} + \vec{k}_{\mathrm{C}}$. The sum of rephasing and nonrephasing spectra produce the total (one-quantum) correlation spectra displayed in Figure 9.3. (c) By imposing the depicted pulse sequence, we isolate the two-quantum coherence correlation spectra presented in Figure 9.4.

absorption is on top of two-quantum contributions due to biexcitons. We measure directly their binding energy and find that biexcitons are strongly bound at room temperature in spite of the strong dynamic disordered highlighted above. In what follows we first present a general discussion of 2D coherent spectroscopy, and how it enables us to draw these conclusions.

Two-dimensional (2D) coherent spectroscopy is a powerful tool to disentangle congested spectral features by measuring the correlations between them [177]. In this spectroscopy, we resolve a nonlinear optical response of the system (coherent radiation from a nonlinear polarization induced in matter by a sequence of three femtosecond pulses) with

two correlated energy variables, the "absorption" and "emission" energies. The response along the absorption energy variable is extracted from a time-domain coherent excitation spectral measurement using a sequence of the three phase-controlled femtosecond pulses, and that along the emission energy variable is obtained by measuring the resulting coherent emission by means of spectral interferometry with a fourth replica pulse. We represent schematically the geometry of the pulse sequence and resulting signal vectorial direction in Figure 9.2. The utility of this family of techniques is that one expects to reproduce the spectral structure observed in the absorption spectrum, manifested by peaks along the diagonal of the 2D spectrum, which expresses optical-transition autocorrelations. On top of this diagonal structure, we can expect off-diagonal cross peaks in the presence of correlations between optical transitions. Furthermore, if a contribution from an excited-state absorption is possible (such as would be expected for a multi-exciton contribution to the absorption spectrum), it would be obscured in a linear measurement or in an incoherent nonlinear measurement such as transient absorption, but it can be uniquely identified in a coherent 2D spectral experiment. In its most common implementation, 2D coherent excitation spectroscopy is achieved by measuring the spectral phase and amplitude of the transient four-wave mixing signal generated by the invoked pulse sequence incident on the sample (see Figure 9.2(a)). The delays between the pulses are scanned and the coherent emission spectrum is recorded by spectral interferometry with the "local oscillator" laser beam at each time step to generate a time-frequency map of the nonlinear response. The time variable that maps the evolution of the coherence dynamics is then Fourier-transformed to generate a frequency-frequency map. The multidimensional spectrometer used in this letter is colloquially referred to as COLBERT (Coherent Optical Laser BEam Recombination Technique), a design of superior phase stability developed by Turner and Nelson [143]. More details concerning the implementation used in this work are presented in Appendix D and in Section S3 in Supplemental Material.

Our experimental configuration allows us to perform two distinct experiments repre-

sented schematically in Figure 9.2. The first one, the one-quantum (1Q) total correlation measurement, probes transitions between the ground state and the first ladder of excited states, as well as the associated transitions to the next ladder of excited states. It is obtained by summing the real parts of the two-dimensional spectra corresponding to the sequences depicted in Figure 9.2(b), the so-called rephasing and nonrephasing spectra. In such spectra, coherence or population transfer between spectral features and excited-state absorption (ESA) manifests as negative and positive features respectively [118]. These two signatures are often spectrally degenerate and give rise to complex lineshapes in a 1Q spectrum. The second experimental scheme involves two-quantum (2Q) nonrephasing measurements, and exclusively probes the direct two-quantum transitions to the second excited-state manifold, making it a more selective measurement of higher-lying states. One performs such a measurement by using the pulse sequence depicted in Figure 9.2(c). It is thus a very useful tool to interpret 1Q spectra ESA features. Due to its high selectivity, ease of interpretation and low time-averaged fluences, these measurements have been used as elegant probes of many-body interactions in various systems such as GaAs quantum wells [43], semiconductor quantum dots [276], monolayers of transition-metal dichalcogenides [82], and multi-layered two-dimensional perovskites [84], to name a few closely related examples.

The 1Q total correlation spectra for $(PEA)_2PbI_4$ are shown in Figure 9.3 for two different population times (0 and 160 fs) at both room temperature ((a) and (c)) and 5 K ((b) and (d)). It must be noted that the amplitudes of the observable features are weighted by the product of the pump and absorption spectra, which are also shown in Figs. 9.3(e) and (f). The pump spectrum does not extend into the free-carrier absorption band, allowing us to uniquely probe excitons and their multi-body counterparts. We also present real and imaginary parts of both rephasing and nonrephasing components for both population times in Figs. S10 and S11, along with a movie of these spectral evolutions, in Supplemental Material.

All spectra harbor negative diagonal (such as peaks 2 and 4) and off-diagonal (such

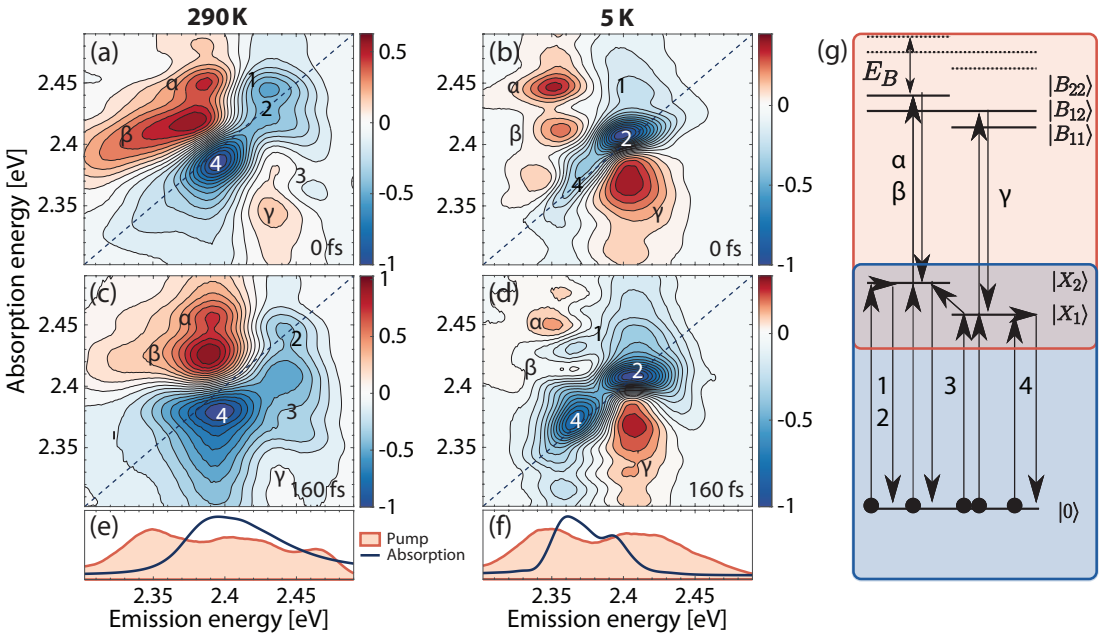

Figure 9.3: **Total-correlation 2D coherent excitation measurements of $(PEA)_2PbI_4$.** 1Q total correlation spectra of $(PEA)_2PbI_4$ monolayer 2D perovskite at 5 K (b,d) and room temperature (a,c) for population times of 0 fs (a,b) and 160 fs (c,d). For comparison, the corresponding absorption spectra and pump laser spectra used during the experiments are shown in (e) and (f). An illustration depicting some of the coherent processes involved in these features is presented in (g). To avoid a crowded diagram, transitions within the same exciton manifold (such as α and β) have been drawn as degenerate.

peaks as 1 and 3) features corresponding to the primary transitions from the ground to the exciton states. Strikingly, large positive features are also present, labelled as α, β and γ. These indicate excited-state absorption from single-quantum states to higher-lying ones, suggesting the existence of a non-trivial excited-state manifold (see Figure 9.3(g) for a summary of the excitation pathways). These features lay atop negative-going cross peaks, as indicated by the population time dependence of the diagonal features (see Supplemental Material), obscuring their true lineshapes. Nevertheless, it is possible to estimate the energy of the higher-lying states responsible for these features by comparing their position along the emission axis in the total correlation maps to upper cross-peak labelled 1 and the diagonal feature labelled 2, respectively [118]. For the features in the upper left corners of the spectra (labelled as α and β), this implies the existence of a state (42 ± 2) and (55 ± 2) meV below twice the energy of the 1Q state for room temperature and 5 K, respectively. Supposing that this higher-lying state consists of a bound biexciton, which is a correlated two-electron, two-hole quasi-particle, this energy difference corresponds to our first estimate of its binding energy (E_B). The positive feature labelled γ can also be caused by ESA into a bound biexciton of two different excitons. In this case, an estimation of the biexciton binding energy is challenging because of the higher proximity and thus higher degree of interference with its corresponding negative feature.

The spectral evolution of the 1Q signal at 5 K suggests electronic relaxation within the exciton manifold. At initial times, the diagonal response is mainly concentrated at higher energies and within < 100 fs, the spectral weight is transferred to the lower-energy resonance via population relaxation. Concurrently, cross peaks associated with the correlation of the lower-energy state with the higher-lying ones gain in intensity, enough to partially cover the positive ESA features.

At room temperature, we do not observe such dominant *relaxation* dynamics apart from a monotonic decay over the entire spectrum (see also Figure S12 in Supplemental Material). This can be attributed to the lack of spectral structure, even in linear absorption, due

to the disorder-induced broadening of the excitonic transitions. We presume that thermal disorder stabilizes a distribution of the photoexcited population within the excited-state manifold, with no substantial relaxation at least within the probed temporal window. On the other hand, we observe that the initial diagonally elongated spectral lineshape broadens along the anti-diagonal axis within tens of femtoseconds. Such behavior is indicative of spectral diffusion due to the energetic re-distribution between the inhomegeneously broadened oscillators via incoherent interactions with the surrounding environnement [277]. The observed ultrafast timescales, though compelling and probably analogous to the ultrafast lattice re-organization dynamics observed in three-dimensional perovskites [278], require more detailed analysis. Nevertheless, cross-peaks arising from these spectral dynamics and from correlations add ambiguity to the estimated E_B from the 1Q measurement alone. To alleviate this, we exclusively probe the higher-lying excited-state manifold by performing a two-quantum (2Q) measurement.

The real part of the nonrephasing 2Q spectra of polycrystalline monolayer $(PEA)_2PbI_4$, both at 5 K and room temperature, are shown in Figure 9.4 alongside a schematic of the energy levels of the excitons $|X\rangle$, biexcitons $|B\rangle$ and unbound exciton pairs (dashed line) involved in the generation of the 2Q signal. The delay between the first and second pulses is set to 20 fs, chosen to be their temporal full width at half-maximum, to minimize contributions from undesired non-resonant four-wave mixing while still maintaining a high signal-to-noise ratio. In both spectra, a strong dispersive lineshape is present on the two-diagonal ($\omega_{2Q} = 2\omega_{emit}$) axis indicating unbound but correlated exciton pairs by many-body interactions such as excitation induced dephasing and excitation induced shift [116]. We emphasize that any spectral feature on the two-diagonal axis reflects correlations between two excitons that include neither attractive nor repulsive contributions. Negative peaks can also be observed above and below these dispersive features, and these signatures do correspond to bound exciton pairs of different and similar species respectively [45]. The negative features slightly below the diagonal are due to oscillations of coherences between a 2Q state

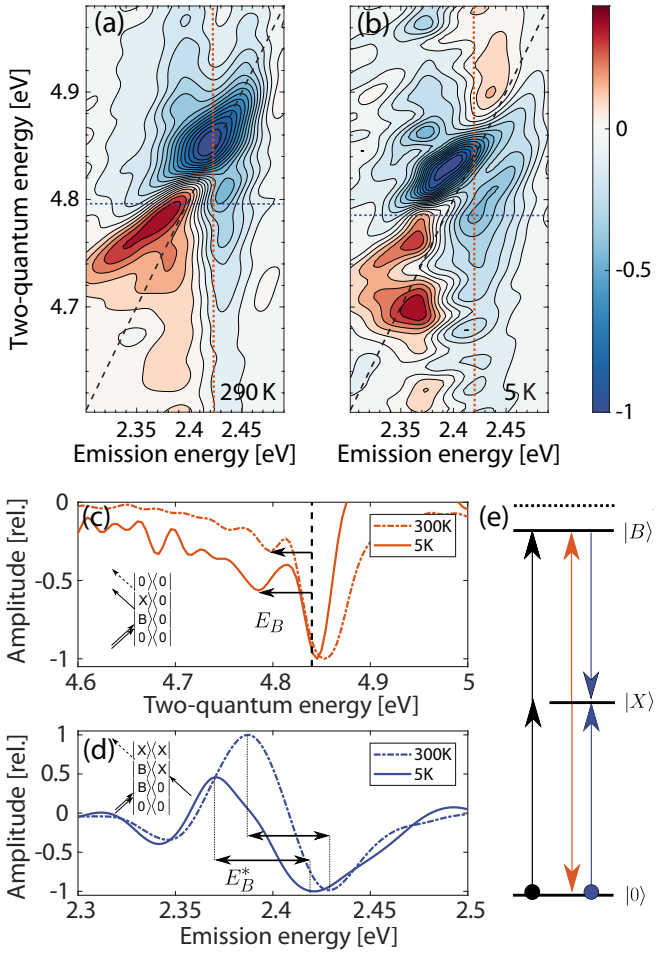

Figure 9.4: **Two-quantum non-rephasing 2D coherent excitation measurements of $(PEA)_2PbI_4$.** Real part of the 2Q non-rephasing spectra of polycrystalline monolayer $(PEA)_2PbI_4$ at room (a) and low temperature (b) for a 1Q waiting time of 20 fs. The dashed black line follows two-quantum energies at twice the emission energy. Cuts along the vertical (c) and horizontal (d) axes were taken along the dashed lines of corresponding color in (a) and (b). The horizontal cuts were taken to coincide with the two-quantum energy at which a biexcitonic feature resides on the vertical axis. Estimates of E_B and E_B^* were obtained from apparent shifts from the diagonal line or from bound biexciton coherences respectively (see text). Insets of (c) and (d) show the Feynmann pathways responsible for these shifts, with $|X\rangle$ the exciton and $|B\rangle$ the biexciton states, respectively. The dashed line in (c) indicates the crossing point between the cut axis and the diagonal. (e) An representation of the coherent pathways that lead to biexciton features below the $\omega_{2Q} = 2\omega_{emit}$ diagonal.

and the ground state. From these features' vertical shift below the two-diagonal, the biexciton binding energy E_B can be extracted yielding (44 ± 5) and (55 ± 5) meV for room- and low-temperature measurements, respectively. By comparing this energy with that previously obtained from ESA features in 1Q total correlation spectra, we conclude that these previous features indeed arise from ESA into a bound-exciton-pair state. This consists of the first *direct* measurement of biexcitons in *monolayered* (i.e. the most quantum-well-like) two-dimensional perovskites.

Theory also predicts the existence of a second positive feature redshifted by the biexciton binding energy along the emission axis (see inset of Figure 9.4(d) and Figure 9.4(e)). This peak arises from the oscillations of coherences between a 2Q state and the single-exciton state [279]. Such a peak can be observed atop the aforementioned dispersive features and yields another estimate of E_B^*, the exciton binding energy. Taking an horizontal cut at the two-quantum energy where the minimum of the biexcitonic peak was previously observed highlights the presence of this feature (see Figure 9.4(d)). From the shift along the emission axis between the two extrema of this cut, we extract a value of E_B^* of (42 ± 5) and (50 ± 5) meV for room- and low-temperature measurements, respectively, corroborating the values of E_B discussed above.

We note that biexciton binding energies are often estimated by PL measurements as previously done by Ishihara et al. [78]. In fact, we do observe an emission peak which could be of biexcitonic origin in PL (Figure S9 in Supplemental Material) and is red-shifted by about 40 meV from the primary excitonic emission peak. However, the energetic position of the exciton in emission is contaminated by self-absorption effects due to small Stokes shift and overlapping spectral contributions from the exciton finestructure, leading to an under-estimation of E_B. Moreover, local heating effects induced by the high average pump powers required make estimates from PL intensity measurements unreliable. It has also been shown that a non-linear increase of the PL with pump fluence can also arise from defect-related effects adding to the ambiguity in the assignement based solely on intensity-

dependent PL mesurements [193]. Furthermore, at room temperature, the PL spectrum is featureless, making it impossible to even identify biexcitonic signatures over this higher temperature range. This highlights the advantage of using multi-dimensional spectroscopy to identify biexcitons and to measure their binding energy, as we have demonstrated here.

9.4 Discussion

In summary, we provide the first direct observation of biexcitons in monolayered $(PEA)_2PbI_4$, using both 1Q and 2Q coherent multidimensional spectroscopy, and we have established that this is so in the presence of strong dynamic energetic disorder at toom temperature. The inferred binding energies are in agreement with the previous report of Ishihara et al. [81]. and approach those measured in monolayer transition metal dichalcogenides [82, 44], another bidimensional system of great fundamental and technological interest. We consider that it is highly significant that biexcitons are as stable in 2D perovskites, which are subject to strong dynamic disorder due to the hybrid organic-inorganic nature of the lattice, and to its ionic nature, as in atomically single-layer, purely covalent 2D semiconductors. We also provide a temperature-dependent measurement of biexciton binding energy using two-quantum, two-dimensional spectroscopy, pointing to a similar effect of lattice temperature to that observed for the exciton binding energy. The large change in biexciton binding energy with temperature, as a fraction of the total binding energy, suggests important contributions of the lattice to the permittivity function in two-dimensional perovskites.

Apart from giving an experimental benchmark for multi-body correlations in these materials, this work highlights the importance of the lattice degrees of freedom in Coulomb screening effects. The contribution of polar lattice vibrations has been successfully unravelled in the case of excitons in polar semiconductors by Kane [280] and Pollmann-Buttner [65] via consideration of an effective permittivity function composed of static and optical frequency dielectric responses. This has been effectively extended even to the case of three-dimensional hybrid perovskites, where the motion of the organic cation has been

shown, both theoretically [90] and experimentally [281], to screen electron-hole correlations. Given the smaller exciton binding energy in bulk perovskites, these minor contributions, though present, are considered to have no substantial effect on the excitation dynamics, especially at low solar densities, though their role at high excitation densities cannot be ruled out.

Intriguingly, two-dimensional perovskites present a contrasting scenario with respect to their 3D counterparts. Dielectric confinement assures an extremely large exciton binding energy accompanied by a small Bohr radius, such that exciton characteristics remain relatively insensitive to lattice fluctuations due to their localized nature. This can be seen in the very modest correction to the exciton binding energy with decreasing temperature, along with the very similar spectral structure evident in both linear and non-linear (1Q) spectra, upon transitioning from a disordered (RT) to ordered (5 K) crystal phase. The temperature dependence of the biexciton binding energy, on the other hand, makes dynamic disorder an extremely pertinent parameter in many-body correlations and thus assumes relevance for high-density ($> 10^{18}$ cm^{-3}) dynamics. We interpret this as a consequence of their more delocalized nature implied by the lower biexciton binding energy with respect to the single-exciton binding energy, which makes them more sensitive to dynamic disorder induced by localized lattice fluctuations.

Of all semiconductor systems probed so far, biexcitons in 2D perovskites are amongst the most strongly bound [246]. This indicates that at room temperature and sufficiently high excitation densities, they will be the dominant photoexcitation, yielding an important non-radiative channel for exciton population. An Auger-like channel is expected to play a major role in the performance of lasing devices by increasing the lasing thresholds [269]. The highlighted effects of dynamic disorder must thus be accounted for in the optimization of these promising materials for optoelectronic applications. In the case that biexcitons are the emissive species used for the lasing action as suggested by Kondo et al. with 2D perovskites [83], crystal lattices that can house stable biexcitons should be appropriately

designed and optimized.

9.5 Conclusions and Outlook

We conclude that in a model metal-halide *single-layer* two-dimensional hybrid semiconductor, biexcitons are primary photoexcitations at sufficiently high density ($\gtrsim 10^{18}\,\mathrm{cm}^{-3}$) in spite of a highly complex disordered energy landscape. By means of temperature-dependent absorption, wide-angle X-ray scattering, and Raman spectroscopies, we have associated contributions of lattice motion to the dynamic disorder that renormalizes exciton energies. These lattice dynamics affect substantially biexciton binding energies such that at 5 K these are 25% higher than at ambient temperature, read directly by means of two-dimensional coherent excitation spectroscopy. Nevertheless, given our measurement of a binding energy of 44 meV at room temperature, only $\sim 10\%$ of biexcitons would dissociate at steady state under ambient conditions. This underlines the importance of studying multiexcitonic structure in these materials as a function of chemical and crystalline structure. We consider it an opportunity to extend these ultrafast spectroscopic studies as a function of lead-halide octahedral distortion induced by the organic templating cation [8]. We suggest that control of the details of dynamic disorder can be achieved by means of the nature of the organic moiety. This will provide a rich materials parameters space to explore many body correlations beyond atomically-single-layer semiconductors such as transition-metal dichalchogenides.

Multi-particle correlations are at the heart of the quantum phase transitions — exciton-Mott transitions and Bose-Einstein condensation [50], which are the primary mechanisms leading to photonic and polaritonic lasing, respectively, in semiconductors. Conceptualizing the effect of lattice fluctuations on the co-operative behavior of the coherent electronic excitations in such phases is thus not only of technological significance, but also a new frontier for semiconductor physics of highly disordered yet strongly excitonic semiconductors.

CHAPTER 10

PERSPECTIVES

In the previous chapters, we have presented strong evidence that the states responsible for the sub bandgap fine structure in 2D-HOIPs are distinct exciton-polarons. We first showed that these states were intrinsic to the lattice and did not arise from defects or grain boundaries. We also showed that the optical lineshape could be reproduced by considering four distinct excitonic transitions coupled differently to lattice modes using a modified Wannier formalism. This assumption was then unambiguously confirmed by resonance Raman spectroscopy and showed how each excitons were coupled to distinct low-energy modes. By definition, this consists in a direct measurement of their polaronic nature. We have shown that this polaronic nature is strongly manifested in their relaxation dynamics as well as in their interactions with other quasiparticles. Exciton-polaron effects in 2D-HOIPs are important and should be treated consequently. This thesis work also shows that multidimensional coherent spectroscopy is a powerful tool to investigate new materials with, exposing with relative ease profound physical phenomena that could only be probed indirectly with other techniques through ambiguous interpretations. It is therefore becoming important for researchers working on the optical properties of materials to educate themselves on this powerful technique so as to benefit from the strong evidences it brings about the fundamental physical phemonena it probes.

In some sense, we have only exposed half the picture regarding polaronic effects. Indeed, vibrational modes too are strongly affected by their coupling to the electronic degrees of freedom [58]. Shifting, broadening and differential population of the phonon bands can occur upon excitation of an electronic transition coupled to them and should be observed as well in 2D-HOIPs. To probe these effects, transient spectroscopies such as pump-visible probe-THz are ideal. As we have determined, many polaronic modes lie between 1 and

10 meV, a range accessible by THz pulsed sources [282]. Moreover, although these modes are Raman active, previous measurements in 3D HOIPs suggest they could be excited by direct THz light absorption as well [215]. This technique has been very recently used to track polaron dynamics in $CsPbBr_3$ following carrier photoexcitation [283]. Given the rich polaronic landscape in 2D-HOIPs, this would shed light on the simultaneous behavior of their lattice and electronic degrees of freedom during relaxation following the absorption of light. However, due to light's vanishingly small momentum, this technique only probes the phonon branch at zero phonon wavevector. Ultrafast electron diffraction, on the other hand, could reveal in great details the lattice's reaction to resonant excitation of the polarons [284]. This technique probes elastic scattering of a pulse of electrons off the lattice's electrostatic potential. Due to the periodicity of the latter, electronic Bragg peaks appear in the far field. Moreover, the high scattering cross-section of electron diffraction allows this technique to be performed on extremely thin samples, comparable to the penetration depth of light. The electron pulse can be made as short as 100 fs, faster than the period of the phonons dressing exciton-polarons and can therefore be timed with a resonant excitation pulse. By observing the dynamics of the Bragg peaks with pump-electron probe delay, the lattice's conformation following excitation, including coherent oscillations, can be time-resolved. This provides a more direct probe of the reaction of the lattice to the presence of polarons than the THz pump-probe experiment [285]. A significant improvement of this technique, ultrafast electron diffuse scattering, probes the inelastic scattering of electrons on the lattice [286]. This is done using the same experimental apparatus, albeit with a much greater signal to noise ratio. This allows the resolution of weak features arising from inelastic scattering with the lattice around the strong elastic Bragg peaks. These features are a direct measure of the occupancy of phonon branches at all wavevectors and can be used to infer the phonon part of the polarons' wavefunctions. Moreover, by monitoring the time dependence of this phonon population, the electron-phonon coupling for all phonon branches at all wavevectors could also be extracted. The latter, however, require the knowl-

edge of the phonon dispersion relations, which has only been measured recently for 3D HOIPs [287] and lacks for their two-dimensional counterparts. Given our measurements of temperature-dependent non-resonant Raman spectroscopy [249], the phonon branches are expected to shift, broaden and split with temperature. Therefore, temperature dependent inelastic neutron scattering must be performed to get a full picture of the phonon degree of freedom in these materials. Nonetheless, such a detailed characterisation of the polaron's phonon part would guide our understanding of exciton-polaron formation dynamics for all 2D exciton-polaronic systems for years to come.

As mentioned in the introduction chapter, the aim of condensed matter physics is to provide from basic principles a hierarchy of models that reproduce to various degrees of accuracy the behavior of complex systems. In this optic, investigations into empirical exciton-polaron Hamiltonians such as that of reference [71] are extremely useful to interpret experimental data. Extensions of the latter to account for many-body interaction could give powerful insights into the role of polaronic effects into biexcitonic binding and the many-body scattering processes. Additional ab-initio studies such as density functional theory calculations should also be steered towards the description of polaronic effects. DFT calculations have been able to describe small polaron formation in 2D-HOIPs [168] but large polarons have resisted this treatment so far. Indeed, 2D-HOIPs, due to their complex and large unit cells, are difficult systems to investigate using DFT. Therefore, performing these calculations on the many supercells spanned by large polarons is an extremely challenging task. However, recent developments in the ab-initio treatment of polaronic effects allow the treatment of large polarons without the need for supercell calculations [288, 289]. These could help elucidate which polaronic regime free carriers in 2D-HOIPs fall into: large or small polarons. In the end, these efforts would highlight which approximations are best suited to describe with accuracy the essential physical phenomena that arise from both strong electron-hole and strong electron-phonon correlations.

Even with regards to the electronic degrees of freedom, the picture painted in this thesis

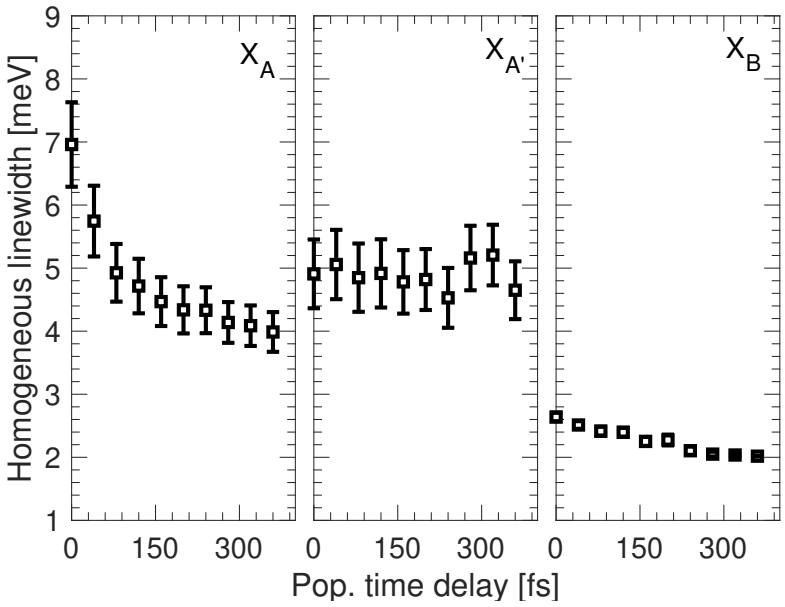

Figure 10.1: **Decrease of the homogeneous linewidth with population time in $(PEA)_2PbI_4$ at 5 K** for each excitonic specie. The error bars represent the robustness of the fits to a small amount of white noise added to the data. These measurements were taken at a fluence of 40 nJ/cm^2.

is incomplete for we have only probed bright states. Recent investigations of 3D HOIPs under intense magnetic fields have shown the fine structure to hide a dark exciton below all optically active excitons [96]. What about 2D-HOIPs? From the data presented in chapter 8 alone, we can infer that other states should be present alongside those directly responsible for the material's optical properties. Indeed, even when extrapolated to zero temperature and exciton density, the decoherence times extracted from the homogeneous linewidths do not correspond to the exciton lifetime extracted from photoluminescence measurements. These short decoherence times but much longer emission decays would imply that excitons scatter in and out of the bright states into dark ones many times before they undergo radiative recombination. This transfer between bright and dark states could be responsible for the decrease in the homogeneous linewidths of bright excitons with population time, shown in Figure 10.1. As part of the bright population scatters into a dark state, the homogeneous linewidth reduces until the population transfer has occured. This would imply

that the bright states themselves are actually near degenerate, and only one of these near-degenerate bright states can scatter into the dark ones. Moreover, the fact that this decrease of homogeneous linewidth with population time depends on the nature of the exciton also suggests this coupling to a ladder of dark states to be complex. This decrease in homogeneous linewidth could also be related to the stabilisation of the polaronic cloud and the susbequent dynamic shielding of the exciton against external disorder. This phenomenon demands further investigations from both the experimental and theoretical sides, using dynamic population models to account for the coherent lineshape as well as probes sensitive to dark states such as two-photon absorption and excitation spectra or 2D photocurrent multidimensional spectroscopies.

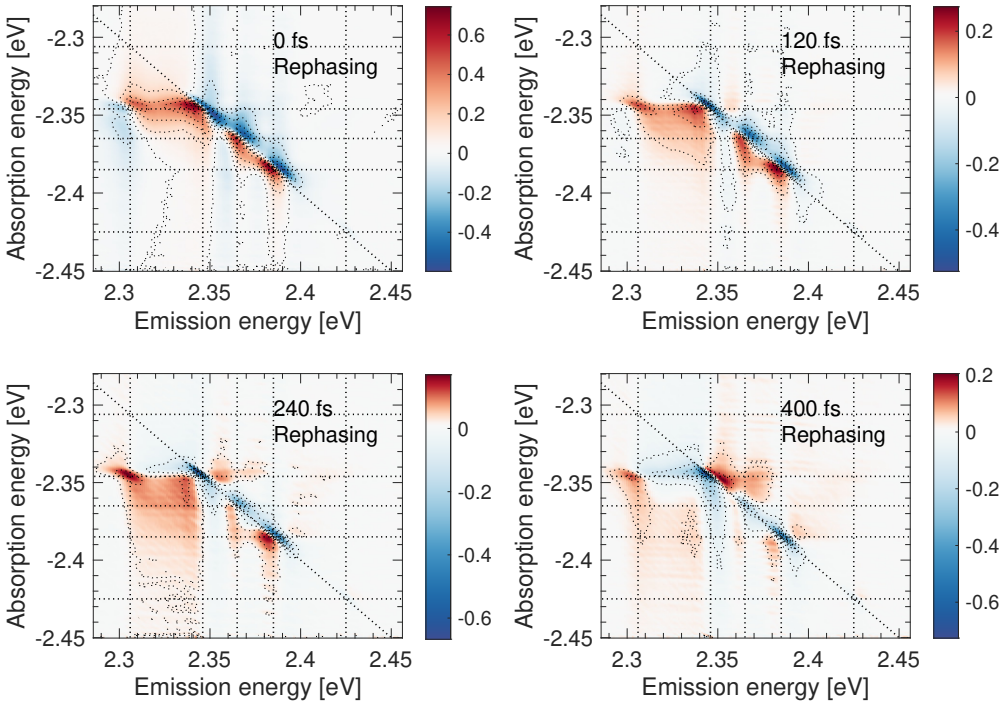

Figure 10.2: **Evolution of the low temperature rephasing two-dimensional lineshape with population time.** Shown is the real part of the rephasing spectra for 0 fs, 120 fs, 240 fs and 400 fs of population time delay for $(PEA)_2PbI_4$ at 5 K at a fluence of 40 nJ/cm^2.

Many mysteries also remain with regards to many-body interactions in 2D-HOIPs. By monitoring the homogeneous linewidth of each transition with increasing exciton density,

we have extracted the exciton-exciton interaction parameter. This parameter is related to dephasing induced by elastic collisions with other excitons and so is called excitation induced dephasing in the literature. However, many-body effects can also change the energy of exciton through excitation induced shift. This effect is usually small but is detectable through changes in the two-dimensional lineshape of an optical transition. This might be the cause of the observed changes in Figure 10.2 with population time. At zero population waiting time, all lineshapes feature a dispersive character. As the population time is increased, the lowest energy exciton becomes absorptive and then dispersive again. Changes in the lineshape of the other excitonic features, however, occur at a much slower pace and only become absorptive after 400 fs of waiting time. This again highlights the strong spectral diversity in many-body interactions present in 2D-HOIPs. An in-depth analysis through optical Bloch equations could reveal more clues regarding the role of the polaronic nature of excitons and its diversity in many-body interactions in these systems.

Another many-body phenomenon probed in this thesis work is that of biexcitonic binding at high-densities. Figure 9.4 of the previous chapter indicates the presence of a complex bound state structure in the second manifold of excited states. Indeed, given the complexity of the excitonic structure in 2D-HOIPs, one expects to have just as complex a biexcitonic structure. Moreover, data from Figure 9.3 also suggests that the binding energies of biexcitons depend on the nature of its exciton components. Due to the large excitation induced dephasing caused by the high excitation fluences used in the previous chapter, we were unable to investigate this complex biexcitonic spectrum without first improving the sensitivity of COLBERT. As shown by the high quality of the data acquired at very low fluences presented in chapter 8, this is now possible. By using a linearly cross-polarized pulse sequence, the correlations that do not arise from biexcitons would be strongly suppressed yielding a background free measurement of their spectrum [43]. This experiment would yield results of interest beyond mere many-body physics. Indeed, as high-energy particle physics has taught us, by observing how different excitons ”stick” or split when smashed

together, much could be learned about the nature of each excitons themselves. Moreover, if COLBERT's optical bandwidth can be increased to also cover the absorption continuum, collisional ionization processes, like excitonic Auger processes, and trion formation could also be investigated. All of the above experiments aim to answer questions regarding the role of polaronic effects in both elastic and inelastic many-body interactions as well as to decorticate the structure of the exciton-polarons themselves.

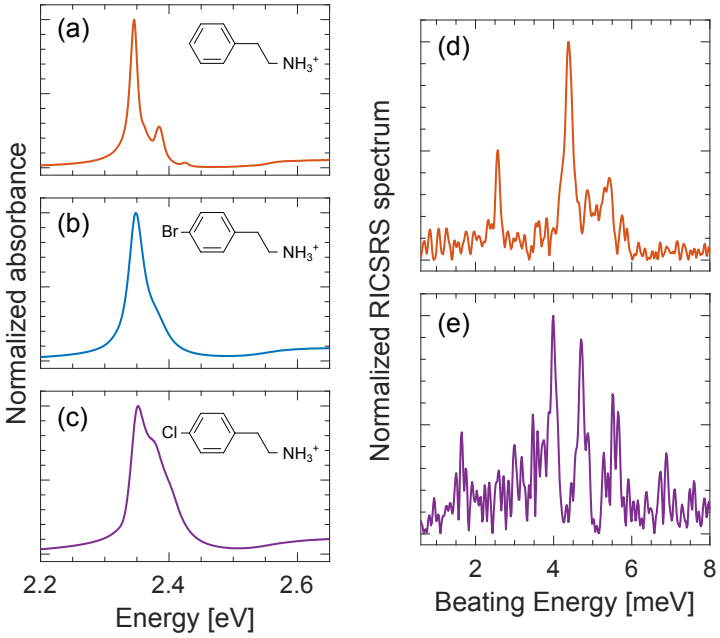

Figure 10.3: **Changes in the absorption spectrum and electron-phonon coupling with halogenation of the organic cation.** The absorption spectrum of (a) $(PEA)_2PbI_4$, (b) $(Br{-}PEA)_2PbI_4$ and (c) $(Cl{-}PEA)_2PbI_4$ at 5 K. The organic cation used in each compound is drawn in inset. The corresponding spectrally integrated RICSRS spectrum for (d) $(PEA)_2PbI_4$ and (e) $(Cl{-}PEA)_2PbI_4$ when pumping at 3.06 eV, in the carrier continuum.

An exciting aspect of the physics occurring in these materials is their occurence in real materials with a vast parameter space in terms of their structure and elemental composition. Now that we have identified many probes which investigate what seems to be the heart of the problem, we can use these material parameters as knobs to change the regime in which we observe these physical phenomena. For instance, we have recently shown that adding a mere nitro group at the fourth position of the PEA cation completely changes the emissive properties of the compound [290]. While this publication and many others are helping

better understand the role of the organic cation in stabilizing the structure of the inorganic layer, very little is known about the role of the latter in the optical properties of 2D-HOIPs. This thesis work shows a new method to tackle this problem: by investigating changes in the electron-phonon coupling using RICSRS and multidimensional spectroscopy. We have begun undertaking this endeavor with a series of halogenated cations shown in Figure 10.3. Due to slightly different interactions between cations and the inorganic lattice, the latter finds a slightly distinct equilibrium positon. This allows us to slightly turn the knob of bond orientation and octahedral distortion in the inorganic layer and study its effect on the polaronic properties. In the case of the halogenated cations, their absorption spectrum changes slightly but the displaced modes by an excitation into the carrier continuum are significantly different. By comparing both of these measurement to non-resonant Raman spectra, one could separate changes in phonon energy from changes in electron-phonon coupling. These measurements can be readily obtained using equipment found in most ultrafast spectroscopy laboratories. Furthermore, the impact of dynamic disorder on the excitonic degrees of freedom can be also be investigated by correlating the degree of disorder in the cation's motion (using NMR for instance [291]), the broadening of features in the non-resonant Raman spectrum and the homogeneous linewidths of the excitonic fine structure. These could be used to verify a recent preliminary claim that longer cation increases the dynamic disorder [9]. Such investigations are important to assess whether physics like that of Anderson localisation by the dynamic disorder could play a role in the extent of the exciton-polaron's wavefunction [292]. The atomic composition of each layers may be changed as well to understand how critical their exact nature is to the photophysics of 2D-HOIPs. For instance, the metal atom typically used if that of lead, a heavy metal with consequentially large spin-orbit interaction. Therefore, the effect of spin-orbit on the properties of excitons can be investigated by using tin instead, where these effects should be weaker. All of these aim at understanding the complex interplay between structure and optoelectronic properties in 2D-HOIPs.

To this end, our work could be the bridge between what seems to be two communities in the field. Those who work on broadband emitting 2D-HOIPs and those working on narrowband emitters. In the former, excitons are thought to be self-trapped excitons (small polarons) [7] while in the latter, they were thought until now to be regular excitons somewhere between the Frenkel and Wannier models [194]. However, I believe this thesis work shows that these are two manifestations of the same underlying phenomenon. Indeed, by taking equation 2.43 in the two-dimensional case, we see that depending on the sign of the difference between the kinetic energy term and the short-range electron-lattice interaction term, either a small or a large polaron forms, as seen in Figure 2.5b. Therefore, although long-range interactions are expected to be stronger due to the image charge effect, the bidimensional nature of the inorganic layer might be what allows short-range interactions to reduce the delocalizing contribution of the kinetic energy term, facilitating large polaron formation. When distorting the inorganic lattice from its ideal geometry, some bonds could become softer thus increasing the contribution of short-range interactions. This reduces the size of the large polarons or, if short-range interactions dominate the kinetic energy term, leads to the collapse into a small polaron or self-trapped exciton. What links the physics observed in broadband emitting 2D-HOIPs to that of narrow emitters could actually lie in the magnitude of short-range electron-phonon interactions. There are a few ways in which this could be tested experimentally. Short-range interactions stem from the interaction of electrons with a deformation potential or the piezoelectric effect. The former can be experimentally probed by monitoring the optical properties of the crystal while stress is applied to the crystalline structure using a diamond anvil. Strong short-range interactions should be manifested as strong electron-acoustic phonon interactions. These could be observed in ultrafast electron diffuse scattering but perhaps in the generation of acoustic wave following photoexcitation as well.

We finally address the elephants in the room: what causes the excitonic fine structure? Why are the states that compose it distinct exciton-polarons? This thesis work holds no

firm answer to these fundamental questions. However, having shown the polaronic nature of each excitons suggests that polaronic effects could be playing an important role in the appearance of the excitonic fine-structure. Indeed, when polaronic effects are present, the excitonic binding energy depends on the magnitude and spectrum of the exciton-phonon coupling. The distinct lattice coupling of each excitons should therefore change their binding energies and could lead to the observed fine-structure if the exciton-phonon couplings are sufficiently strong and distinct [71]. Only an accurate modelling of exciton-polarons in these systems using experimentally measured parameters will tell if this hypothesis is valid. Nonetheless, whether the fine-structure arises from exciton-polaronic effects or not, we are left with a problem of similar nature. We need to determine by which mechanisms are these states distinct from one another, with respect to either their energy or their polaronic nature. One strong contender for such a mechanism is that of spin-orbit coupling. It is known to be strong in 2D-HOIPs due to the presence of heavy metal atoms and can either shift the position of bands leading to the observed fine-structure directly or through the polaronic effect. This could be tested by investigating tin-based 2D-HOIPs as well as high-magnetic field measurements. However, the lack of a fine structure in recent calculations including spin-orbit coupling [10] indicate this effect might not arise when Coulomb coupling are not taken in consideration. However, the Wannier model does not predict the lifting of degeneracies of any kind but merely a reorganization of the existing Bloch waves into new states. This arises due to the Wannier approximation, which neglects the Coulomb exchange interaction by supposing paired electrons and holes are far appart. As we have shown in section 2.2.1, this leads to the disappearance of the exchange term in equation 2.9. The validity of the Wannier approximation in 2D-HOIPs, however, has been questioned ever since excitons were observed in these materials due to their small excitonic Bohr radius. Therefore, without completely invalidating the Wannier formalism, the Coulomb exchange term might induce corrections to the Wannier orbitals which lead to the observed fine structure, the polaronic character of excitons or both. Coulomb exchange in-

teractions were recently shown to give rise to the excitonic fine structure in 3D HOIPs [96]. Further crystalline fields then split the degeneracies of the resulting bright triplet. Given the larger excitonic Bohr radius of excitons in these systems, this effect should only be amplified in 2D-HOIPs. Then, crystalline fields due to the two-dimensional nature of the inorganic layers or polaronic effects could result in the observed fine structure. This claim could be verified in DFT calculations accounting for excitonic effects or solving the Hamiltonian of equation 2.9 without neglecting the exchange term and include polaronic effects as well. On the experimental side, experiments in high-magnetic fields could also help confirm or infirm this hypothesis. If it is found to be true, this would also cast doubts on the assignment of the low-energy excited state absorption observed in two-dimensional spectra to a biexcitonic transition. Indeed, exchange interactions predict the presence of a singlet dark state below an optically active triplet. The excited state absorption feature could then arise from a transition from a bright exciton to two unbound dark excitons. This would also explain the appearance of the feature labelled A^* in the absorption spectra of thick $(PEA)_2PbI_4$ samples where defects could relax the selection rules that darkened this state.

What all of the aforementioned perspectives show is that there is much more to do in order to understand these fascinating systems. My hope is that this thesis work motivates the community to investigate the most fundamental aspects of 2D-HOIPs in order to push our understanding of these materials to match those of well understood semiconductors are like GaAs quantum wells, Si or monolayers of transition metal dichalcogenides. This is necessary if these materials are to fulfill their technological promises by being used in optoelectronics applications or as materials in novel architectures exhibiting quantum phases of matter such as quantum fluids [50]. This would also significantly enrich our current understanding of two-dimensional physics and how dimensionality impacts physical models. These materials push semiconductor physics to their limits and the community has no choice but to rise up to the challenge they pose.

REFERENCES

[1] E. Schrödinger, "An Undulatory Theory of the Mechanics of Atoms and Molecules," *Physical Review*, vol. 28, no. 6, pp. 1049–1070, 1926.

[2] D. Fraser and A. Koberinski, "The Higgs mechanism and superconductivity: A case study of formal analogies," *Studies in History and Philosophy of Science Part B: Studies in History and Philosophy of Modern Physics*, vol. 55, pp. 72–91, 2016.

[3] D. B. Mitzi, "Templating and structural engineering in organic-inorganic perovskites," *Journal of the Chemical Society, Dalton Transactions*, no. 1, pp. 1–12, 2001.

[4] B. Saparov and D. B. Mitzi, "Organic-Inorganic Perovskites: Structural Versatility for Functional Materials Design," *Chemical Reviews*, vol. 116, no. 7, pp. 4558–4596, 2016.

[5] C. R. Groom, I. J. Bruno, M. P. Lightfoot, and S. C. Ward, "The Cambridge Structural Database," *Acta Crystallographica Section B*, vol. 72, no. 2, pp. 171–179, 2016.

[6] A. Shulgin and A. Shulgin, *Pihkal: A Chemical Love Story*. Transform Press, 1995, ISBN: 978-0-9630096-0-9.

[7] M. D. Smith and H. I. Karunadasa, "White-Light Emission from Layered Halide Perovskites," *Accounts of Chemical Research*, vol. 51, no. 3, pp. 619–627, 2018.

[8] D. Cortecchia, S. Neutzner, A. R. Srimath Kandada, E. Mosconi, D. Meggiolaro, F. D. Angelis, C. Soci, and A. Petrozza, "Broadband Emission in Two-Dimensional Hybrid Perovskites: The Role of Structural Deformation," *J. Am. Chem. Soc.*, vol. 139, pp. 39–42, 2017.

[9] D. B. Straus, N. Iotov, M. R. Gau, Q. Zhao, P. J. Carroll, and C. R. Kagan, "Longer Cations Increase Energetic Disorder in Excitonic 2D Hybrid Perovskites," *The Journal of Physical Chemistry Letters*, pp. 1198–1205, 2019.

[10] J. Even, L. Pedesseau, M.-A. Dupertuis, J.-M. Jancu, and C. Katan, "Electronic model for self-assembled hybrid organic/perovskite semiconductors: Reverse band edge electronic states ordering and spin-orbit coupling," *Physical Review B*, vol. 86, no. 20, p. 205 301, 2012.

[11] F. Bloch, "Über die Quantenmechanik der Elektronen in Kristallgittern.," *Zeitschrift für Physik*, vol. 52, no. 7-8, pp. 555–600, 1929.

[12] L. D. Landau, "The Theory of a Fermi Liquid," *Soviet Physics JETP*, vol. 3, no. 6, pp. 920–952, 1957.

[13] S Tomonaga, "Remark on Bloch's Method of Sound waves applied to Many-Fermion Problems," *Progress of Theoretical Physics*, vol. 5, no. 4, pp. 544–569, 1950.

[14] J. Luttinger, "An Exactly Soluble Model of a Many-Fermion System," *Journal of Mathematical Physics*, vol. 4, no. 9, pp. 1154–1162, 1963.

[15] J. Bardeen, L. N. Cooper, and J. R. Schrieffer, "Theory of Superconductivity," *Physical Review*, vol. 108, no. 5, pp. 1175–1204, 1957.

[16] ——, "Microscopic Theory of Superconductivity," *Physical Review*, vol. 106, no. 1, pp. 162–164, 1957.

[17] J. Frenkel, "On the Transformation of light into Heat in Solids. I," *Physical Review*, vol. 37, no. 1, pp. 17–44, 1931.

[18] G. H. Wannier, "The Structure of Electronic Excitation Levels in Insulating Crystals," *Physical Review*, vol. 52, no. 3, pp. 191–197, 1937.

[19] E. Hanamura and H. Haug, "Condensation effects of excitons," *Physics Reports*, vol. 33, no. 4, pp. 209–284, 1977.

[20] M. Combescot and S. Shiau, *Excitons and Cooper Pairs: Two Composite Bosons in Many-body Physics*, ser. Oxford graduate texts. Oxford University Press, 2016, ISBN: 978-0-19-875373-5.

[21] G. Dresselhaus, "Effective mass approximation for excitons," *J. Phys. Chem. Solids*, vol. 1, pp. 14–23, 1956.

[22] D. Griffiths, *Introduction to Quantum Mechanics*. Cambridge University Press, 2016, ISBN: 978-1-107-17986-8.

[23] H. Haug and S. W. Koch, *Quantum theory of the optical and electronic properties of semiconductors*, 4th ed. Singapore ; River Edge, NJ: World Scientific, 2004, ISBN: 978-981-238-609-0 978-981-238-756-1.

[24] S. A. Moskalenko and D. W. Snoke, *Bose-Einstein Condensation of Excitons and Biexcitons: And Coherent Nonlinear Optics with Excitons*. Cambridge University Press, 2000.

[25] B. Laikhtman and R. Rapaport, "Exciton correlations in coupled quantum wells and their luminescence blue shift," *Physical Review B*, vol. 80, no. 19, p. 195 313, 2009.

[26] N. F. Mott, "Metal-Insulator Transition," *Reviews of Modern Physics*, vol. 40, no. 4, pp. 677–683, 1968.

[27] J. Shah, M. Combescot, and A. H. Dayem, "Investigation of Exciton-Plasma Mott Transition in Si," *Physical Review Letters*, vol. 38, no. 25, pp. 1497–1500, 1977.

[28] A. Splendiani, L. Sun, Y. Zhang, T. Li, J. Kim, C.-Y. Chim, G. Galli, and F. Wang, "Emerging Photoluminescence in Monolayer MoS $_2$," *Nano Letters*, vol. 10, no. 4, pp. 1271–1275, 2010.

[29] E. F. Gross, "Optical spectrum of excitons in the crystal lattice," *Il Nuovo Cimento*, vol. 3, no. S4, pp. 672–701, 1956.

[30] J. H. Apfel and L. N. Hadley, "Exciton Absorption in Cuprous Oxide," *Physical Review*, vol. 100, no. 6, pp. 1689–1691, 1955.

[31] S. B. Nam, D. C. Reynolds, C. W. Litton, R. J. Almassy, T. C. Collins, and C. M. Wolfe, "Free-exciton energy spectrum in GaAs," *Physical Review B*, vol. 13, no. 2, pp. 761–767, 1976.

[32] R. C. Miller and D. Kleinman, "Excitons in GaAs quantum wells," *Journal of Luminescence*, vol. 30, pp. 520–540, 1985.

[33] D. Thomas, "The exciton spectrum of zinc oxide," *Journal of Physics and Chemistry of Solids*, vol. 15, no. 1-2, pp. 86–96, 1960.

[34] L. C. Thanh, C Depeursinge, F Levy, and E Mooser, "The band gap exciton in PbI_2," *J. Phys. Chem. Solids*, vol. 36, pp. 699–702, 1975.

[35] G. Macfarlane, T. McLean, J. Quarrington, and V. Roberts, "Exciton and phonon effects in the absorption spectra of germanium and silicon," *Journal of Physics and Chemistry of Solids*, vol. 8, pp. 388–392, 1959.

[36] C. Kittel, *Introduction to solid state physics*, 8th ed. Hoboken, NJ: Wiley, 2005, ISBN: 978-0-471-41526-8.

[37] A. Rustagi and A. F. Kemper, "Photoemission signature of excitons," *Physical Review B*, vol. 97, no. 23, p. 235 310, 2018.

[38] R. J. Elliott, "Intensity of Optical Absorption by Excitons," *Physical Review*, vol. 108, no. 6, pp. 1384–1389, 1957.

[39] E. R. Bittner, *Quantum dynamics: applications in biological and materials systems*. CRC press, 2009.

[40] T. Kazimierczuk, D. Frhlich, S. Scheel, H. Stolz, and M. Bayer, "Giant Rydberg excitons in the copper oxide Cu_2O," *Nature*, vol. 514, no. 7522, pp. 343–347, 2014.

[41] T. Meier, P. Thomas, and S. Koch, *Coherent Semiconductor Optics: From Basic Concepts to Nanostructure Applications*. Springer Berlin Heidelberg, 2006, ISBN: 978-3-540-32554-3.

[42] K. F. Mak, K. He, C. Lee, G. H. Lee, J. Hone, T. F. Heinz, and J. Shan, "Tightly bound trions in monolayer MoS_2," *Nature Materials*, vol. 12, no. 3, pp. 207–211, 2013.

[43] K. W. Stone, D. B. Turner, K. Gundogdu, S. T. Cundiff, and K. A. Nelson, "Exciton-exciton correlations revealed by two quantum, two-dimensional Fourier transform optical spectroscopy," *Accounts of Chemical Research*, vol. 42, no. 9, pp. 1452–1461, 2009.

[44] Y. You, X.-X. Zhang, T. C. Berkelbach, M. S. Hybertsen, D. R. Reichman, and T. F. Heinz, "Observation of biexcitons in monolayer WSe_2," *Nature Physics*, vol. 11, pp. 477–482, 2015.

[45] D. B. Turner and K. A. Nelson, "Coherent measurements of high-order electronic correlations in quantum wells," *Nature*, vol. 466, p. 1089, 2010.

[46] J. R. Haynes, "Experimental Observation of the Excitonic Molecule," *Physical Review Letters*, vol. 17, no. 16, pp. 860–862, 1966.

[47] M. Stern, V. Umansky, and I. Bar-Joseph, "Exciton liquid in coupled quantum wells.," *Science (New York, N.Y.)*, vol. 343, no. 6166, pp. 55–7, 2014.

[48] T. M. Rice, "The Electron-Hole Liquid in Semiconductors: Theoretical Aspects," in, ser. Solid State Physics, H. Ehrenreich, F. Seitz, and D. Turnbull, Eds., vol. 32, Academic Press, 1978, pp. 1 –86.

[49] C. Ciuti, V. Savona, C. Piermarocchi, A. Quattropani, and P. Schwendimann, "Role of the exchange of carriers in elastic exciton-exciton scattering in quantum wells," *Physical Review B*, vol. 58, no. 12, pp. 7926–7933, 1998.

[50] I. Carusotto and C. Ciuti, "Quantum fluids of light," *Reviews of Modern Physics*, vol. 85, no. 1, pp. 299–368, 2013.

[51] J Franck, "Elementary processes of photochemical reactions," *Transactions of the Faraday Society*, vol. 21, pp. 536–542, 1926.

[52] E. Condon, "A Theory of Intensity Distribution in Band Systems," *Physical Review*, vol. 28, no. 6, pp. 1182–1201, 1926.

[53] M Pope and C. E. Swenberg, *Electronic processes in organic crystals and polymers*. Oxford: Oxford University Press, 1999.

[54] M. Kasha, "Characterization of electronic transitions in complex molecules," *Discussions of the Faraday Society*, vol. 9, p. 14, 1950.

[55] F. C. Spano and C. Silva, "H- and J-aggregate behavior in polymeric semiconductors," *Annual review of physical chemistry*, vol. 65, pp. 477–500, 2014.

[56] A. B. Myers, "'Time-Dependent' Resonance Raman Theory," *J. Raman Spectrosc.*, vol. 28, pp. 389–401, 1997.

[57] S.-Y. Lee and E. J. Heller, "Time-dependent theory of Raman scattering," *The Journal of Chemical Physics*, vol. 71, no. 12, p. 4777, 1979.

[58] D. Emin, *Polarons*. Cambridge University press, 2013.

[59] J. T. Devreese and A. S. Alexandrov, "Fröhlich polaron and bipolaron: Recent developments," *Reports on Progress in Physics*, vol. 72, no. 6, p. 066 501, 2009.

[60] H. Fröhlich, "Electrons in lattice fields," *Advances in Physics*, vol. 3, no. 11, pp. 325–361, 1954.

[61] D. Snoke, *Solid State Physics: Essential Concepts*. Addison-Wesley, 2009, ISBN: 978-0-321-60550-4.

[62] S. Neutzner, F. Thouin, D. Cortecchia, A. Petrozza, C. Silva, and A. R. Srimath Kandada, "Exciton-polaron spectral structures in two-dimensional hybrid lead-halide perovskites," *Physical Review Materials*, vol. 2, no. 6, p. 064 605, 2018.

[63] D. Emin and T. Holstein, "Adiabatic Theory of an Electron in a Deformable Continuum," *Physical Review Letters*, vol. 36, no. 6, pp. 323–326, 1976.

[64] Y. Toyozawa, "Self-Trapping of an Electron by the Acoustical Mode of Lattice Vibration. I," *Progress of Theoretical Physics*, vol. 26, no. 1, pp. 29–44, 1961.

[65] J. Pollmann and H. Buttner, "Effective Hamiltonians and bindings energies of Wannier excitons in polar semiconductors," *Phys. Rev. B*, vol. 16, no. 10, pp. 4480–4490, 1977.

[66] O. Verzelen, R. Ferreira, and G. Bastard, "Excitonic Polarons in Semiconductor Quantum Dots," *Physical Review Letters*, vol. 88, no. 14, p. 146 803, 2002.

[67] R. T. Senger and K. K. Bajaj, "Binding energies of excitons in polar quantum well heterostructures," *Phys. Rev. B*, vol. 68, no. 20, p. 205 314, 2003.

[68] V. Preisler, T. Grange, R. Ferreira, L. A. de Vaulchier, Y. Guldner, F. J. Teran, M. Potemski, and A. Lematre, "Evidence for excitonic polarons in InAs/GaAs quantum dots," *Physical Review B*, vol. 73, no. 7, p. 075 320, 2006.

[69] U. Woggon, D. Miller, F. Kalina, B. Gerlach, D. Kayser, K. Leonardi, and D. Hommel, "Bound polarons in semiconductor nanostructures," *Physical Review B*, vol. 67, no. 4, p. 045 204, 2003.

[70] J. Conradi and R. R Haering, "Oscillatory Exciton Emission in CdS," *Physical Review Letters*, vol. 20, no. 24, pp. 1344–1346, 1968.

[71] R. Zheng and M. Matsuura, "Polaronic effects on excitons in quantum wells," *Physical Review B*, vol. 57, no. 3, pp. 1749–1761, 1998.

[72] G. Dresselhaus, "Spin-Orbit Coupling Effects in Zinc Blende Structures," *Physical Review*, vol. 100, no. 2, pp. 580–586, 1955.

[73] F. T. Vas'ko, "Spin splitting in the spectrum of two-dimensional electrons due to the surface potential," *Soviet Journal of Experimental and Theoretical Physics Letters*, vol. 30, p. 541, 1979.

[74] Y. A. Bychkov and e. I. Rashba, "Properties of a 2D electron gas with lifted spectral degeneracy," *Soviet Journal of Experimental and Theoretical Physics Letters*, vol. 39, p. 78, 1984.

[75] C. R. Ast, J. Henk, A. Ernst, L. Moreschini, M. C. Falub, D. Pacilé, P. Bruno, K. Kern, and M. Grioni, "Giant Spin Splitting through Surface Alloying," *Physical Review Letters*, vol. 98, no. 18, p. 186 807, 2007.

[76] J. Nitta, T. Akazaki, H. Takayanagi, and T. Enoki, "Gate Control of Spin-Orbit Interaction in an Inverted $In_{0.53}Ga_{0.47}As/In_{0.52}Al_{0.48}As$ Heterostructure," *Physical Review Letters*, vol. 78, no. 7, pp. 1335–1338, 1997.

[77] G. Bihlmayer, Y. Koroteev, P. Echenique, E. Chulkov, and S. Blgel, "The Rashba-effect at metallic surfaces," *Surface Science*, vol. 600, no. 18, pp. 3888–3891, 2006.

[78] T. Ishihara, J. Takahashi, and T. Goto, "Exciton state in two-dimensional perovskite semiconductor $(C_{10}H_{21}NH_3)_2PbI_4$," *Solid State Communications*, vol. 69, no. 9, pp. 933–936, 1989.

[79] X. Hong, T. Ishihara, and A. V. Nurmikko, "Dielectric confinement effect on excitons in PbI_4-based layered semiconductors," *Physical Review B*, vol. 45, no. 12, pp. 6961–6964, 1992.

[80] G. Wang, A. Chernikov, M. M. Glazov, T. F. Heinz, X. Marie, T. Amand, and B. Urbaszek, "Colloquium : Excitons in atomically thin transition metal dichalcogenides," *Reviews of Modern Physics*, vol. 90, no. 2, p. 021 001, 2018.

[81] T Ishihara, X Hong, and J Ding, "Dielectric confinement effect for exciton and biexciton states in PbI_4-based two-dimensional semiconductor structures," *Surface Science*, vol. 267, pp. 323–326, 1992.

[82] K. Hao, J. F. Specht, P. Nagler, L. Xu, K. Tran, A. Singh, C. K. Dass, C. Schller, T. Korn, M. Richter, A. Knorr, X. Li, and G. Moody, "Neutral and charged intervalley biexcitons in monolayer MoSe," *Nat. Commun.*, vol. 8, p. 15 552, 2017.

[83] T. Kondo, T. Azuma, T. Yuasa, and R. Ito, "Biexciton lasing in the layered perovskite-type material $(C_6H_{13}NH_3)_2PbI_4$," *Solid State Commun.*, vol. 105, no. 4, pp. 253–255, 1998.

[84] M. H. Elkins, R. Pensack, A. H. Proppe, O. Voznyy, L. N. Quan, S. O. Kelley, E. H. Sargent, and G. D. Scholes, "Biexciton Resonances Reveal Exciton Localization in Stacked Perovskite Quantum Wells," *Journal of Physical Chemistry Letters*, vol. 8, no. 16, pp. 3895–3901, 2017.

[85] N. Kitazawa, T. Ito, D. Sakasegawa, and Y. Watanabe, "Excitons in self-organized layered perovskite films prepared by the two-step growth process," *Thin Solid Films*, vol. 500, no. 1-2, pp. 133–137, 2006.

[86] D. Sapori, M. Kepenekian, L. Pedesseau, C. Katan, and J. Even, "Quantum confinement and dielectric profiles of colloidal nanoplatelets of halide inorganic and hybrid organic-inorganic perovskites," *Nanoscale*, vol. 8, no. 12, pp. 6369–6378, 2016.

[87] A. R. Amori, Z. Hou, and T. D. Krauss, "Excitons in Single-Walled Carbon Nanotubes and Their Dynamics," *Annual Review of Physical Chemistry*, vol. 69, no. 1, pp. 81–99, 2018.

[88] M. Kumagai and T. Takagahara, "Excitonic and nonlinear-optical properties of dielectric quantum-well structures," *Physical Review B*, vol. 40, no. 18, pp. 12 359–12 381, 1989.

[89] K. Tanaka and T. Kondo, "Bandgap and exciton binding energies in lead-iodide-based natural quantum-well crystals," *Science and Technology of Advanced Materials*, vol. 4, no. 6, pp. 599–604, 2003.

[90] J. Even, L. Pedesseau, and C. Katan, "Understanding Quantum Confinement of Charge Carriers in Layered 2D Hybrid Perovskites," *ChemPhysChem*, vol. 15, no. 17, pp. 3733–3741, 2014.

[91] T. Kataoka, T. Kondo, R. Ito, S. Sasaki, K. Uchida, and N. Miura, "Magneto-optical study on excitonic spectra in $(C_6H_{13}NH_3)_2PbI_4$," *Physical Review B*, vol. 47, no. 4, pp. 2010–2018, 1993.

[92] K. Ema, K. Umeda, M. Toda, C. Yajima, Y. Arai, H. Kunugita, D. Wolverson, and J. J. Davies, "Huge exchange energy and fine structure of excitons in an organic-inorganic quantum well material," *Physical Review B*, vol. 73, no. 24, p. 241 310, 2006.

[93] T. Goto, H. Makino, T. Yao, C. H. Chia, T. Makino, Y. Segawa, G. A. Mousdis, and G. C. Papavassiliou, "Localization of triplet excitons and biexcitons in the two-dimensional semiconductor ($CH_3C_6H_4CH_2NH_3)_2PbBr_4$," *Physical Review B*, vol. 73, no. 11, p. 115 206, 2006.

[94] A. Fieramosca, L. De Marco, M. Passoni, L. Polimeno, A. Rizzo, B. L. T. Rosa, G. Cruciani, L. Dominici, M. De Giorgi, G. Gigli, L. C. Andreani, D. Gerace, D. Ballarini, and D. Sanvitto, "Tunable Out-of-Plane Excitons in 2D Single-Crystal Perovskites," *ACS Photonics*, vol. 5, no. 10, pp. 4179–4185, 2018.

[95] C. Yin, L. Chen, N. Song, Y. Lv, F. Hu, C. Sun, W. W. Yu, C. Zhang, X. Wang, Y. Zhang, and M. Xiao, "Bright-Exciton Fine-Structure Splittings in Single Perovskite Nanocrystals," *Physical Review Letters*, vol. 119, no. 2, p. 026 401, 2017.

[96] P. Tamarat, M. I. Bodnarchuk, J.-B. Trebbia, R. Erni, M. V. Kovalenko, J. Even, and B. Lounis, "The ground exciton state of formamidinium lead bromide perovskite nanocrystals is a singlet dark state," *Nature Materials*, 2019.

[97] M. A. Becker, R. Vaxenburg, G. Nedelcu, P. C. Sercel, A. Shabaev, M. J. Mehl, J. G. Michopoulos, S. G. Lambrakos, N. Bernstein, J. L. Lyons, T. Stferle, R. F. Mahrt, M. V. Kovalenko, D. J. Norris, G. Rain, and A. L. Efros, "Bright triplet excitons in caesium lead halide perovskites," *Nature*, vol. 553, p. 189, 2018.

[98] D. B. Straus, S. Hurtado Parra, N. Iotov, J. Gebhardt, A. M. Rappe, J. E. Subotnik, J. M. Kikkawa, and C. R. Kagan, "Direct Observation of Electron-Phonon Coupling and Slow Vibrational Relaxation in Organic-Inorganic Hybrid Perovskites," *Journal of the American Chemical Society*, vol. 138, no. 42, pp. 13 798–13 801, 2016.

[99] X.-Y. Zhu and V. Podzorov, "Charge Carriers in Hybrid Organic-Inorganic Lead Halide Perovskites Might Be Protected as Large Polarons," *The Journal of Physical Chemistry Letters*, vol. 6, no. 23, pp. 4758–4761, 2015.

[100] K. Miyata, D. Meggiolaro, M. T. Trinh, P. P. Joshi, E. Mosconi, S. C. Jones, F. De Angelis, and X.-Y. Zhu, "Large polarons in lead halide perovskites," *Science Advances*, vol. 3, no. 8, e1701217, 2017.

[101] Y. Yang, D. P. Ostrowski, R. M. France, K. Zhu, J. van de Lagemaat, J. M. Luther, and M. C. Beard, "Observation of a hot-phonon bottleneck in lead-iodide perovskites," *Nature Photonics*, vol. 10, no. 1, pp. 53–59, 2016.

[102] J. M. Frost, L. D. Whalley, and A. Walsh, "Slow Cooling of Hot Polarons in Halide Perovskite Solar Cells," *ACS Energy Letters*, vol. 2, no. 12, pp. 2647–2652, 2017.

[103] M. Park, A. J. Neukirch, S. E. Reyes-Lillo, M. Lai, S. R. Ellis, D. Dietze, J. B. Neaton, P. Yang, S. Tretiak, and R. A. Mathies, "Excited-state vibrational dynamics toward the polaron in methylammonium lead iodide perovskite," *Nature Commun.*, vol. 9, no. 1, p. 2525, 2018.

[104] K. Gauthron, J.-S. Lauret, L. Doyennette, G. Lanty, A. A. Choueiry, S. J. Zhang, A. Brehier, L. Largeau, O. Mauguin, J. Bloch, and E. Deleporte, "Optical spectroscopy of two-dimensional layered $(C_6H_5C_2H_4NH_3)_2PbI_4$ perovskite," *Opt. Express*, vol. 18, no. 6, pp. 5912–5919, 2010.

[105] M. Kepenekian and J. Even, "Rashba and Dresselhaus Couplings in Halide Perovskites: Accomplishments and Opportunities for Spintronics and Spin-Orbitronics," *The Journal of Physical Chemistry Letters*, vol. 8, no. 14, pp. 3362–3370, 2017.

[106] D. Niesner, M. Wilhelm, I. Levchuk, A. Osvet, S. Shrestha, M. Batentschuk, C. Brabec, and T. Fauster, "Giant Rashba Splitting in $CH_3NH_3PbBr_3$ Organic-Inorganic Perovskite," *Physical Review Letters*, vol. 117, no. 12, p. 126 401, 2016.

[107] Y. Zhai, S. Baniya, C. Zhang, J. Li, P. Haney, C.-X. Sheng, E. Ehrenfreund, and Z. V. Vardeny, "Giant Rashba splitting in 2D organic-inorganic halide perovskites measured by transient spectroscopies," *Science Advances*, vol. 3, no. 7, e1700704, 2017.

[108] J. D. Hybl, A. W. Albrecht, S. M. G. Faeder, and D. M. Jonas, "Two-dimensional electronic spectroscopy," vol. 297, no. 3-4, pp. 307–313, 1998.

[109] S. Mukamel, *Principles of nonlinear optical spectroscopy*, ser. Oxford series in optical and imaging sciences. Oxford University Press, 1995, ISBN: 978-0-19-509278-3.

[110] P. Kjellberg, B. Brggemann, and T. Pullerits, "Two-dimensional electronic spectroscopy of an excitonically coupled dimer," *Physical Review B*, vol. 74, no. 2, p. 024 303, 2006.

[111] S. M. Gallagher Faeder and D. M. Jonas, "Two-Dimensional Electronic Correlation and Relaxation Spectra: Theory and Model Calculations," *The Journal of Physical Chemistry A*, vol. 103, no. 49, pp. 10 489–10 505, 1999.

[112] A. T. Kumar, F. Rosca, A. Widom, and P. M. Champion, "Investigations of amplitude and phase excitation profiles in femtosecond coherence spectroscopy," *J. Chem. Phys.*, vol. 114, no. 2, pp. 701–724, 2001.

[113] R Merlin, "Generating coherent THz phonons with light pulses," *Solid State Commun.*, vol. 102, no. 2-3, pp. 207–220, 1997.

[114] L. Dhar, J. A. Rogers, and K. A. Nelson, "Time-resolved vibrational spectroscopy in the impulsive limit," *Chem. Rev.*, vol. 94, no. 1, pp. 157–193, 1994.

[115] A. Tokmakoff, "Two-Dimensional Line Shapes Derived from Coherent Third-Order Nonlinear Spectroscopy," *The Journal of Physical Chemistry A*, vol. 104, no. 18, pp. 4247–4255, 2000.

[116] D. Karaiskaj, A. D. Bristow, L. Yang, X. Dai, R. P. Mirin, S. Mukamel, and S. T. Cundiff, "Two-Quantum Many-Body Coherences in Two-Dimensional Fourier-Transform Spectra of Exciton Resonances in Semiconductor Quantum Wells," *Physical Review Letters*, vol. 104, no. 11, p. 117 401, 2010.

[117] J. O. Tollerud, S. T. Cundiff, and J. A. Davis, "Revealing and Characterizing Dark Excitons Through Coherent Multidimensional Spectroscopy," vol. 097401, no. August, pp. 1–6, 2016.

[118] P. Hamm and M. Zanni, *Concepts and Methods of 2D Infrared Spectroscopy*. Cambridge: Cambridge University Press, 2011, ISBN: 978-1-107-00005-6.

[119] F. V.D. A. Camargo, L. Grimmelsmann, H. L. Anderson, S. R. Meech, and I. A. Heisler, "Resolving Vibrational from Electronic Coherences in Two-Dimensional Electronic Spectroscopy : The Role of the Laser Spectrum," vol. 033001, no. January, pp. 1–6, 2017.

[120] N. Christensson, F. Milota, J. Hauer, J. Sperling, O. Bixner, A. Nemeth, and H. F. Kauffmann, "High Frequency Vibrational Modulations in Two-Dimensional Electronic Spectra and Their Resemblance to Electronic Coherence Signatures," *The Journal of Physical Chemistry B*, vol. 115, no. 18, pp. 5383–5391, 2011.

[121] P. Hamm, "Principles of Nonlinear Optical Spectroscopy : A Practical Approach or : Mukamel for Dummies," *University of Zurich*, vol. 41, no. 5, p. 77, 2005.

[122] M. E. Siemens, G. Moody, H. Li, A. D. Bristow, and S. T. Cundiff, "Resonance lineshapes in two-dimensional Fourier transform spectroscopy," *Optics Express*, vol. 18, no. 17, pp. 17 699–17 708, 2010.

[123] A. D. Bristow, T. Zhang, M. E. Siemens, S. T. Cundiff, and R. P. Mirin, "Separating Homogeneous and Inhomogeneous Line Widths of Heavy- and Light-Hole

Excitons in Weakly Disordered Semiconductor Quantum Wells," *The Journal of Physical Chemistry B*, vol. 115, no. 18, pp. 5365–5371, 2011.

[124] X. Li, T. Zhang, C. N. Borca, and S. T. Cundiff, "Many-Body Interactions in Semiconductors Probed by Optical Two-Dimensional Fourier Transform Spectroscopy," *Physical Review Letters*, vol. 96, no. 5, p. 057 406, 2006.

[125] J. M. Shacklette and S. T. Cundiff, "Role of excitation-induced shift in the coherent optical response of semiconductors," *Physical Review B*, vol. 66, no. 4, p. 045 309, 2002.

[126] G. Moody, C. Kavir Dass, K. Hao, C.-H. Chen, L.-J. Li, A. Singh, K. Tran, G. Clark, X. Xu, G. Berghuser, E. Malic, A. Knorr, and X. Li, "Intrinsic homogeneous linewidth and broadening mechanisms of excitons in monolayer transition metal dichalcogenides," *Nature Communications*, vol. 6, no. 1, p. 8315, 2015.

[127] H. O. Sibum, "What Kind of Science Is Experimental Physics?" *Science*, vol. 306, no. 5693, pp. 60–61, 2004.

[128] D. Strickland and G. Mourou, "Compression of amplified chirped optical pulses," *Optics Communications*, vol. 56, no. 3, pp. 219 –221, 1985.

[129] R Baumgartner and R Byer, "Optical parametric amplification," *Quantum Electronics, IEEE Journal of*, vol. 15, no. 6, pp. 432–444, 1979.

[130] J. A. Giordmaine and R. C. Miller, "Tunable Coherent Parametric Oscillation in $LiNbO_3$ at Optical Frequencies," *Physical Review Letters*, vol. 14, no. 24, pp. 973–976, 1965.

[131] S. Akhmanov, A. Kovrigin, A. Piskarskas, V. Fadeev, and R. Khokhlov, "Observation of parametric amplification in the optical range," *Jetp Lett*, vol. 2, no. 7, p. 191, 1965.

[132] A. L. Gaeta, "Catastrophic Collapse of Ultrashort Pulses," *Physical Review Letters*, vol. 84, no. 16, pp. 3582–3585, 2000.

[133] R. R. Alfano and S. L. Shapiro, "Emission in the Region 4000 to 7000 å Via Four-Photon Coupling in Glass," *Physical Review Letters*, vol. 24, no. 11, pp. 584–587, 1970.

[134] R. W. Boyd, *Nonlinear Optics, Third Edition*, 3rd. Orlando, FL, USA: Academic Press, Inc., 2008, ISBN: 0-12-369470-1 978-0-12-369470-6.

[135] G. Cerullo and S. De Silvestri, "Ultrafast optical parametric amplifiers," *Review of Scientific Instruments*, vol. 74, no. 1, p. 1, 2003.

[136] B. Saleh and M. Teich, *Fundamentals of Photonics*, ser. Wiley Series in Pure and Applied Optics. Wiley, 2007, ISBN: 978-0-471-35832-9.

[137] C Manzoni and G Cerullo, "Design criteria for ultrafast optical parametric amplifiers," *Journal of Optics*, vol. 18, no. 10, pp. 1–33, 2016, Publisher: IOP Publishing.

[138] C Homann, C Schriever, P Baum, and E Riedle, "Octave wide tunable UV-pumped NOPA : Pulses down to 20 fs at 0.5 MHz repetition rate," *Optics Express*, vol. 16, no. 8, pp. 5746–5756, 2008, ISBN: 1062710630.

[139] P. F. Tekavec, G. A. Lott, and A. H. Marcus, "Fluorescence-detected two-dimensional electronic coherence spectroscopy by acousto-optic phase modulation," *J. Chem. Phys.*, vol. 127, no. 21, p. 214 307, 2007.

[140] D. Brida, C. Manzoni, and G. Cerullo, "Phase-locked pulses for two-dimensional spectroscopy by a birefringent delay line," vol. 37, no. 15, pp. 3027–3029, 2012.

[141] B. Lomsadze and S. T. Cundiff, "Frequency combs enable rapid and high-resolution multidimensional coherent spectroscopy," *Science*, vol. 357, no. 6358, pp. 1389–1391, 2017.

[142] A. D. Bristow, D. Karaiskaj, X. Dai, T. Zhang, C. Carlsson, K. R. Hagen, R. Jimenez, and S. T. Cundiff, "A versatile ultrastable platform for optical multidimensional Fourier-transform spectroscopy," *Review of Scientific Instruments*, vol. 80, no. 7, p. 073 108, 2009.

[143] D. B. Turner, K. W. Stone, K. Gundogdu, and K. A. Nelson, "Invited Article: The coherent optical laser beam recombination technique (COLBERT) spectrometer: Coherent multidimensional spectroscopy made easier," *Review of Scientific Instruments*, vol. 82, no. 8, p. 081 301, 2011.

[144] S. Akturk, X. Gu, E. Zeek, and R. Trebino, "Pulse-front tilt caused by spatial and temporal chirp.," *Optics express*, vol. 12, no. 19, pp. 4399–4410, 2004.

[145] J. Hebling, "Derivation of the pulse front tilt caused by angular dispersion," *Optical and Quantum Electronics*, vol. 28, pp. 1759–1763, 1996.

[146] A. A. Maznev, T. F. Crimmins, and K. A. Nelson, "How to make femtosecond pulses overlap.," *Optics letters*, vol. 23, no. 17, pp. 1378–80, 1998.

[147] A. M. Weiner, "Femtosecond pulse shaping using spatial light modulators," *Review of Scientific Instruments*, vol. 71, no. 5, pp. 1929–1960, 2000.

[148] J. C. Vaughan, T Feurer, and K. A. Nelson, "Automated two-dimensional femtosecond pulse shaping," vol. 19, no. 10, pp. 2489–2495, 2002.

[149] J. C. Vaughan, T. Hornung, T Feurer, and K. a. Nelson, "Diffraction-based femtosecond pulse shaping with a two-dimensional spatial light modulator.," *Optics letters*, vol. 30, no. 3, pp. 323–325, 2005.

[150] B. von Vacano, T. Buckup, and M. Motzkus, "Shaper-assisted collinear SPIDER: Fast and simple broadband pulse compression in nonlinear microscopy," *Journal of the Optical Society of America B*, vol. 24, no. 5, p. 1091, 2007.

[151] I. Amat-Roldn, I. Cormack, P. Loza-Alvarez, E. Gualda, and D. Artigas, "Ultrashort pulse characterisation with SHG collinear-FROG.," *Optics express*, vol. 12, no. 6, pp. 1169–1178, 2004.

[152] J. Vaughan, T Feurer, K. Stone, and K. Nelson, "Analysis of replica pulses in femtosecond pulse shaping with pixelated devices.," *Optics express*, vol. 14, no. 3, pp. 1314–1328, 2006.

[153] C. Dorrer, N. Belabas, J.-P. Likforman, and M. Joffre, "Spectral resolution and sampling issues in Fourier-transform spectral interferometry," *Journal of the Optical Society of America B*, vol. 17, no. 10, p. 1795, 2000.

[154] M. H. Levitt, P. Madhu, and C. E. Hughes, "Cogwheel Phase Cycling," *Journal of Magnetic Resonance*, vol. 155, no. 2, pp. 300–306, 2002.

[155] V. Loriot, G. Gitzinger, and N. Forget, "Self-referenced characterization of femtosecond laser pulses by chirp scan," *Optics Express*, vol. 21, no. 21, pp. 24 879–24 893, 2013.

[156] V. V. Lozovoy, I. Pastirk, and M. Dantus, "Multiphoton intrapulse interference IV Ultrashort laser pulse spectral phase characterization and compensation," *Optics Letters*, vol. 29, no. 7, p. 775, 2004.

[157] S. Roberson and P. Pellegrino, "Compression of Ultrafast Laser Beams," Defense Technical Information Center, Fort Belvoir, VA, Tech. Rep., 2016.

[158] R. Trebino, *Frequency-Resolved Optical Gating: The Measurement of Ultrashort Laser Pulses: The Measurement of Ultrashort Laser Pulses*. Springer US, 2000, ISBN: 978-1-4020-7066-2.

[159] K. W. DeLong, R. Trebino, J. Hunter, and W. E. White, "Frequency-resolved optical gating with the use of second-harmonic generation," *Journal of the Optical Society of America B*, vol. 11, no. 11, p. 2206, 1994.

[160] J. Even, L. Pedesseau, and C. Katan, "Analysis of multivalley and multibandgap absorption and enhancement of free carriers related to exciton screening in hybrid

perovskites," *Journal of Physical Chemistry C*, vol. 118, no. 22, pp. 11 566–11 572, 2014, ISBN: 1932-7447.

[161] G. Bastard, E. Mendez, L. Chang, and L. Esaki, "Exciton binding energy in quantum wells," *Physical Review B - Condensed Matter and Materials Physics*, vol. 26, no. 4, pp. 1974–1979, 1982.

[162] J. C. Maan, G. Belle, A. Fasolino, M. Altarelli, and K. Ploog, "Magneto-optical determination of exciton binding energy in GaAs-$Ga_{1-x}Al_xAs$ quantum wells," *Physical Review B*, vol. 30, no. 4, pp. 2253–2256, 1984.

[163] K. Miyata, T. L. Atallah, and X. Zhu, "Lead halide perovskites: Crystal-liquid duality, phonon glass electron crystals, and large polaron formation," *Sci. Adv.*, vol. 3, no. 10, e1701469, 2017.

[164] J. Even, L. Pedesseau, C. Katan, M. Kepenekian, J.-S. Lauret, D. Sapori, and E. Deleporte, "Solid-State Physics Perspective on Hybrid Perovskite Semiconductors," *J. Phys. Chem. C*, vol. 119, pp. 10 161–10 177, 2015.

[165] O. Yaffe, A. Chernikov, Z. M. Norman, Y. Zhong, A. Velauthapillai, A. van der Zande, J. S. Owen, and T. F. Heinz, "Excitons in ultrathin organic-inorganic perovskite crystals," *Phys. Rev. B*, vol. 92, no. 4, p. 045 414, 2015.

[166] M. Bonn, K. Miyata, E. Hendry, and X. Y. Zhu, "Role of Dielectric Drag in Polaron Mobility in Lead Halide Perovskites," *ACS Energy Lett.*, vol. 2, no. 11, pp. 2555–2562, 2017.

[167] F. Thouin, S. Neutzner, D. Cortecchia, V. A. Dragomir, C. Soci, T. Salim, Y. M. Lam, R. Leonelli, A. Petrozza, A. R. S. Kandada, and C. Silva, "Stable biexcitons in two-dimensional metal-halide perovskites with strong dynamic lattice disorder," *Physical Review Materials*, vol. 2, no. 3, p. 034 001, 2018.

[168] D. Cortecchia, J. Yin, A. Bruno, S.-Z. A. Lo, G. G. Gurzadyan, S. Mhaisalkar, J.-L. Brédas, and C. Soci, "Polaron self-localization in white-light emitting hybrid perovskites," *J. Mater. Chem. C*, vol. 5, no. 11, pp. 2771–2780, 2017.

[169] H. Haug and S. W. Koch, *Quantum theory of the optical and electronic properties of semiconductors*. London: World Scientific, 2008, ISBN: 978-981-283-883-4.

[170] B. Xu, J. M. Gunn, J. M. D. Cruz, V. V. Lozovoy, and M. Dantus, "Quantitative investigation of the multiphoton intrapulse interference phase scan method for simultaneous phase measurement and compensation of femtosecond laser pulses," *J. Opt. Soc. Am. B*, vol. 23, no. 4, pp. 750–759, 2006.

[171] J Blancon, A. V. Stier, H Tsai, W Nie, C. C. Stoumpos, B Traoré, L Pedesseau, M Kepenekian, S. Tretiak, S. A. Crooker, C Katan, M. G. Kanatzidis, J. J. Crochet, J Even, and A. D. Mohite, "Unusual thickness dependence of exciton characteristics in 2D perovskite quantum wells," *ArXiv*, arXiv:1710.07653, 2017.

[172] M. Saba, M. Cadelano, D. Marongiu, F. Chen, V. Sarritzu, N. Sestu, C. Figus, M. Aresti, R. Piras, A. Geddo Lehmann, C. Cannas, A. Musinu, F. Quochi, A. Mura, and G. Bongiovanni, "Correlated electron-hole plasma in organometal perovskites.," *Nat. Commun.*, vol. 5, p. 5049, 2014.

[173] M. de Jong, L. Seijo, A. Meijerink, and F. T. Rabouw, "Resolving the ambiguity in the relation between Stokes shift and Huang-Rhys parameter," *Phys. Chem. Chem. Phys.*, vol. 17, no. 26, pp. 16 959–16 969, 2015.

[174] Y. Varshni, "Temperature dependence of the energy gap in semiconductors," *Physica*, vol. 34, no. 1, pp. 149–154, 1967.

[175] A. D. Wright, C. Verdi, R. L. Milot, G. E. Eperon, M. A. Pérez-Osorio, H. J. Snaith, F. Giustino, M. B. Johnston, and L. M. Herz, "Electron-phonon coupling in hybrid lead halide perovskites," *Nat. Commun.*, vol. 7, no. May, p. 11 755, 2016.

[176] J. Lee, E. S. Koteles, and M. O. Vassell, "Luminescence linewidths of excitons in GaAs quantum wells below 150 K," *Phys. Rev. B*, vol. 33, no. 8, pp. 5512–5516, 1986.

[177] F. D. Fuller and J. P. Ogilvie, "Experimental implementations of two-dimensional Fourier transform electronic spectroscopy.," *Ann. Rev. Phys. Chem.*, vol. 66, pp. 667–690, 2015.

[178] M. Yuan, L. N. Quan, R. Comin, G. Walters, R. Sabatini, O. Voznyy, S. Hoogland, Y. Zhao, E. M. Beauregard, P. Kanjanaboos, Z. Lu, D. H. Kim, and E. H. Sargent, "Perovskite energy funnels for efficient light-emitting diodes," *Nat. Nanotech.*, vol. 11, no. 10, pp. 872–877, 2016.

[179] X. B. Zhang, T Taliercio, S Kolliakos, and P Lefebvre, "Influence of electron-phonon interaction on the optical properties of III nitride semiconductors," *J. Phys. Condens. Matter*, vol. 13, p. 7053, 2001.

[180] C. B. Duke and G. D. Mahan, "Phonon-broadened impurity spectra I. Density of states," *Phys. Rev.*, vol. 139, A1965, 1965.

[181] A. L. Gurskii and S. V. Voitikov, "Quantum defect approach for the effect of electron-phonon coupling on impurity recombination in semiconductors," *Solid State Commun.*, vol. 112, no. 6, pp. 339–343, 1999.

[182] E. I. Rashba, "Optical spectra of phonons bound to impurity centers," *Sov. Phys. JETP*, vol. 44, pp. 166–171, 1976.

[183] A. S. Davydov, *Theory of molecular excitons*. Springer: Springer Science and Businnes Media New York, 1971.

[184] G. Batignani, G. Fumero, A. R. Srimath Kandada, G. Cerullo, M. Gandini, C. Ferrante, A. Petrozza, and T. Scopigno, "Probing femtosecond lattice displacement upon photo-carrier generation in lead halide perovskite," *Nature Commun.*, vol. 9, no. 1, p. 1971, 2018.

[185] R. M. Hochstrasser and P. N. Prasad, "Phonon sidebands of electronic transitions in molecular crystals and mixed crystals," *J. Chem. Phys.*, vol. 56, no. 6, pp. 2814–2823, 1972.

[186] O. V. Selyugin and M. A. Smondyrev, "Phase transitions and Pade approximations for Fröhlich polarons," *Phys. Status. Solidi.*, vol. 155, pp. 155–167, 1989.

[187] T. Itoh, M. Nishijima, A. I. Ekimov, C. Gourdon, A. L. Efros, and M. Rosen, "Polaron and exciton-phonon complexes in CuCl nanocrystals," *Phys. Rev. Lett.*, vol. 74, no. 9, pp. 1645–1648, 1995.

[188] M Geddo and G Iadonisi, "Polaronic Effects on Two-Dimensional Excitons," *Il Nuovo Cimento D*, vol. 12, no. 12, pp. 1641–1650, 1990.

[189] P. R. Moran, "Effects of Dynamic Lattice Distortions on the Structure of the F Band in the Cesium Halides," *Phys. Rev.*, vol. 137, no. 3A, pp. 1016–1026, 1965.

[190] A. Manchon, H. C. Koo, J. Nitta, S. M. Frolov, and R. A. Duine, "New perspectives for Rashba spin-orbit coupling," *Nat. Mater.*, vol. 14, no. 9, pp. 871–882, 2015.

[191] F. Thouin, D. A. Valverde-Chvez, C. Quarti, D. Cortecchia, I. Bargigia, D. Beljonne, A. Petrozza, C. Silva, and A. R. Srimath Kandada, "Phonon coherences reveal the polaronic character of excitons in two-dimensional lead halide perovskites," *Nature Materials*, vol. 11, pp. 349–356, 2019.

[192] J.-C. Blancon, A. V. Stier, H. Tsai, W. Nie, C. C. Stoumpos, B. Traoré, L. Pedesseau, M. Kepenekian, F. Katsutani, G. T. Noe, J. Kono, S. Tretiak, S. A. Crooker, C. Katan, M. G. Kanatzidis, J. J. Crochet, J. Even, and A. D. Mohite, "Scaling law for excitons in 2D perovskite quantum wells," *Nature Communications*, vol. 9, no. 1, p. 2254, 2018.

[193] A. R. Srimath Kandada and A. Petrozza, "Photophysics of hybrid lead halide perovskites: The role of microstructure," *Acc. Chem. Res.*, vol. 49, no. 3, pp. 536–544, 2016.

[194] D. B. Straus and C. R. Kagan, "Electrons, Excitons, and Phonons in Two-Dimensional Hybrid Perovskites: Connecting Structural, Optical, and Electronic Properties," *J. Phys. Chem. Lett.*, vol. 9, no. 6, pp. 1434–1447, 2018.

[195] L. N. Quan, Y. Zhao, F. P. Garca de Arquer, R. Sabatini, G. Walters, O. Voznyy, R. Comin, Y. Li, J. Z. Fan, H. Tan, and others, "Tailoring the energy landscape in quasi-2d halide perovskites enables efficient green-light emission," *Nano Lett.*, vol. 17, no. 6, pp. 3701–3709, 2017.

[196] R. Su, C. Diederichs, J. Wang, T. C. Liew, J. Zhao, S. Liu, W. Xu, Z. Chen, and Q. Xiong, "Room-Temperature Polariton Lasing in All-Inorganic Perovskite Nanoplatelets," *Nano Letters*, vol. 17, no. 6, pp. 3982–3988, 2017.

[197] E. P. Booker, M. B. Price, P. J. Budden, H. Abolins, Y. del Valle-Inclan Redondo, L. Eyre, I. Nasrallah, R. T. Phillips, R. H. Friend, F. Deschler, and N. C. Greenham, "Vertical Cavity Biexciton Lasing in 2D Dodecylammonium Lead Iodide Perovskites," *Adv. Opt. Mater.*, p. 1 800 616, 2018.

[198] M. Dvorak, S.-H. Wei, and Z. Wu, "Origin of the Variation of Exciton Binding Energy in Semiconductors," *Phys. Rev. Lett.*, vol. 110, no. 1, p. 016 402, 2013.

[199] T. Ishihara, J. Takahashi, and T. Goto, "Optical properties due to electronic transitions in two-dimensional semiconductors (C$_n$$H_{2n+1}$NH)PbI," *Phys. Rev. B*, vol. 42, no. 17, pp. 11 099–11 107, 1990.

[200] K. Tanaka, T. Takahashi, T. Kondo, K. Umeda, K. Ema, T. Umebayashi, K. Asai, K. Uchida, and N. Miura, "Electronic and excitonic structures of inorganic-organic perovskite-type quantum-well crystal (CHNH)PbBr," *Jap. J. Appl. Phys., Part 1*, vol. 44, no. 8, pp. 5923–5932, 2005.

[201] M. Shimizu, J. I. Fujisawa, and J. Ishi-Hayase, "Influence of dielectric confinement on excitonic nonlinearity in inorganic-organic layered semiconductors," *Phys. Rev. B*, vol. 71, no. 20, pp. 1–9, 2005.

[202] N. Kitazawa and Y. Watanabe, "Optical properties of natural quantum-well compounds (CH-C$_n$$H_{2n}$-NH)PbBr ($n$=1-4)," *J. Phys. Chem. Solids*, vol. 71, no. 5, pp. 797–802, 2010.

[203] C. Quarti, N. Marchal, and D. Beljonne, "Tuning the optoelectronic properties of 2d hybrid perovskite semiconductors with alkyl chain spacers," *J. Phys. Chem. Lett*, vol. 9, no. 12, pp. 3416 –3424, 2018.

[204] A. Sood, J Menendez, M Cardona, and K Ploog, "Resonance Raman scattering by confined LO and TO phonons in GaAs-AlAs superlattices," *Phys. Rev. Lett.*, vol. 54, no. 19, p. 2111, 1985.

[205] Z. Guo, X. Wu, T. Zhu, X. Zhu, and L. Huang, "Electron-phonon scattering in atomically thin 2d perovskites," *ACS nano*, vol. 10, no. 11, pp. 9992–9998, 2016.

[206] G. Grancini, A. R. S. Kandada, J. M. Frost, A. J. Barker, M. De Bastiani, M. Gandini, S. Marras, G. Lanzani, A. Walsh, and A. Petrozza, "Role of microstructure in the electron-hole interaction of hybrid lead halide perovskites," *Nat. Photon.*, vol. 9, no. 10, p. 695, 2015.

[207] T. Ivanovska, C. Quarti, G. Grancini, A. Petrozza, F. De Angelis, A. Milani, and G. Ruani, "Vibrational response of methylammonium lead iodide: From cation dynamics to phonon-phonon interactions," *ChemSusChem*, vol. 9, no. 20, pp. 2994–3004, 2016.

[208] M. Corno, C. Busco, B. Civalleri, and P. Ugliengo, "Periodic ab initio study of structural and vibrational features of hexagonal hydroxyapatite Ca$_10$(PO)(OH)," *Phys. Chem. Chem. Phys.*, vol. 8, no. 21, pp. 2464–2472, 2006.

[209] F. Brivio, J. M. Frost, J. M. Skelton, A. J. Jackson, O. J. Weber, M. T. Weller, A. R. Goni, A. M. Leguy, P. R. Barnes, and A. Walsh, "Lattice dynamics and vibrational spectra of the orthorhombic, tetragonal, and cubic phases of methylammonium lead iodide," *Phys. Rev. B*, vol. 92, no. 14, p. 144 308, 2015.

[210] C. Quarti, G. Grancini, E. Mosconi, P. Bruno, J. M. Ball, M. M. Lee, H. J. Snaith, A. Petrozza, and F. De Angelis, "The Raman spectrum of the CHNHPbI hybrid perovskite: Interplay of theory and experiment," *J. Phys. Chem. Lett.*, vol. 5, no. 2, pp. 279–284, 2013.

[211] L. Grisanti, Y. Olivier, L. Wang, S. Athanasopoulos, J. Cornil, and D. Beljonne, "Roles of local and nonlocal electron-phonon couplings in triplet exciton diffusion in the anthracene crystal," *Phys. Rev. B*, vol. 88, no. 3, p. 035 450, 2013.

[212] V. Coropceanu, J. Cornil, D. A. da Silva Filho, Y. Olivier, R. Silbey, and J.-L. Brédas, "Charge transport in organic semiconductors," *Chem. Rev.*, vol. 107, no. 4, pp. 926–952, 2007.

[213] O. Yaffe, Y. Guo, L. Z. Tan, D. A. Egger, T. Hull, C. C. Stoumpos, F. Zheng, T. F. Heinz, L. Kronik, M. G. Kanatzidis, and others, "Local polar fluctuations in lead halide perovskite crystals," *Phys. Rev. Lett.*, vol. 118, no. 13, p. 136 001, 2017.

[214] A. M. A. Leguy, A. R. Goi, J. M. Frost, J. Skelton, F. Brivio, X. Rodrguez-Martnez, O. J. Weber, A. Pallipurath, M. I. Alonso, M. Campoy-Quiles, M. T. Weller, J. Nelson, A. Walsh, and P. R. F. Barnes, "Dynamic disorder, phonon lifetimes, and the assignment of modes to the vibrational spectra of methylammonium lead halide perovskites," *Phys. Chem. Chem. Phys.*, vol. 18, no. 39, pp. 27 051–27 066, 2016.

[215] C. La-O-Vorakiat, H. Xia, J. Kadro, T. Salim, D. Zhao, T. Ahmed, Y. M. Lam, J.-X. Zhu, R. A. Marcus, M.-E. Michel-Beyerle, and others, "Phonon Mode Transformation Across the Orthohombic-Tetragonal Phase Transition in a Lead Iodide Perovskite CHNHPbI: A Terahertz Time-Domain Spectroscopy Approach," *J. Phys. Chem. Lett.*, vol. 7, no. 1, pp. 1–6, 2015.

[216] S. De Silvestri, G. Cerullo, and G. Lanzani, *Coherent vibrational dynamics*. CRC Press, 2008.

[217] L. Ler, C. Gadermaier, J. Crochet, T. Hertel, D. Brida, and G. Lanzani, "Coherent phonon dynamics in semiconducting carbon nanotubes: A quantitative study of electron-phonon coupling," *Phys. Rev. Lett.*, vol. 102, no. 12, p. 127 401, 2009.

[218] X. Gong, O. Voznyy, A. Jain, W. Liu, R. Sabatini, Z. Piontkowski, G. Walters, G. Bappi, S. Nokhrin, O. Bushuyev, and others, "Electron-phonon interaction in efficient perovskite blue emitters," *Nat. Mater.*, vol. 17, pp. 550–556, 2018.

[219] A. J. Neukirch, W. Nie, J.-C. Blancon, K. Appavoo, H. Tsai, M. Y. Sfeir, C. Katan, L. Pedesseau, J. Even, J. J. Crochet, and others, "Polaron stabilization by cooperative lattice distortion and cation rotations in hybrid perovskite materials," *Nano letters*, vol. 16, no. 6, pp. 3809–3816, 2016.

[220] H. Takagi, H. Kunugita, and K. Ema, "Influence of the image charge effect on excitonic energy structure in organic-inorganic multiple quantum well crystals," *Phys. Rev. B*, vol. 87, no. 12, p. 125 421, 2013.

[221] H. Zhu, K. Miyata, Y. Fu, J. Wang, P. P. Joshi, D. Niesner, K. W. Williams, S. Jin, and X.-Y. Zhu, "Screening in crystalline liquids protects energetic carriers in hybrid perovskites," *Science*, vol. 353, no. 6306, pp. 1409–1413, 2016.

[222] J. Calabrese, N. L. Jones, R. L. Harlow, N. Herron, D. L. Thorn, and Y. Wang, "Preparation and characterization of layered lead halide compounds," *J. Am. Chem. Soc.*, vol. 113, no. 6, pp. 2328–2330, 1991.

[223] R. Dovesi, A. Erba, R. Orlando, C. M. Zicovich-Wilson, B. Civalleri, L. Maschio, M. Rérat, S. Casassa, J. Baima, S. Salustro, and others, "Quantum-mechanical condensed matter simulations with CRYSTAL," *Wiley Interdisciplinary Reviews: Computational Molecular Science*, e1360, 2018.

[224] J. P. Perdew, K. Burke, and M. Ernzerhof, "Generalized gradient approximation made simple," *Phys. Rev. Lett.*, vol. 77, no. 18, p. 3865, 1996.

[225] H. J. Monkhorst and J. D. Pack, "Special points for Brillouin-zone integrations," *Phys. Rev. B*, vol. 13, no. 12, p. 5188, 1976.

[226] G. Grancini and M. K. Nazeeruddin, "Dimensional tailoring of hybrid perovskites for photovoltaics," *Nature Reviews Materials*, vol. 4, pp. 4–22, 2018.

[227] Y. Chen, Y. Sun, J. Peng, J. Tang, K. Zheng, and Z. Liang, "2D Ruddlesden-Popper perovskites for optoelectronics," *Advanced Materials*, vol. 30, no. 2, p. 1 703 487, 2018.

[228] M. D. Smith, B. A. Connor, and H. I. Karunadasa, "Tuning the Luminescence of Layered Halide Perovskites," *Chemical Reviews*, vol. 119, no. 5, pp. 3104–3139, 2019.

[229] R. Quintero-Bermudez, A. Gold-Parker, A. H. Proppe, R. Munir, Z. Yang, S. O. Kelley, A. Amassian, M. F. Toney, and E. Sargent, "Compositional and orientational control in metal halide perovskites of reduced dimensionality," *Nature Materials*, vol. 17, no. 10, p. 900, 2018.

[230] A. Pereverzev, E. R. Bittner, and I. Burghardt, "Energy and charge-transfer dynamics using projected modes," *The Journal of Chemical Physics*, vol. 131, no. 3, p. 034 104, 2009.

[231] X. Yang and E. R. Bittner, "Intramolecular Charge- and Energy-Transfer Rates with Reduced Modes: Comparison to Marcus Theory for Donor-Bridge-Acceptor Systems," *The Journal of Physical Chemistry A*, vol. 118, no. 28, pp. 5196–5203, 2014.

[232] ——, "Computing intramolecular charge and energy transfer rates using optimal modes," *The Journal of Chemical Physics*, vol. 142, no. 24, p. 244 114, 2015.

[233] X. Yang, T. Keane, M. Delor, A. J.H. M. Meijer, J. Weinstein, and E. R. Bittner, "Identifying electron transfer coordinates in donor-bridge-acceptor systems using mode projection analysis," *Nature Communications*, vol. 8, p. 14 554, 2017.

[234] X. Wu, M. T. Trinh, D. Niesner, H. Zhu, Z. Norman, J. S. Owen, O. Yaffe, B. J. Kudisch, and X.-Y. Zhu, "Trap states in lead iodide perovskites," *Journal of the American Chemical Society*, vol. 137, no. 5, pp. 2089–2096, 2015.

[235] D. Giovanni, W. K. Chong, Y. Y. F. Liu, H. A. Dewi, T. Yin, Y. Lekina, Z. X. Shen, N. Mathews, C. K. Gan, and T. C. Sum, "Coherent Spin and Quasiparticle Dynamics in Solution-Processed Layered 2D Lead Halide Perovskites," *Advanced Science*, vol. 5, no. 10, p. 1 800 664, 2018.

[236] S. Schmitt-Rink, D. S. Chemla, and D. A. B. Miller, "Theory of transient excitonic optical nonlinearities in semiconductor quantum-well structures," *Physical Review B*, vol. 32, no. 10, pp. 6601–6609, 1985.

[237] M. B. Price, J. Butkus, T. C. Jellicoe, A. Sadhanala, A. Briane, J. E. Halpert, K. Broch, J. M. Hodgkiss, R. H. Friend, and F. Deschler, "Hot-carrier cooling and photoinduced refractive index changes in organic-inorganic lead halide perovskites," *Nature Communications*, vol. 6, p. 8420, 2015.

[238] D. Giovanni, W. K. Chong, H. A. Dewi, K. Thirumal, I. Neogi, R. Ramesh, S. Mhaisalkar, N. Mathews, and T. C. Sum, "Tunable room-temperature spin-selective optical Stark effect in solution-processed layered halide perovskites," *Science Advances*, vol. 2, no. 6, e1600477, 2016.

[239] S Hunsche, H Heesel, A Ewertz, H Kurz, and J. Collet, "Spectral-hole burning and carrier thermalization in GaAs at room temperature," *Physical Review B*, vol. 48, no. 24, p. 17 818, 1993.

[240] A. Nitzan, *Chemical dynamics in condensed phases: relaxation, transfer and reactions in condensed molecular systems*. Oxford university press, 2006.

[241] A. Pereverzev and E. R. Bittner, "Time-convolutionless master equation for mesoscopic electron-phonon systems," *The Journal of Chemical Physics*, vol. 125, no. 10, p. 104 906, 2006.

[242] F. Thouin, D. Cortecchia, A. Petrozza, A. R. S. Kandada, and C. Silva, "Enhanced screening and spectral diversity in many-body elastic scattering of excitons in two-dimensional hybrid metal-halide perovskites," 2019.

[243] G. Xing, B. Wu, X. Wu, M. Li, B. Du, Q. Wei, J. Guo, E. K. L. Yeow, T. C. Sum, and W. Huang, "Transcending the slow bimolecular recombination in lead-halide perovskites for electroluminescence," *Nature Communications*, vol. 8, p. 14 558, 2017.

[244] K. Abdel-Baki, F. Boitier, H. Diab, G. Lanty, K. Jemli, F. Lédée, D. Garrot, E. Deleporte, and J. S. Lauret, "Exciton dynamics and non-linearities in two-dimensional hybrid organic perovskites," *Journal of Applied Physics*, vol. 119, no. 6, 2016.

[245] E. W. Martin, J. Horng, H. G. Ruth, E. Paik, M.-H. Wentzel, H. Deng, and S. T. Cundiff, "Encapsulation Narrows Excitonic Homogeneous Linewidth of Exfoliated $MoSe_2$ Monolayer," 2018.

[246] I. Kylnp and H. P. Komsa, "Binding energies of exciton complexes in transition metal dichalcogenide monolayers and effect of dielectric environment," *Phys. Rev. B*, vol. 92, no. 20, p. 205 418, 2015.

[247] A. Honold, L. Schultheis, J. Kuhl, and C. W. Tu, "Collision broadening of two-dimensional excitons in a GaAs single quantum well," *Physical Review B*, vol. 40, no. 9, pp. 6442–6445, 1989.

[248] H. P. Wagner, A. Schtz, R. Maier, W. Langbein, and J. M. Hvam, "Coherent optical nonlinearities and phase relaxation of quasi-three-dimensional and quasi-two-dimensional excitons in ZnS_xSe_{1-x}/ZnSe structures," *Physical Review B*, vol. 56, no. 19, pp. 12 581–12 588, 1997.

[249] V. Alexandru Dragomir, S. Neutzner, C. Quarti, D. Cortecchia, A. Petrozza, S. Roorda, D. Beljonne, R. Leonelli, A. R. S. Kandada, and C. Silva, "Lattice vibrations and dynamic disorder in two-dimensional hybrid lead-halide perovskites," 2018.

[250] P. P. Joshi, S. F. Maehrlein, and X. Zhu, "Dynamic Screening and Slow Cooling of Hot Carriers in Lead Halide Perovskites," *Advanced Materials*, p. 1 803 054, 2019.

[251] C. Wehrenfennig, M. Liu, H. J. Snaith, M. B. Johnston, and L. M. Herz, "Charge-carrier dynamics in vapour-deposited films of the organolead halide perovskite $CH_3NH_3PbI_{3-x}Clx$," *Energy Environ. Sci.*, vol. 7, no. 7, pp. 2269–2275, 2014.

[252] T. M. Brenner, D. A. Egger, A. M. Rappe, L. Kronik, G. Hodes, and D. Cahen, "Are Mobilities in Hybrid Organic-Inorganic Halide Perovskites Actually High?" *The Journal of Physical Chemistry Letters*, vol. 6, no. 23, pp. 4754–4757, 2015.

[253] S. A. March, D. B. Riley, C. Clegg, D. Webber, X. Liu, M. Dobrowolska, J. K. Furdyna, I. G. Hill, and K. C. Hall, "Four-Wave Mixing in Perovskite Photovoltaic Materials Reveals Long Dephasing Times and Weaker Many-Body Interactions than GaAs," *ACS Photonics*, vol. 4, no. 6, pp. 1515–1521, 2017.

[254] H. Utzat, W. Sun, A. E. Kaplan, F. Krieg, M. Ginterseder, B. Spokoyny, N. D. Klein, K. E. Shulenberger, C. F. Perkinson, M. V. Kovalenko, and others, "Coherent single-photon emission from colloidal lead halide perovskite quantum dots," *Science*, vol. 363, no. 6431, pp. 1068–1072, 2019.

[255] A Fieramosca, L Polimeno, V Ardizzone, L De Marco, M Pugliese, V Maiorano, M De Giorgi, L Dominici, G Gigli, D Gerace, and others, "Two-Dimensional hybrid perovskites sustaining strong polariton interactions at room temperature," 2018.

[256] A. Brehier, R. Parashkov, J. S. Lauret, and E. Deleporte, "Strong exciton-photon coupling in a microcavity containing layered perovskite semiconductors," *Applied Physics Letters*, vol. 89, no. 17, p. 171 110, 2006.

[257] S. Z. Butler, S. M. Hollen, L. Cao, Y. Cui, J. A. Gupta, H. R. Gutiérrez, T. F. Heinz, S. S. Hong, J. Huang, A. F. Ismach, E. Johnston-Halperin, M. Kuno, V. V. Plashnitsa, R. D. Robinson, R. S. Ruoff, S. Salahuddin, J. Shan, L. Shi, M. G. Spencer, M. Terrones, W. Windl, and J. E. Goldberger, "Progress, challenges, and opportunities in two-dimensional materials beyond graphene," *ACS Nano*, vol. 7, no. 4, pp. 2898–2926, 2013.

[258] Q. H. Wang, K. Kalantar-Zadeh, A. Kis, J. N. Coleman, and M. S. Strano, "Electronics and optoelectronics of two-dimensional transition metal dichalcogenides," *Nat. Nanotech.*, vol. 7, no. 11, pp. 699–712, 2012.

[259] M. M. Ugeda, A. J. Bradley, S.-F. Shi, F. H. da Jornada, Y. Zhang, D. Y. Qiu, W. Ruan, S.-K. Mo, Z. Hussain, Z.-X. Shen, F. Wang, S. G. Louie, and M. F. Crommie, "Giant bandgap renormalization and excitonic effects in a monolayer transition metal dichalcogenide semiconductor," *Nat. Mater.*, vol. 13, no. 12, pp. 1091–1095, 2014.

[260] K. He, N. Kumar, L. Zhao, Z. Wang, K. F. Mak, H. Zhao, and J. Shan, "Tightly bound excitons in monolayer WSe_2," *Phys. Rev. Lett.*, vol. 113, no. 2, p. 026 803, 2014.

[261] A. Chernikov, T. C. Berkelbach, H. M. Hill, A. Rigosi, Y. Li, O. B. Aslan, D. R. Reichman, M. S. Hybertsen, and T. F. Heinz, "Exciton binding energy and nonhydrogenic Rydberg series in monolayer WS_2," *Phys. Rev. Lett.*, vol. 113, no. 7, p. 076 802, 2014.

[262] X. Liu, T. Galfsky, Z. Sun, F. Xia, E.-c. Lin, Y.-H. Lee, S. Kéna-Cohen, and V. M. Menon, "Strong light-matter coupling in two-dimensional atomic crystals," *Nat. Photon.*, vol. 9, no. 1, pp. 30–34, 2014.

[263] L. Pedesseau, D. Sapori, B. Traore, R. Robles, H. H. Fang, M. A. Loi, H. Tsai, W. Nie, J. C. Blancon, A. Neukirch, S. Tretiak, A. D. Mohite, C. Katan, J. Even, and M. Kepenekian, "Advances and Promises of Layered Halide Hybrid Perovskite Semiconductors," *ACS Nano*, vol. 10, no. 11, pp. 9776–9786, 2016.

[264] K. Hattori, "Exciton Binding Energies in Polar Crystals," *Physica Status Solidi (B)*, vol. 76, no. 1, pp. 281–287, 1976.

[265] X. Wu, L. Z. Tan, X. Shen, T. Hu, K. Miyata, M. T. Trinh, R. Li, R. Coffee, S. Liu, D. A. Egger, I. Makasyuk, Q. Zheng, A. Fry, J. S. Robinson, M. D. Smith, B. Guzelturk, H. I. Karunadasa, X. Wang, X. Zhu, L. Kronik, A. M. Rappe, and A. M. Lindenberg, "Light-induced picosecond rotational disordering of the inorganic sublattice in hybrid perovskites," *Sci. Adv.*, vol. 3, no. 7, e1602388, 2017.

[266] M. D. Smith, L. Pedesseau, M. Kepenekian, I. C. Smith, C. Katan, J. Even, and H. I. Karunadasa, "Decreasing the electronic confinement in layered perovskites through intercalation," *Chem. Sci.*, vol. 8, no. 3, pp. 1960–1968, 2017.

[267] M. D. Smith, A. Jaffe, E. R. Dohner, A. M. Lindenberg, and H. I. Karunadasa, "Structural origins of broadband emission from layered Pb-Br hybrid perovskites," *Chem. Sci.*, vol. 8, no. 6, pp. 4497–4504, 2017.

[268] C. M. M. Soe, C. C. Stoumpos, M. Kepenekian, B. Traoré, H. Tsai, W. Nie, B. Wang, C. Katan, R. Seshadri, A. D. Mohite, J. Even, T. J. Marks, and M. G. Kanatzidis, "New Type of 2D Perovskites with Alternating Cations in the Interlayer Space, $C(NH_2)_3(CH_3NH_3)_nPb_nI_{3n+1}$: Structure, Properties, and Photovoltaic Performance," *J. Am. Che. Soc.*, no. 139, pp. 16 297–16 309, 2017.

[269] V. I. Klimov, "Mechanisms for photogeneration and recombination of multiexcitons in semiconductor nanocrystals: Implications for lasing and solar energy conversion," *J. Phys. Chem. B*, vol. 110, no. 34, pp. 16 827–16 845, 2006.

[270] Y. Kato, D. Ichii, K. Ohashi, H. Kunugita, K. Ema, K. Tanaka, T. Takahashi, and T. Kondo, "Extremely large binding energy of biexcitons in an organic-inorganic quantum-well material $(C_4H_9NH_3)_2PbBr_4$," *Solid State Commun.*, vol. 128, no. 1, pp. 15 –18, 2003.

[271] J.-i. Fujisawa and T. Ishihara, "Excitons and biexcitons bound to a positive ion in a bismuth-doped inorganic-organic layered lead iodide semiconductor," *Phys. Rev. B*, vol. 70, no. 20, p. 205 330, 2004.

[272] L. Ni, U. Huynh, A. Cheminal, T. H. Thomas, R. Shivanna, T. F. Hinrichsen, S. Ahmad, A. Sadhanala, and A. Rao, "Real-Time Observation of Exciton-Phonon Coupling Dynamics in Self-Assembled Hybrid Perovskite Quantum Wells," *ACS Nano*, no. 11, pp. 10 834–10 843, 2017.

[273] T. Ishihara, "Optical properties of Pb-based inorganic-organic perovskites," in *Optical properties of low-dimensional materials (Volume I)*, T Ogawa and Y. Kanemitsu, Eds., World Scientific, 1996, pp. 288–339.

[274] Y Abid, "X-ray and Raman studies of the re-entrant phase and phase transitions in the perovskite-type layer compound bis(n-propylammonium) lead tetrabromide," *J. Phys. Condens. Matter*, vol. 6, no. 32, pp. 6447–6454, 1994.

[275] A. Caretta, R. Miranti, R. W. A. Havenith, E. Rampi, M. C. Donker, G. R. Blake, M. Montagnese, A. O. Polyakov, R. Broer, T. T. M. Palstra, and P. H. M. van Loosdrecht, "Low-frequency Raman study of the ferroelectric phase transition in a layered $CuCl_4$-based organic-inorganic hybrid," *Phys. Rev. B*, vol. 89, no. 2, p. 024 301, 2014.

[276] G. Moody, I. A. Akimov, H. Li, R. Singh, D. R. Yakovlev, G. Karczewski, M. Wiater, T. Wojtowicz, M. Bayer, and S. T. Cundiff, "Coherent coupling of excitons and trions in a photoexcited CdTe/CdMgTe quantum well," *Phys. Rev. Lett.*, vol. 112, no. 9, p. 097 401, 2014.

[277] M. Koziski, S. Garrett-Roe, and P. Hamm, "Vibrational spectral diffusion of CN- in water," *Chem. Phys.*, vol. 341, no. 1-3, pp. 5–10, 2007.

[278] G. Batignani, G. Fumero, A. R. S. Kandada, G. Cerullo, M. Gandini, C. Ferrante, A. Petrozza, and T. Scopigno, "Probing Femtosecond Lattice Displacement upon Photo-carrier generation in Lead Halide Perovskite," *ArXiv*, p. 1705.08687, 2017.

[279] L. Yang and S. Mukamel, "Two-Dimensional Correlation Spectroscopy of Two-Exciton Resonances in Semiconductor Quantum Wells," *Phys. Rev. Lett.*, vol. 100, no. 5, p. 057 402, 2008.

[280] E. O. Kane, *Pollmann-Buttner variational method for excitonic polarons*, 12. 1978, vol. 18.

[281] A. R. Srimath Kandada, S. Neutzner, V. D'Innocenzo, F. Tassone, M. Gandini, Q. A. Akkerman, M. Prato, L. Manna, A. Petrozza, and G. Lanzani, "Non-linear carrier Interactions in lead halide perovskites and the role of defects.," *J. Am. Chem. Soc.*, vol. 138, pp. 13 604–13 611, 2016.

[282] P. Jepsen, D. Cooke, and M. Koch, "Terahertz spectroscopy and imaging - Modern techniques and applications," *Laser & Photonics Reviews*, vol. 5, no. 1, pp. 124–166, Jan. 2011.

[283] E. Cinquanta, D. Meggiolaro, S. G. Motti, M. Gandini, M. J. Alcocer, Q. A. Akkerman, C. Vozzi, L. Manna, F. De Angelis, A. Petrozza, and S. Stagira, "Ultrafast THz Probe of Photoinduced Polarons in Lead-Halide Perovskites," *Physical Review Letters*, vol. 122, no. 16, p. 166 601, Apr. 2019.

[284] M. Chergui and A. H. Zewail, "Electron and X-Ray Methods of Ultrafast Structural Dynamics: Advances and Applications," *ChemPhysChem*, vol. 10, no. 1, pp. 28–43, Jan. 2009.

[285] M. R. Otto, L. P. Ren de Cotret, D. A. Valverde-Chavez, K. L. Tiwari, N. mond, M. Chaker, D. G. Cooke, and B. J. Siwick, "How optical excitation controls the structure and properties of vanadium dioxide," *Proceedings of the National Academy of Sciences*, vol. 116, no. 2, pp. 450–455, Jan. 2019.

[286] M. J. Stern, L. P. Ren de Cotret, M. R. Otto, R. P. Chatelain, J.-P. Boisvert, M. Sutton, and B. J. Siwick, "Mapping momentum-dependent electron-phonon coupling and nonequilibrium phonon dynamics with ultrafast electron diffuse scattering," *Physical Review B*, vol. 97, no. 16, p. 165 416, Apr. 2018.

[287] H. Ma, Y. Ma, H. Wang, C. Slebodnick, A. Alatas, J. J. Urban, and Z. Tian, "Experimental Phonon Dispersion and Lifetimes of Tetragonal $CH_3NH_3PbI_3$ Perovskite Crystals," *The Journal of Physical Chemistry Letters*, vol. 10, no. 1, pp. 1–6, Jan. 2019.

[288] W. H. Sio, C. Verdi, S. Ponc, and F. Giustino, "Polarons from First Principles, without Supercells," *Physical Review Letters*, vol. 122, no. 24, p. 246 403, Jun. 2019.

[289] ——, "Ab-initio theory of polarons: Formalism and applications," *Physical Review B*, vol. 99, no. 23, p. 235 139, Jun. 2019.

[290] M.-H. Tremblay, F. Thouin, J. Leisen, J. Bacsa, A. Kandada, J. Hoffman, M. Kanatzidis, A. Mohite, C. Silva, S. Barlow, and S. Marder, "$(4NPEA)_2PbI_4$ (4NPEA = 4-nitrophenylethylammonium): Structural, NMR, and optical properties of a 3 by 3 corrugated 2D hybrid perovskite," *Journal of the American Chemical Society*, 2019.

[291] Ueda T., Shimizu K., Ohki H., and Okuda T., "13C CP/MAS NMR Study of the Layered Compounds $[(C_6H_5CH_2CH_2NH_3)_2CH_3NH_3]_{n-1}PbnI_{n+1}$ (n = 1, 2)," *Zeitschrift für Naturforschung A*, vol. 51, no. 8, p. 910, 2014.

[292] P. W. Anderson, "Absence of Diffusion in Certain Random Lattices," *Physical Review*, vol. 109, no. 5, pp. 1492–1505, Mar. 1958.